Understanding the Interactions of Luminescent Coinage Metal Nanoclusters with Target Analytes Using Various Spectroscopic and Microscopic Techniques

By

Amit Akhuli
CHEM11201804010

National Institute of Science Education and Research
Bhubaneswar, Odisha

A thesis submitted to the
Board of Studies in Chemical Sciences
In partial fulfilment of requirements
for the degree of

DOCTOR OF PHILOSOPHY
of
HOMI BHABHA NATIONAL INSTITUTE

January, 2024

Homi Bhabha National Institute

Recommendations of the Viva Voce Committee

As members of the Viva Voce Committee, we certify that we have read the dissertation prepared by Mr. Amit Akhuli entitled "**Understanding the Interactions of Luminescent Coinage Metal Nanoclusters with Target Analytes Using Various Spectroscopic and Microscopic Techniques**" and recommend that it may be accepted as fulfilling the thesis requirement for the award of Degree of Doctor of Philosophy.

Chairman	(Name: Prof. Alagar Srinivasan)	Date: 16.04.'24
Guide/ Convenor	(Name: Dr. Moloy Sarkar)	Date: 16.04.2024
Co-guide (if any)		Date:
Examiner	(Prof. Tushar Kanti Mukherjee)	Date: 16.04.2024
Member 1	(Name: Dr. Sharanappa Nembenna)	Date: 16.04.2024
Member 2	(Name: Dr. Bhargava B. L)	Date: 16.04.2024
Member 3	(Name: Dr. Yatendra Singh Chaudhary)	Date: 16.04.2024

Final approval and acceptance of this thesis is contingent upon the candidate's submission of the final thesis copies to HBNI. I/We hereby certify that I/we have read this thesis prepared under my/our direction and recommend that it may be accepted as fulfilling the thesis requirement.

Date: 16.04.2024	Signature	Signature
Place: NISER	Co-guide (if any)	Guide

STATEMENT BY AUTHOR

This dissertation has been submitted in partial fulfilment of requirements for an advanced degree at Homi Bhabha National Institute (HBNI) and is deposited in the library to be made available to borrowers under rules of the HBNI. Brief quotations from this dissertation are allowable without special permission, provided that accurate acknowledgement of source is made. Requests for permission for extended quotation from or reproduction of this manuscript in whole or in part may be granted by the Competent Authority of HBNI when in his or her judgment the proposed use of the material is in the interests of scholarship. In all other instances, however, permission must be obtained from the author.

Amit Akhuli

DECLARATION

I, hereby declare that the investigation presented in the thesis has been carried out by me. The work is original and has not been submitted earlier as a whole or in part for a degree/diploma at this or any other Institution / University.

Amit Akhuli

LIST OF PUBLICATIONS

1. [#] **Akhuli, A**.; Chakraborty, D.; Agrawal, K. A.; Sarkar, M. Probing the Interaction of Bovine Serum Albumin with Copper Nanoclusters: Realization of Binding Pathway Different from Protein Corona. *Langmuir* ***202*****1,** 37, 1823−1837.
2. [#] **Akhuli, A**,; Preeyanka, N.; Chakraborty, D.; Sarkar, M. Turn-Off Detection of Reactive Oxidative Species and Turn-On Detection of Antioxidants Using Fluorescent Copper Nanoclusters. *ACS Appl. Nano Mater.* ***2022***, 5, 4, 5826–5837.
3. [#]**Akhuli, A**,; Chakraborty, D.; Preeyanka, N.; Dora, S. A.; Sarkar, M. Copper Nanoclusters as an Effective Enzyme Inhibitor on the Activity Modulation of α Chymotrypsin. *ACS Appl. Nano Mater.* ***2023***, 6, 6, 4910–4924.
4. [#]**Akhuli, A**,; Mahanty, A,; Chakraborty, D.; Ligand Mediated Surface Restructuring of Copper Nanoclusters and Its Impact on the Reduction of 4-Nitrophenol to 4-Aminophenol. (Manuscript communicated)
5. [#]**Akhuli, A**,; Preeyanka, N.; Chakraborty, D.; Sarkar, M.. Understanding the mechanism of the energy transfer process from non-plasmonic fluorescence bimetallic nanoparticles to plasmonic gold nanoparticles. *Phys. Chem. Chem. Phys.* ***2023***, 25, 17470-17481.
6. **Akhuli, A**,; Mahanty, A,; Barik, S.; Mahapatra, A.; Chakraborty, D.; Chakraborty, D.; Sarkar, M. Understanding the Resonance Energy Transfer between Fluorescencent Bimetallic Nanoparticles and Organic Dye molecules. *ISRAPS Bulletin* **2024,** 36, 24-34.
7. Banerjee, S.**; Akhuli, A**,; Sarkar, M. Probing the Influence of Alkyl Chain Length on the Aggregation Behaviour of Some Naphthalene Sulphonamide Derivatives through Spectroscopic and Microscopic. *Chem. Phys.* ***2023***, 565, 111762.
8. Chakraborty, D.; **Akhuli, A**,; Preeyanka, N.; Sarkar, M. Energy-Transfer-Induced Enhanced Valley Splitting of Excitonic Emission of Inorganic CdTe@ZnS QDs in the Presence of Organic J-Aggregates: A Spectroscopic Insight into the Efficient Exciton (Inorganic)–Exciton (Organic) Coupling. *J. Phys. Chem. C* ***2023***, 127, 10, 5082–5089.
9. Preeyanka, N.; **Akhuli, A**,; Dey, H.; Chakraborty, D.; Rahaman, A.; Sarkar , M.Realization of a Model-Free Pathway for Quantum Dot−Protein Interaction Beyond Classical Protein Corona or Protein Complex. *Langmuir* ***2022***, 38, 34, 10704-10715.

10. Preeyanka, N.; Tanmay Goswami, T.; Ramchandra Saha, R.; **Akhuli, A**,; Dehury, K. A.; Sarkar, M. Defect-Mediated Charge Carrier Recombination of Zinc–Silver–Indium Sulfide QDs in the Presence of Naphthoquinone Derivatives: An Insight into the Interfacial Surface Dynamics. *J. Phys. Chem. C* ***2022***, 126, 15838−15848.
11. Chakraborty,D.; Preeyanka, N.; **Akhuli, A**,; Sarkar, M. Enhancing the Stability and Photoluminescence Quantum Yield of CsPbX3 (X = Cl and Br) Perovskite Nanocrystals by Treatment with Imidazolium-Based Ionic Liquids through Surface Modification *J. Phys. Chem. C* ***2021***, 125, 48, 26652–26660.

List of publications pertaining to the thesis.

Amit Akhuli

Amit Akhuli

CONFERENCE/SYMPOSIUM

1. Presented a flash presentation in 14th National Symposium on Radiation & Photochemistry, (NSRP-2021) held at Indian Institute of Technology Gandhinagar, Gandhinagar.[25th – 26th June, 2021]
2. Present poster in international conference on "aggregation-induced emission-from fundamentals to applications" (ICAIEFA2022), organized by department of chemistry, BITS Pilani. [16th – 18th December, 2022]
3. Presented poster in "National Workshop on Fluorescence and Raman Spectroscopy", organized by IIT Bombay, Mumbai, India. [7th – 12th December, 2020]
4. Presented poster in International E-conference on Advances in Chemical Research (ACR-2021) Organized by department of chemistry, Institute of Science, GITAM Deemed to be University, Visakhapatnam. [19th - 20th April 2021]
5. Presented poster in " 36th Annual Conference of Orissa Chemical Society and National Conference on Advances in Materials Chemistry and Applications (OCS-AMCA-2022)" organised by department of chemistry, utkal university, Bhubaneswar, Odisha, India. [18th-19th December, 2022]

Amit Akhuli

Amit Akhuli

Dedicated

To

My Beloved Parents and Sister

ACKNOWLEDGEMENTS

I extend my heartfelt gratitude to my supervisor, Dr. Moloy Sarkar, for his invaluable guidance, which played a crucial role in the successful completion of this thesis work. I am deeply greateful for his unwavering support, both in the professional and personal life, throughout this Ph.D. journey. His mentorship, encouragement, and insightful advice have been instrumental in my academic journey, and I am truly thankful for his contributions to my personal and professional growth.

I express my gratitude to Prof. Hirendra Nath Ghosh (Director, NISER), Prof. Sudhakar Panda (Former Director, NISER), and Prof. T.K. Chandrasekhar (Founder Director, NISER) for their efforts in establishing well-equipped research facilities at NISER. I extend my sincere thanks to Dr. Pranay Swain, the Dean of Academic Affairs at NISER, for his understanding and support in addressing various academic issues. I want to express my gratitude to my thesis committee members: Prof. Alagar Srinivasan, Dr. Bhargava B. L, Dr. Sharanappa Nembenna, and Dr. Yatendra Singh Chaudhary, for their invaluable suggestions during my Ph.D. tenure. I wish to extend my acknowledgement to my course instructors, Dr. Upakarasamy Louderaj, Dr. A. Srinivasan, Dr. Himanshu Sekhar Biswal, Dr. Bidraha Bag, and Dr. Sudip Barman, for their dedicated teaching during my coursework. I express my acknowledgement to the current Chairperson, Dr. Sharanappa Nembenna, and former Chairpersons, Dr. Himansu S. Biswal and Dr. A. Srinivasan, of the School of Chemical Sciences (SCS) during my research tenure at NISER. I am grateful to all the faculty members, scientific officers (Dr. Arun Kumar and Dr. Priyanka Pandey), and the non-teaching staff of School of Chemical Sciences (SCS) department for creating a conducive and supportive environment. I am greateful to NISER, Bhubaneswar, for furnishing appropriate infrastructure that facilitated my research endeavours. I also acknowledge to the Department of Science and Technology (DST) for providing financial support.

I want to convey my warm and sincere thanks to both my present and former lab members for making this journey enjoyable and memorable. I express my sincere gratitude to Dr. Debasish Majhi, Dr. Muhaiminul Islam and Dr. Lakkoji Satish for their invaluable advice and constructive comments, which have greatly contributed to the successful execution of meaningful research work. I greatly enjoyed my time with Somnath da, who supported me academically and personally by sharing valuable insights and perspectives. I will surely miss the delicious food cooked by Somnath Da.

My PhD journey would be incomplete without expressing gratitude to Preeyanka di. I am sincerely thankful for the enriching discussions on experiments, analysis, and fundamental research concepts. Foremost, I am greateful to her for her caring nature and for fostering a homely atmosphere and creating a supportive environment during our research journey. I am grateful to Manjari di for her invaluable support in my professional and personal life. I feel fortunate to have Sahadev Bhaina as a senior and a friend, always standing beside me in every situation throughout this journey. The countless memories we created inside and outside the lab are something I will undoubtedly cherish.

The friendship with Debabrata and Amita means a lot to me. The times we laughed, shared, and took care of each other are memories I'll always remember. Debu is like a brother with whom I openly share and discuss every facet of my life. The kindness and helpful manner of Amita have left a lasting imprint on my life. I appreciate the moments when we poke fun at each other, adding a delightful and light-hearted dimension to our connection.

A heartfelt thanks to my dear juniors, Joyoti, Jyoti, Rashmita, Yashaswini, and Subhakant, for infusing the final stages of my Ph.D. journey with joy and laughter. I take immense pleasure in expressing my heartfelt gratitude to Aditi for her valuable assistance in my research work and for providing unwavering mental support. I will also miss the time spent with Dinesh, Ramya, Biswa, Aditya, Nilesh and Aradhana in this journey. I extend my gratitude to Aman for his valuable contributions in gearing up my research journey. I would like to acknowledge Simanchal and Debasish da for helping me with biological studies.

I will always cherish my hostel days, filled with fun, enjoyment, and memorable moments of gossiping with Tanmoy da, Shyamal da, Milan da, Ashis, Sudip, Rahul, and Surajit. Parties, late-night discussions, and travels with the DAT'S group (Debu, Amit, Tanmoy, and Sahadev) will forever hold a special place in my heart. My Ph.D. journey has been truly remarkable due to the meaningful associations with Sushanta, Nachiketa, Pradeep, Subhashini, Ayendrila, Shubhashree, Sonali, Prajna, Rakesh, Unmesh, and Subrata. I would also like to express my gratitude to my dear friends Swadesh, Santosh, Sudip, Sintu, Sourav Nandi, Sourav Kundu, and Subhajit da for their helps in my academic and personal life.

I extend my sincere regards to all the teachers who guided me in the right direction, both personally and professionally, at various stages of my life. My sincere gratitude to my Dadu (maternal and paternal grandfather) and Thakuma (maternal and paternal grandmother) for their blessings in reaching this platform. I also like to thank my extended family members,

kaku(s) (uncles), kakima(s)(aunties), my cousins brothers and sisters for their individual contributions and support.

Finally, I am happy to express my gratitude to my parents. My sincere appreciation goes to my baba (Sailen Akhuli) for his constant support, blessings, love and scacrifices to fullfil my wishes. My humble words are not enough to express my feelings for him. I have learned a lot of things from him, shaping the person I am today. The ability to do hard work is one of the components that I have got a little bit from him that makes me what I am. My heartfelt thanks go to my Maa (Sandhya Akhuli) for her unconditional love and blessings. Learning to be simple and mentally strong, qualities I've acquired from her, has helped me overcome various challenging situations in my life. I am deeply thankful to my buni, (sister, Suchitra Akhuli) who always felt proud of me anytime, anywhere.

Lastly, I express my deep appreciation to all those who have played a role in my life.

Foremost, my gratitude goes to the Almighty for granting me the courage and strength to navigate the challenges of my real life.

CONTENTS

Synopsis

In recent years, research related to nanomaterials has emerged as one of the most cutting-edge and modish areas of scientific exploration.[1-4] It has been demonstrated that nanomaterials, due to their smaller size (nanometre length scale), exhibit very different physical and chemical properties as compared to their bulk counterpart. These interesting properties of the nanoscale materials have facilitated the interdisciplinary research involving these systems.[5-9] Among these nanomaterials, metal nanoclusters (MNCs) have garnered significant attention from researchers due to their ultra-small size (<2 nm), low toxicity, advantageous optical properties, and excellent water solubility.[10-13] Even though, substantial research works are directed towards probing the interactions of larger-sized nanomaterials with various target analytes, studies on the interactions of MNCs with important analytes are still in their infancy.[1, 14-16] Moreover, knowledge about their interfacial chemistry is still not adequate. As a result of these issues, understanding of how MNCs communicate with target analytes is rather limited. Therefore, to fill this knowledge gap, further investigations on the said aspects are very much essential. Understanding the behaviour of MNCs, both in the absence and presence of different analytes, is expected to provide valuable information not only to comprehend the fundamental mechanisms governing their actions but also to generate knowledge that can be applied to various MNC-mediated applications such as bio-analysis, bioimaging, nanomedicine, sensing, optoelectronics, catalysis, energy harvesting etc.[10, 17, 18] The primary objective of this thesis is basically to address the aforementioned issues. Specifically, the fundamentals behind the interaction of luminescent coinage metal nanoclusters with biologically and environmentally important analytes have been investigated in the present thesis work. Attempts have also been made to understand the pivotal role of the surface chemistry of MNCs on the binding events with target analytes as well as on the field

of catalysis. All the above studies have been carried out by employing several spectroscopic and microscopic techniques at both ensemble average and single particle levels.

Organization of thesis

The current thesis has been divided into seven chapters. The contents of each chapters of the present thesis are briefly described below.

Chapter 1: Introduction

Chapter 1 serves as a comprehensive introduction to a wide range of nanomaterials and their optoelectronic properties. This chapter has initially categorized inorganic nanomaterials on the basis of particle size, which greatly influences their physical and chemical properties. In particular, significant attention has been paid to ultra-small sized MNCs by discussing their optical properties, synthetic procedures, surface chemistry and applications. Moreover, some important processes, such as MNCs-biomolecule interactions, sensing, excitation energy transfer, and electron/hole transfer etc., which are relevant to the thesis work has also been highlighted in this chapter.[19, 20] Chapter 1 concludes by outlining the thesis's objectives with an emphasis on the need to address current challenges in this field.

Chapter 2: Experimental Techniques and Methods

This chapter provides a concise introduction and basic principles to various experimental techniques used in the present study, including steady-state absorption and emission spectroscopy, time-resolved fluorescence spectroscopy, fluorescence correlation spectroscopy (FCS), field emission scanning electron microscopy (FESEM), transmission electron microscopy (TEM), fourier-transform infrared spectroscopy (FTIR), dynamic light scattering (DLS), zeta potential measurements, isothermal titration calorimetry (ITC), cyclic voltammetry (CV) and circular dichroism (CD). The chapter also delves into the working

principles of time-correlated single photon counting (TCSPC) and fluorescence correlation spectroscopic (FCS) techniques by providing detailed explanations and layout diagrams of the concerned instrumentations. Furthermore, various methodologies employed for data analysis have been discussed in this chapter. At the end of this chapter, standard error limits for different experimental measurements are provided, offering essential information about the precision and reliability of the obtained data.

Chapter 3: Interaction of Bovine Serum Albumin with Copper Nanoclusters: Realization of Binding Pathway Different from Protein Corona

This chapter has explored the interaction mechanism of bovine serum albumin (BSA) with three distinct types of copper nanoclusters (CuNCs) possessing chemically different surface ligands: tannic acid (TA), chitosan, and cysteine (Cys) (Scheme 1). The main focus of this chapter is to reveal the role of these surface ligands over CuNCs in the overall protein-CuNCs interaction event and, most importantly to investigate whether CuNCs can interact with proteins in a unique way, distinct from the formation of a "protein corona" which is typically observed with larger nanoparticles when exposed to biological fluids. The protein-NCs interaction has been investigated by monitoring the fluorescence of CuNCs and the intrinsic fluorescence of BSA. Thermodynamic parameters for the binding process are determined through steady-state and isothermal titration calorimetric (ITC) experiments. The analysis of data obtained from fluorescence, ζ-potential, and ITC measurements has revealed that BSA, in the presence of CuNCs, does not achieve the binding stoichiometry (BSA/CuNCs > 1) necessary for "protein corona" formation. These findings are further supported by the results obtained from fluorescence correlation spectroscopy (FCS). Further analysis of data and thermodynamic calculations has highlighted the significant role of CuNCs' surface ligands in the protein-NCs binding events, affecting both the mode and thermodynamics of the process. Specifically, it has been observed that the binding of BSA

with TA-CuNCs and Chitosan-CuNCs follows two distinct binding modes, whereas Cys-CuNCs exhibit a single binding mode (Figure 1a,b,c). Circular dichroism (CD) measurements have indicated that the basic structure of BSA remains almost unaltered in the presence of CuNCs. To gain deeper insights into the binding of protein molecules with various CuNCs at the single-particle levels, fluorescence correlation spectroscopy (FCS) has been employed (Figure 1d,e,f). The data analysis yields intriguing insights into the binding pathways of protein molecules in the presence of various CuNC. The outcome of this study is expected to be useful in utilizing CuNCs for biological applications.

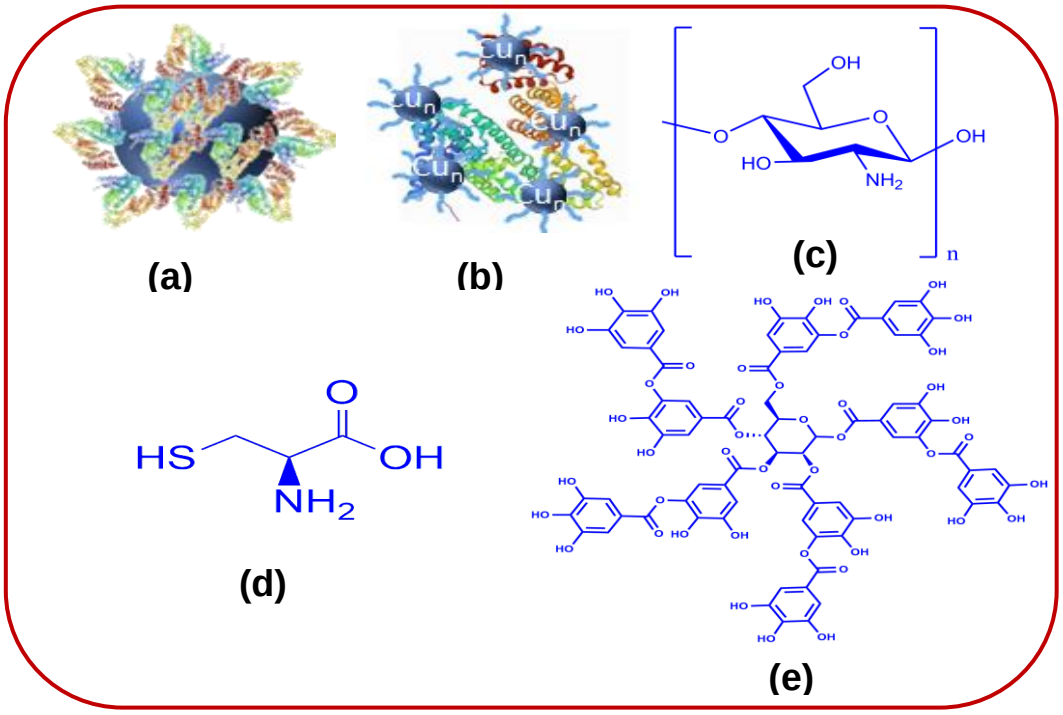

Scheme 1. Schematic represenation of (a) "protein-corona" and (b) protein complex; Chemical Structures of: (c) Chitosan, (d) Cysteine, and (e) Tannic Acid.

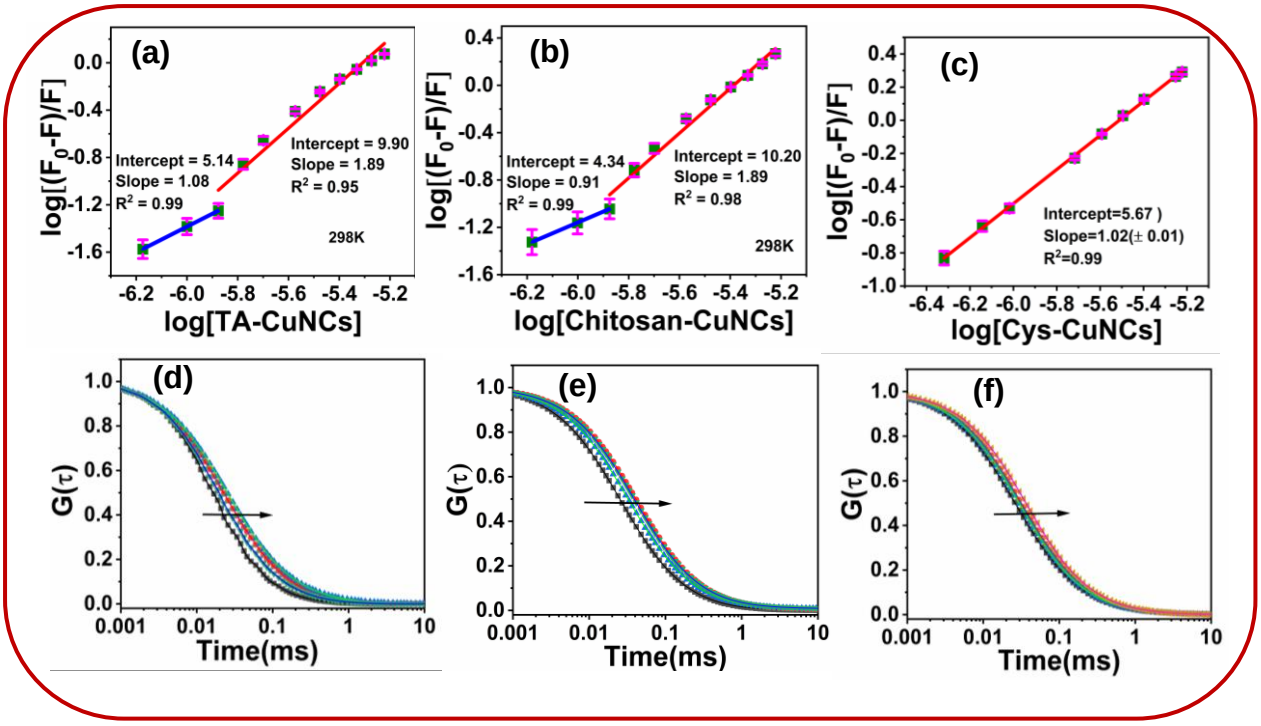

Figure 1. Double-logarithmic plot for the binding of (a) TA-CuNCs, (b) Chitosan-CuNCs, and (c) Cys-CuNCs with BSA at 298 K; Normalized autocorrelation curves for (d) TA-CuNCs (e) Chitosan-CuNCs and (f) Cys-CuNCs with increasing concentrations of BSA.

Chapter 4: Copper Nanoclusters as an Effective Enzyme Inhibitor on the Activity Modulation of α-Chymotrypsin

This chapter basically tells about the potential of CuNCs as an effective enzyme inhibitor on the activity modulation of α-Chymotrypsin and the associated interaction mechanism. This chapter has also highlighted the role of surface ligands of CuNCs on the overall enzyme-CuNCs interaction events. For the investigations, two distinct CuNCs have been synthesized; each capped with different surface ligands, namely, cysteine (Cys) and tannic acid (TA). Subsequently, we have investigated the interaction between these CuNCs and α-ChT using various spectroscopic techniques at both the ensemble average and single-molecule levels. The results obtained from enzyme kinetics studies (Figure 2a,b) have revealed that both types of CuNCs effectively act as enzyme inhibitors. Cys-CuNCs has completely suppressed the α-ChT activity through a competitive inhibition mechanism, while TA-CuNCs has partially reduced enzyme activity via a noncompetitive inhibition mechanism. This observation

underscores the crucial role of surface ligands in regulating α-ChT activity. To obtain deeper insights into the enzyme-inhibitor interaction mechanism, we have employed fluorescence spectroscopy, isothermal titration calorimetry (ITC), fluorescence correlation spectroscopy (FCS), agarose gel electrophoresis, and circular dichroism (CD) spectroscopy. Thermodynamic data obtained from fluorescence titration and ITC experiments have indicated that Cys-CuNCs follow a one-step binding process, whereas TA-CuNCs undergo a two-step binding process (Scheme 2). Moreover, FCS studies have provided evidence in favour of the interaction between CuNCs and α-ChT at the single-molecule level. Importantly, CD measurements (Figure 2c,d) demonstrate that the fundamental structure of α-ChT remains almost unchanged in the presence of CuNCs. Overall, this study has suggested that CuNCs have the potential to serve as effective nanoscale regulators of enzyme activity for various biological applications.

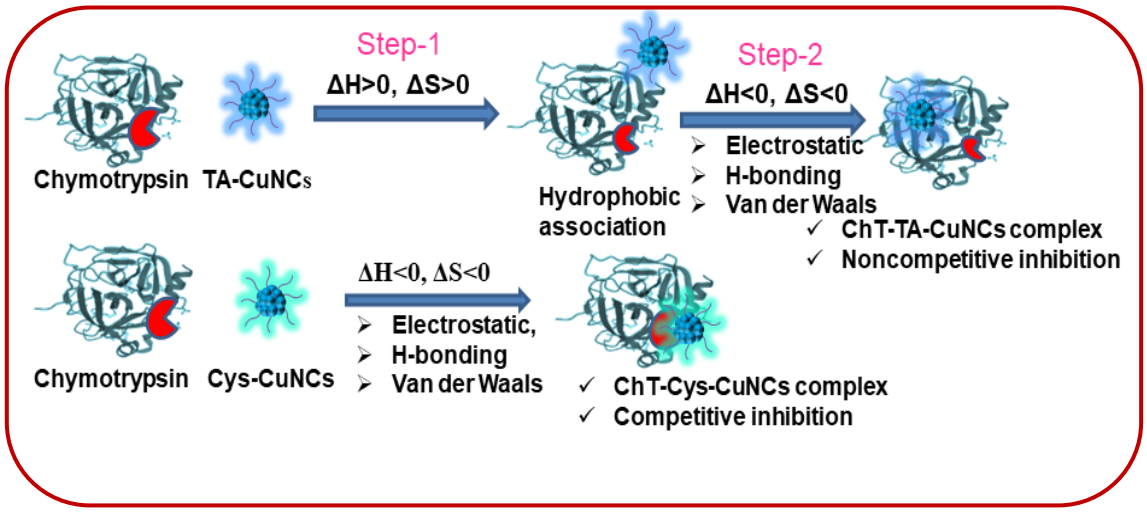

Scheme 2. Schematic representation of the binding event between α-ChT and CuNCs.

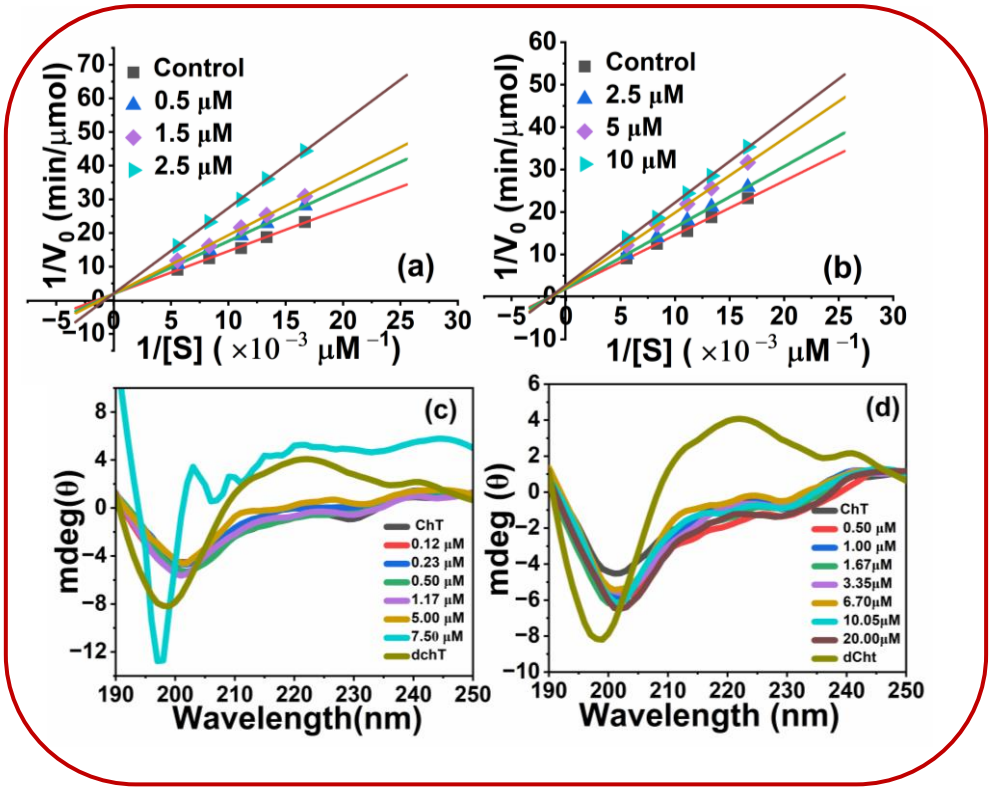

Figure 2. Lineweaver−Burk plots of α-ChT in the absence and presence of different concentrations of (a) Cys-CuNCs and (b) TA-CuNCs using SPNA as a substrate; Far-UV CD spectra of 2 μM α-ChT in the absence and presence of increasing concentration of (c) Cys-CuNCs and (d) TA-CuNCs.

Chapter 5: Turn-Off Detection of Reactive Oxidative Species and Turn-On Detection of Antioxidants Using Fluorescent Copper Nanoclusters

The goal of this chapter is to design and develop a nanoscale fluorescence-based sensory system which can selectively and sensitively detect highly reactive oxidative species (hROS) and antioxidants within a single chemical entity (Scheme 3). To achieve this, we have synthesized water-soluble, economical, non-toxic fluorescent copper nanoclusters (CuNCs) capped with chitosan and characterized them by conventional analytical methods. The sensory action of CuNCs for various analytes of interest has been evaluated at both the ensemble-averaged and single-particle levels by employing a range of spectroscopic and microscopic techniques. The steady-state fluorescence studies (Figure 3a,b,c) have revealed

that CuNCs serve as efficient turn-off sensors for hROS (•OH and ClO^-) and turn-on sensors for antioxidants (ascorbic acid and glutathione). Notably, our study has demonstrated the effectiveness of this sensory system in detecting antioxidants at low concentrations in commercial fruit juices and human blood samples. Additionally, the ability of CuNCs to sense hROS at the single-particle level has also been showcased with the help of fluorescence correlation spectroscopy (FCS). X-ray photoelectron spectroscopy (XPS) data analysis has indicated that the turn-off sensing mechanism arises from the oxidation of Cu(0)NCs to Cu(II) by hROS (Figure 3d,e,f). Conversely, the fluorescence studies have revealed that the turn-on sensing mechanism is caused due to the presence of antioxidants, which prevents the oxidation of CuNCs by hROS. Interestingly, the present investigations have also demonstrated that the optical output signals of the probe–analyte interaction during the hROS/antioxidant signaling can successfully be exploited to construct NAND and IMPLICATION logic gates. In summary, the work in this chapter demonstrates that CuNCs-based nanoscale sensory systems can be developed for applications in electronics and medical diagnostics.

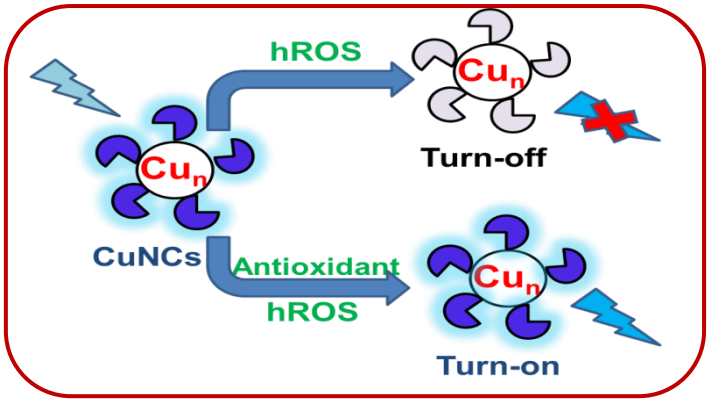

Scheme 3. Sensing Strategy for the detection of hROS and Antioxidants by CuNCs

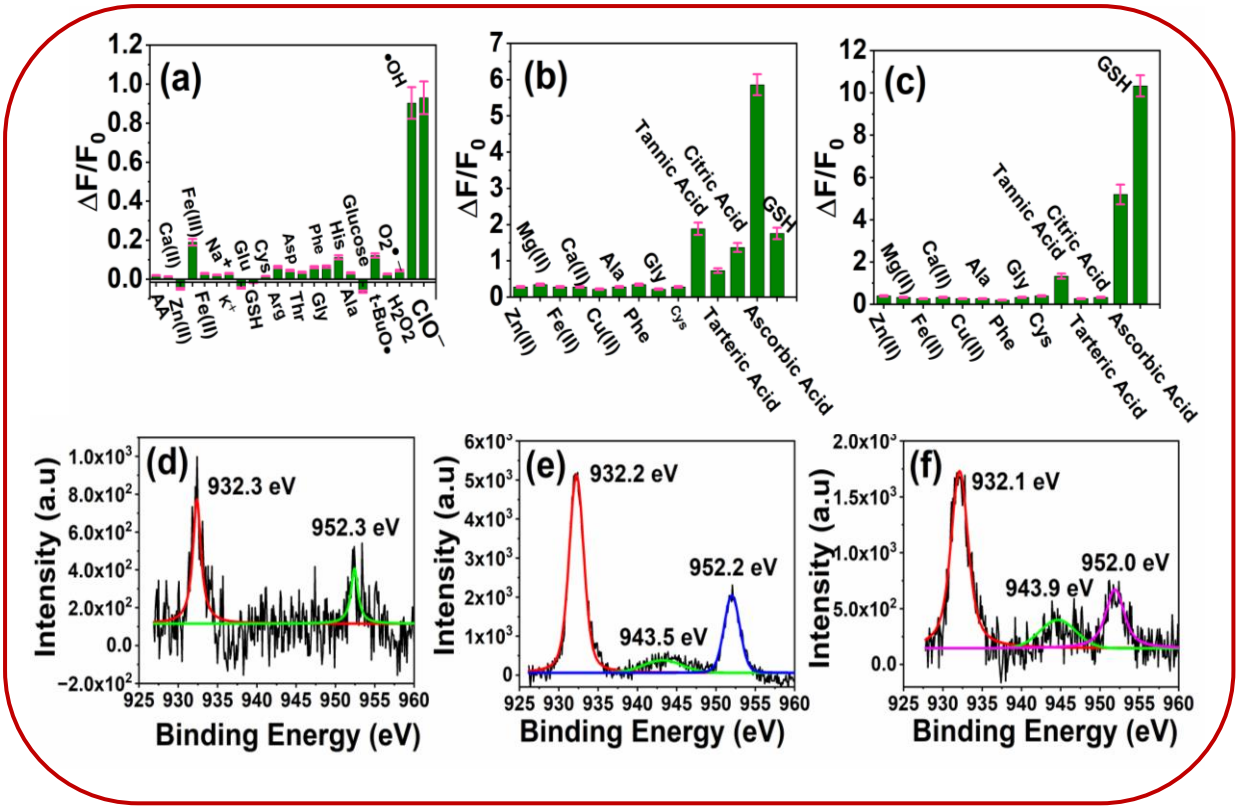

Figure 3. Fluorescence response of (a) CuNC sensor in the presence of hROS (•OH and ClO^-) (b) CuNCs/•OH system in the presence of AA and (c) CuNCs/ ClO^- system in the presence of GSH and different coexistents; High-resolution Cu (2P) XPS spectra of (d) CuNCs (e) CuNCs in presence of •OH and (f) CuNCs in presence of ClO^-.

Chapter 6: Effect of Surface Ligands of Copper Nanoclusters on P-Nitrophenol Reduction: A Spectroscopic approach

In Chapter 6, we have investigated the influence of surface ligands on copper nanoclusters (CuNCs) in catalyzing the $NaBH_4$-mediated reduction of 4-nitrophenol to 4-aminophenol. Two types of CuNCs, one capped with tannic acid (TA-CuNCs) and the other with cysteine (Cys-CuNCs) have been synthesized and utilized as nano-catalysts. We have compared the catalytic performance of these ligand-capped CuNCs with that of ligand-free CuNCs in aqueous medium. To understand the catalytic mechanisms at a molecular level, we have utilized the absorption signals of reactants and the fluorescence signals of the CuNCs catalysts. Kinetic data obtained from absorption studies (Figure 4) have revealed that the rate

constant for the reaction, catalyzed by these nano-catalysts, follows the order: $k_{TA-CuNCs} > k_{CuNCs} > k_{Cys-CuNCs}$. Notably, Cys-CuNCs and ligand-free CuNCs have exhibited an induction time before the reaction commenced, whereas no induction time has been observed with TA-CuNCs. This observation has suggested that surface modification of CuNCs by ligands play a crucial role in the catalytic reaction. Furthermore, the removal of dissolved oxygen from the reaction medium is found to increase the rate constants for all catalysts and effectively eliminates the induction time. This finding has essentially indicated the influence of dissolved oxygen in facilitating the reverse oxidation of 4-nitrosophenol (an intermediate) to 4-nitrophenol.[21] In order to find out the potential of the nano-systems in catalyzing the above reaction, the reduction potentials of these CuNCs are determined through cyclic voltammetry studies. Moreover, the observation of a decrease in the catalytic activity with increasing 4-nitrophenol concentration has pointed out that a Langmuir-Hinshelwood mechanism is responsible for the reaction (Scheme 4). Interestingly, from the fluorescence studies, it has been observed that when the nano-catalysts are added to the mixture of 4-nitrophenol and $NaBH_4$, the fluorescence intensities of the catalysts get reduced drastically at the beginning of the reaction but subsequently get recovered over time, indicating the progress of the reaction. Quite interestingly, the rate constants estimated from the fluorescence recovery data is found to follow a similar trend to those obtained from absorption data. Furthermore, it has been demonstrated that CuNCs-based nano-catalysts are not only limited to the conversion of 4-nitrophenol to 4-aminophenol but are quite useful in catalyzing various types of substrates. The outcome of the present work sheds light on the role of surface ligands in nano-catalysis and presents new opportunities in designing new nano-catalysts for practical applications.

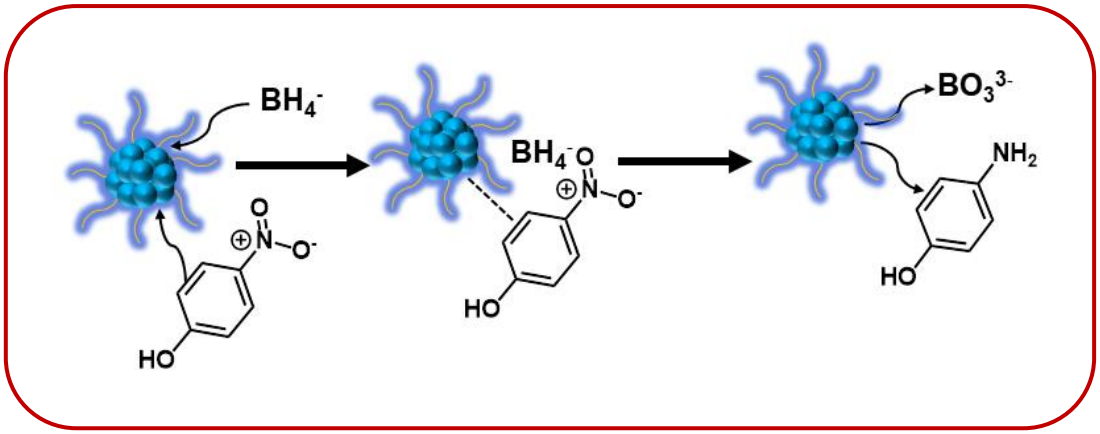

Scheme 4. Schematic representation of the catalytic mechanism.

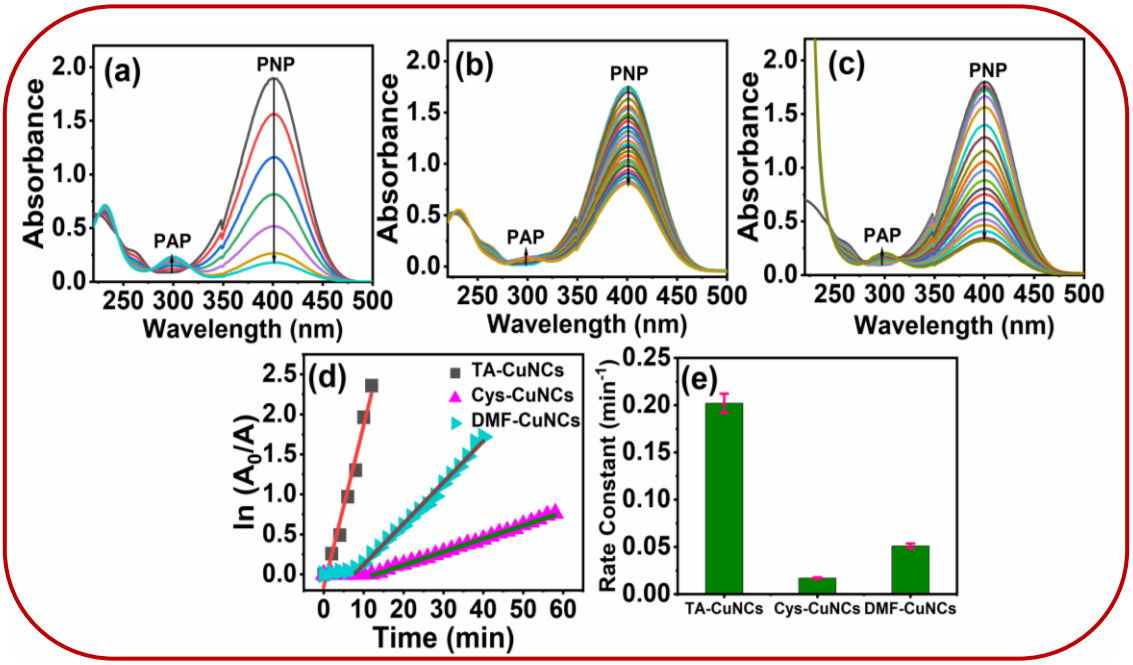

Figure 4. Absorption spectra of 4-nitrophenol reduced by $NaBH_4$ in the presence of (a) TA-CuNCs (b) Cys-CuNCs and (c) ligand free CuNCs with 2 min time interval; (d) ln(Ao/At) vs time (t) plot for determination of rate constants; (e) Bar diagram of catalytic reaction rate constant vs various CuNCs.

Chapter 7: Investigation on Energy Transfer from Non-Plasmonic Fluorescent Bimetallic Nanoparticle to Plasmonic Gold Nanoparticles

This study is aimed at understanding the electronic interaction between non-plasmonic fluorescence bimetallic silver capped gold (F-AgAu) nanoparticles and plasmonic gold nanoparticles (AuNPs) by investigating the excitation energy transfer (EET) studies.

Additionally, attempts have also been made to know how the surface modification of AuNPs with cetyltrimethylammonium bromide (CTAB) can affect the electronic interaction between the said units (Scheme 5). For this purpose, F-AgAu and AuNPs are used as donor and acceptor respectively. These nanomaterials have been synthesised by following reported protocols and characterised by using conventional methods prior investigating their photo-physics. Steady-state and time-resolved fluorescence studies (Figure 5) have revealed substantial quenching of the fluorescence intensity and lifetime of F-AgAu in the presence of AuNPs. The data obtained from cyclic voltammetry (CV) and polarity-dependent studies have ruled out the possibility of electron transfer mechanism. The observed increase in non-radiative decay rate for F-AgAu has provided evidence in favour of the fact that the photoluminescence quenching is primarily a result of excitation energy transfer from F-AgAu to AuNPs. Interestingly, our investigations have revealed that the energy transfer efficiency drops from 87% to 28% in the presence of CTAB modified AuNPs due to the formation of a CTAB bilayer over AuNPs. Data analysis through various methods such as conventional EET, nanomaterial surface energy transfer (NSET), and stretched exponential models have firmly established that the EET process follows a $1/d^4$ distance dependence (NSET), rather than the conventional $1/d^6$ distance dependence as predicted by the Förster resonance energy transfer model. Furthermore, single-particle level measurements through fluorescence lifetime imaging microscopy (FLIM) have elucidated the role of the surfactant (CTAB) in controlling the EET process from non-plasmonic to plasmonic nanoparticles.

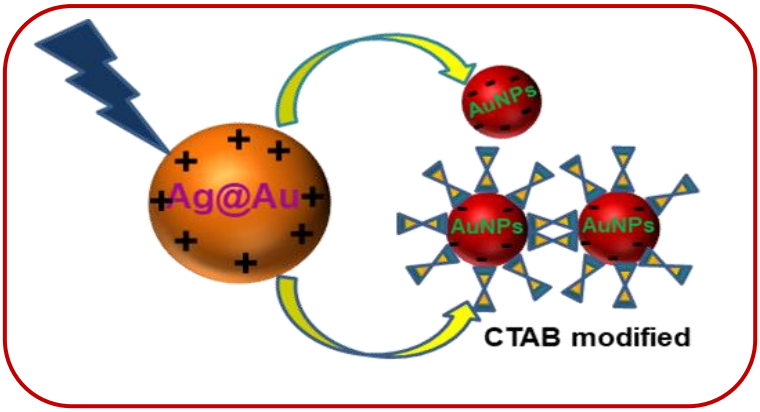

Scheme 5. Schematic representation of the interaction of F-AgAu with AuNPs and CTAB modified AuNPs.

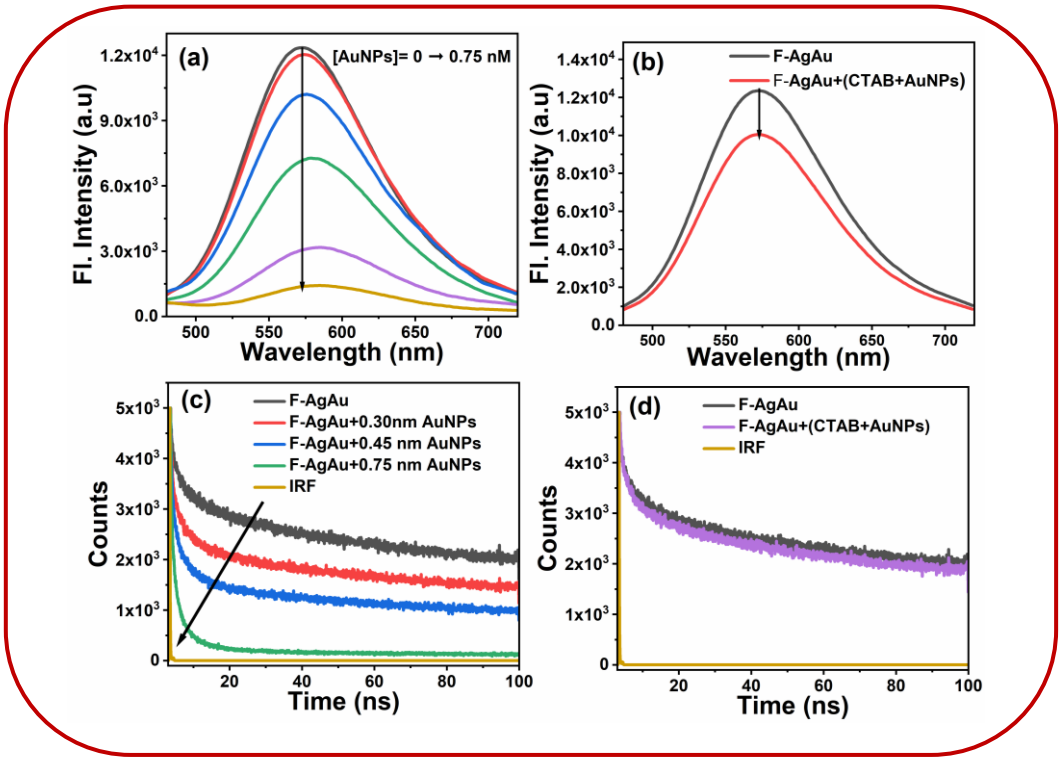

Figure 5. Fluorescence spectra of F-AgAu in the absence and presence of (a) AuNPs and (b) CTAB modified AuNPs. Time-resolved fluorescence decay curve of F-AgAu in the absence and presence of (c) AuNPs and (d) CTAB modified AuNPs (λ_{ex} = 375 nm).

References

1. Mahmoudi, M.; Lynch, I.; Ejtehadi, M. R.; Monopoli, M. P.; Bombelli, F. B.; Laurent, S. *Chem. Rev.* **2011,** *111* (9), 5610-5637.
2. Guo, S.; Dong, S. *Chem. Soc. Rev.* **2011,** *40* (5), 2644-2672.
3. Aragay, G.; Pino, F.; Merkoçi, A. *Chem. Rev.* **2012,** *112* (10), 5317-5338.

4. Guo, S.; Wang, E. *Acc. Chem. Res.* **2011,** *44* (7), 491-500.
5. Mahmoudi, M.; Sahraian, M. A.; Shokrgozar, M. A.; Laurent, S. *ACS Chem. Neurosci.* **2011,** *2* (3), 118-140.
6. Guo, S.; Wang, E. *Nano Today* **2011,** *6* (3), 240-264.
7. Sau, T. K.; Rogach, A. L. *Adv. Mater.* **2010,** *22* (16), 1781-1804.
8. Philip, R.; Chantharasupawong, P.; Qian, H.; Jin, R.; Thomas, J. *Nano Lett.* **2012,** *12* (9), 4661-4667.
9. Dass, A., Faradaurate Nanomolecules: A Superstable Plasmonic 76.3 kDa Cluster. *J.e Am. Chem. Soc.* **2011,** *133* (48), 19259-19261.
10. Zhang, L.; Wang, E. *Nano Today* **2014,** *9* (1), 132-157.
11. Latorre, A.; Somoza, Á. *ChemBioChem* **2012,** *13* (7), 951-958.
12. Shang, L.; Dong, S.; Nienhaus, G. U. *Nano Today* **2011,** *6* (4), 401-418.
13. Shiang, Y.-C.; Huang, C.-C.; Chen, W.-Y.; Chen, P.-C.; Chang, H.-T. *J. Mater. Chem.* **2012,** *22* (26), 12972-12982.
14. Lynch, I.; Dawson, K. A.; Linse, S. *Science's STKE* **2006,** *2006* (327), pe14-pe14.
15. Lundqvist, M.; Stigler, J.; Elia, G.; Lynch, I.; Cedervall, T.; Dawson, K. A. *Proc. Nalt. Acad. Sci.* **2008,** *105* (38), 14265-14270.
16. You, C.-C.; De, M.; Han, G.; Rotello, V. M. *J. Am. Chem. Soc.* **2005,** *127* (37), 12873-12881.
17. Goswami, N.; Zheng, K.; Xie, J. *Nanoscale* **2014,** *6* (22), 13328-13347.
18. Jin, R.; Zeng, C.; Zhou, M.; Chen, Y. *Chem. Rev.* **2016,** *116* (18), 10346-10413.
19. Lakowicz, J. R., Principles of Fluorescence Spectroscopy;. *Springer: USA,* **2006**.

20. Valeur, B., Molecular Fluorescence: Principles and Applications;. *Wiley-VCH:* Weinheim, **2002**.
21. Strachan, J.; Barnett, C.; Masters, A. F.; Maschmeyer, T. *ACS Catal.* **2020,** *10* (10), 5516-5521.

List of Schemes

List of Figures

List of Tables

Glossary of Acronyms

NPs	Nanoparticles
MNCs	Metal nanoclusters
CNTs	Carbon nanotubes
UV	Ultra-Violet
PL	Photoluminescence
GSH	Glutathione
BSA	Bovine serum albumin
α-ChT	α-chymotrypsin
SPNA	N-succinyl-L-phenylalanine-p-nitroanilide
LB	Lineweaver– Burk
CD	Circular Dichroism
ITC	Isothermal titration calorimetry
QY	Quantum yield

FRET	Förster resonance energy transfer
NSET	Nanoparticle surface nergy transfer
EET	Excitation energy transfer
J(λ)	Overlap integral
R_{DA}	Donor to acceptor distance
ϕ_D	Quantum yield of donor
R_0	Förster distance
GGT	γ-glutamyltranspeptidase
hROS	Highly reactive oxidative species
ROS	Reactive oxidative species
AA	Ascorbic acid
TA	Tannic acid
FLIM	Fluorescence lifetime imaging
TEM	Transmission electron microscopy
EDX	Energy dispersive X-ray analysis
XPS	X-ray photoelectron spectroscopy
DLS	Dynamic light scattering
CV	Cyclic Voltammetry
TCSPC	Time-Correlated Single Photon Counting
PMT	Photo multiplier tube
CFD	Constant fraction discriminator
TAC	Time to amplitude converter
PGA	Programmable gain amplifier
ADC	Analog to digital converter
WD	Window discriminator
MCA	Multichannel analyzer
MCP	Microchannel plate
IRF	Instrument response function
CCD	Charged coupled device
SPADs	single-photon avalanche photodiodes
NLLS	Nonlinear least squares
TTTR	time-tagged time-resolved

FCS	Fluorescence Correlation Spectroscopy
D	Diffusion coefficient
η	Refractive index
τ_f	Fluorescence lifetime
$\emptyset_f$	Fluorescence quantum yield
k_{nr}	Non-radiative rate constant
k_r	Radiative rate constant
λ_{exc}	Excitation wavelength
APX	Appendix

CHAPTER 1

INTRODUCTION

This chapter tries to provide a comprehensive introduction to a wide range of nanomaterials and their optoelectronic properties. It begins by categorizing the nanomaterials on the basis of particle size, which greatly influences their physical and chemical properties. In particular, significant attention has been paid to ultra-small sized metal nanoclusters (MNCs) by discussing their optical properties, synthetic procedures, surface chemistry and applications. Moreover, some important processes, such as nanoparticles-biomolecule interactions, sensing, excitation energy transfer, etc., involving various MNCs have also been highlighted in this chapter. This chapter concludes by outlining the thesis's objectives with an emphasis on the need to address current challenges in this field.

1.1. Introduction to Nanomaterials

Nanomaterials are substances with structures at the nanoscale (typically 1-100 nm) regime, showcasing remarkable physical and chemical properties.[1-2] In the past decades, nanomaterials have drawn considerable attention from all branches of sciences, as well as technologies, due to their potential applications in molecular imaging, biosensors, nanomedicine, nanoscale devices, catalysis, nanoelectronics, data storage, etc.[1, 3-8] Based on their composition, nanomaterials are broadly categorized into two classes: inorganic nanoparticles and organic nano / microparticles. Inorganic nanoparticles are further subdivided into metal nanoparticles and semiconductor nanoparticles or quantum dots (QDs). On the other hand, organic nano/microparticles form another class, encompassing a diverse range of carbon-containing compounds and molecules with distinct applications in various fields. In recent years, the rapid development of noble metal (e.g., Cu, Ag, Au, Pt, etc.) nanoparticles has been renowned as the most trendy research topic. Interestingly, the nanomaterials show unusual properties (mechanical, chemical, electrical, optical, magnetic, etc.) different from their bulk counterpart and the differences are strongly dependent on the

particle size (Scheme 1.1).[2, 9-11] It is to be noted that bulk metals possesses continuous energy bands. The conduction band of a bulk metal is overlapped with the valence band to some

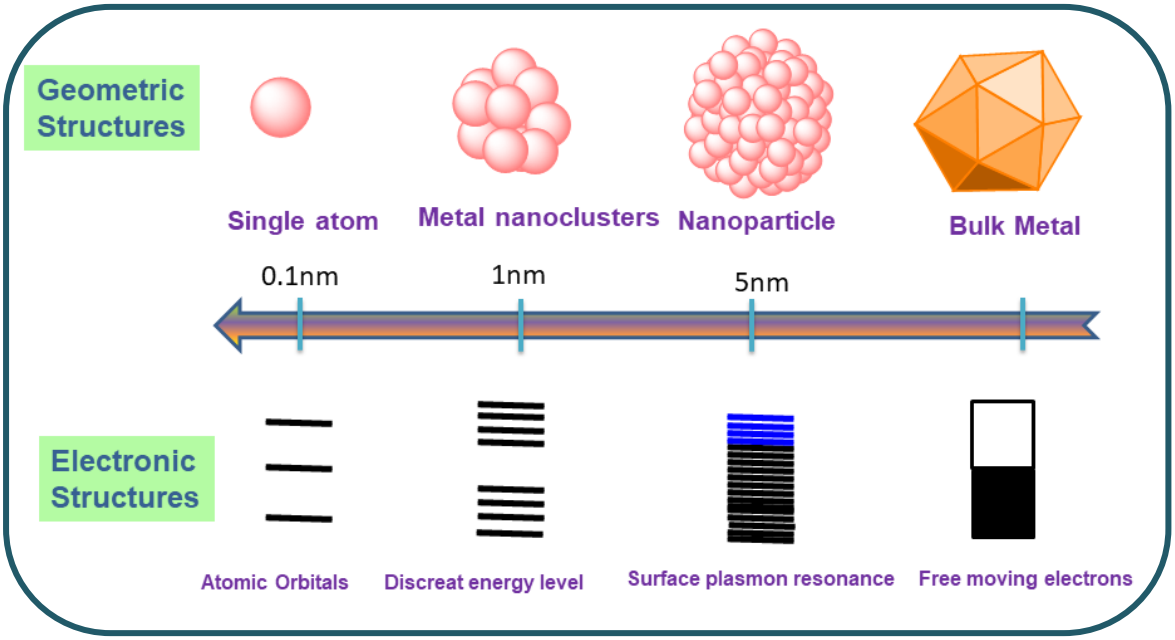

Scheme 1.1. Effect of size on the electronic structure of metal.

extent and is partially occupied with movable electrons, which are responsible for the electric conductivity of metals.[2] When the size of metals cuts to develop metal nanoparticles (NPs), the motion of electrons is restricted to some extent and there occurs collective oscillations of the conduction electrons upon interaction with incident light, giving rise to the localised surface plasmon resonance (LSPR) effect.[12] Due to this effect, NPs exhibit a strong absorption band in the near-UV to the visible region, known as surface plasmon resonance (SPR) absorption.[13-14] This gives rise to vibrant colours in their colloidal solutions that are highly contingent on the size and shape of the nanoparticles.[12] The oscillation frequency of plasmon electrons, determined by the size and shape of the nanoparticles, also influences their absorption frequency. When the size of the NPs is further reduced to sub-nanometer level (< 2nm), it gives a fascinating class of nanomaterials called metal nanoclusters (MNCs). The energy bands of MNCs are split into discrete energy levels due to quantum confinement

effect, resulting in surprising properties compared to larger-sized nanoparticles.[2, 15] In the upcoming discussion, our focus will be exclusively on fluorescent MNCs, a key component of the present thesis.

1.2. Metal Nanoclusters

Metal nanoclusters (MNCs), usually composed of a few to hundred atoms, are a new class of fluorescent nanomaterials.[1, 16-17] The sizes of MNCs are typically below 2 nm which approaches the Fermi wavelength of electron. Due to having ultra-small size, the continuous density of states are split up into discrete energy levels, which leads to unusual optical, electrical and chemical properties dramatically different from plasmonic nanoparticles.[18-21] This special class of nanomaterials make a bridge between metal nanoparticles and metal atoms. These MNCs are considered as promising candidates for bio-analysis, bio-imaging, sensing, catalysis, etc. due to having fascinating properties like photoluminescence, good photostability, large Stokes shift, water solubility, etc.[22-28]

1.2.1. Optical Properties of MNCs

1.2.1.1. Absorption Properties

Usually, the absorption properties of metal nanoparticles are governed by the surface plasmon resonance of conduction electrons. However, MNCs reveal molecular-like HOMO-LUMO electronic features and multiband electronic transitions, which are responsible for the light-matter interactions of MNCs.[2, 29] Typically, the absorption spectra of metal nanoclusters (MNCs) exhibit pronounced absorption in the UV region and an extended absorption tail in the visible region. It is important to highlight that these absorption characteristics of MNCs markedly differ from the distinctive surface plasmon resonance (SPR) band observed in relatively larger

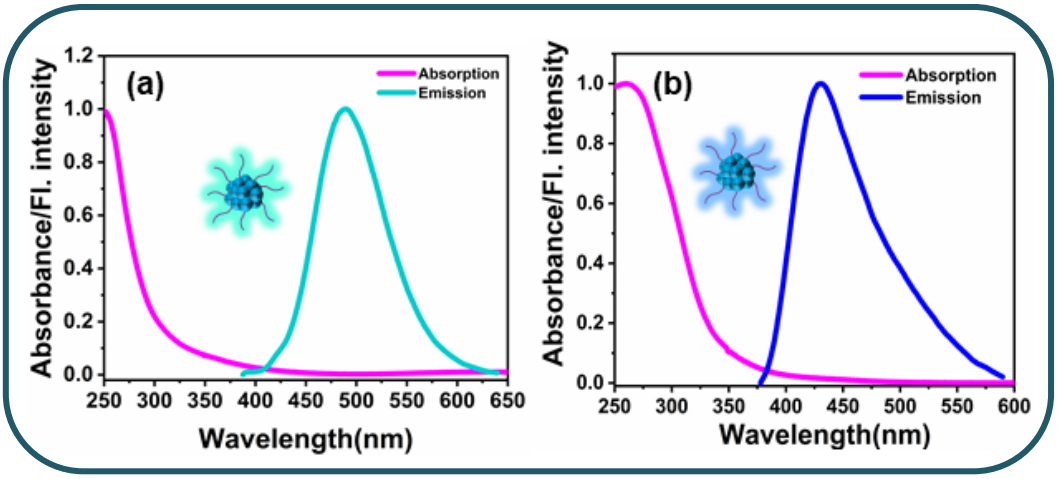

Figure 1.1. Absorption and emission spectra ($\lambda_{Excitation}$ = 360 nm) of (a) Cysteine capped CuNCs and (b) Tannic acid capped CuNCs.

nanoparticles.[30] In the current thesis work, strong absorption in the UV region and an extended absorption tail in the visible region has been observed in the absorption spectra of CuNCs, distinctly differing from the characteristic surface plasmon resonance (SPR) band (ca. 560−600 nm) observed in relatively larger CuNPs (Figure 1.1).[31] Assigning the bands in the UV–vis spectrum of MNCs to specific electronic transitions necessitate the use of density functional theory (DFT) calculations.[2] Notably, CuNCs, in contrast to AuNCs, do not exhibit intricate multi-band UV–vis spectra, particularly in the visible region. The optical spectra of CuNCs typically feature a gradual exponential rise in absorbance at lower energies. Multiple bands and transitions at higher energies are predominantly influenced by the absorption of the protective ligand.[32] It is to be mentioned here that Jin and co-workers[29] have shown that glutathione-protected Au_{25}NCs exhibit characteristic absorption features in the range 400—1000 nm due to the intraband (sp←sp) or interband (sp←d) transitions. In another work, Tsukuda and co-workers[33] have demonstrated that with decreasing the core size of AuNCs, the spacing between the discrete energy levels in each band increases, leading to a blue shift in the absorption spectra.

1.2.1.2. Fluorescence Properties

Ultra-small sized MNCs exhibit good fluorescence properties, which make them ideal candidates for bioimaging, biolabelling and fluorescence analysis, etc. The fluorescence mechanism may vary with the variation of sizes, surface ligands and different synthetic routs of MNCs.[2, 28, 34-36] Presently, several mechanisms have been suggested to explain the fluorescence properties of MNCs. Commonly, the metal core with its quantum confinement effect (QCE) and the surface property of MNCs are considered to be the main sources of the emission properties of MNCs. In this context, it is relevant to mention here that Murray and co-workers[37-38] have proposed that the fluorescence of monolayer-protected MNCs is due to the interband transitions between the filled d band and the sp conduction band. In another work, Whetten and co-workers[39] have ascribed the relaxed radiative recombination across the HOMO—LUMO gap within the sp conduction band (intraband transition) is responsible for the infrared fluorescence from glutathione-protected AuNCs. In certain instances, CuNCs display dual-emission characteristics. The lower-energy emission is linked to intraband transitions occurring within the sp-band (HOMO–LUMO transitions), while the higher-energy emission is associated with interband transitions from excited states in the sp-band to the d-band.[40-41] The electronic transitions within MNCs are pictorially given in the Scheme 1.2.

It is to be noted here that using sophisticated synthetic and characterization methods, researchers have successfully achieved atomically precise MNCs. Recently, Pradeep and co-workers[42] have synthesized Ag_7NCs and Ag_8NCs with almost identical particle sizes, utilizing mercaptosuccinic acid as capping ligands. Notably, they have observed distinct photoluminescence (PL) emissions at approximately 440 nm and 650 nm for Ag_7NCs and Ag_8NCs, respectively. The remarkable shift in emission colour from blue to red, despite only

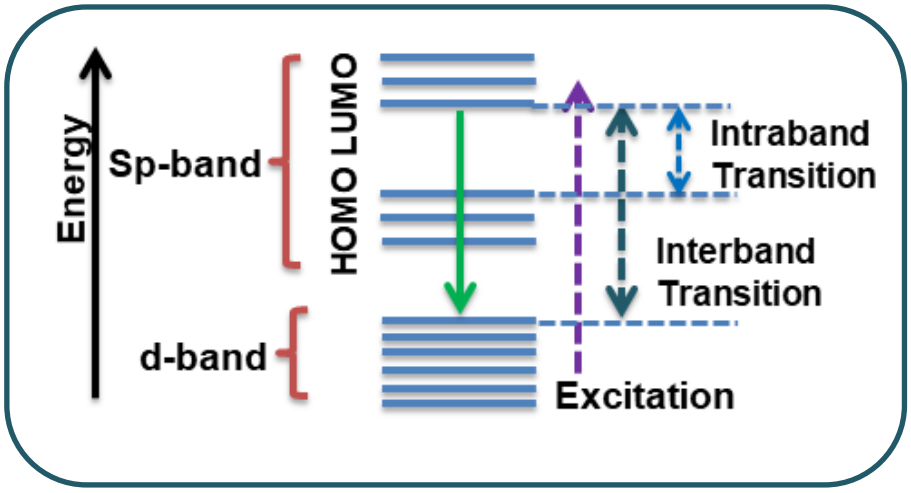

Scheme 1.2. Schematic band structure of a noble metal showing the excitation and recombination transitions.

one-atom difference in cluster structures, challenges a simplistic interpretation based solely on size-dependent quantum confinement effects (QCE). Moreover, despite the robust size-dependent photoluminescence (PL) properties exhibited by MNCs, the fluorescence lifetime and quantum yield (QY) calculated through theoretical models are notably lower than the experimentally observed values. When solely accounting for the metal's contribution to PL emission, the theoretically predicted wavelength of PL emissions should fall within the near-infrared range, contrasting with the experimentally observed visible wavelength emission.[43] These disparities between experimental and theoretical data suggest the inadequacy of metal-centered quantum confinement mechanics. In a recent study, Luo and co-workers[44] have synthesized a series of glutathione (GSH)-protected gold nanoclusters with precise atomic compositions ($Au_{29}SG_{27}$, $Au_{30}SG_{28}$, $Au_{36}SG_{32}$, $Au_{39}SG_{35}$, $Au_{43}SG_{37}$). Surprisingly, all these nanoclusters exhibited identical emission at approximately 610 nm, challenging the conventional explanation of the classical quantum confinement effect (QCE) mechanism. Moreover, by finely adjusting the surface ligands' coverage, the emission wavelength could be readily tuned from 600 nm to 810 nm, highlighting the crucial role of surface-protective ligands in modulating the photoluminescence (PL) of AuNCs.[45]

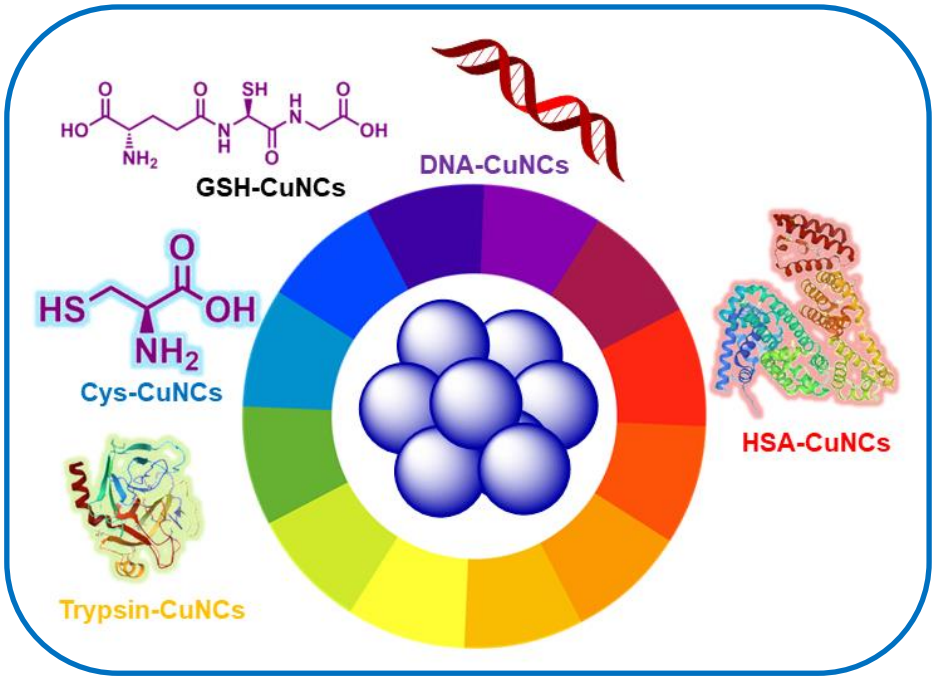

Scheme 1.3. Ligand effect to tune the emission properties of MNCs from current reports[46-50]

Additionally, AuNCs with the same number of core atoms but different protecting ligands displayed distinct PL properties.[18, 51-52] Effect of ligands on the tunability of emission wavelength of CuNCs has been schematically shown in the Scheme 1.3. These findings underscore that the metal core alone is not the sole determinant of the photoemission in MNCs. Other components, including the nature of coordinate ligands, ligand to metal charge transfer (LMCT), ligand to metal to metal charge transfer (LMMT), valence states of surface metal atoms, and assembly architectures of nanoclusters, also significantly influence the emission properties of MNCs.[44, 53-59]

1.2.1.3. Solvatochromic Properties

The solvatochromic effect, commonly observed in larger metal nanoparticles, is primarily associated with their surface plasmon phenomenon.[60] Recent studies have indicated that ultra-small sized MNCs also exhibit a comparable dependence of their optical behaviour on the solvent.[61-63] It has been observed that both the optical and emission properties of MNCs can be tuned significantly with the proper choice of solvents. The splitting of energy levels and

electron redistribution on the cluster surface may be affected by the change in the chemical environment, leading to a variation in the optical properties of the MNCs .[64] It is expected that the solvatochromic effect of MNCs may be useful for the sensing of various sensitive analytes.[65]

1.2.2. Surface Ligand Chemistry of MNCs

Surface ligands play a crucial role in the synthesis, stability, and properties of metal nanoclusters. These ligands are generally molecules or ions that bind to the surface of metal nanoclusters, providing stability and influencing their chemical, physical, and electronic properties. Here are some key points which highlight the importance of stabilizing ligands for metal nanoclusters:

(i) Stability and Kinetic Control

Metal nanoclusters are often highly reactive and thermodynamically unstable due to their high surface-to-volume ratio. Stabilizing ligands passivate the surface of these nanoclusters, preventing them from aggregating or undergoing uncontrolled growth.[66] This ensures that the nanoclusters maintain their desired size and structure over time, allowing for precise control of their properties.

(ii) Tuneable Properties

By selecting different ligands, researchers can fine-tune the physical and chemical properties of nanoclusters, such as their catalytic activity, optical properties, and electronic structure. This tunability is crucial for tailoring nanoclusters to specific applications.

(iii) Solubility and Dispersion

Ligands can enhance the solubility of metal nanoclusters in various solvents, enabling their

use in solution-phase reactions and applications. They also help disperse nanoclusters uniformly, preventing agglomeration and ensuring even distribution in solution.

(iv) Biological Compatibility

Stabilizing ligands can make metal nanoclusters biocompatible, allowing their use in various biomedical applications, such as drug delivery, imaging, biomolecular sensing and therapy.[67-68] Ligands can be designed to minimize toxicity and enhance the nanoclusters' interaction with biological systems. Surface ligands of MNCs play crucial role in the interaction mechanism of MNCs with bio-molecules that has been discussed in the chapter 3 and chapter 4 in details.

(v) Protection from Oxidation and Corrosion

Stabilizing ligands act as a protective shell around metal nanoclusters, shielding them from environmental factors, such as oxygen and moisture that can lead to oxidation or corrosion of metal atoms. This ensures the long-term stability of nanoclusters.[69]

(vi) Electronic Structure

Ligands can modify the electronic structure of metal nanoclusters, leading to changes in their electronic properties, such as bandgap and conductivity.[69-70] This makes them suitable for applications in electronics, sensors, and optoelectronics.

In summary, stabilizing ligands are essential for controlling the size, shape, stability, and properties of metal nanoclusters, making them versatile materials with applications in catalysis, nanotechnology, materials science, and biomedicine. In recent times, researchers are actively exploring novel ligand strategies to unleash the complete potential of MNCs for a diverse range of innovative applications. The impact of surface ligands on various aspects has been addressed in different sections of this thesis.

1.2.3. Synthesis of MNCs

Obtaining high-quality nanomaterials relies heavily on effective synthesis protocols. The widespread interest in synthesizing nanomaterials stems from their unique applications in modern science. To achieve large-scale synthesis of MNCs with precise atomic compositions, diverse chemical and physical methods have been developed. Various synthetic approaches have been reported for the formation of MNCs, and these methods can be broadly categorized into two subclasses: (i) top-down process, where external forces play a pivotal role in reducing relatively larger-sized nanoparticles (NPs) to smaller-sized MNCs, and (ii) bottom-up process, which involves the nucleation of the cluster-core from metal atoms obtained through the reduction of metal ions (Scheme 1.4). These two methods have been discussed below.

1.2.3.1. Top-down Synthesis Methods

In the top-down synthesis of nanomaterials, macroscopic structures are broken down into nano-sized fragments and subsequently transformed into thermodynamically stable species. In this approach, usually, two principal methods, namely dry grinding and wet grinding, are employed for the synthesis of metal nanoclusters (MNCs).[34] Dry grinding involves the application of mechanical forces, such as shearing mill, ball mill, and tumbling mill, to disintegrate solid materials into smaller particles, characterized by high surface energy. However, this method often leads to aggregation, resulting in the formation of larger non-luminescent nanoparticles. In the wet grinding process, the likelihood of forming larger-sized particles is reduced in comparison to the dry grinding method. Generally, the wet chemical synthesis of MNCs involves the etching or digestive ripening of larger nanoparticles[71] or nanocrystals[59] in the presence of excess ligands by controlling the factors such as pH,

temperature, and initial concentrations of reacting materials. Recently, Patra and co-workers[71] have successfully synthesized atomically precise CuNCs from non-luminescent plasmonic

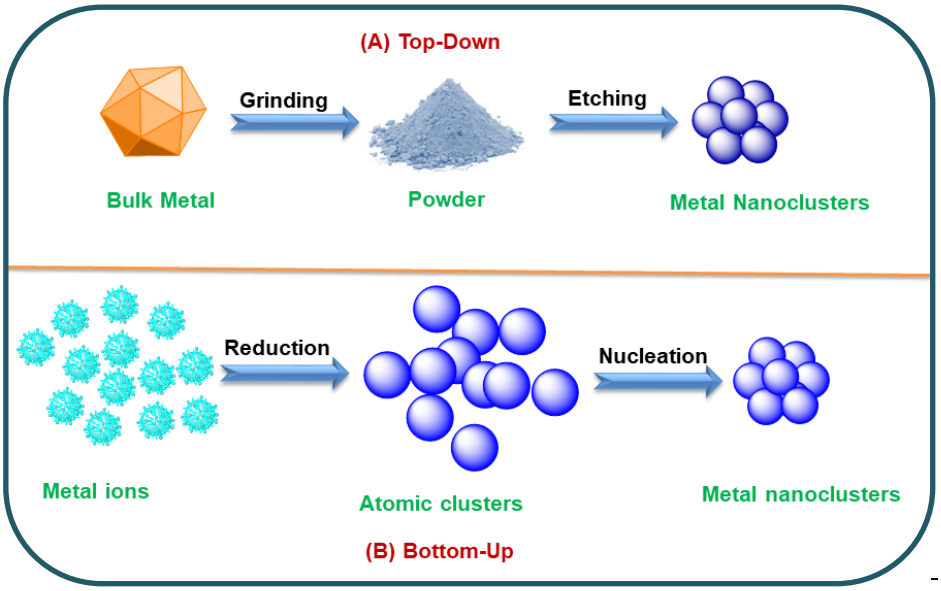

Scheme 1.4. Schematic representation of the (A) Top-Down approach and (B) Bottom-Up approach for the synthesis of MNCs

CuNPs through core etching using excess reduced GSH. In another recent study, Chen and co-workers[72] have reported a novel, straightforward, and expeditious top-down etching method for the synthesis of luminescent CuNCs, utilizing CuNPs as the precursor and NH_3 as the etchant.[34] Despite the potential advantages of wet grinding methods, the top-down process has garnered limited attention due to unsatisfactory product yields.[73-74]

1.2.3.2. Bottom-up Synthesis Methods

The most preferred bottom-up approach for the synthesis of metal nanoclusters is the chemical reduction method. This method begins by reducing metal ions to a zero-valent state, facilitated by ligands or external reducing agents. This reduction is followed by nucleation of metal atoms and protection by capping ligands. Additional bottom-up methods include

physical vapour deposition (PVD), chemical vapour deposition (CVD), electrochemical synthesis, microwave-assisted synthesis, micro-emulsion method, and modified Brust-Schiffrin method. However, many of these techniques necessitate high-cost instruments, and their productivity is often unsatisfactory. Hence, reducing metal ions and capping with ligands is the preferred method for synthesizing diverse metal nanoclusters like AuNCs, AgNCs, CuNCs, etc.

1.1.3.2.1. Ligand-based Synthesis Methods

In the past decades, ligand-based synthetic methods are considered as efficient synthetic techniques for the preparation of fluorescent MNCs. Throughout this thesis, this method has been employed for the preparation of MNCs. In general, during the synthesis of MNCs, there is a high tendency of aggregation of multiple clusters-cores in order to decrease the surface energy. Therefore, suitable ligands are required to overcome this pitfall for the synthesis of stable MNCs. The choice of ligand plays a crucial role in determining the size, shape, and properties of the resulting nanoclusters. The ligands are chosen based on their affinities for different metals or precursors. In this method a metal precursor (metal salts or organometallic compounds) is taken according to the desire metal composition of the MNCs. The metal precursors are dissolved in an appropriate solvent and suitable ligands are added to that solution, which give rise to metal-ligand intermediate complex. Then the metal ions are reduced by adding reducing agents, under photo irradiation or heating. Upon reduction of metal ion, metal-ligand bonds are weakened, and few metal atoms aggregated to form metal nanoclusters through aurophilic interactions, argentophilic interaction, cuprophilic interaction, etc.[33, 53, 75] In the current thesis, we have used cysteine, tannic acid, chitosan and glutathione as capping ligand for the synthesis of various MNCs. Some common ligands used in ligand-based synthesis of metal nanoclusters are discussed below and shown in the Scheme 1.5.

Thiols: Thiol containing small molecules such as glutathione, cysteine, dihydrolipoic acid, alkyl or aryl mercaptans, etc. is commonly used as stabilizing agents for the synthesis of

MNCs as many transition metals have strong affinity for thiols. They form robust metal-sulphur bonds and provide excellent stabilization for metal nanoclusters. It is pertinent to

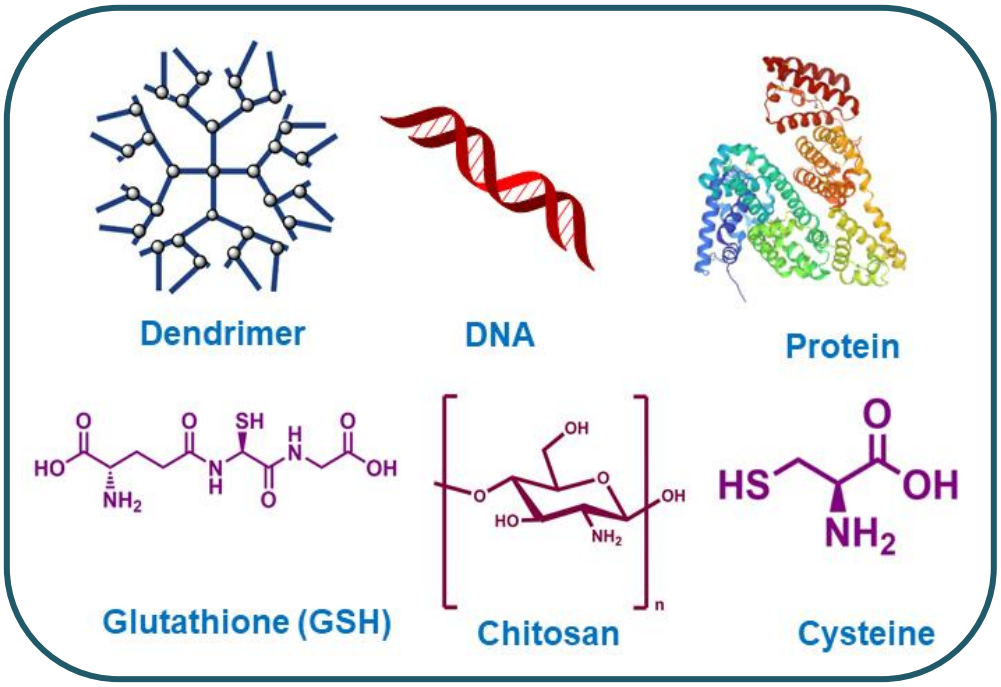

Scheme 1.5. Pictorial representation of some ligands used in the synthesis of MNCs.

mention here that there are several reports on the synthesis of glutathione-protected AuNCs with defined chemical compositions.[33, 76] Similar attempts have also been made for the synthesis of AuNCs, stabilized with various thiols such as phenylethylthiolate[77] tiopronin[37], 3- mercaptopropionic acid[78], thiolate -cyclodextrin[79] etc. Recently, Banerjee and co-workers[80] have reported the synthesis of fluorescent AgNCs using dihydrolipoic acid (DHLA) as the stabilizing agent. In another recent work, Chen and co-workers[47] have synthesised green-emitting and pH-responsive CuNCs by using cysteine as capping agent.

Carboxyl/ Hydroxyl Group Containing Species: Carboxyl group and /or hydroxyl group containing ligands have been widely used for the polyhydroxyl group has been employed in

the synthesis of CuNCs.[69] Additionally, O-carboxymethyl chitosan has been used as a surface ligand in the synthesis of another blue-emissive CuNC.[31]

Phosphines: Phosphine ligands have been extensively used as protecting ligands in the synthesis of various MNCs.[3, 83-86] For examples, Bartlett et al.[83] have synthesised AuNCs with a diameter of approximately 0.8 nm by using amino-substituted triarylphosphine ligands as capping agents. The choice of the phosphine ligands likely provides strong coordination with the gold atoms, effectively stabilizing the resulting nanoclusters.

1.2.3.2.2. Template-based Synthesis Methods

Template-based synthesis methods are extensively employed for the fabrication of ultra-small and well-defined metal nanoclusters (MNCs). Various templates, including dendrimers, polymers, proteins, polyelectrolytes, and DNA, have been utilized for this purpose. These template-based techniques offer predetermined environments for cluster formation, facilitating the production of nanoclusters with precisely controlled size and shape. Commonly used templates for the synthesis of MNCs are discussed below:

Dendrimers: Dendrimers, with their well-defined structures and the ability to sequester metal ions from solutions, have been employed as templates for the synthesis of MNCs. Recently, Dickson and co-workers[87] have synthesised photostable luminescent AgNCs within PAMAM dendrimers through direct photoreduction. The same group[88] have further described the synthesis of AuNCs stabilized by dendrimers, specifically PAMAM dendrimers. By varying the relative concentrations of PAMAM dendrimers and metal precursors, as well as the generation of the dendrimers, it is possible to obtain MNCs with emission colours ranging from ultraviolet (UV) to near-infrared (NIR) regions.[55] In another work, Lin and co-workers[89] have proposed a simple strategy for synthesizing dendrimer-encapsulated AuNCs, primarily Au_8, by incorporating a specific counter ion (AuX_4^-, X = chloride or bromide) into a

dendritic microcavity with pH-dependent polarity. Upon microwave irradiation, they have achieved dendrimer-encapsulated AuNCs with high quantum yields ranging from 20% to 62%.

Polymers: Polymers, containing abundant carboxylic acid groups have shown promise as templates for the synthesis of highly fluorescent MNCs. An earlier report[90] has described the synthesis of fluorescent AgNCs using polymer microgels composed of poly (N-isopropylacrylamide-acrylic acid-2-hydroxyethyl acrylate) by UV irradiation. In this study,[90] a mixture of the polymer microgel and Ag^+ ions was exposed to UV irradiation. The carboxylic acid groups present in the polymer microgel likely served as coordinating sites for the Ag^+ ions, facilitating their reduction and subsequent formation of fluorescent Ag NCs within the polymer matrix. In another work, Frey and co-workers[91] utilized a molecular hydrogel composed of multi-arm star polyglycerol-block-poly (acrylic acid) copolymers as a template for synthesizing fluorescent AgNCs via photoreduction. Numerous recent studies have detailed the synthesis of AuNCs stabilized by various polymers. In one instance, AuNCs capped with polyethylenimine (PEI), a multivalent polymer, have been prepared by etching preformed dodecylamine-capped gold nanoparticles.

Proteins: Proteins have emerged as effective scaffolds for the synthesis of various MNCs.[18, 92-95] Proteins possess chelating and functional groups, such as amines, carboxyls, and thiols, which exhibit specific affinities towards noble metal atoms, thereby stabilizing the synthesized MNCs. Yiang and co-workers[18] have demonstrated that BSA, under basic conditions (pH > 12.0), not only stabilizes Au ions but also facilitates their reduction through a redox reaction involving the tyrosine residue in BSA. Similar templates (i.e., BSA) have been used by Pradeep and co-workers[96] for the synthesis of AgNCs with a QY of approximately 11%. Other serum proteins, such as Human Serum Albumin (HSA), have been utilized for the synthesis of AgNCs and CuNCs by Mukherjee and co-workers[97-98].

Various other proteins, including egg white protein, bovine pancreatic ribonuclease A (RNase-A), and lysozyme, have also been widely used to synthesize various MNCs.[99-102]

DNA: DNA has emerged as a promising template for the synthesis of MNCs due to its non-toxicity, biocompatibility, and functional properties. The interactions between metal cations and DNA have facilitated the design and fabrication of various DNA-templated metal nanostructures.[103] Silver ions, in particular, exhibit a high affinity for cytosine bases on single-stranded DNA, making DNA oligonucleotides effective stabilizers for the synthesis of small Ag NCs. In a pioneering study, Dickson and coworkers[104] have synthesised Ag NCs by using single-stranded DNA (ssDNA) templates containing the 12-base sequence 5'-AGGTCGCCGCCC-3 in a phosphate buffer. In another study, Richards and co-workers[105] have used five different DNA sequences as scaffolds for Ag NCs. They obtained five distinct AgNCs with tunable fluorescence emission throughout the visible and near-infrared regions. Unlike AgNCs, there have been limited reports on the synthesis of AuNCs using DNA oligonucleotides as a scaffold. This is likely due to the weak association between the negatively charged DNA and the commonly used gold precursor, $AuCl4^-$.[106] It is to be noted here that DNA is found to be an effective template for the preparation of CuNCs.[34]

1.2.4. Nano-Bio Interfacial Chemistry

Exploring the interplay between biomolecules and various nanomaterials, such as metal nanoparticles, metal nanoclusters, semiconductor chalcogenides, graphene quantum dots and carbon-based nanoparticles, constitutes a captivating interdisciplinary field at the intersection of physics, chemistry, and biology.[1, 107-111] The capability of these nanomaterials to interact with a variety of biomolecules has rendered them highly attractive for diverse biological applications such as bioimaging, nanomedicines, catalysts, nano-bio sensors etc. Among these nanomaterials, NPs have been extensively studied in the field of biomedicine and nano-

bio technologies due to their remarkable attributes. However, it is also known that the behaviour of nanoparticles in biological media is highly complex, and the resulting interaction between nanoparticles and biomolecules is not straightforward. Consequently, comprehending the intricacies of the nanoparticles–biomolecules interaction mechanism poses a formidable challenge. Without addressing these issues, the conceptualization and development of an effective nano-probe for a target-specific application may cause

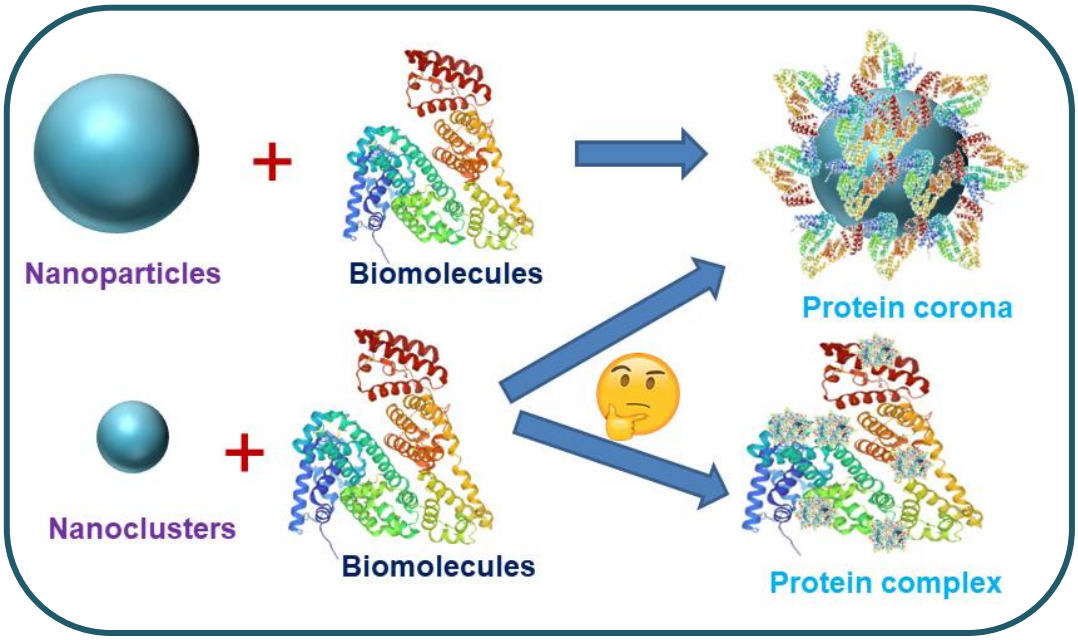

Scheme 1.6. Formation of "protein-corona" and "protein-complex". (Biomolecules have been taken from Protein Data Bank, PDB Code 4F5S)

further challenges for these systems to be used in real-time applications. It has been well documented that upon dispersion in a biological medium, NPs undergo a dynamic process wherein their surfaces are covered by an intricate layer of biomolecules, forming "protein-corona".[112-115] Consequently, biomolecules interact with nanomaterials coated with proteins rather than bare NPs. The "protein-corona" serves as a protective shield for the inherent surface properties of NPs. It not only modifies the size and composition of the NPs but also imparts a new biological identity to them. This entity significantly influences various physiological processes, including signalling, cellular uptake, circulation lifetime,

biodistribution, therapeutic effects, toxicity effect etc. The establishment of the new biological identity of the NP occurs through the creation of a new interface between the NPs and the biological medium, commonly referred to as the "nano-bio interface".[116-119] The responses of biomolecules to NPs are significantly influenced by the primary forces acting at the bio-nano interface, including electrostatic interaction, hydrogen bonding, van der Waals force of attraction, hydrophobic interaction, etc. In addition, the intrinsic characteristics of NPs, such as size, shape, charge, crystallinity, electronic states, surface modifications with ligands, hydrophobicity, etc., play a crucial role in modelling the formation of the "protein-corona" and in controlling the associated interaction mechanism.[120] In the realm of NP characteristics, the morphology, specifically the size and shape, has been proposed as a significant factor in governing nano-bio interactions. Even though several studies have been reported on protein-NPs interaction where the diameter of the NPs was above that of most abundant serum proteins (6−12 nm), studies on the MNCs having sizes smaller than proteins have not been adequately addressed. Consequently, the understanding of how MNCs communicate with biomolecules is rather limited. It's worth noting that ultra-small (<2 nm) fluorescence MNCs are anticipated to be more effective nanoprobes compared to larger candidates due to their larger specific surface area and curvature. They exhibit lower susceptibility to opsonisation and possess significantly longer lifetimes in the bloodstream. Additionally, they demonstrate faster biodegradation (e.g., dissolution) and excretion profiles, mitigating unwanted bioaccumulation. Moreover, these MNCs possess favourable fluorescence properties, and their environment-sensitive fluorescence behaviour can provide valuable insights into nano-bio interaction events.[31, 121] Furthermore, knowledge about the influence of surface functionalities on MNCs in shaping protein−MNC interactions remains unclear. A few recent researches have proposed that when MNCs interact with protein molecules, they form "protein complex" rather than "protein corona," indicating the

adsorption of one or more MNCs on a single protein due to their ultra-small sizes and weak noncovalent interactions between MNCs and proteins.[31, 122-124] In contrast, another recent research has shown that despite the ultra-small size of GSH capped CuNCs, the interaction with proteins is mediated through a "protein-corona"-like structure rather than a "protein-complex".[125] Despite the availability of various methodologies for designing and developing MNCs with suitable functionalization, the understanding of MNC behaviour in complex biological fluids remains unclear. A visual representation of the aforementioned pathways is depicted in Scheme 1.6. In chapter 3 of this thesis, we have explored the interaction mechanism of BSA with three distinct types of CuNCs possessing chemically different surface ligands: tannic acid (TA), chitosan, and cysteine (Cys). In chapter 4, we have discussed about the potential of CuNCs as an effective enzyme inhibitor on the activity modulation of α Chymotrypsin and the associated interaction mechanism.

1.2.5. Applications

The distinctive physicochemical properties of metal nanoclusters (MNCs) make them compelling for applications in diverse fields including, sensing, catalysis, optoelectronics, bio-imaging, etc. [19, 126-131] This section provides an overview of recent progress in utilizing metal nanoclusters as novel fluorescent probes, in the realms of various applications.

1.2.5.1. Sensing

(i) Inorganic Ion Sensing

The precise detection of inorganic ionic species holds paramount importance in forensic, biomedical, and environmental sciences.[132-134] Over time, metal nanoclusters (MNCs) have played a pivotal role in developing sensory systems for the detection of inorganic ions by utilizing diverse strategies such as enzyme mimetic activity, electrochemical signalling and

optical responses. Among these approaches, the detection methods based on fluorescence emission properties have been particularly prevalent. Fluorescence sensing of a wide range of chemical and biochemical analytes is a prominent and active research area in the modern era.[2, 135] The fluorescence quenching technique, in particular, holds significant advantages, including high sensitivity, operability at low concentration limits, and the capability for remote sensing. Leveraging its exceptional sensitivity, fluorescence surpasses many other techniques in sensing measurements. This strategy includes the turn-on/turn-off mechanism, fluorescent quenching through the inner filter effect (IFE), Förster resonance energy transfer (FRET), electron transfer, oxidation of metal atoms etc. Numerous studies have recently demonstrated the potential of MNCs as fluorescent sensors. The efficiency of MNCs in sensing can be quantified by calculating the limit of detection (LOD), where a lower LOD signifies higher sensing efficiency. While instrumental techniques like AAS, AFS, ICP-OES, ICP-MS, and X-ray-based methods can be employed for elemental detection, they often involve complex instrumentation, extended analysis times, high costs, and limitations in *in vivo* analysis.[136-137] Luminescent MNCs address these challenges by serving as selective and sensitive sensors. Their biocompatibility, water solubility, photo-stability, and non-toxic nature make them valuable nano-sensor for both *in vivo* and *in vitro* investigations, even at single-molecular resolution. Numerous recent studies have explored the potential applications of MNCs as fluorescent sensors for detecting various important inorganic ions including Hg^{2+}, Co^{2+}, Zn^{2+}, Fe^{3+}, Pb^{2+}, Cd^{2+}, Al^{3+}, Na^{+}, K^{+}, NO_2^{-}, CN^{-}, S^{2-} ions, etc. [68, 92, 94, 131, 134, 138-148]

(ii) Biomolecule Sensing

In the progress of biomedical research, achieving sensitive and selective detection of trace-level biomolecules holds significant importance for identifying various diseases and facilitating early disease diagnosis. In this context, it is pertinent to mention that wang and

co-workers[149] have observed that GSH-capped AuNCs initiates an interaction with lysine and cysteine through GSH's thiol groups, which eventually leads to the quenching of fluorescence intensity. This technique achieved notably low LOD for lysine and cysteine at 2.0 and 50 nM, respectively. In another work, Feng and co-workers[150] have introduced a method for the detection of cysteine using fibrinogen-assisted AuNCs with an LOD of 0.79 μM. Recently, Tseng and co-workers[151] synthesized Au_8NCs with lysozyme type IV as a ligand and demonstrated its utility as a sensor for GSH detection. The method demonstrated an LOD of 20 nM for GSH and an impressive quantum yield of 56% for lysozyme–AuNCs. Moreover, significant efforts were given in constructing MNCs-base sensory system for the selective detection of protein molecules.[152-157] The development of fluorescent protein sensors based on MNCs has involved the conjugation of selective receptor molecules, such as antibodies and aptamers, to the surface of these MNCs. The inaugural use of fluorescent metal nanoclusters for protein detection was reported in 2006 by Leblanc and co-workers.[158] Proteases, a prominent class of enzymes catalyzing peptide bond hydrolysis in the process of proteolysis, play a crucial role in breaking down proteins into smaller fragments.[159] Xia and co-workers[154] introduced a novel nanoscale platform utilizing protein-protected AuNCs for highly sensitive and selective fluorescence detection of proteases. Platelet-derived growth factor B-chain homodimer (PDGF-BB), a protein growth factor, is implicated in regulating cell proliferation or differentiation, including fibroblasts, smooth muscle cells, and glial cells. Its overexpression is noted in certain human tumors, making it a potential protein marker for cancer diagnosis. Detecting PDGF-BB with high sensitivity and speed is crucial for early cancer diagnosis, treatment, and prognosis. Yang and colleagues[155] innovatively reported a turn-on and homogeneous aptasensor for PDGF-BB detection, relying on the target-induced formation of AgNCs. Thrombin, present in the bloodstream, serves as a coagulation protein. It plays a vital role in converting soluble fibrin into insoluble fibrin strands, and it catalyzes

various other coagulation-related reactions. Several MNCs-based sensory systems have been developed for the selective detection of thrombin.[152-153, 160] Accurate detection and measurement of DNA are essential for real-time monitoring of cellular activities in living organisms, as well as for biosensing applications and clinical diagnostics in laboratory settings.[161-163] Exploiting the highly sequence-dependent generation of fluorescent AgNCs within hybridized DNA duplex scaffolds, Wang and colleagues[161] innovatively developed a novel AgNCs-based fluorescent assay with the capability to specifically identify single nucleotide modifications. In another report, Pramanik and co-workers[164] have demonstrated the discrimination ability of GSH stabilized CuNCs towards well-matched DNA and single mismatched DNA. These CuNCs exhibited a stronger affinity to bind with DNA having cytosine-thymine mismatch.

(iii) Sensing of Reactive Oxidative Species And Antioxidants

Recently, there has been significant interest in developing fluorescent probes for detecting reactive oxygen species (ROS) like superoxide (O_2^-), hydrogen peroxide (H_2O_2), hydroxyl radical (•OH), hypochlorite (ClO^-), peroxynitrite ($ONOO^-$), etc. It is known that an appropriate level of ROS in human body plays crucial roles in physiological events such as ageing, cancer, inflammation, regulatory functions, and signalling. A complex antioxidant defence system, including enzymes like superoxide dismutase (SOD), catalase, and glutathione peroxidase, balances the burden of ROS production in our body. However, highly reactive oxidative species like •OH, ClO^-, and $ONOO^-$ possess strong oxidant properties. Excessive intracellular accumulation of these ROS can lead to severe damage in living cells. Factors like stress, alcohol intake, smoking, radiation, and toxins contribute to increased ROS levels in the human body. Therefore, detecting these ROS is crucial for well-being. It is to be noted that antioxidants such as ascorbic acid (AA) and glutathione (GSH) counteract oxidative stress, maintaining physiological homeostasis. Detecting antioxidants in various

samples, including pharmaceuticals, food and cell biology samples, is essential for understanding their presence and impact. It is also noted that consuming antioxidants through fruits and vegetables aids in maintaining sufficient antioxidant levels in the human body.

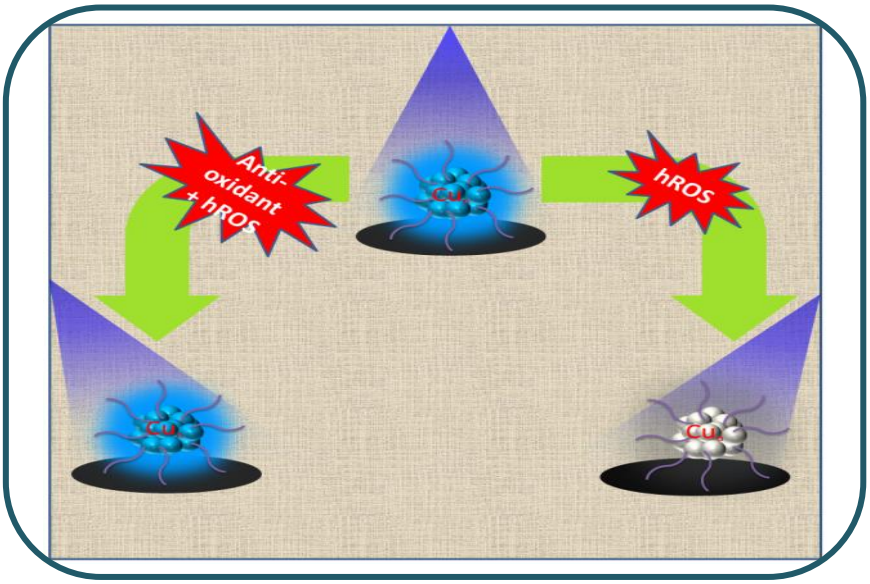

Scheme 1.7. Sensing of hROS and antioxidants by using CuNCs.

Therefore, detecting the presence of antioxidants is crucial in various sample types, including pharmaceuticals, food, and cell biology samples and so forth, and their detection is also important for the diagnosis of some diseases and their therapy in clinical chemistry. Detecting reactive oxygen species (ROS) along with antioxidants is a valuable objective. Various methods, including fluorescence spectroscopy, chemiluminescence-derived techniques, chromatography, electrochemical biosensors, and electron spin resonance, have been developed for this purpose. Among these, fluorescence-based techniques offer advantages like simplicity, high sensitivity, and nondestructive nature. Molecular-based organic fluorescent probes are commonly designed for ROS and antioxidant detection. However, these probes have limitations, including low solubility in aqueous media, susceptibility to photobleaching, spontaneous autoxidation, complex chemical synthesis, and biotoxicity. To overcome these challenges, several MNCs-based fluorescence nanosensor have been

developed for the detection of ROS and antioxidants.[165-167] In the present thesis work, we have designed and developed a material-based nanoscale fluorescence sensory system for the selective and sensitive detection of both highly reactive oxidative species (hROS) and antioxidants in a single chemical entity by exploiting two optically distinguishable useful signals (Scheme 1.7).

1.2.5.2. Catalysis

Catalysts are chemical heroes that shape our world in numerous ways. They're the accelerators in industries, making processes more efficient, and they play a pivotal role in environmental protection by converting pollutants into less harmful forms. From powering clean energy production to influencing everyday products and facilitating biochemical reactions, catalysts are silent contributors to progress and sustainability. In recent years, the catalytic potential of nanomaterials has garnered significant attention within the scientific community, particularly in the nanoscale domain.[130] Surprisingly, fluorescent metal nanoclusters (MNCs) have received less scrutiny as nano-catalysts compared to their larger nanoparticle counterparts. Nonetheless, MNCs offer distinct advantages, featuring a unique metal core that sets them apart from conventional nanoparticles and bulk materials. Metal NCs are regarded as a class of classical catalysts because of their high surface-to-volume ratio, low-coordinated sites, monodispersity, versatile crystal packing, and sharp electronic variations at the atomic level. This inherent flexibility of nanoclusters opens avenues for the exploration of innovative catalytic processes.[168-170] It has been reported that MNCs-based nanocatalysts demonstrate versatility across a broad range of chemical reactions, including electrocatalysis,[171-174] photocatalysis,[175-177] oxidation,[178-179] reduction,[180-181] coupling reactions,[182-185] and more. A pictorial representation of various catalytic reactions using MNCs-based nano-catalyst has been given in the Scheme 1.8. Despite numerous reports on catalytic reactions mediated by MNCs in recent years, a clear understanding of the intricate

catalytic pathways remains elusive. It is crucial to note that the surface ligands of nanomaterials play a pivotal role in modulating the electronic energy states of the MNCs, thereby influencing various catalytic properties. While ligands are

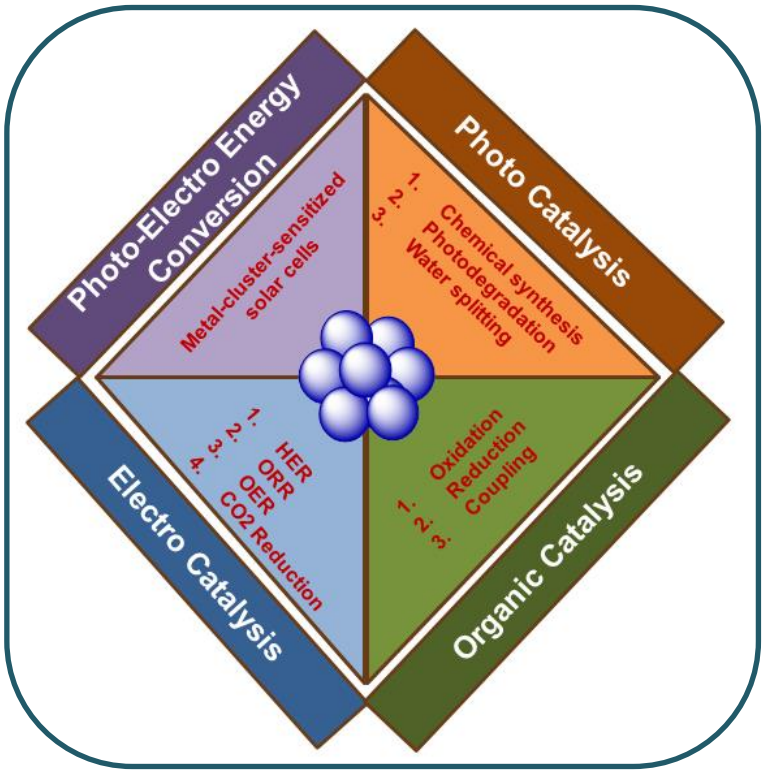

Scheme 1.8. Schematic representation of MNCs-mediated various catalytic reactions.

essential for designing and preserving nanostructured catalysts, their impact on catalytic turnover in different reactions can be obscured by competing factors. At the interface of nanomaterials, it is plausible that ligands could impede catalytic activity by obstructing accessibility to potential active sites on the catalyst surface.[186-187] As anticipated, several studies have documented a reduction in catalytic rates primarily attributable to this phenomenon.[186, 188] However, disparate observations exist, with certain studies indicating no adverse effects from capping ligands, and in some instances, an enhancement in selectivity towards specific reaction products has been reported.[189-190] These observations underscore the intricate nature of ligand interactions and their consequential role in catalytic processes.

Hence, a precise kinetic analysis is expected to be highly valuable to figure out the exact mechanistic pathway of a catalytic reaction. In the chapter 6 of this thesis, the influence of surface ligands on CuNCs in catalyzing the reduction of 4-nitrophenol to 4-aminophenol has been discussed in details.

1.2.5.3. Bio-medical Applications

(i) Bio-imaging

Fluorescent probes used in biological imaging often face challenges like low photostability (e.g, organic dyes) and potential toxicity (semiconductor quantum dots). Luminescent noble MNCs, especially protein- and peptide-protected MNCs, have emerged as optical probes for both in vitro (cell imaging) and in vivo (tumour imaging) applications due to having extraordinary chemical stability, good photo-stability, inherent biocompatibility, water solubility and tuneable physicochemical properties.[191-193] Recent studies have reported successful applications of MNCs in bio-imaging, showcasing their potential in providing precise and biocompatible platforms for various applications.[19-20, 194-198] For example, Wu and co-workers[199] pioneered out the use of red-emitting BSA-protected AuNCs for tumour imaging. In another instance, Yu and co-workers.[200] have synthesised luminescent AgNCs using an intracellular protocol and utilized them for live cell bio-imaging. In a recent work, Wang and co-workers[201] have introduced an efficient strategy for preparing luminescent Au NCs, demonstrating their *in vivo* imaging application. In this work, it has been demonstrated the spontaneously biosynthesized luminescent AuNCs, concentrated around the nuclei of cancer cells (HepG2, human hepatocarcinoma cell line; K562, leukaemia cell line), facilitated clear and precise bioimaging within cancerous cells whereas with non-cancerous cells exhibiting no synthesis of luminescent AuNCs. Additionally, Zheng and co-workers[193] utilized fluorescence imaging to demonstrate the efficient renal clearance of NIR-emitting

GSH-protected Au NPs in mice, with a hydrodynamic diameter of 3.0 ± 0.4 nm and an emission peak at 810 nm.

(ii) Antibacterial Activity

Since the Greco-Roman period, the utilization of silver plates or spoons has been recognized

for its hygienic benefits. Dating back to ancient times, metallic silver had been widely utilized to combat infections and control spoilage. This historical application persists into modern times, where there are extensive investigations into the antibacterial activity of AgNPs.[202-203] Notably, the inability of bacteria to develop resistance to Ag-based materials has fuelled ongoing research in this area. However, direct use of silver ions or their complexes as antimicrobial agents is discouraged due to potential adverse cytotoxic effects. The delicate design of functional bio-nanoclusters (Bio-NCs) has emerged as a significant focus for antibacterial applications.[204-205] Functionalization of MNCs with biomolecules, such as peptides and proteins, further enhances the potential of MNCs while reducing inherent cytotoxicity. The antimicrobial activity of protein and peptide-protected Au/Ag NCs can be attributed to the ligand shell, metal core, or a combination of both. For instance, lysozymes, known for damaging bacterial cell walls, has been employed by chen and co-workers[206] in synthesizing lysozyme-protected AuNCs with retained bioactivity. These MNCs inhibit the growth of antibiotic-resistant bacteria, showcasing their efficacy against challenging strains. In another work, Yuan et al.[207] have synthesised luminescent glutathione-protected AgNCs which exhibit superior bactericidal properties against Pseudomonas aeruginosa. The potential of these ultrafine luminescent AgNCs as highly efficient antimicrobial agents is promising, although additional studies on their toxicity are essential for the development of more biocompatible options.

(iii) Radiotherapy

Cancer remains a prevalent and serious global health challenge, necessitating innovative approaches to diagnosis and treatment. Functionalized nanomaterials hold transformative potential in addressing various diseases, particularly cancer, a leading cause of human mortality. The development of therapeutic nanocomposite agents offers promise in understanding drug resistance mechanisms and enhancing treatment outcomes. A variety of nanomaterials, including iron oxide NPs, quantum dots, carbon nanotubes, AuNPs, and silica NPs, have been investigated for creating theranostic agents.[208-210] Notably, efforts have been directed towards leveraging functionalized MNCs for constructing therapeutic platforms.[195, 211-212] In cancer treatment, improvements in radiotherapy, which uses high-energy rays, have occurred by incorporating nanotechnology. For instance, AuNPs, known for their strong absorption and efficient secondary radiation generation, serve as radiosensitizers.[213-215] The use of bio-AuNCs, such as BSA- and GSH-protected Au_{25}NCs, have demonstrated a synergistic effect in enhancing radiotherapy, combining the potent effects of the Au core with the biocompatibility provided by the protecting ligands.[216] Recent exploration of peptide-protected AuNCs and utilizing the enhanced permeability and retention (EPR) effect have shown their potential for tumour uptake and targeting specificity.[217]

1.3. Excitaton Energy Transfer (EET)

Apart from the above mentioned utilities of MNCs, these systems are sometimes used as the nano-scale light harvesting systems.[218-220] Excitation energy transfer is a vital process where energy absorbed by one fluorophore or molecule is efficiently transferred to another nearby fluorophore or molecule. Energy transfer in the form of $D^* + A \rightarrow D + A^*$ is termed heterotransfer and occurs when an excited molecule (donor) transfers energy to a chemically distinct molecule (acceptor). This transfer is feasible when the emission spectrum of the donor partially overlaps with the absorption spectrum of the acceptor. On the other hand, if the donor and acceptor are identical, it results in homotransfer, represented as $D^* + D \rightarrow D +$

D*. When this energy transfer process repeats itself, allowing excitation to migrate across several molecules, it is referred to as excitation transport or energy migration. This phenomenon is crucial in various fields, including photosynthesis, where it enables the efficient transfer of energy in light-harvesting systems. It has far-reaching applications, from elucidating protein interactions to developing energy-efficient technologies, making it a cornerstone in scientific research and technology development. It is pertinent to mention here that EET process can happen either through radiative or non-radiative pathways, which have been discussed below.

1.3.1. Radiative Energy Transfer

Radiative energy transfer involves the emission and subsequent reabsorption of photons and is primarily a result of inner filter effects. This process is influenced by various non-molecular optical properties of the sample, including the size of the sample container, the path length of light, the optical densities of the sample at both the excitation and emission wavelengths, and the geometric arrangement of the excitation and emission light paths. Radiative transfer comprises two distinct steps: first, a photon is emitted by a donor molecule (D), represented as $D^* \rightarrow D + h\nu$, and then this emitted photon is absorbed by an acceptor molecule, which can be chemically different (A) or identical (D), resulting in A* or D*. The process is often termed "trivial transfer" due to its straightforward nature.[221-222] However, describing this phenomenon quantitatively is complex as it depends on factors such as sample size and its configuration concerning the excitation and observation paths. These factors can significantly affect the efficiency and characteristics of radiative energy transfer in a given system.

1.3.2. Non-radioactive Energy Transfer

The non-radiative transfer of excitation energy necessitates interaction between a donor molecule and an acceptor molecule. This process becomes feasible when the emission spectrum of the donor overlaps with the absorption spectrum of the acceptor, resulting in multiple vibronic transitions in the donor that closely match the corresponding transitions in the acceptor. Non-radiative energy transfer occurs without the appearance of a photon and is the result of different interaction mechanisms, which may be due to columbic interaction and/or due to intermolecular orbital overlap. It is known that most of the non-radiative energy transfer processes are mediated either through long-range dipole-dipole interactions (Forster's mechanism) or intermolecular orbital overlap, which includes electron exchange (Dexter's mechanism). Forster's resonance energy transfer (FRET) is a non-radiative energy

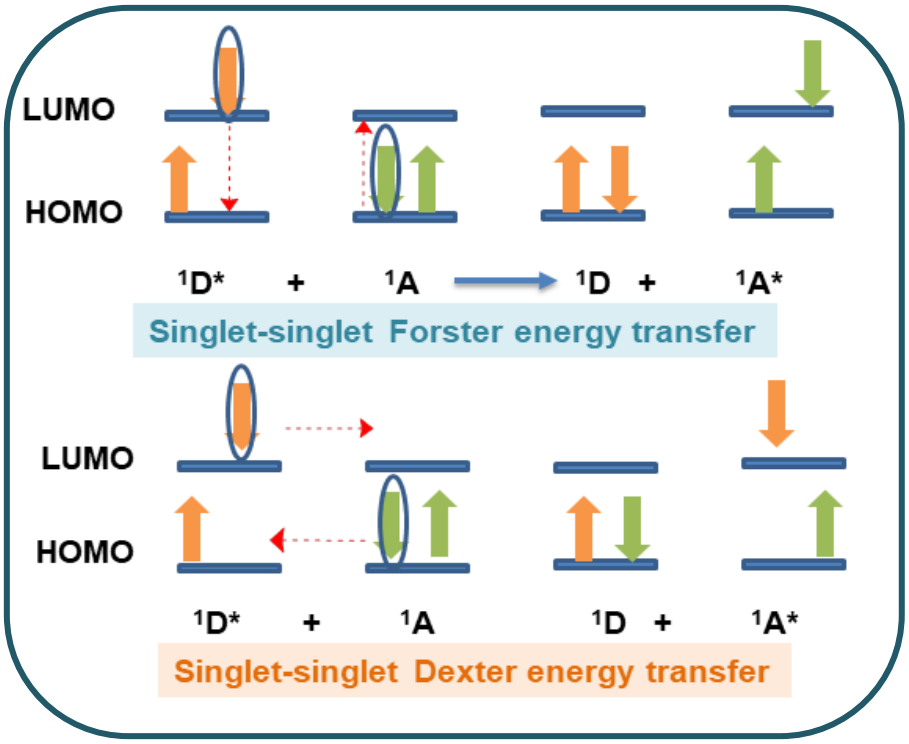

Scheme 1.9. The diagrammatic representation of Dexter and Förster type of energy transfer.

transfer mechanism that occurs when a photoexcited donor molecule transfers its energy to an acceptor molecule through dipole-dipole interactions. FRET is a distance-dependent phenomenon, typically occurring over distances less than 10 nm. Some crucial factors

influencing FRET efficiency encompass the overlap integral between donor emission and acceptor absorption, donor-acceptor distance, orientation factor (dipole alignment), medium's refractive index, and donor quantum yield. These elements collectively dictate the effectiveness of energy transfer in FRET.

(i) Overlap Integral, J (λ)

The degree of spectral overlap between donor emission and acceptor absorbance has been expressed by the overlap integral, which is given by the following equation

$$J(\lambda) = \int F_D(\lambda)\varepsilon_A(\lambda)\lambda^4 d\lambda \qquad (1.1)$$

where $F_D(\lambda)$ is the area-normalized emission spectrum of the donor, and $\varepsilon_A(\lambda)$ denotes the molar absorption coefficient of the acceptor.

(ii) Förster Distance (R_0)

The distance at which efficiency of RET between donor and acceptor is 50% is called Förster distance which has been expressed by the following equation:

$$R_0 = 0.211\ [\kappa^2 \eta^{-4} \phi_D J(\lambda)]^{1/6} \qquad \text{(In Å)} \qquad (1.2)$$

where κ^2 (= 2/3) is the orientation factor of the transition dipoles of the donor and the acceptor, η is the refractive index of the medium, ϕ_D is the quantum yield of the donor, and J(λ) is the spectral overlap integral between the donor emission and the acceptor absorption.[221-222]

(iii) Quantum Yield, ϕ_D

The relative quantum yield of the fluorophore is usually given as

$$\phi_s = \frac{A_s}{A_r} \times \frac{\eta_s^2}{\eta_r^2} \times \frac{OD_r}{OD_s} \times Q_r \qquad (1.3)$$

Here, As and Ar are the area under emission spectrum for the sample and reference, ηs and ηr are the refractive index of the sample and reference, OD_s and OD_r is the optical density of the sample and reference, and ϕr is the quantum yield of the reference.[221-222]

1.1.6.3. Nanoparticle Surface Energy Transfer (NSET)

Recently, resonance energy transfer studies employing metallic nanoparticles have gained paramount importance in modern technology, significantly broadening their applications in investigating specific biological and chemical processes. In the context of metallic nanoparticles, energy transfer between donor-acceptor pairs is often referred to as nanoparticle surface energy transfer (NSET) due to its unique dipole-surface energy characteristics. Notably, NSET typically exhibits higher efficiency compared to traditional FRET. In recent years, Nanoparticle (mediated) surface energy transfer (NSET), conceptualized by Persson and Lang, has gained significant attention for its applicability in determining donor-acceptor systems at distances beyond the limits of FRET. NSET, similar to FRET, involves non-radiative dipole-dipole energy transfer but is distinctive in that it occurs through the interaction of the donor dipole's electromagnetic field with the free conduction electrons of the metal nanoparticle (acceptor). This differs from FRET, where both donor and acceptor are treated as point dipoles. Extensive experimental and theoretical research has confirmed that the efficiency of energy transfer in NSET is dependent on the separation distance between the donor and acceptor, following a $1/d^4$ relationship. For the NSET model, the donor-acceptor separation distance (d_0) at which the efficiency of energy transfer becomes 50 % is estimated by using equation 4.[223-224]

$$d_0 = \left(\frac{0.225\phi_D C^3}{\omega_D^2 \omega_F k_F}\right)^{1/4} \qquad (1.4)$$

where ϕ_D is the quantum yield of the donor, c is the velocity of light, ω_D is the angular frequency of the donor electronic transition, ω_F is the Fermi frequency, and k_F is the Fermi wave vector of the metal. The distance (d) between donor and acceptor is estimated by using the following equation[41]

$$d = d_0^{NSET}\left(\frac{\tau_{DA}}{\tau_D - \tau_{DA}}\right)^{1/4} \quad (1.5)$$

Where τ_D and τ_{DA} are the fluorescence lifetime of the donor in the absence and presence of acceptor respectively. According to the NSET mechanism, the rate of energy transfer can be expressed by the following equation

$$k_{NSET} = \frac{1}{\tau_D}\left(\frac{d_0}{d}\right)^4 \quad (1.6)$$

1.1.7. Objective of the Thesis

In the preceding section, we have discussed about the various aspects of ultra-small sized MNCs, emphasizing their optical properties, synthetic methodologies, surface chemistry, and applications. These discussions have revealed that although numerous studies have been conducted on the above- mentioned systems in the past decade, certain challenges still need to be addressed. Some of the specific challenges are:

- Although extensive research has been conducted to explore the interactions of larger-sized nanomaterials with various biologically and environmentally significant analytes, investigations on the interactions of ultra-small sized MNCs with important analytes are still at an early stage.
- The behaviours of MNCs are not exactly like molecular dyes. The interaction mechanism between MNCs and analytes may not follow the conventional pathways

that are usually observed in molecule-analyte interactions. Hence, a thorough understanding of the MNCs-analytes interaction pathways is very much essential.

- ❖ The impact of surface chemistry on elucidating the binding mechanisms of MNCs with important target analytes still remains unclear. Essentially, interfacial chemistry relating to MNCs is not properly understood.
- ❖ Proper knowledge of the photophysical processes like energy and electron transfer in various MNCs mediated nano-hybrid systems is currently lacking.
- ❖ Notably, within the realm of MNCs, the exploration of gold and silver nanoclusters has been prevalent, however, investigations into copper nanoclusters are considerably limited. Despite copper's biological significance, cost-effectiveness, biocompatibility, water solubility, and widespread availability, there is a considerable research gap in this area. These facts highlight the need for more comprehensive studies on copper nanoclusters.

Therefore, the core objective of this thesis is basically to address the aforementioned issues. In particular, the fundamentals behind the interaction of luminescent coinage metal nanoclusters with biologically and environmentally important analytes have been investigated in the present thesis work. To achieve the thesis objective, numerous MNCs having different surface ligands have been synthesised and their photophysical behaviour has been investigated both in the absence and presence of relevant analytes, utilizing an array of spectroscopic and microscopic techniques. In particular, several fluorescent CuNCs, capped with various ligands have been synthesised and characterised. Efforts have also been exerted to comprehend the crucial influence of the surface chemistry of MNCs on the various events that are exploited during investigations. Additionally, we have made an attempt to understand the fundamentals behind the photophysical response

of MNCs in the vicinity of plasmonic nanoparticles to make a suitable nano-hybrid system for energy-related applications.

1.1.8. Chapter Wise Organization of the Thesis

The current thesis has been divided into seven chapters. *Chapter 1* provides a comprehensive introduction to nanomaterials and their optoelectronic properties. Special focus has been given to ultra-small sized MNCs, covering their optical properties, synthesis, surface chemistry, and applications. The chapter also highlights key processes relevant to the thesis work, such as MNCs-biomolecule interactions, sensing, excitation energy transfer, etc. This chapter concludes by outlining the thesis's objectives with an emphasis on the need to address current challenges in this field.

Chapter 2 delineates various methods and instrumental techniques employed in experimental investigations during thesis work, encompassing steady-state absorption and fluorescence techniques, as well as time-resolved fluorescence spectroscopy methods such as time-correlated single photon counting (TCSPC) and single-molecule fluorescence techniques. This chapter extensively details the synthesis and characterization of various nanomaterials crucial to the thesis work. Finally, this chapter incorporates the error limits for the various measurements employed in the experimental procedures.

Chapter 3 focuses the interaction between bovine serum albumin (BSA) and three distinct CuNCs with different surface ligands: tannic acid (TA), chitosan, and cysteine (Cys). The primary focus of this chapter is to understand the role of these surface ligands in governing the protein-CuNC interaction and, to find if CuNCs exhibit a unique interaction pathway with proteins which is distinct from the usually observed "protein corona". Through fluorescence, ζ-potential and isothermal titration calorimetric (ITC) studies, it has been revealed that BSA and CuNCs do not reach the binding stoichiometry (BSA/CuNCs > 1) required for "protein-

corona" formation. It has also been observed that surface ligands significantly influence the binding events, affecting both binding mode and thermodynamics of the interaction. Circular dichroism (CD) measurements have indicated minimal changes in BSA's native structure in the presence of CuNCs. Fluorescence correlation spectroscopic (FCS) studies at the single-particle level have also provided further insights into protein-CuNC binding pathways. Essentially, this study has suggested that the binding of CuNCs with BSA happens through “protein-complex” like structure formation rather than “protein-corona” formation.

Chapter 4 explores the potential of CuNCs as nanoscale enzyme inhibitors with regard to modulation of the activity of α-Chymotrypsin (α-ChT). The study also elucidates the interaction mechanisms associated with the said event. For this purpose, two distinct CuNCs, capped with different surface ligands (cysteine and tannic acid), have been synthesized and their interaction with α-ChT have been investigated using various spectroscopic and microscopic techniques at both ensemble average and single-molecule levels. Results obtained from enzyme kinetics studies have revealed that both CuNCs can act as effective enzyme inhibitors. It has been observed that while Cys-CuNCs inhibit the enzyme activity through competitive inhibition, TA-CuNCs partially reduce enzyme activity via noncompetitive inhibition. Interestingly, it has been found that surface ligands play a crucial role in regulating α-ChT activity. Thermodynamic data from fluorescence titration and ITC experiments have indicated one-step and two-step binding processes for Cys-CuNCs and TA-CuNCs, respectively. Additionally, FCS studies have provided evidence of the interaction at the single-molecule level. CD measurements have demonstrated minimal changes in α-ChT's fundamental structure in the presence of CuNCs. Overall, outcome of this study has suggested that CuNCs have the potential to be used as effective nano-regulator for enzyme activity in diverse biological applications.

Chapter 5 illustrates the development of a material-based nanoscale fluorescence sensory system (chitosan capped CuNCs) for the selective and sensitive detection of highly reactive oxidative species (hROS) and antioxidants within a single chemical entity. In this regard, various spectroscopic and microscopic techniques have demonstrated the efficacy of CuNCs in serving as efficient turn-off sensors for highly reactive oxidative species (hROS) and turn-on sensors for antioxidants. Quite interestingly, it has been observed that the system effectively detects antioxidants at low concentrations in commercial fruit juices and human blood samples. Additionally, FCS studies have further shown that CuNCs possess the capability to detect hROS at the single-particle level. During the investigations, it has been found that the turn-off sensing mechanism involves the oxidation of Cu(0)NCs to Cu(II) by hROS, whereas the turn-on mechanism happens due to the prevention of oxidation of CuNCs by antioxidants. Interestingly, studies have also demonstrated optical output signals of the probe−analyte interaction during the hROS/antioxidant signalling can be harnessed for constructing NAND and IMPLICATION logic gates, emphasizing the potential of CuNCs in electronics and medical diagnostics.

In *Chapter 6*, we have investigated the impact of surface ligands of CuNCs in catalyzing the $NaBH_4$-mediated reduction of 4-nitrophenol to 4-aminophenol, thereby we have tried to understand some issues related to the reaction mechanism. For this purpose, tannic acid (TA-CuNCs) and cysteine-capped (Cys-CuNCs) CuNCs have been synthesized as nano-catalysts, and their catalytic performance has been compared with ligand-free CuNCs. Kinetic data obtained from absorption studies, have revealed that the rate constant for the reaction, catalyzed by these nano-catalysts, follows the order: $k_{TA-CuNCs} > k_{CuNCs} > k_{Cys-CuNCs}$. Cys-CuNCs and ligand-free CuNCs exhibit an induction time in catalytic reactions, unlike TA-CuNCs, indicating the crucial role of ligand-mediated surface modification. Furthermore, it has been found that elimination of dissolved oxygen from the reaction medium increases rate

constants and eliminates induction time, suggesting its role in facilitating reverse oxidation. It has also been observed that the catalytic activity decreases with rising 4-NP concentration, suggesting a Langmuir-Hinshelwood mechanism for the event. Moreover, the fluorescence property of the nano-catalysts has also been employed to extract various important information regarding the catalytic reaction at both ensemble average and single particle level. Furthermore, it has been demonstrated that CuNCs-based nano-catalysts are not only limited to the conversion of 4-nitrophenol to 4-aminophenol but are quite useful in the conversion of various types of organic substrates.

Chapter 7 has provided various interesting aspects of the electronic interaction between non-plasmonic fluorescence bimetallic silver-capped gold (F-AgAu) nanoparticles and plasmonic gold nanoparticles (AuNPs). Specifically, the excitation energy transfer (EET) from fluorescence bimetallic silver-capped gold (F-AgAu) to gold nanoparticles (AuNPs) and the modulation of this process by cetyltrimethylammonium bromide (CTAB) has been investigated at both ensemble average and single-particle levels. Steady-state and time-resolved fluorescence studies have revealed significant quenching of both fluorescence intensity and lifetime of F-AgAu in the presence of AuNPs. Both cyclic voltammetry and polarity-dependent studies have pointed that electron transfer mechanism is not responsible for the observed fluorescence quenching behaviour of CuNCs in presence of AuNPs. In fact the studies have indicated that the fluorescence quenching of F-AgAu is due to the EET from F-AgAu to AuNPs. Interestingly, it has also been observed that CTAB can reduce the energy transfer efficiency from 87% to 28% by forming a bilayer over AuNPs. Careful analysis of data has suggested $1/d^4$ distance dependence (nanoparticle surface energy transfer, NSET) rather than the conventional $1/d^6$ distance dependence of the Förster resonance energy transfer model. Furthermore, fluorescence lifetime imaging microscopy (FLIM) studies have

also indicated the role of CTAB in controlling EET from non-plasmonic to plasmonic nanoparticles.

References

1. Jin, R.; Zeng, C.; Zhou, M.; Chen, Y. *Chem. Rev.* **2016**, *116*, 10346-10413.
2. Zhang, L.; Wang, E. *Nano Today* **2014**, *9*, 132-157.
3. Lu, Y.; Chen, W. *Chem. Soc. Rev.* **2012**, *41*, 3594-3623.
4. Schmid, G.; Bäumle, M.; Geerkens, M.; Heim, I.; Osemann, C.; Sawitowski, T. *Chem. Soc. Rev.* **1999**, *28*, 179-185.
5. Jung, J. H.; Lee, J. H.; Shinkai, S. *Chem. Soc. Rev.* **2011**, *40*, 4464-4474.
6. Dupont, J.; Scholten, J. D. *Chem. Soc. Rev.* **2010**, *39*, 1780-1804.
7. Chiang, C.-K.; Chen, W.-T.; Chang, H.-T. *Chem. Soc. Rev.* **2011**, *40*, 1269-1281.
8. Cortie, M. B.; McDonagh, A. M. *Chem. Rev.* **2011**, *111*, 3713-3735.
9. Wang, Y. *Acc. Chem. Res.* **1991**, *24*, 133-139.
10. Steigerwald, M. L.; Brus, L. E., *Acc. Chem. Res.* **1990**, *23*, 183-188.
11. Weller, H. *Adv. Mater.* **1993**, *5*, 88-95.
12. Eustis, S.; El-Sayed, M. A. *Chem. Soc. Rev.* **2006**, *35*, 209-217.
13. Kelly, K. L.; Coronado, E.; Zhao, L. L.; Schatz, G. C. *J. Phys. Chem. B* **2003**, *107*, 668– 677.
14. Kerker, M. *J. Colloid Interface Sci.* **1985**, *105*, 297-314.
15. Díez, I.; Ras, R. H. A. *Advanced Fluorescence Reporters in Chemistry and Biology II: Molecular Constructions, Polymers and Nanoparticles*, Demchenko, A. P., Ed. Springer: Berlin/Heidelberg, Germany, 2010; pp 307-332.
16. Yan, J.; Teo, B. K.; Zheng, N. *Acc. Chem. Res.* **2018**, *51*, 3084-3093.
17. Chakraborty, S.; Mukherjee, S. *ChemComm.* **2022**, *58*, 29-47.
18. Xie, J.; Zheng, Y.; Ying, J. Y. *J. Am. Chem. Soc.* **2009**, *131*, 888-889.
19. Retnakumari, A.; Setua, S.; Menon, D.; Ravindran, P.; Muhammed, H.; Pradeep, T.; Nair, S.; Koyakutty, M. *Nanotechnology* **2010**, *21*, 055103.
20. Shang, L.; Nienhaus, G. U. *Biophys. Rev.* **2012**, *4*, 313-322.
21. Hasegawa, S.; Takano, S.; Harano, K.; Tsukuda, T. *JACS Au* **2021**, *1*, 660-668.
22. Liu, X.; Astruc, D. *Coord. Chem. Rev.* **2018**, *359*, 112-126.
23. Jin, R.; Li, G.; Sharma, S.; Li, Y.; Du, X. *Chem. Rev.* **2021**, *121*, 567-648.
24. Rong, W.; Zou, H.; Zang, W.; Xi, S.; Wei, S.; Long, B.; Hu, J.; Ji, Y.; Duan, L. *Angew. Chem. Int. Ed.* **2021**, *60*, 466-472.
25. Shiang, Y.-C.; Huang, C.-C.; Chen, W.-Y.; Chen, P.-C.; Chang, H.-T. *J. Mater. Chem.* **2012**, *22*, 12972-12982.
26. Shellaiah, M.; Sun, K. W. *Chemosensors* **2017**, *5*, 36.
27. Zhao, T.; Zhou, T.; Yao, Q.; Hao, C.; Chen, X. *J. Environ. Sci. Health C* **2015**, *33*, 168-187.
28. Shang, L.; Dong, S.; Nienhaus, G. U. *Nano Today* **2011**, *6*, 401-418.

29. Zhu, M.; Aikens, C. M.; Hollander, F. J.; Schatz, G. C.; Jin, R. *J. Am. Chem. Soc.* **2008**, *130*, 5883-5885.
30. Wei, W.; Lu, Y.; Chen, W.; Chen, S. *J. Am. Chem. Soc.* **2011**, *133*, 2060-3.
31. Akhuli, A.; Chakraborty, D.; Agrawal, A. K.; Sarkar, M. *Langmuir* **2021**, *37*, 1823-1837.
32. Jin, R. *Nanoscale* **2015**, *7*, 1549-1565.
33. Negishi, Y.; Nobusada, K.; Tsukuda, T. *J. Am. Chem. Soc.* **2005**, *127*, 5261-5270.
34. Baghdasaryan, A.; Bürgi, T. *Nanoscale* **2021**, *13*, 6283-6340.
35. Yang, T. Q.; Peng, B.; Shan, B. Q.; Zong, Y. X.; Jiang, J. G.; Wu, P.; Zhang, K. *Nanomaterials (Basel)* **2020**, *10*.
36. An, Y.; Ren, Y.; Bick, M.; Dudek, A.; Hong-Wang Waworuntu, E.; Tang, J.; Chen, J.; Chang, B. *Biosens. Bioelectron.* **2020**, *154*, 112078.
37. Huang, T.; Murray, R. W. *J. Phys. Chem. B* **2001**, *105*, 12498-12502.
38. Huang, T.; Murray, R. W. *J. Phys. Chem. B* **2003**, *107*, 7434-7440.
39. Link, S.; Beeby, A.; FitzGerald, S.; El-Sayed, M. A.; Schaaff, T. G.; Whetten, R. L. *J. Phys. Chem. B* **2002**, *106*, 3410-3415.
40. Wei, W.; Lu, Y.; Chen, W.; Chen, S. *J. Am. Chem. Soc.* **2011**, *133*, 2060-2063.
41. Yang, J.; Li, Z.; Jia, Q. *Sens. Actuators, B* **2019**, *297*, 126807.
42. Udaya Bhaskara Rao, T.; Pradeep, T. *Angew. Chem. Int. Ed.* **2010**, *49*, 3925-3929.
43. Yang, T.-Q.; Peng, B.; Shan, B.-Q.; Zong, Y.-X.; Jiang, J.-G.; Wu, P.; Zhang, K. *Nanomaterials* **2020**, *10*, 261.
44. Luo, Z.; Yuan, X.; Yu, Y.; Zhang, Q.; Leong, D. T.; Lee, J. Y.; Xie, J. *J. Am. Chem. Soc.* **2012**, *134*, 16662-16670.
45. Liu, J.; Duchesne, P. N.; Yu, M.; Jiang, X.; Ning, X.; Vinluan III, R. D.; Zhang, P.; Zheng, J. *Angew. Chem. Int. Ed.* **2016**, *55*, 8894-8898.
46. Rajamanikandan, R.; Ilanchelian, M., *Mater. Sci. Eng. C* . **2019**, *98*, 1064-1072.
47. Zhou, T.; Xu, W.; Yao, Q.; Zhao, T.; Chen, X. *Methods Appl. Fluoresc.* **2015**, *3*, 044002.
48. Cai, Z.; Wu, L.; Qi, K.; Deng, C.; Zhang, C. *Spectrochim. Acta - A: Mol. Biomol. Spectrosc.* **2021**, *247*, 119145.
49. Feng, J.; Chen, Y.; Han, Y.; Liu, J.; Ma, S.; Zhang, H.; Chen, X. *ACS Omega* **2017**, *2*, 9109-9117.
50. Borghei, Y.-S.; Hosseini, M.; Ganjali, M. R.; Hosseinkhani, S. *Sens. Actuators, B* **2017**, *248*, 133-139.
51. Cha, S.-H.; Kim, J.-U.; Kim, K.-H.; Lee, J.-C. *Chem. Mater.* **2007**, *19*, 6297-6303.
52. Wu, Z.; Wang, M.; Yang, J.; Zheng, X.; Cai, W.; Meng, G.; Qian, H.; Wang, H.; Jin, R. *Small* **2012**, *8*, 2028-2035.
53. Wu, Z.; Jin, R. *Nano Lett.* **2010**, *10*, 2568-2573.
54. Pyo, K.; Thanthirige, V. D.; Kwak, K.; Pandurangan, P.; Ramakrishna, G.; Lee, D. *J. Am. Chem. Soc.* **2015**, *137*, 8244-8250.
55. Zheng, J.; Zhang, C.; Dickson, R. M. *Phys. Rev. Lett.* **2004**, *93*, 077402.
56. Londoño-Larrea, P.; Vanegas, J. P.; Cuaran-Acosta, D.; Zaballos-García, E.; Pérez-Prieto, J. *Chem. Eur. J.* **2017**, *23*, 8137-8141.

57. Zhou, C.; Sun, C.; Yu, M.; Qin, Y.; Wang, J.; Kim, M.; Zheng, J. *J. Phys. Chem. C* **2010**, *114*, 7727-7732.
58. Negishi, Y.; Chaki, N. K.; Shichibu, Y.; Whetten, R. L.; Tsukuda, T. *J. Am. Chem. Soc.* **2007**, *129*, 11322-11323.
59. Jia, X.; Li, J.; Wang, E. *Small* **2013**, *9*, 3873-3879.
60. Chen, H.; Kou, X.; Yang, Z.; Ni, W.; Wang, J. *Langmuir* **2008**, *24*, 5233-5237.
61. Zhou, R.; Shi, M.; Chen, X.; Wang, M.; Chen, H. *Chem. Eur. J.* **2009**, *15*, 4944-4951.
62. Maretti, L.; Billone, P. S.; Liu, Y.; Scaiano, J. C. *J. Am. Chem. Soc.* **2009**, *131*, 13972-13980.
63. Díez, I.; Pusa, M.; Kulmala, S.; Jiang, H.; Walther, A.; Goldmann, A. S.; Müller, A. H. E.; Ikkala, O.; Ras, R. H. A. *Angew. Chem. Int. Ed.* **2009**, *48*, 2122-2125.
64. Zhou, R.; Shi, M.; Chen, X.; Wang, M.; Chen, H. *Chem. Eur. J.* **2009**, *15*, 4944-4951.
65. Willets, K. A.; Van Duyne, R. P. *Annu. Rev. Phys. Chem.* **2007**, *58*, 267-297.
66. Shen, X. S.; Wang, G. Z.; Hong, X.; Zhu, W. *Phys. Chem. Chem. Phys.* **2009**, *11*, 7450-7454.
67. Xiao, Y.; Wu, Z.; Yao, Q.; Xie, J. *Aggregate* **2021**, *2*, 114-132.
68. Chakraborty, S.; Nandy, A.; Ghosh, S.; Das, N. K.; Parveen, S.; Datta, S.; Mukherjee, S. *Analyst* **2021**, *146*, 1455-1463.
69. Cao, H.; Chen, Z.; Zheng, H.; Huang, Y. *Biosens. Bioelectron.* **2014**, *62*, 189-195.
70. Song, Y.; Zhong, J.; Yang, S.; Wang, S.; Cao, T.; Zhang, J.; Li, P.; Hu, D.; Pei, Y.; Zhu, M. *Nanoscale* **2014**, *6*, 13977-13985.
71. Maity, S.; Bain, D.; Patra, A. *J. Phys. Chem. C* **2019**, *123*, 2506-2515.
72. Deng, H.-H.; Li, K.-L.; Zhuang, Q.-Q.; Peng, H.-P.; Zhuang, Q.-Q.; Liu, A.-L.; Xia, X.-H.; Chen, W. *Nanoscale* **2018**, *10*, 6467-6473.
73. Wang, Y.; Xia, Y. *Nano Lett.* **2004**, *4*, 2047-2050.
74. Velikov, K. P.; Pelan, E. *Soft Matter* **2008**, *4*, 1964-1980.
75. Dhenadhayalan, N.; Lin, K.-C.; Suresh, R.; Ramamurthy, P. *J. Phys. Chem. C* **2016**, *120*, 1252-1261.
76. Negishi, Y.; Takasugi, Y.; Sato, S.; Yao, H.; Kimura, K.; Tsukuda, T. *J. Am. Chem. Soc.* **2004**, *126*, 6518-6519.
77. Lee, D.; Donkers, R. L.; Wang, G.; Harper, A. S.; Murray, R. W. *J. Am. Chem. Soc.* **2004**, *126*, 6193-6199.
78. Wang, Z.; Cai, W.; Sui, J. *ChemPhysChem* **2009**, *10*, 2012-2015.
79. Paau, M. C.; Lo, C. K.; Yang, X.; Choi, M. M. F. *J. Phys. Chem. C* **2010**, *114*, 15995-16003.
80. Adhikari, B.; Banerjee, A. *Chem. Mater.* **2010**, *22*, 4364-4371.
81. Zheng, X.-J.; Liang, R.-P.; Li, Z.-J.; Zhang, L.; Qiu, J.-D. *Chemical* **2016**, *230*, 314-319.
82. Wang, Z.; Chen, B.; Rogach, A. L. *Nanoscale Horiz.* **2017**, *2*, 135-146.
83. Bartlett, P. A.; Bauer, B.; Singer, S. *J. Am. Chem. Soc.* **1978**, *100*, 5085-5089.
84. Ambrosi, A.; Chua, C. K.; Bonanni, A.; Pumera, M. *Chem. Rev.* **2014**, *114*, 7150-7188.
85. Schmid, G.; Pfeil, R.; Boese, R.; Bandermann, F.; Meyer, S.; Calis, G. H. M.; van der Velden, J. W. A. *Chem. Ber.* **1981**, *114*, 3634-3642.

86. Weare, W. W.; Reed, S. M.; Warner, M. G.; Hutchison, J. E. *J. Am. Chem. Soc.* **2000**, *122*, 12890-12891.
87. Zheng, J.; Dickson, R. M. *J. Am. Chem. Soc.* **2002**, *124*, 13982-13983.
88. Ye, H.; Scott, R. W. J.; Crooks, R. M. *Langmuir* **2004**, *20*, 2915-2920.
89. Liu, H.-Y.; Zhu, J.-J. *Chin. J. Anal. Chem.* **2013**, *41*, 658-663.
90. Zhang, J.; Xu, S.; Kumacheva, E. *Adv. Mater.* **2005**, *17*, 2336-2340.
91. Shen, Z.; Duan, H.; Frey, H. *Adv. Mater.* **2007**, *19*, 349-352.
92. Xie, J.; Zheng, Y.; Ying, J. Y. *Chem. Commun.* **2010**, *46*, 961-963.
93. Hu, D.; Sheng, Z.; Gong, P.; Zhang, P.; Cai, L. *Analyst* **2010**, *135*, 1411-1416.
94. Wei, H.; Wang, Z.; Yang, L.; Tian, S.; Hou, C.; Lu, Y. *Analyst* **2010**, *135*, 1406-1410.
95. Kawasaki, H.; Yoshimura, K.; Hamaguchi, K.; Arakawa, R. *Anal. Sci.* **2011**, *27*, 591-591.
96. Mathew, A.; Sajanlal, P.; Pradeep, T. *J. Mater. Chem.* **2011**, *21*, 11205-11212.
97. Ghosh, S.; Das, N. K.; Anand, U.; Mukherjee, S. *J. Phys. Chem. Lett.* **2015**, *6*, 1293-1298.
98. Anand, U.; Ghosh, S.; Mukherjee, S. *J. Phys. Chem. Lett.* **2012**, *3*, 3605-3609.
99. Tian, L.; Li, Y.; Ren, T.; Tong, Y.; Yang, B.; Li, Y. *Talanta* **2017**, *170*, 530-539.
100. Zhao, T.; He, X.-W.; Li, W.-Y.; Zhang, Y.-K. *J. Mater. Chem. B* **2015**, *3*, 2388-2394.
101. Kong, Y.; Chen, J.; Gao, F.; Brydson, R.; Johnson, B.; Heath, G.; Zhang, Y.; Wu, L.; Zhou, D. *Nanoscale* **2013**, *5*, 1009-1017.
102. Zhang, Y.; Liu, Y.; Li, Y.; Yang, Z.; Liu, S. *J. Mater. Chem. C* **2016**, *4*, 9172-9178.
103. Pitchiaya, S.; Krishnan, Y. *Chem. Soc. Rev.* **2006**, *35*, 1111-1121.
104. Petty, J. T.; Zheng, J.; Hud, N. V. *J. Am. Chem. Soc.* **2004**, *126*, 5207-5212.
105. Richards, C. I.; Choi, S.; Hsiang, J.-C.; Antoku, Y.; Vosch, T.; Bongiorno, A.; Tzeng, Y.-L.; Dickson, R. M. *J. Am. Chem. Soc.* **2008**, *130*, 5038-5039.
106. Li, J.; Zhu, J.-J.; Xu, K. *TrAC Trends Anal. Chem.* **2014**, *58*, 90-98.
107. Aubin-Tam, M.-E.; Hamad-Schifferli, K., *Biomed Mater.* **2008**, *3*, 034001.
108. Bruchez, M., Jr.; Moronne, M.; Gin, P.; Weiss, S.; Alivisatos, A. P. *sci.* **1998**, *281*, 2013-6.
109. Sarkar, R.; Narayanan, S. S.; Pålsson, L. O.; Dias, F.; Monkman, A.; Pal, S. K. *J. Phys. Chem. B.* **2007**, *111*, 12294-8.
110. Goswami, N.; Zheng, K.; Xie, J. *Nanoscale* **2014**, *6*, 13328-13347.
111. Choi, S.; Dickson, R. M.; Yu, J. *Chem. Soc. Rev.* **2012**, *41*, 1867-1891.
112. Mahmoudi, M.; Lynch, I.; Ejtehadi, M. R.; Monopoli, M. P.; Bombelli, F. B.; Laurent, S. *Chem. Rev.* **2011**, *111*, 5610-5637.

113. Casals, E.; Pfaller, T.; Duschl, A.; Oostingh, G. J.; Puntes, V. *ACS Nano* **2010**, *4*, 3623-3632.

114. Cui, M.; Liu, R.; Deng, Z.; Ge, G.; Liu, Y.; Xie, L. *Nano Res.* **2014**, *7*, 345-352.

115. Lundqvist, M.; Stigler, J.; Elia, G.; Lynch, I.; Cedervall, T.; Dawson, K. A. *PNAS* **2008**, *105*, 14265-14270.

116. Cedervall, T.; Lynch, I.; Lindman, S.; Berggård, T.; Thulin, E.; Nilsson, H.; Dawson, K. A.; Linse, S. *PNAS* **2007**, *104*, 2050-2055.

117. Nel, A. E.; Mädler, L.; Velegol, D.; Xia, T.; Hoek, E. M. V.; Somasundaran, P.; Klaessig, F.; Castranova, V.; Thompson, M. *Nat. Mater.* **2009**, *8*, 543-557.

118. Cedervall, T.; Lynch, I.; Foy, M.; Berggård, T.; Donnelly, S. C.; Cagney, G.; Linse, S.; Dawson, K. A. *Angew. Chem. Int. Ed.* **2007**, *46*, 5754-5756.

119. Mahmoudi, M.; Lynch, I.; Ejtehadi, M. R.; Monopoli, M. P.; Bombelli, F. B.; Laurent, S. *Chem. Rev.* **2011**, *111*, 5610-5637.

120. Piella, J.; Bastús, N. G.; Puntes, V. *Bioconjug. Chem.* **2017**, *28*, 88-97.

121. Akhuli, A.; Chakraborty, D.; Preeyanka, N.; Dora, A. S.; Sarkar, M. *ACS Appl. Nano Mater.* **2023**, *6*, 4910-4924.

122. Yin, M.-M.; Chen, W.-Q.; Lu, Y.-Q.; Han, J.-Y.; Liu, Y.; Jiang, F.-L. *Nanoscale* **2020**, *12*, 4573-4585.

123. Kopp, M.; Kollenda, S.; Epple, M. *Acc. Chem. Res.* **2017**, *50*, 1383-1390.

124. Boselli, L.; Polo, E.; Castagnola, V.; Dawson, K. A. *Angew. Chem. Int. Ed.* **2017**, *56*, 4215-4218.

125. Kumar Das, N.; Chakraborty, S.; Mukherjee, M.; Mukherjee, S. *ChemPhysChem* **2018**, *19*, 2218-2223.

126. Tao, Y.; Li, M.; Ren, J.; Qu, X. *Chem. Soc. Rev.* **2015**, *44*, 8636-8663.

127. Qu, F.; Dou, L. L.; Li, N. B.; Luo, H. Q. *J. Mater. Chem. C* **2013**, *1*, 4008-4013.

128. Liu, Z.; Wu, Z.; Yao, Q.; Cao, Y.; Chai, O. J. H.; Xie, J. *Nano Today* **2021**, *36*, 101053.

129. Bhattacharyya, K.; Mukherjee, S., *Bulletin of the Chemical Society of Japan* 2018, *91*, 447-454.

130. Du, Y.; Sheng, H.; Astruc, D.; Zhu, M. *Chem. Rev.* **2020**, *120*, 526-622.

131. Shahsavari, S.; Hadian-Ghazvini, S.; Hooriabad Saboor, F.; Menbari Oskouie, I.; Hasany, M.; Simchi, A.; Rogach, A. L. *Mater. Chem. Front.* **2019**, *3*, 2326-2356.

132. Song, X.-R.; Goswami, N.; Yang, H.-H.; Xie, J. *Analyst* **2016**, *141*, 3126-3140.

133. Su, Y.; Xue, T.; Liu, Y.; Qi, J.; Jin, R.; Lin, Z. *Nano Res.* **2019**, *12*, 1251-1265.

134. Guo, W.; Yuan, J.; Wang, E. *ChemComm* **2009**, 3395-3397.

135. Su, Y.; Xue, T.; Liu, Y.; Qi, J.; Jin, R.; Lin, Z. *Nano Res.* **2019**, *12*, 1251-1265.

136. Wei, B.; Yang, L. *Microchem. J.* **2010**, *94*, 99-107.

137. Peña-Vázquez, E.; Villanueva-Alonso, J.; Bermejo-Barrera, P. *J. Anal. At. Spectrom.* **2007**, *22*, 642-649.

138. Lettieri, M.; Palladino, P.; Scarano, S.; Minunni, M. *Sens. Actuator A Phys.* **2022**, *4*, 100108.

139. Deng, L.; Zhou, Z.; Li, J.; Li, T.; Dong, S. *Chem. Comm.* **2011**, *47*, 11065-11067.

140. Zhou, T.; Huang, Y.; Li, W.; Cai, Z.; Luo, F.; Yang, C. J.; Chen, X. *Nanoscale* **2012**, *4*, 5312-5315.

141. Shang, L.; Yang, L.; Stockmar, F.; Popescu, R.; Trouillet, V.; Bruns, M.; Gerthsen, D.; Nienhaus, G. U. *Nanoscale* **2012**, *4*, 4155-4160.

142. Tao, H.; Zhang, Z.; Cao, Q.; Li, L.; Xu, S.; Jiang, C.; Li, Y.; Liu, Y. *RSC Adv.* **2022**, *12*, 12655-12662.

143. Jin, L.; Zhang, Z.; Tang, A.; Li, C.; Shen, Y. *Biosens. Bioelectron.* **2016**, *79*, 108-113.

144. Cai, Z.; Li, H.; Wu, J.; Zhu, L.; Ma, X.; Zhang, C. *RSC Adv.* **2020**, *10*, 8989-8993.

145. Liu, J.; Wang, B.; Xu, M.; Wang, L.; Zhou, Z., *J. Lumin.* **2017**, *185*, 258-262.

146. Feng, D.-Q.; Zhu, W.; Liu, G.; Wang, W. *RSC Adv.* **2016**, *6*, 96729-96734.

147. Lin, Y.-S.; Chiu, T.-C.; Hu, C.-C. *RSC Adv.* **2019**, *9*, 9228-9234.

148. Ghosh, S.; Anand, U.; Mukherjee, S. *Anal. Chem.* **2014**, *86*, 3188-3194.

149. Liu, G.; Feng, D. Q.; Hua, D.; Liu, T.; Qi, G.; Wang, W. *Langmuir* **2017**, *33*, 14643-14648.

150. Suo, Z.; Hou, X.; Hu, Z.; Liu, Y.; Xing, F.; Feng, L. *Mikrochim. Acta* **2019**, *186*, 799.

151. Chen, T. H.; Tseng, W. L. *Small* **2012**, *8*, 1912-9.

152. Li, J.; Zhong, X.; Zhang, H.; Le, X. C.; Zhu, J.-J. *Anal. Chem.* **2012**, *84*, 5170-5174.

153. Zhang, L.; Zhu, J.; Zhou, Z.; Guo, S.; Li, J.; Dong, S.; Wang, E. *Chem. Sci.* **2013**, *4*, 4004-4010.

154. Wang, Y.; Wang, Y.; Zhou, F.; Kim, P.; Xia, Y. *Small* **2012**, *8*, 3769-3773.

155. Liu, J.-J.; Song, X.-R.; Wang, Y.-W.; Zheng, A.-X.; Chen, G.-N.; Yang. *Anal. Chim. Acta* **2012**, *749*, 70-74.

156. Yourston, L. E.; Krasnoslobodtsev, A. V. *Molecules* **2020**, *25*.

157. Kuhn, H.; Demidov, V. V.; Coull, J. M.; Fiandaca, M. J.; Gildea, B. D. *J. Am. Chem. Soc.* **2002**, *124*, 1097-1103.

158. Triulzi, R. C.; Micic, M.; Giordani, S.; Serry, M.; Chiou, W.-A.; Leblanc, R. M. *ChemComm.* **2006**, 5068-5070.

159. Wolfe, M. S. *Chem. Rev.* **2009**, *109*, 1599-1612.

160. Sharma, J.; Yeh, H.-C.; Yoo, H.; Werner, J. H.; Martinez, J. S. *ChemComm.* **2011**, *47*, 2294-2296.

161. Guo, W.; Yuan, J.; Dong, Q.; Wang, E. *J. Am. Chem. Soc.* **2010**, *132*, 932-934.

162. Huang, Z.; Pu, F.; Hu, D.; Wang, C.; Ren, J.; Qu, X. *Chem. Eur. J.* **2011**, *17*, 3774-3780.

163. Jia, X.; Li, J.; Han, L.; Ren, J.; Yang, X.; Wang, E. *ACS Nano* **2012**, *6*, 3311-3317.

164. Pramanik, S.; Khamari, L.; Mukherjee, S. *J. Phys. Chem. Lett.* **2021**, *12*, 2547-2554.

165. Ju, E.; Liu, Z.; Du, Y.; Tao, Y.; Ren, J.; Qu, X. *ACS Nano* **2014**, *8*, 6014-6023.

166. Xie, Y.; Xianyu, Y.; Wang, N.; Yan, Z.; Liu, Y.; Zhu, K.; Hatzakis, N. S.; Jiang, X. *Adv. Funct. Mater.* **2018**, *28*, 1702026.

167. Akhuli, A.; Preeyanka, N.; Chakraborty, D.; Sarkar, M. *ACS Appl. Nano Mater.* **2022**, *5*, 5826-5837.

168. Fang, J.; Zhang, B.; Yao, Q.; Yang, Y.; Xie, J.; Yan, N. *Coord. Chem. Rev.* **2016**, *322*, 1-29.

169. De Heer, W. A. *RMP* **1993**, *65*, 611.

170. Zhai, H.-J.; Pan, L.-L.; Dai, B.; Kiran, B.; Li, J.; Wang, L.-S. *J. Phys. Chem. C* **2008**, *112*, 11920-11928.

171. Zou, X.; Zhang, Y. *Chem Soc Rev* **2015**, *44*, 5148-5180.

172. Xu, Y.; Kraft, M.; Xu, R. *Chem Soc Rev* **2016**, *45*, 3039-3052.

173. Suen, N.-T.; Hung, S.-F.; Quan, Q.; Zhang, N.; Xu, Y.-J.; Chen, H. M. *Chem Soc Rev* **2017**, *46*, 337-365.

174. Morales-Guio, C. G.; Stern, L.-A.; Hu, X. *Chem Soc Rev* **2014**, *43*, 6555-6569.

175. Kawasaki, H.; Kumar, S.; Li, G.; Zeng, C.; Kauffman, D. R.; Yoshimoto, J.; Iwasaki, Y.; Jin, R. *Chem. Mater.* **2014**, *26*, 2777-2788.

176. Negishi, Y.; Kamimura, U.; Ide, M.; Hirayama, M. *Nanoscale* **2012**, *4*, 4263-4268.

177. Aikens, C. M. *J. Phys. Chem. Lett.* **2010**, *1*, 2594-2599.

178. Widmann, D.; Behm, R. J. *Acc. Chem. Res.* **2014**, *47*, 740-749.

179. Sanchez, A.; Abbet, S.; Heiz, U.; Schneider, W. D.; Häkkinen, H.; Barnett, R. N.; Landman, U. *J. Phys. Chem. A* **1999**, *103*, 9573-9578.

180. Cao, S.; Tao, F.; Tang, Y.; Li, Y.; Yu, J. *Chem Soc Rev* **2016**, *45*, 4747-4765.

181. Mitsudome, T.; Kaneda, K. *Green Chem.* **2013**, *15*, 2636-2654.

182. Li, G.; Abroshan, H.; Liu, C.; Zhuo, S.; Li, Z.; Xie, Y.; Kim, H. J.; Rosi, N. L.; Jin, R. *ACS Nano* **2016**, *10*, 7998-8005.

183. Oliver-Meseguer, J.; Cabrero-Antonino, J. R.; Domínguez, I.; Leyva-Pérez, A.; Corma, A. *Sci* **2012**, *338*, 1452-5.

184. Leyva-Pérez, A.; Oliver-Meseguer, J.; Rubio-Marqués, P.; Corma, A. *Angew. Chem. Int. Ed.* **2013**, *52*, 11554-11559.

185. Lv, C., et al. *Nano Res.* **2016**, *9*, 2544-2550.

186. Ansar, S. M.; Kitchens, C. L. *ACS Catal.* **2016**, *6*, 5553-5560.

187. Campisi, S.; Schiavoni, M.; Chan-Thaw, C. E.; Villa, A. *Catal.* **2016**, *6*, 185.

188. Lopez-Sanchez, J. A., et al. *Nat. Chem.* **2011**, *3*, 551-556.

189. Schrader, I.; Warneke, J.; Backenköhler, J.; Kunz, S. *J. Am. Chem. Soc.* **2015**, *137*, 905-912.

190. Yoskamtorn, T.; Yamazoe, S.; Takahata, R.; Nishigaki, J.-i.; Thivasasith, A.; Limtrakul, J.; Tsukuda, T. *ACS Catal.* **2014**, *4*, 3696-3700.

191. Liu, J.; Yu, M.; Zhou, C.; Yang, S.; Ning, X.; Zheng, J. *J. Am. Chem. Soc.* **2013**, *135*, 4978-4981.

192. Zhou, C.; Long, M.; Qin, Y.; Sun, X.; Zheng, J. *Angew. Chem., Int. Ed. Engl.* **2011**, *50*, 3168-72.

193. Zhou, C.; Hao, G.; Thomas, P.; Liu, J.; Yu, M.; Sun, S.; Öz, O. K.; Sun, X.; Zheng, J. *Angew. Chem., Int. Ed. Engl.* **2012**, *51*, 10118-22.

194. Goswami, N.; Zheng, K.; Xie, J. *Nanoscale* **2014**, *6*, 13328-13347.

195. Gao, S.; Chen, D.; Li, Q.; Ye, J.; Jiang, H.; Amatore, C.; Wang, X. *Sci. Rep.* **2014**, *4*, 4384.

196. Das, N. K.; Ghosh, S.; Priya, A.; Datta, S.; Mukherjee, S. *J. Phys. Chem. C* **2015**, *119*, 24657-24664.

197. Chen, H.; Li, B.; Ren, X.; Li, S.; Ma, Y.; Cui, S.; Gu, Y. *Biomater.* **2012**, *33*, 8461-8476.

198. Chen, T.; Xu, S.; Zhao, T.; Zhu, L.; Wei, D.; Li, Y.; Zhang, H.; Zhao, C. *ACS Appl. Mater. Interfaces* **2012**, *4*, 5766-5774.

199. Wu, X.; He, X.; Wang, K.; Xie, C.; Zhou, B.; Qing, Z. *Nanoscale* **2010**, *2*, 2244-2249.

200. Yu, J.; Patel, S. A.; Dickson, R. M. *Angew. Chem. Int. Ed.* **2007**, *46*, 2028-2030.

201. Wang, J.; Zhang, G.; Li, Q.; Jiang, H.; Liu, C.; Amatore, C.; Wang, X. *Sci. Rep.* **2013**, *3*, 1157.

202. Taglietti, A.; Diaz Fernandez, Y. A.; Amato, E.; Cucca, L.; Dacarro, G.; Grisoli, P.; Necchi, V.; Pallavicini, P.; Pasotti, L.; Patrini, M. *Langmuir* **2012**, *28*, 8140-8.

203. Amato, E.; Diaz-Fernandez, Y. A.; Taglietti, A.; Pallavicini, P.; Pasotti, L.; Cucca, L.; Milanese, C.; Grisoli, P.; Dacarro, C.; Fernandez-Hechavarria, J. M.; Necchi, V. *Langmuir* **2011**, *27*, 9165-73.

204. Yuan, X.; Setyawati, M. I.; Tan, A. S.; Ong, C. N.; Leong, D. T.; Xie, J. *NPG Asia Mater.* **2013**, *5*, e39-e39.

205. Chan, P.-H.; Chen, Y.-C. *Anal. Chem.* **2012**, *84*, 8952-8956.

206. Chen, W.-Y.; Lin, J.-Y.; Chen, W.-J.; Luo, L.; Wei-Guang Diau, E.; Chen, Y.-C. *Nanomed.* **2010**, *5*, 755-764.

207. Yuan, X.; Setyawati, M. I.; Tan, A. S.; Ong, C. N.; Leong, D. T.; Xie, J. *NPG Asia Mater.* **2013,** *5* (2), e39-e392013.

208. Xie, J.; Lee, S.; Chen, X. *Adv. Drug Deliv. Rev.* **2010**, *62*, 1064-79.

209. Fan, Z.; Fu, P. P.; Yu, H.; Ray, P. C. *J. Food Drug Anal.* **2014**, *22*, 3-17.

210. Zhu, C.-L.; Wang, X.-W.; Lin, Z.-Z.; Xie, Z.-H.; Wang, X.-R. *J. Food Drug Anal.* **2014**, *22*, 18-28.

211. Wang, Y.; Chen, J.; Irudayaraj, J. *ACS Nano* **2011**, *5*, 9718-9725.

212. Zhang, X. D., et al., *Adv. Healthc. Mater* **2014**, *3*, 133-41.

213. Kutty, R. V.; Wei Leong, D. T.; Feng, S.-S. *Nanomed.* **2014**, *9*, 561-564.

214. Zhang, X.-D.; Wu, D.; Shen, X.; Chen, J.; Sun, Y.-M.; Liu, P.-X.; Liang, X.-J. *Biomat.* **2012**, *33*, 6408-6419.

215. Setyawati, M. I.; Tay, C. Y.; Leong, D. T. *Nanomedicine* **2014**, *9*, 369-371.

216. Zhang, X.-D., et al., *Adv. Healthc. Mater* **2014**, *3*, 133-141.

217. Zhang, X.-D.; Luo, Z.; Chen, J.; Shen, X.; Song, S.; Sun, Y.; Fan, S.; Fan, F.; Leong, D. T.; Xie, J. *Adv Mater* **2014**, *26*, 4565-4568.

218. Oh, E.; Huston, A. L.; Shabaev, A.; Efros, A.; Currie, M.; Susumu, K.; Bussmann, K.; Goswami, R.; Fatemi, F. K.; Medintz, I. L. *Sci. Rep.* **2016**, *6*, 35538.

219. Ghosh, S.; Das, N. K.; Anand, U.; Mukherjee, S. *J. Phys. Chem. Lett.* **2015**, *6*, 1293-1298.

220. Akhuli, A.; Preeyanka, N.; Chakraborty, D.; Sarkar, M. *Phys. Chem. Chem. Phys.2023, 25, 17470-17481*.

221. Lakowicz, J. R., Principles of Fluorescence Spectroscopy. *Springer*, **2006**.

222. Valeur, B., Molecular Fluorescence: Principles and Applications. *Wiley-VCH: Weinheim* **2002**.

223. Persson, B.; Lang, N. *Phys. Rev. B Condens. Matter* **1982**, *26*, 5409.

224. Jennings, T. L.; Singh, M. P.; Strouse, G. F. *J. Am. Chem. Soc.* **2006**, *128*, 5462-7.

CHAPTER 2

Materials, Experimental Techniques, Instrumentation, and Methods

This chapter outlines the synthetic procedure, experimental techniques, and methodologies employed in the current thesis. It covers various aspects, including chemical sources, preparation of nanomaterials, and sample preparation methods for both spectroscopic and microscopic studies. The working principles of instruments such as a spectrophotometer, spectroflurimeter, time-correlated single photon counting (TCSPC) setup, and time-resolved confocal fluorescence microscope (FCS) setup have been discussed. Additionally, brief explanations of field emission scanning electron microscopy (FESEM), transmission electron microscopy (TEM), Fourier transform infrared spectroscopy (FTIR), dynamic light scattering (DLS), and zeta potential measurements are provided. The chapter also delves into different theories and methodologies employed for data analysis, concluding with the presentation of standard error limits corresponding to various experimental measurements.

2.1. Materials

For this thesis work, a variety of chemicals were procured from various suppliers and utilized for synthesis and studies without undergoing subsequent purification. The details of these chemicals are provided below.

2.1.1. Metal Salts

Copper sulphate pentahydrate ($CuSO_4 \cdot 5H_2O$), copper nitrate (Cu $(NO_3)_2$), Silver nitrate ($AgNO_3$), chloroauric acid trihydrate ($HAuCl_4,3H_2O$) were purchased from HiMedia. Calcium chloride ($CaCl_2$), zinc chloride ($ZnCl_2$), ferric chloride ($FeCl_3$) and ferrous sulphate ($FeSO_4$) were purchased from Sigma-Aldrich.

2.1.2. Protein and Amino Acids

Bovine serum albumin (BSA), α-chymotrypsin from bovine pancreas, L-glutathione (GSH), cysteine (Cys), glutamine (Glu), arginine (Arg), aspartic acid (Asp), phenylalanine (Phe), threonine (Thr), histidine (His), glycine (Gly) and alanine (Ala) were bought from Sigma-Aldrich.

2.1.2. Other Chemicals and Solvents

Sodium hydroxide (NaOH), tannic acid (TA), 4-nitrophenol, P-Nitrotoluene and Trion X100 were purchased from HiMedia. Low-molecular-weight chitosan, ascorbic acid, monochloroacetic acid, N-succinyl-L-phenylalanine-p-nitroanilide (SPNA), sodium dodecyl sulphate (SDS), hydrogen peroxide (H_2O_2), sodium hypochlorite (NaOCl), potassium dioxide (KO_2), N, N-diethyl-p-phenylenediamine (DPD), 2,6-dichloroindophenol sodium salt hydrate (DCPIP), Potassium Ferricyanide $K_3[Fe(CN)_6]$, Ethyl-4-nitro benzoate, 4, 4-Sulfonylbis (nitrobenzene), Rhodamine 6G, Methyl orange Phosphate buffer of pH 7.4 were bought from Sigma-Aldrich. Tertiary butyl hydroperoxide (TBHP) was purchased from Alfa Aesar. Tri-sodium citrate dehydrate ($C_6H_5Na_3O_7$2H2O), cetyl trimethyl ammonium bromide (CTAB) and N, N-dimethylformamide were bought from Spectrochem. Commercial fruit juices (apple, mango, and pomegranate) were purchased from the local market of Janati, Odisha,

2.2. Synthesis Procedure and Characterization of the Systems Investigated

2.2.1. Synthesis of Tannic Acid Capped Copper Nanoclusters (TA-CuNCs)

Tannic acid-stabilized CuNCs (TA-CuNCs) have been synthesized by following a previously reported method.[1] Briefly, a solution of $CuSO_4$ (0.2 mL, 0.1 M) and tannic acid (0.1 mL, 1 mM) was added to 20 mL of water and stirred for 5 min. After that, ascorbic acid (0.2 mL, 1 M) was added to the mixture and the resulting pale blue mixture solution was stirred for eight hr at 50 °C to obtain yellowish CuNCs. The resulting CuNCs was dialyzed using a dialysis membrane (MWCO: 3500 Da; pore size: ca. 0.35 nm) to separate the CuNCs from unreacted species. The synthesized TA-stabilized CuNCs were stored at 4 °C until use.

2.2.2. Synthesis of Chitosan Capped Copper Nanoclusters (Cht-CuNCs)

In the preparation of Chitosan-capped CuNCs, O-carboxymethyl chitosan (0.05 mL, 1 mM)

was employed in lieu of tannic acid, using the same procedure applied for the synthesis of TA-CuNCs. O-carboxymethyl chitosan was synthesized from chitosan of low molecular weight by following a known procedure to make the system water-soluble.[2]

2.2.3. Synthesis of Cysteine Capped Copper Nanoclusters (Cys-CuNCs)

Cysteine capped CuNCs (Cys-CuNCs) have been synthesized by following a reported protocol.[3] In brief, 2.0 mL of 10 mM Cys and 0.1 mL of 100 mM $Cu(NO_3)_2$ were added into 7.5 mL of water under stirring conditions and kept stirring for 5 min. After that, 0.25 mL of 1 M NaOH was added dropwise into the aqueous solution under vigorous stirring, and it was continued for 2.5 h at room temperature.

2.2.4. Synthesis of Fluorescent Silver–Gold Nanoparticles (F-AgAu)

Fluorescent silver–gold nanoparticles were synthesized by following a reported protocol with little modification.[4] Briefly, in a 15 mL vial, 4 mL of Milli-Q water, 2 mL of aqueous GSH solution (5 mM), 200 mL of HAuCl4 (10 mM), and 340 mL of AgNO3 (10 mM) were mixed. A white turbid solution appeared immediately. The solution was then kept under ultraviolet light (350 nm) for 17 h under vigorous stirring conditions. A faint yellow solution was obtained, which was stored at 4 1C for further use.

2.2.5. Synthesis of Gold Nanoparticles (AuNPs)

Gold nanoparticles were synthesized by following a previously reported method.[5] In brief, 20 mL of 1.0 mM HAuCl4 was taken in a 50 mL round bottom flux and kept on a stirring hot plate (105 1C). Then, it was heated up to its boiling point. After that, 5 mL of 1% tri-sodium citrate solution was added to the rapidly stirred boiling solution. Then, the solution was removed from the hot plate when a deep red colour appeared. The synthesized gold nanoparticles were kept at 4 °C for further use.

2.2.6. Synthesis of Ligand-Free Copper Nanoclusters

Ligand-free copper nanoclusters (CuNCs) were synthesized following a previously reported protocol.[6] In a two-necked round-bottom flask, 15 ml of DMF was heated to 140 °C for 20 minutes with vigorous stirring. Following this, 150 μL of a 0.1 M aqueous solution of $Cu(NO_3)_2$ was introduced to the preheated DMF solution, and the mixture was refluxed over an oil bath, maintaining a temperature of approximately 140 °C. The initially colourless solution transformed into a yellow hue and gradually transitioned to brown within a minute, indicative of CuNCs formation. Optimal fluorescence was achieved through continuous refluxing for 9 hours, as shown in the supplementary information (see ESI, figure S1). After cooling to room temperature, the reaction mixture underwent three rounds of centrifugation (12000 rpm, 30 minutes each) to eliminate larger nanoparticles. Subsequently, a clear, light yellow solution of CuNCs was obtained.

2.3. Instrumentation

During the thesis work, various spectroscopic and microscopic techniques were utilized to characterize the synthesized nanomaterials and conduct various photophysical studies. The working principle and utilisation of the majorly used instruments has been discussed in this section.

2.3.1. Instrumental Techniques for Steady-State Measurements

2.3.1.1. Ultraviolet-Visible Spectroscopy

UV-visible absorption spectroscopy is commonly used to analyze the ground electronic state of chromophoric entities. This technique reveals information about electronic energy levels by measuring absorption bands at specific wavelengths and the molar extinction coefficient.

It facilitates the identification of chromophoric groups and their surrounding environments. The absorption profile is influenced by factors such as solvent polarity, polarizability, and

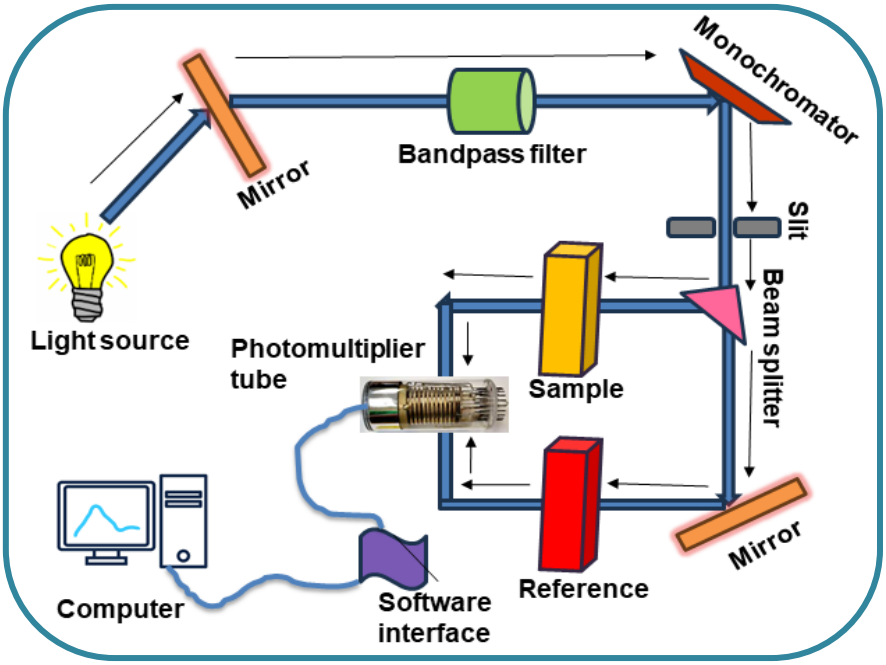

Scheme 2.1. Schematic representation of a UV-Vis spectrophotometer.

hydrogen bonding interactions in the ground state, providing insights into interactions within the microenvironment.[7]

UV-Visible absorption spectroscopy operates on the principle of Lambert-Beer's law, stating that the absorbance (A) of an absorbing species at a specific wavelength (λ) in a solution is directly proportional to the molar concentration (C) of that species in the solution and its molar extinction coefficient (ε) at that particular wavelength. This relationship is mathematically expressed by the following equation:

$$A = log\left(I_0/I\right) = \varepsilon Cl \qquad (2.1)$$

where Io is the intensity of the incident light and I is the intensity of the transmitted light after absorption by the sample solution and l is the path length (1 cm) of the sample solution.

In the present thesis work, UV-Vis spectroscopy experiments were conducted using a Cary 100 Bio UV-VIS spectrophotometer with a wavelength resolution of 0.15 nm. This instrument measures absorbance in both the UV and Visible regions, employing a D2O lamp for UV excitation and a xenon lamp for excitation in the visible region. A layout of a typical

UV-Vis Spectrophotometer has been provided in the scheme 2.1.

2.3.1.2. Steady-State Fluorescence Spectroscopy

Fluorescence spectroscopy is a highly sensitive optical technique employed to investigate various photophysical and photochemical processes in the excited state of a fluorophore molecule. Even a subtle alteration in the energetics or interactions among fluorophore molecules in their excited state can lead to changes in the shape, intensity, and emission maximum of the corresponding species' emission spectra.[7-9] As a result, this method provides a means to gain a deeper understanding of the microenvironment surrounding the emitting species. In this thesis, fluorescence spectroscopy has been extensively employed to probe the

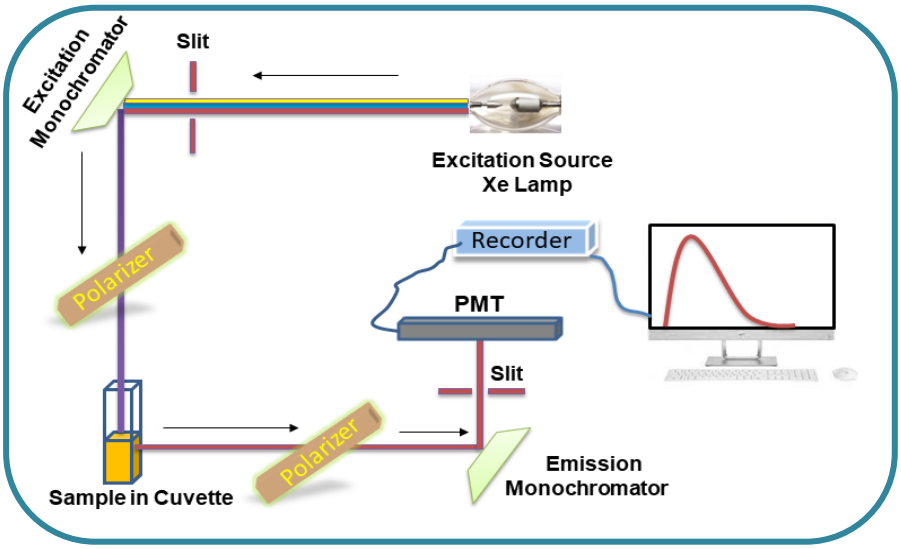

Figure 2.2. Schematic representation of a typical fluorimeter.

photophysical properties of all the systems. Additionally, the interparticle interaction between MNCs and various crucial analytes has been thoroughly examined using fluorescence spectroscopy.

2.3.2. Instrumental Techniques for Time-Resolved Studies

2.3.2.1. Fluorescence Lifetime Measurements

Time-resolved fluorescence spectroscopy measurements are valuable for elucidating the dynamics and kinetics of various photophysical and photochemical processes. This method is preferable over steady-state fluorescence as it focuses more on the dynamic aspects of systems rather than their equilibrium state. In this technique, a very short laser pulse excites the fluorophore to the excited state, establishing an initial population (n_o) in the excited state. Subsequently, the excited state population decays over time through both radiative and non-radiative pathways. The rate of population decay of the excited state is described by following equation[7, 10-12]

$$-\frac{dn\,(t)}{dt} = (k_r + k_{nr})n\,(t) \qquad (2.2)$$

where n(t) is the number of excited molecules at time t following the excitation of fluorophore molecules with a very short pulse light. The k_r and k_{nr} denotes the radiative and nonradiative rate constant respectively.[7] As emission is regarded as a random event, the probability of fluorophore emission remains consistent over a given period of time. The decay of the excited state population follows an exponential pattern using the following using

$$n\,(t) = n_0\, exp^{-t/\tau} \qquad (2.3)$$

where τ is the lifetime of the excited fluorophore. The number of excited state molecules present in the solution at time t is directly proportional to the fluorescence intensity of the

sample at that time. Hence, by replacing n(t) with time-dependent fluorescence intensity I(t), the above equation 2.3 can be rewritten as equation 2.4, which is shown below:

$$I\ (t) = \ I_0\ exp^{\ -t/\tau_f} \qquad (2.4)$$

where I_0 is the intensity at zero time and τ_f is the fluorescence lifetime of the fluorophore. The relationship between τ_f and the radiative (k_r) and non-radiative (k_{nr}) decay rate constants is expressed by equation 2.5

$$\tau_f = \frac{1}{(k_r + k_{nr})} \qquad (2.5)$$

The fluorescence lifetime of a fluorophore molecule is determined using the Time-Correlated Single Photon Counting (TCSPC) technique. It's important to note in this context that the time spent by different molecules in a given sample in the excited state varies. Consequently, some molecules may take longer to emit, while others may emit on a very short timescale in their excited state. Therefore, the lifetime obtained using the TCSPC setup represents the statistical average of the times the fluorophore molecules spend in their excited state.

In this thesis, time-resolved fluorescence measurements were conducted using Edinburgh OB-920 and Edinburgh Life Spec II TCSPC spectrometers. Picosecond diode lasers, emitting laser pulses at 280 nm and 375 nm have been used as per the experimental requirement. A Micro channel Plate (MCP) photomultiplier (Hamamatsu R3809U-50) with a response time of 40 ps was employed as the detector. A dilute ludox solution in water, acting as a scatterer, is employed instead of the actual sample to assess the lamp profile. The decay curves are subjected to analysis through a nonlinear least squares (NLLS) iteration procedure using F900 decay analysis software. The fittings were judged by considering the value of chi-square (χ^2) and the visual observation of residuals.

2.3.2.2. Working Principle of TCSPC Instrument

The Time-Correlated Single Photon Counting (TCSPC) technique operates on the fundamental principle of detecting a single photon following the pulsed excitation of a fluorophore.[8, 13-14] TCSPC typically measures the time gap between the short excitation pulse and the first detected photon, representing the time-dependent probability distribution of a single photon emission from an excited fluorophore. The fluctuations in fluorescence intensity over time, upon fluorophore excitation, correspond to the time-dependent probability distribution of molecules in excited states. TCSPC, being a statistical approach, necessitates a high repetition rate of the excitation source to detect a significant number of photons quickly, ensuring accuracy in statistical data. The resulting data is stored in the form of a histogram, essentially representing the fluorescence decay profile of the fluorophore.

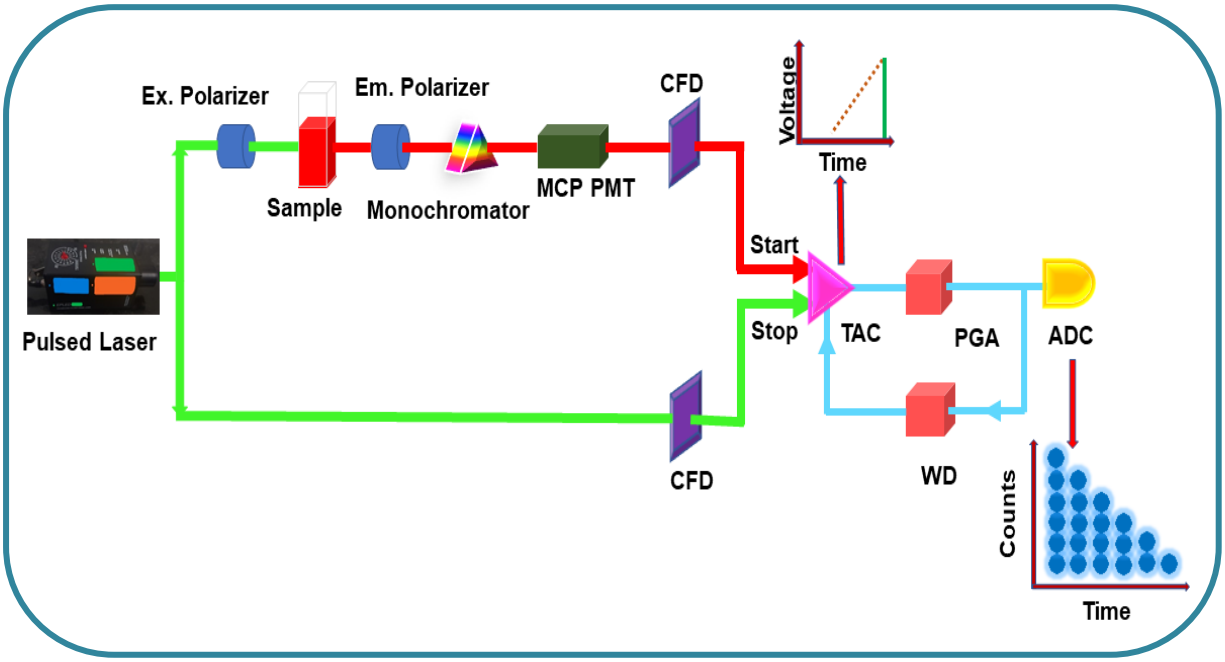

Scheme 2.3. A schematic diagram for the working principle of TCSPC setup.

The TCSPC setup functions akin to a stopwatch, operating in either the "forward mode," started by a photon from the excitation source, or the "reverse mode," started by the emission

of the sample. A schematic representation illustrating the working principle of the TCSPC setup in reverse mode is depicted in Scheme 2.3. In the reverse mode, the excitation pulse is divided into two parts: one part is directed towards sample excitation, while the other part is directed towards the electronics. The optical signal, generated by the emitted photon, traverses through a Photomultiplier Tube (PMT), producing an electrical signal that corresponds to the START pulse. The START pulse travels through the Constant Fraction Discriminator (CFD), accurately measuring the actual arrival time of the pulse. Subsequently, the signal enters the Time to Amplitude Converter (TAC), creating a voltage ramp that rises linearly over time. Simultaneously, the second channel, composed of excited photons, travels through a variable delay line and the CFD before reaching the same TAC unit. These signals represent the STOP pulses and are utilized as the STOP input for the TAC unit. The TAC unit halts the voltage ramp upon detecting the first STOP pulse, resulting in a voltage proportional to the time interval (Δt) between the emission (START) and excitation (STOP) pulses. The TAC output signals pass through a Pulsed Gain Amplifier (PGA) to an Analog-to-Digital Converter (ADC). The ADC produces a numerical value proportionate to the height of the TAC output pulse signal, and the data is stored in the multichannel analyzer (MCA). This cyclic procedure is repeated, generating a collection of histograms in the MCA channels. In today's use, most Time-Correlated Single Photon Counting (TCSPC) measurements prefer the "reverse mode" due to advanced high repetition rate pulsed-light sources. Before each measurement, the Time to Amplitude Converter (TAC) needs a quick reset and set to zero. If start signals come in too fast, TAC stays in reset mode to prevent data loss. TCSPC settings are adjusted so that less than one photon is detected per hundred laser pulses. So, the emission pulses kickstart the voltage ramp in TAC, and the following laser pulse stops the TAC. The current electronics in TCSPC setups can only detect the first arriving photon. The

analysis procedure for estimating fluorescence lifetime from measured decay curves is also discussed in a later section of this chapter.

2.3.3. Experimental Technique for Single-Particles Studies

2.3.3.1. Time-Resolved Confocal Fluorescence Microscopy

Optical microscopes play a crucial role in magnifying small objects, but achieving clear observation of micro-objects depends significantly on the microscope's overall resolution. The resolution is influenced by the excitation wavelength and the numerical aperture of the objective lens. Adjusting the microscope's resolution is possible by changing the excitation source and configuration. Confocal Fluorescence Microscopy (CFM) stands out with its higher temporal resolution, reaching up to a few nanoseconds. It utilizes multiple pinholes in the detection path, allowing only focused light and enabling measurements within a confocal region. Scheme 2.4 depicts a schematic diagram of the time-resolved confocal microscope In this thesis, all measurements have been conducted using the PicoQuant MicroTime 200. In this setup, a pulsed picosecond diode laser, operating at an excitation wavelength of 403 nm and featuring a tuneable repetition rate (ranging from 1 to 80 MHz), has been utilized as the excitation source. The laser output is connected to the primary optical unit through a polarization-maintaining single-mode optical fiber. This fiber is guided through a dichroic mirror, directing the collimated laser beam into the entrance port of an inverted microscope (Olympus IX71). The inverted microscope setup incorporates a water immersion objective, UPlansApo NA 1.2, 60X. The sample is positioned on a coverslip using a sample holder, and its location is precisely controlled by a piezo scanning stage mounted within the microscope body. For manual adjustments, micro-meter screws are employed in conjunction with the software-controlled piezo-scanner, facilitating precise and repeatable XY scanning as well as

Z-position adjustments. Monitoring the focal point's position on the sample is achieved with a

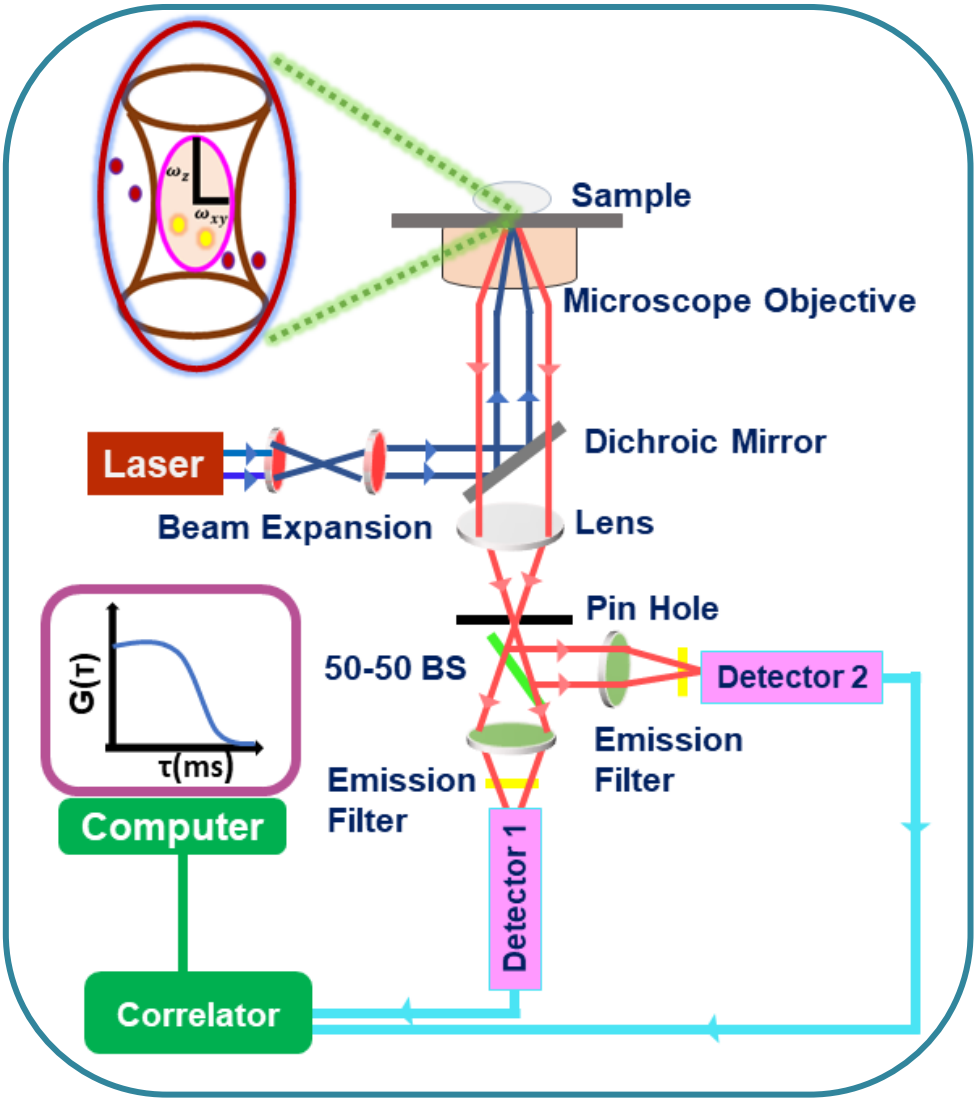

Scheme 2.4. Time-resolved confocal fluorescence microscope setup.

charged coupled device (CCD) detector. The fluorescence emitted by the sample, gathered by the same objective, passes through a dichroic mirror. The fluorescence signal is then directed to focus into a 50 μm diameter pinhole, effectively eliminating out-of-focus signals. Subsequently, it is re-collimated and directed towards single-photon avalanche photodiodes (SPADs). Depending on the experimental design, various types of single or multiple SPAD detectors can be employed. Data analysis is carried out using SymPhoTime software-controlled PicoHarp 300 Time-Correlated Single Photon Counting (TCSPC) module in a time-tagged time-resolved (TTTR) mode. The time-resolved confocal fluorescence

measurements involve techniques such as fluorescence correlation spectroscopy (FCS) and fluorescence lifetime imaging (FLIM), which will be discussed in the next section.

2.3.3.2. Fluorescence Correlation Spectroscopy (FCS)

Fluorescence Correlation Spectroscopy (FCS) is a non-invasive technique based on fluorescence intensity fluctuations, providing insights into dynamic processes responsible for the observed fluctuations. This technique is applicable in a confocal fluorescence microscope setup. In solution-based measurements, fluorophores freely diffuse through the confocal volume, generating signals attributed to fluctuations in fluorescence intensity. These fluctuations can arise from processes such as binding interactions, translational or rotational diffusion, or other excited state phenomena. To effectively monitor sharp fluctuations, it is crucial to have a small number of fluorophore species. Consequently, a nanomolar concentration range is used to achieve single-molecule sensitivity, depending on the size of the confocal volume. The obtained signals are then correlated to derive correlation curves. FCS, being a diffusion-based technique rooted in random events, follows Poisson statistics in determining the presence of fluorescent species within the confocal volume.

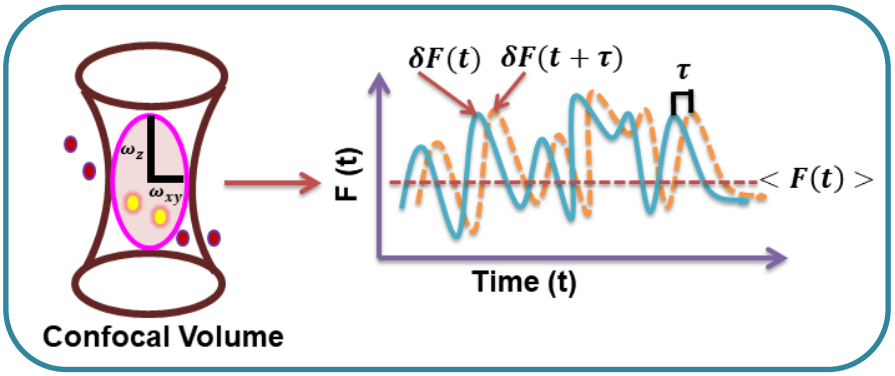

Scheme 2.5 Schematic representation of diffusion of a fluorophore through the ellipsoidal confocal volume.

Cross-correlation of the autocorrelation curves detected from both detectors serves to improve temporal resolution and enhance the signal-to-noise ratio in the fluorescence correlation spectroscopy (FCS) analysis.

The autocorrelation function $G(\tau)$ is defined as the product of fluorescence fluctuation intensities $\delta F(t)$ and) $\delta F(t+\tau)$ at times t and $t+\tau$, respectively. This product is then averaged over a large number of measurements, as shown in Equation 2.6.

$$G(\tau) = \frac{<\delta F(t)\delta F(t+\tau)>}{<F(t)>^2} \quad (2.6)$$

Here, δF(t) and δF(t+τ) are defined in equation 2.7 and 2.8

$$\delta F(t) = F(t) - < F(t) >, \quad (2.7)$$

$$\delta F(t+\tau) = F(t+\tau) - < F(t+\tau) > \quad (2.8)$$

Autocorrelation function for pure diffusion in three dimensions can be written as in equation 2.9

$$G(\tau) = \frac{1}{N}\left(1+\frac{\tau}{\tau_D}\right)^{-1}\left(1+\frac{\tau}{\kappa^2\tau_D}\right)^{-\frac{1}{2}} \quad (2.9)$$

In the given equations, N represents the average number of fluorophores in the confocal volume, τ_D is the diffusion time, κ is the structure parameter of the confocal volume, equal to $\omega z \omega xy2$. The diffusion coefficient (D) of the fluorophore can be derived from Equation 2.18:

$$D = \frac{\omega_{xy}^2}{4\tau_D} \quad (2.10)$$

The hydrodynamic radius (R_h) of the fluorophore species is related to the diffusion coefficient (D) as provided in Equation 2.19:

$$R_H = \frac{kT}{6\pi\eta D} \quad (2.11)$$

2.3.3.3. Fluorescence Lifetime Imaging (FLIM)

In the TTTR mode of the time-resolved confocal setup, fluorescence lifetime imaging can be conducted using the same arrangement. By manipulating the sample stage via a piezo scanner, 2D images of the fluorophore can be acquired. The spatial distribution of photons is recorded alongside the Time-Correlated Single Photon Counting (TCSPC) data. The obtained lifetime from the detected photons at each pixel can be employed to construct a fluorescence lifetime image. This image provides insights into the spatial variation of the lifetime of different fluorophores in a system. It establishes a direct correlation between structure/morphology, fluorescence intensity, and the lifetime of the fluorophore, offering valuable information, especially in the context of nanomaterial systems.

2.3.4. Transmission Electron Microscopy (TEM)

The microscopic examination of nanomaterials involves the application of transmission electron microscopy (TEM). In this thesis work, JEOL microscope (JEM-2100 model) has been utilized, functioning with an acceleration power of 200 kV. To capture a transmission electron microscopy (TEM) micrograph of nanomaterials, the following steps for sample preparation are undertaken: The sample is appropriately diluted as needed, followed by sonication for a specified duration. Subsequently, the solution is drop-casted onto a 300-mesh size copper/gold grid. The grid is then placed under a bulb for 10–15 minutes and subjected to vacuum conditions for 4–5 hours. This preparation process ensures the creation of a suitable specimen for TEM analysis.

2.3.5. Cyclic Voltammetry (CV) Measurements

Cyclic voltammetry (CV) was employed to determine the oxidation and reduction potential of the systems. All the measurements during the current thesis work were conducted in a three-

electrode electrochemical cell controlled by Corr test, Electrochemical workstation. Glassy carbon (GC), bare platinum wire and aqueous Ag/AgCl acted as working electrode, counter electrode and reference electrode, respectively. The GC electrode was well polished with alumina slurry (1, 0.3, and 0.05 mL of alumina in deionized water) prior to each measurement and washed in a bath sonicator. Na_2SO_4 was used as a supporting electrolyte.

2.3.6. Isothermal Titration Calorimetry (ITC)

The Isothermal Titration Calorimetry (ITC) technique is employed for determining the thermodynamic parameters associated with interactions in solutions, particularly focusing on the binding events between small molecules or ligands and macromolecules. The fundamental principle of this method revolves around measuring the heat changes occurring between two cells contained within an adiabatic jacket. The nature of the interaction dictates whether heat is released or absorbed, providing valuable insights into the thermodynamics of the binding process. In the course of this thesis, the Malvern MicroCal iTC200 calorimeter was employed to investigate the binding interactions between MNCs and protein molecules (BSA, α-ChT). For investigating the interaction between BSA and CuNCs, a total of 20 aliquots of CuNCs (each aliquot contains 2 μL) were injected from a rotating syringe (500 rpm) to the ITC cell containing BSA (5 μm).[15] The corresponding titration data were fitted using the "sequential binding model" for the case of TA-CuNCs and Chitosan-CuNCs and the "one set of sites" binding model for the case of Cys-CuNCs system with the help of ORIGIN software (MicroCal ITC200, Northampton). Further, to investigate the interaction of α-ChT with CuNCs, a total of 20 aliquots of CuNCs (each aliquot contains 2 μL) were injected from a rotating syringe (600 rpm) into the ITC cell containing α-ChT (2 μm).[16] The data obtained from the interaction of α-ChT with TA-CuNCs were fitted by the "sequential binding model" whereas that of Cys-CuNCs was fitted with a "one set of sites" binding model with the help of ORIGIN software (MicroCal ITC200, Northampton). The heat of

ligand dilution into the buffer was subtracted from the reaction heat data before analyzing the data.

2.3.7. Circular Dichroism Spectroscopy

Circular Dichroism (CD), a type of absorption spectroscopy, employs circularly polarized light to explore the structural characteristics of optically active chiral media. Its primary application lies in the examination of biological molecules, allowing for a detailed analysis of their structure and interactions with metals and other molecules. This technique is particularly valuable in uncovering information about the secondary and tertiary structures of biomolecules, providing insights into conformational changes and molecular interactions.[17-19] In the current thesis, CD experiments of protein molecules in the absence and presence of analytes were performed with a JASCO J-1000 spectrometer at 298 K. A quartz cuvette of 2 mm optical path length was used for recording the spectrum in a nitrogen atmosphere. A Baseline was performed with an appropriate buffer solution and subtracted from sample spectra, and each spectrum was the average of three scans.

2.3.8. Dynamic Light Scattering

Dynamic Light Scattering (DLS) is a technique used to analyze the size distribution and zeta potential of nanomaterials. This method provides valuable insights into the behaviour of these materials in colloidal systems, aiding in the optimization of applications like drug delivery, nanomedicine, and material synthesis. DLS is crucial for characterizing the dynamic features of nanoparticles and understanding their interactions with analytes, enabling informed design and development of nanomaterial-based technologies. In the current thesis work, Malvern Zetasizer instrument has been used for determining the zeta potential of nanomaterials in the absence and presence of analytes of interest.

2.4. Methods

2.4.1. Analysis of the Fluorescence Decay Curves

2.4.1.1. Data Analysis

In Time-Correlated Single Photon Counting (TCSPC), observing the true intensity decay becomes challenging as the fluorescence decay curve obtained from time-resolved measurements is a convolution or mixture of the laser pulse and the actual fluorescence from the sample. This complication arises because the estimated fluorescence decay time of any fluorophore tends to be higher than the pulse-width of the excitation source. Consequently, experimental data can be influenced by the response time of the photomultiplier tube (PMT), finite decay time of the source pulse, and related electronics.[8] The overall Instrument Response Function (IRF) is thus dependent on the decay time of the laser pulse and the response time of the detector, along with other associated electronics. To extract the actual fluorescence lifetime of a sample, deconvolution of the IRF from the fluorescence decay curves is necessary. Consequently, the fluorescence decay profiles were analyzed using the iterative reconvolution least squares method, expressed mathematically as the following equation.[8, 20-21]

$$Im\,(t) = \int_0^t I_R\,(t - t')\,R\,(t')\,dt' \qquad (2.12)$$

where $I_m(t)$ = fluorescence intensity at time t, $I_R(t-t')$ = response function of the experimental system, R(t') = intensity of the exciting pulse at time t'. The IRF was determined by utilizing a dilute ludox solution, and the deconvolution algorithm was applied through the iterative reconvolution method.

The analysis of fluorescence decay curves involves the application of a Nonlinear Least Squares (NLLS) data processing technique, where the curves are fitted with an assumed

functional form. The least squares approach is effective under specific criteria, such as having a sufficient number of independent data points, experimental data points exhibiting a Gaussian distribution of uncertainty, and the absence of systematic errors. Both Im(t) and R(t') are experimentally obtained from the Time-Correlated Single Photon Counting (TCSPC) setup. In the analysis process, a decay function specific to the sample, denoted as (t), is initially assumed. This function is then deconvoluted with the observed R(t') following Equation 2.6, resulting in a calculated curve Y(t). The Y (t) curve is subsequently compared with the experimentally observed decay curve I_m (t). The variables in the function G(t) are iteratively adjusted until a satisfactory fit between Y(t) and Im(t) is achieved. The function G(t) is typically assumed to be a sum of exponentials, as shown in equation 2.13.

$$G\ (t) = \sum_i B_i\ \exp\left(\frac{-t}{\tau_i}\right) \qquad (2.13)$$

where Bi is the pre-exponential factor for the i^{th} component and τ_i is the fluorescence lifetime of the corresponding i^{th} component. The average lifetime ($< \tau >$) of the fluorophore is estimated using equation 2.14

$$< \tau > = \sum_i b_i\ \tau_i \qquad (2.14)$$

where bi are the normalized amplitude weighted components and τi is its corresponding lifetime component. Achieving a good fit to the observed decay curves relies on two key factors: reduced chi-square values and the distribution of weighted residuals.

2.4.1.2. Reduced Chi-Square (χ^2) Values

The reduced $\chi 2$ is defined as equation 2.15

$$\chi 2 = \frac{\sum_i W_i\,(Y_i - I_i)^2}{n - P} \qquad (2.15)$$

where Yi is the count of i^{th} channel of the calculated curve, I_i is count at the i^{th} channel of the curve measured experimentally. Wi [Wi=I/Ii] is the weighting factor of the counts in the i^{th} channel, n is the number of channels used for the decay to be analyzed and p is the number of degrees of freedom in the decay function considered for the analysis which is equal to the number of variables in the function G(t). To achieve a good fit, χ^2 values should be close to unity. In general, values of χ^2 ranging between 1.0 and 1.2 are considered indicative of a good fit to the data points.

2.4.1.3. Distribution of Weighted Residuals

The weighted residual represents the difference between the measured decay function and the fitted function. It is a crucial parameter for analyzing Time-Correlated Single Photon Counting (TCSPC) data and is defined by the following equation (2.16):

$$r_i = \sqrt{W_i}\,(Y_i - I_i) \qquad (2.16)$$

A good fit is typically indicated by a random distribution of the weighted residuals around the zero line across the entire data range.

2.5. Calculation of Quantum Yield

The fluorescence quantum yields of the systems were estimated using a standard reference Rhodamine 6G (R6G) dissolved in water, by using the following equation

$$QY_S = \frac{I_S}{I_R} \times \frac{\eta_S^2}{\eta_R^2} \times QY_R \qquad (2.17)$$

where QY_S and QY_R are the quantum yields of the sample and reference (for R6G in water, QYr = 95%), respectively. I_S and I_R are the integrated fluorescence emission of the sample and the reference, respectively, determined by integrating the emission spectra over the whole spectral range. η_S and η_R are the refractive index of water (1.33).

2.6. Calculation of the Number of Cu Atoms in the CuNCs

We employed the Jellium model, a well-accepted theoretical approach based on the Drude theory and the concept of free electrons, to decipher the probable composition of the cluster core. This model governs the fluorescence properties of the MNCs in relation to their composition. In accordance with this model, the correlation between Fermi energy (E_{Fermi}), emission energy (E_{em}), corresponding to the maximum of the emission wavelength), and the number of metal atoms constituting the cluster core (N) is expressed as follows:

$$E_{em} = E_{Fermi}/n^{0.33} \quad (2.18)$$

where E_{Fermi} is the fermi energy of the metal atom. The number of Cu atoms in the metal core (Cu_n) of the nanoclusters has been estimated with the help of the Jellium model by utilizing emission energy, which is mathematically defined by equation (2.18)

In our thesis works, E_{Fermi} of Cu is 7ev, and the emission maximum of TA-CuNCs, Chit-CuNCs and Cys-CuNCs are 430 nm (2.88ev), 432 nm (2.87ev) and 490 nm (2.53ev) and number of atoms(n) in the metal core were ~15, ~15 and ~21 respectively.

2.7. Calculation of Limit of Detection (LOD)

We have determined the LOD for highly reactive oxidative species (hROS) sensing investigations using the widely employed 3σ rule[22], as expressed by the following equation.

$$LOD = \frac{3 \times \sigma}{Slope} \quad (2.19)$$

where σ is the standard deviation (SD) and slope is the ratio of relative fluorescence intensity versus quencher concentration. The SD is expressed by the following relation.[23]

$$(SD) = SE \times \sqrt{n} \quad (2.20)$$

Where n is the number of data points.

2.8. Calculation of Spectral Overlap Integral

The calculation of the overlap integral involves several steps. Initially, the molar absorption coefficient (ε (λ)) is determined by dividing the absorbance by the concentration of the acceptor and the path length. Subsequently, the emission spectrum of the donor is normalized to obtain the value of (λ) for each wavelength. The wavelengths are then arranged in ascending order, and values for λ^4 are computed. Following this, all three columns are multiplied to create a new column. The area of this spectrum corresponding to the new column is denoted as A_1. Simultaneously, the area of the normalized emission spectrum of the donor is calculated as A_2. Finally, the overlap integral is computed by dividing the area A_1 by A_2, as expressed in equation 1.1 (from Chapter 1).

2.9. Standard Error Limits

Standard error limits involved in the experimental results are

Experimental Parameters	**Error**
λmax (abs./flu.)	±1-2 nm
τ_f (> 1ns)	±5%
QY	±2
The energy transfer rate	±5%
Diffusion coefficient (through FCS)	±5-10%

References

1. Cao, H.; Chen, Z.; Zheng, H.; Huang, Y. *Biosens. Bioelectron.* **2014**, *62*, 189-195.
2. Cheng, L.-C.; Huang, J.-H.; Chen, H. M.; Lai, T.-C.; Yang, K.-Y.; Liu, R.-S.; Hsiao, M.; Chen, C.-H.; Her, L.-J.; Tsai, D. P. *J. Mater. Chem.* **2012**, *22*, 2244-2253.
3. Zhou, T.; Xu, W.; Yao, Q.; Zhao, T.; Chen, X. *Methods Appl. Fluoresc.* **2015**, *3*, 044002.
4. Ganguly, M.; Pal, A.; Negishi, Y.; Pal, T. *Langmuir* **2013**, *29*, 2033-43.
5. Ankita U. Patela, G. K. J., Ketan Ranchc, Kapil Patila, Abhay Dharamsi. *Int. J. Pharm. Biol., 8*, 5.
6. Sahu, D. K.; Sahu, K. *J. Photochem. Photobiol.* **2017**, *347*, 17-25.
7. Rohatgi-Mukherjee, K. *New Age International,* **1978**.
8. Lakowicz, J. R., Principles of Fluorescence Spectroscopy. *Springer,* **2006**.
9. Berberan-Santos, B. V. a. M. N., Molecular Fluorescence: Principles and Applications,. *John Wiley & Sons,* **2012**.
10. Lakowicz, J. R., Principles of Fluorescence Spectroscopy. **2006**.
11. Valeur, B., Molecular Fluorescence: Principles and Applications;. *Wiley-VCH:* **2002**.
12. W. Becker, Advanced Time-Correlated Single Photon Counting Techniques. *Springer Science & Business Media,* **2005**.
13. Nan, Y.; Shao, J.; Li, D.; Guo, X.; Willatzen, M.; Wang, Z. *Nano Res.* **2023**, *16*, 11545-11555.
14. Becker, W., Advanced Time-Correlated Single Photon Counting Techniques. *Springer Science & Business Media* **2005**.
15. Akhuli, A.; Chakraborty, D.; Agrawal, A. K.; Sarkar, M. *Langmuir* **2021**, *37*, 1823-1837.
16. Akhuli, A.; Chakraborty, D.; Preeyanka, N.; Dora, A. S.; Sarkar, M. *ACS Appl. Nano Mate* **2023**, *6*, 4910-4924.
17. De, M.; Chou, S. S.; Dravid, V. P. *J. Am. Chem. Soc.* **2011**, *133*, 17524-17527.
18. Xu, M.; Yuan, S.; Chen, X.-Y.; Chang, Y.-J.; Day, G.; Gu, Z.-Y.; Zhou, H.-C. *J. Am. Chem. Soc.* **2017**, *139*, 8312-8319.
19. Chen, W.-Q.; Yin, M.-M.; Song, P.-J.; He, X.-H.; Liu, Y.; Jiang, F.-L. *Langmuir* **2020**, *36*, 6447-6457.
20. McKinnon, A.; Szabo, A.; Miller, D. *J. Phys. Chem.* **1977**, *81*, 1564-1570.
21. O'Connor, D. V.; Ware, W. R.; Andre, J. C. *J. Phys. Chem.* **1979**, *83*, 1333-1343.
22. Das, N. K.; Ghosh, S.; Priya, A.; Datta, S.; Mukherjee, S. *J. Phys. Chem. C* **2015**, *119*, 24657-24664.
23. Rana, M.; Chowdhury, P. *J. Lumin.* **2019**, *206*, 105-112.

CHAPTER 3

Probing the Interaction of Bovine Serum Albumin with Copper Nanoclusters: Realization of Binding Pathway Different from Protein-Corona

With an aim to understand the interaction mechanism of bovine serum albumin (BSA) with copper nanoclusters (CuNCs), three different types CuNCs having chemically different surface ligands, namely, tannic acid (TA), chitosan, and cysteine (Cys), have been fabricated, and investigations are carried out in the absence and presence of protein (BSA) at ensemble-averaged and single-molecule levels. The CuNCs, capped with different surface ligands, are consciously chosen so that the role of surface ligands in the overall protein− NCs interactions is clearly understood, but, more importantly, to find whether these CuNCs can interact with protein in a new pathway without forming the "protein corona", which otherwise has been observed in relatively larger nanoparticles when they are exposed to biological fluids. Analysis of the data obtained from fluorescence, ζ-potential, and ITC measurements has clearly indicated that the BSA protein in the presence of CuNCs does not attain the binding stoichiometry (BSA/CuNCs > 1) that is required for the formation of "protein corona". This conclusion is further substantiated by the outcome of the fluorescence correlation spectroscopy (FCS) study. Further analysis of data and thermodynamic calculations have revealed that the surface ligands of the CuNCs play an important role in the protein−NCs binding events, and they can alter the mode and thermodynamics of the process. Specifically, the data have demonstrated that the binding of BSA with TACuNCs and Chitosan-CuNCs follows two types of binding modes; however, the same with Cys-CuNCs goes through only one type of binding mode. Circular dichroism (CD) measurements have indicated that the basic structure of BSA remains almost unaltered in the presence of CuNCs. The outcome of the present study is expected to encourage and enable better application of NCs in biological applications.

3.1. Introduction

In recent times, fluorescent nanomaterials by virtue of their size, useful optical properties and low toxicity behavior have been considered as promising candidates for bioanalysis, sensing, labelling and bio-imaging applications.[1-7] This has driven the scientific community to investigate how these nanomaterials interact with biomolecules and thus the study of interaction of nanomaterials with biomolecules has evolved as an emerging field of research in physics,

chemistry and biology in recent times. In this context, the fluorescent metal nanoclusters (NCs) are thought to be more attractive candidates for biological studies than quantum dot (QDs) nanoparticles primarily due to the good water solubility and relatively less toxic nature of the former.[8,9] As compared to nanoparticles (NPs; size > 3nm) the NCs are usually smaller sized (2-3 nm) particles having molecule-like optical properties. It has been shown that the nanoparticles (NPs) (> 3nm) upon immediate exposure to biomolecules form "protein corona".[10-16] As a result, subsequently, biomolecules interact with protein coated nanomaterials instead of bare NPs. Therefore, this "protein-corona" acts as an extremely significant entity in governing the NP-biomolecule interaction in general. More importantly, this observation also shows that the surface ligand chemistry of the nanoparticles would be a crucial factor in influencing the formation of "protein-corona" and subsequent protein-ligand interaction. Even though several studies have been reported on protein-NP interactions, little is known about how the NCs interact with biomolecules both at ensemble-averaged and at single molecule level. Additionally, it has also been shown that in case of NCs the protein-NCs interaction need not be mediated through corona formation.[17-20] Very recently Jiang and coworkers[17] have shown a new interaction model beyond the "protein-corona" while they investigated the interaction of gold nanoclusters with different proteins. They have shown the possibility of the formation of a "protein-complex" by adsorption of one or more NCs on a single protein owing to their ultra-small sizes and by virtue of weak non-covalent interactions. In another work, Dawson and coworkers[19] have reported that ultra-small NPs have distinct properties than the larger size particles in their biological interaction which is governed by both particle size and particle surface and it is also noted that larger NPs form more conventional protein corona while smaller NPs do not. It may be noted here that among the NCs mostly gold and silver nanoclusters have been mostly exploited but

such studies on copper NCs are rather limited. In particular, the knowledge about the role of surface functionalities on the copper NCs in influencing the protein-CuNCs interaction is rare. Therefore, it is essential to obtain a comprehensive understanding on the protein-CuNCs interaction and its implications on biological studies.

In this perspective, it is relevant to mention that there are several studies reported on the interaction between proteins and nanomaterials such as quantum dots,[21-27] metal nanoparticles,[16,28-31] metal nanoclusters,[32-36,] graphene quantum dots[37] and carbon-based nanoparticles.[38,39] In these works it has been demonstrated that protein-NP interaction mainly mediated either through the formation of protein-NPs complex or "protein corona".[26,31,32,35,36,38]The observation of the above studies are interpreted by analyzing binding constants, number of binding sites, protein conformational change, hydrodynamic size alteration etc.[29,32,34] Interestingly, some studies have also shown that the size of nanoparticle and surface ligands can have a profound influence on the protein-NPs interaction event. In this context, Nyokong and coworkers[27] while working on the interaction between different CdTe QDs, capped with various thiol ligands with protein have found that the binding affinity of those QDs with protein can vary significantly with a change in the nature of thiol ligands, signifying the important role of surface chemistry in these interactions. In another work, Monteiro-Riviere and coworkers[31] have investigated the kinetics of adsorption and formation of "protein-corona" with citrate and lipoic acid coated both Au and Ag nanoparticles where they have observed that surface ligand influences the size of "protein- corona" formed during the same time interval. We note that most of the studies are focused on the interaction of larger-sized nanoparticles with protein but the interaction of smaller size NCs with protein is relatively unexplored. In a very recent work, Dawson and coworkers[35] have reported that the surface chemistry of ultra-small

AuNPs plays a crucial role in cellular uptake mechanism and in determining the transient interaction with protein molecules and they have also observed the opposite trend for ultra-small AuNPs in cellular uptake to that of larger NPs. In another recent work Jiang and coworkers[36] while investigating the interaction of AuNCs with chymotrypsin (Cht) have observed that surface ligands around the nanomaterials play an important role in regulating the activity of Cht and it is also observed that the AuNCs-protein interaction is mediated through protein complex formation with a stoichiometry of ∼1:1 (AuNCs/ChT) rather than protein-corona" formation and two-step interaction model is proposed for the interaction between dihydrolipoic acid (DHLA)-coated AuNCs (DHLA-AuNCs) and Cht. Recently, Liu and coworkers[32] have investigated the mechanism and thermodynamics of interaction between AuNCs and different plasmatic proteins and compared the results to that of NPs having relatively larger sized. During the study they have found that the binding constant values gradually increased on increasing the size of the particle. Nienhaus and co-workers[33,] and Mukherjee and coworkers[34], in separate works, have noted an increase in the fluorescence intensity of dihydrolipoic acid functionalized AgNCs and Glutathione (GSH) capped CuNCs respectively, due to adsorption of HSA protein on the surface of NCs. The above discussion shows that even though the several studies are done on the protein-NPs interaction, such studies on protein-NCs are rather limited, and in particular knowledge about CuNCs-biological system is even lesser. Since it has also been shown in a few recent works that in case of NCs, protein-NCs interaction may not necessarily proceed through "protein-corona" formation,[17,18] and hence, understanding the protein-NCs (Cu) interaction on this aspect is expected to be crucial. We would like to note here that it has been shown that some specific ligands such as polymers, surfactants, etc. can alter protein-ligand binding mode in particular and mechanism of binding events in general. [40-45] Therefore, it will be interesting to

look at the outcomes of the protein-NCs binding event if the interaction of protein is done with NCs modified with such type of ligands.

Keeping in mind the above facts, in the present work, the interaction of BSA with highly fluorescent water-soluble CuNCs capped with three different ligands, namely tannic acid, chitosan and cysteine has been investigated by exploring various spectroscopic techniques. Basically, the aim of this work is focused on how various CuNCs modified with chemically different surface ligands can influence the protein-NCs binding modes during the interaction event. Copper has been chosen as a material of interest because of its biological importance and its favorable properties like high water solubility, good biocompatibility, low cost, and ready availability.[46-47] Various CuNCs are synthesized by employing environment-friendly synthetic protocol. BSA has been chosen as a model protein in this work as it is the most abundant protein in blood plasma and it is also useful in various biological functions such as storage and transport for a variety of compounds like fatty acids, amino acids, metals, hormones, drugs, etc.[48-51] In this study, protein-NC interaction has been investigated by monitoring both the fluorescence of the CuNCs and the intrinsic fluorescence of protein. Important thermodynamic parameters for the binding process have been determined by steady-state and isothermal titration calorimetric experiments (ITC) experiments. The conformation of the protein structure in absence and presence of various CuNCs has been investigated through synchronous fluorescence and far-UV circular dichroism (CD) measurements. Single molecule technique, FCS has also been used to obtain further insight into the protein-NCs binding at single molecular level. In the present study the analysis of data has demonstrated new interesting insights in terms of binding pathways of protein molecules in presence of various CuNCs. Additionally, Outcome of the overall work is expected to give a molecular level understanding on the role of surface ligand of CuNCs in

interaction with BSA protein which would encourage and enable better application of NCs in biological studies. The structure of BSA in folded form and the chemical structure of all the ligands used for synthesizing those CuNCs that are used in the present study are given in scheme 3.1.

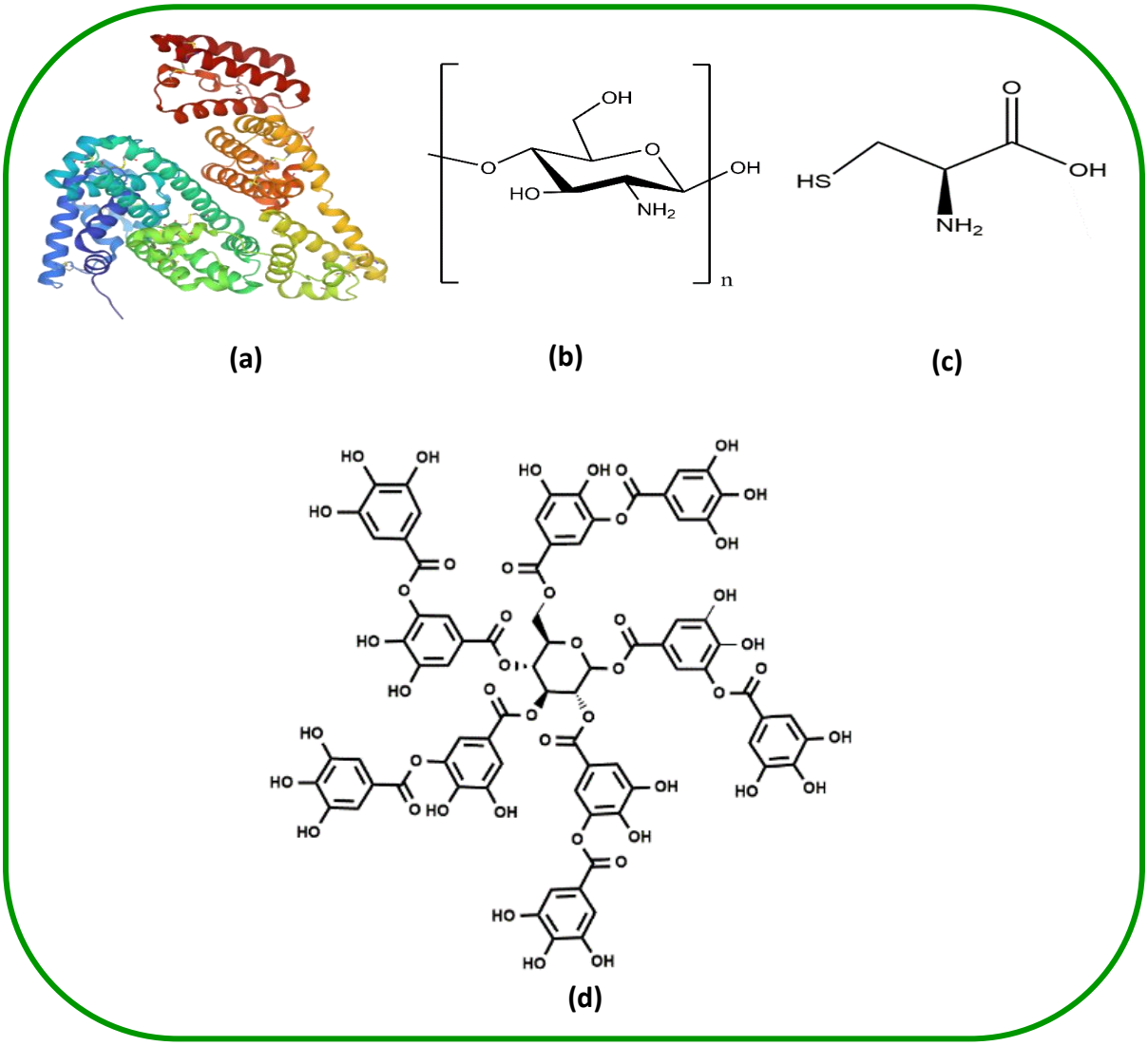

Scheme 3.1. (a) Three-Dimensional Structure of BSA in Folded Form (Data from Protein Data Bank, PDB Code 4F5S), Chemical Structures of All Three ligands used in This Study: (b) chitosan (c) cysteine and (d) tannic acid.

3.2. Characterization of CuNCs

The synthesized CuNCs were characterized by optical absorption and emission measurement, transmission electron microscopy (TEM), energy dispersive X-ray analysis (EDAX) and Fourier transform infrared spectroscopy (FTIR). The absorption and emission spectra of the synthesized CuNCs are shown in Figure APX3.3. The size and shape of the corresponding NCs were determined from TEM measurements, the images of which are shown in Figure APX3.1a,b and c. The sizes of TA-CuNCs, Chitosan-CuNCs and Cys-CuNCs were estimated to be 2.2 ± 0.5 nm, 2.3 ± 0.5 nm and 2.3 ± 0.5 nm respectively and all the CuNCs were observed to be spherical in shape (Figure APX3.1a,b and c). EDAX spectra (Figure APX3.1d,e and f) confirms the presence of desire elements corresponding to the CuNCs and the compositional analysis has been shown in the individual figure. FTIR study has been performed to confirm the successful introduction of the ligand onto the surface of CuNCs. Figure APX3.1g, shows the FT-IR spectra of the TA and the TA-CuNCs. The vibrational frequency of some specific major bands of TA are 3300 cm^{-1} (O-H, stretching), 1716 cm^{-1} (C=O, stretching), 1205 cm^{-1} (C-O), 1055 cm^{-1} (O-H, bending). The FTIR spectrum of TA-CuNCs reveals that the C–OH (1205 cm^{-1}) and O-H (1055 cm^{-1}, bending) vibration from tannic acid are disrupted after capping on the surface of CuNCs, confirming the attachment of TA onto the surface of CuNCs. Figure APX3.1h shows the FTIR spectra of o-carboxymethyl chitosan and O-carboxymethyl chitosan capped CuNCs (Chitosan-CuNCs). The vibrational frequencies of the specific functional groups of O-carboxymethyl chitosan are 3405 cm^{-1} (O-H, N-H, stretching), 2918 cm^{-1} (C-H, stretching), 1740 cm^{-1} (C=0, stretching), 1630 cm^{-1} (N–H, bend), 1403 cm^{-1} (C-H, bend) and 1092 cm^{-1} (O-H, bend). By comparing the peak position of Chitosan-CuNCs with the peak position of modified chitosan it is confirmed that there occurs successful introduction of modified chitosan onto the surface of CuNCs . Figure

APX3.1.i shows the FTIR spectra of Cysteine and Cys-CuNCs. From the figure it is observed that the characteristic peak of –COOH group (asymmetric and symmetric stretching at 1590 cm^{-1} and 1400 cm^{-1} respectively) and $-NH_2$ (3000−3800 cm^{-1}, stretching) group remains unaltered and the S-H stretching band is disappeared in the FTIR spectrum of Cys-CuNCs which confirms that cysteine ligands are attached onto the surface of CuNCs by the thiol moieties. Surface charges of those CuNCs were determined by zeta potential measurements which have been shown in Figure APX3.2. For determining the number of Cu atoms in the metal core (Cu_n) of those nanoclusters, a model called the jellium model has been used which is shown in supporting information.[55,56]

3.3. Result and Discussion

3.3.1 Steady-state Absorption and Emission Profile of the CuNCs

Prior to the protein-NCs interaction study, the photophysical properties of various CuNCs that are used in this study have been investigated. The absorption and emission spectra of the synthesized and well-characterized CuNCs are shown in Figure APX3.3. As can be seen from Figure APX3.3, the absorption spectra of all three CuNCs (tannic acid, chitosan and cysteine-capped) show strong absorption in the UV region and long absorption tail in the visible region. Please note that, these absorption profiles of the CuNCs are very different from the characteristic Surface Plasmon Resonance (SPR) band (~560–600 nm) of relatively larger CuNPs .[57] The absorption profiles of the present CuNCs can be attributed to the discrete electronic energy band structure of CuNCs but not due to SPR of CuNPs.[1,52] Figure APX3.3 also shows the excitation and emission spectra of the three Cu NCs in an aqueous medium at room temperature. As shown in Figure APX3.3. TA-CuNCs, Chitosan-CuNCs, and Cys-CuNCs exhibit fluorescence maxima at 430 nm, 432 nm, and 490 nm respectively when the samples are excited at 360 nm. The

fluorescence of metal nanoclusters is thought to have originated due to the electronic excitation between occupied d bands and states above the fermi level.[58,59] However, recently, it has also been suggested that the fluorescence of MNCs may arise due to the interaction of the metal core and surface ligands.[60-62]

3.3.2 Protein-metal Nanoclusters Interaction through Steady State and Time Resolve Fluorescence Measurements

Initially, the steady state absorption and fluorescence measurements have been carried out to investigate the effect of NC's surface upon protein adsorption. Specifically, fluorescence behaviour of three CuNCs has been monitored separately in absence and presence of BSA. Figure 3.1a,b and c demonstrates the change in fluorescence behaviour of various CuNCs upon gradual addition of BSA. As it can be seen from Figure 3.1a,b and c, the fluorescence intensity of all three CuNCs have increased in presence of BSA. Again, when we have monitored the fluorescence decay profiles of all the three CuNCs in presence of BSA, we have also observed that the average fluorescence lifetime of the CuNCs have increased upon addition of BSA (Table APX3.1). The decay profiles of TA-CuNCs, Chitosan-CuNCs and Cys-CuNCs in absance and presence of BSA are shown in Figure APX3.4 and the relevant decay parameters are also collected in Table APX3.1. The enhancement of fluorescence intensity as well as average fluorescence lifetime of these CuNCs indicate the adsorption of protein on the surface of CuNCs and this behaviour is consistent with literature reports.[34,63] Large number of amine and carboxylic groups of BSA are expected to interact with CuNCs which can gives stability of those systems and led in increase in the fluorescence intensity. [61,64] It is expected that protein molecules surround the CuNCs surface and prevent the contact of water molecules from CuNCs

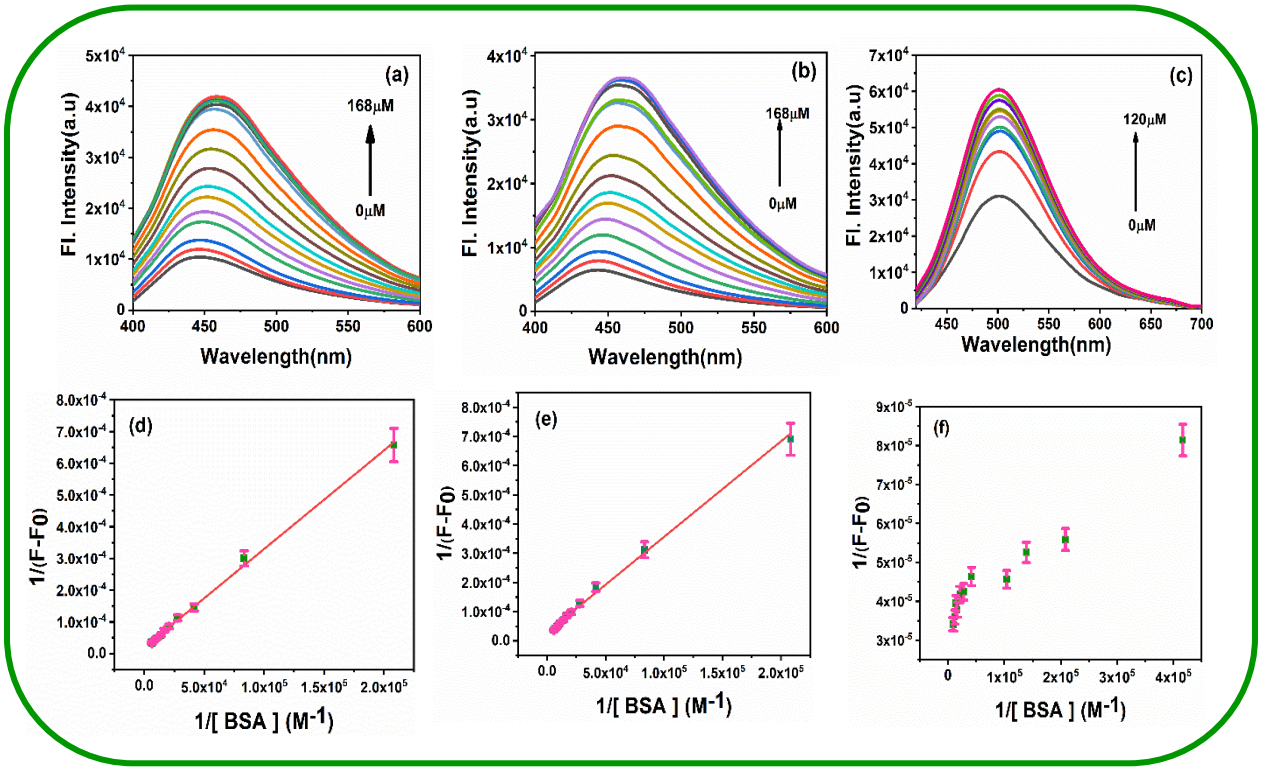

Figure 3.1. (a,b,c) Emission spectra of TA-CuNCs, Chitosan-CuNCs and Cys-CuNCs respectively with gradual addition of BSA. (Conc. of CuNCs-12μM, λ_{ex}=390 nm). (d,e,f) Benesi-Hildebrand double reciprocal plot of TA-CuNCs, Chitosan-CuNCs and Cys-CuNCs with BSA respectively.

surface and cause the reduction in the nonradiative relaxation process which otherwise would have occurred due to the presence of water molecules.[65,66] However, upon careful look, one can also see from Figure 3.1a,b and c that the fluorescence enhancement for all three CuNCs are not same. For example fluorescence intensity for TA-CuNCs, Chitosan-CuNCs and Cys-CuNCs in presence of BSA get enhanced by 4.0 times, 5.6 times and 1.9 times respectively. The different extent of fluorescence increment for various CuNCs in the present study indicate different surface chemical properties of these CuNCs. It is pertinent to mention here that the increase in the NPs fluorescence in presence of protein has been attributed to the "protein-corona" formation.[26,67] However, in case of MNCs the fluorescence enhancement alone cannot

conclusively state that interaction of NCs with protein has led to the formation of "protein-corona" like structure.[17] Pioneering work by Dawson and co-workers[68] and later on Puntes and co-workers[11] have shown that to form stable "protein corona" via adsorption of at least a few to tens (sometimes hundred) of protein onto the surface of one nanoparticle are needed. Essentially, according to the earlier experiments, for effective "protein-corona" formation the protein/nanoparticle ratio is predicted to be always >1. Hence, the conclusion of "protein-corona" formation just by looking at the fluorescence enhancement for NCs would be premature and thus this issue warrants further careful investigation. So, in the present study we have thought to determine the stoichiometry of the binding events of CuNCs with BSA. For this purpose, the fluorescence data has been analyzed based on modified Benesi-Hildebrand (B-H) double reciprocal plot by using equation (3.5) for 1:1 (BSA: NCs) complexation and equation (3.6) for 2:1 (BSA: NCs) complexation, [55,69-71] independently

$$\frac{1}{F-F_0} = \frac{1}{F_m - F_0} + \frac{1}{(F_m - F_0)K[BSA]} \qquad (3.5)$$

$$\frac{1}{F-F_0} = \frac{1}{F_m - F_0} + \frac{1}{(F_m - F_0)K[BSA]^2} \qquad (3.6)$$

where, F and F_m are the fluorescence intensities of CuNCs with successive addition of BSA and maximum BSA concentrations respectively, F_0 is the fluorescence intensity in absence of BSA and K is the equilibrium constant related to CuNCs and BSA association.

From the B-H plot, the stoichiometric information for binding can be conveniently obtained which eventually can help one to get idea about whether any layer of protein is formed or not over concerned NCs surface. The B-H plots for TA-CuNCs, Chitosan-CuNCs and cys-CuNCs for 1:1 complexation with BSA are shown in Figure 3.1d,e and f. From the plots it is evident that in the case of TA-CuNCs and chitosan-CuNCs systems, a good linear correlation is

obtained when $1/(F-F_0)$ is plotted against 1/[BSA], which indicates a 1:1 (BSA:NCs) stoichiometry for the said protein-NCs binding events. However, in case of Cys-CuNCs, as can be seen from Figure 3.1f, when $1/(F-F_0)$ is plotted against 1/[BSA], fit of the data points deviate from linearity. Again, when these data points are fitted with the equation (3.6), it can be seen that the data points do not produce linear fit (Figure APX3.5). The present observation for Cys-CuNCs indicates that the BSA/CuNCs is neither 1:1 nor 2:1, rather it indicates multiple Cys-CuNCs bind to BSA.[69] Further, the binding stoichiometries corresponding to CuNCs to BSA binding events are also estimated by exploiting zeta potential measurements. From these measurements it has been observed that the increase in the mean zeta potential value of BSA solution is observed when TA-CuNCs and Chitosan-CuNCs are added up to 3 equivalents (in each case) independently to BSA solution. After addition of 3 equivalents of TA-CuNCs and Chitosan-CuNCs to BSA in separate experiments, the change in mean zeta potential of BSA becomes insignificant upon further addition of CuNCs (Figure APX3.6a and b). However, for Cys-CuNCs the maximum change in mean zeta potential of BSA is observed when 4 equivalents of Cys-CuNCs is added to BSA and after that binding gets saturated (Figure APX3.6c). Therefore, one can simply say from zeta potential measurements that the binding stoichiometry ratio of CuNCs to BSA is greater than one in the present cases. Again, from ITC studies, the trend in the binding stoichiometries for protein-NCs interaction events are observed to be similar i.e; protein/NCs ratio is found to be less than one (*vide infra*). The deviation in binding stoichiometry for specific binding events is not unusual due to different measuring principles and sensitivity of different instruments that are employed to obtain the data. The outcomes of the above study essentially indicate that "protein-corona" like structure has not been formed in the present interaction events. To gain deeper insight into this issue we have carried out FCS studies.

We would like to mention that FCS study at single molecule level can give valuable information about "protein-corona" formation.[72,73] This technique is widely used as highly precise single molecular technique for the study of molecular diffusion, kinetics, binding affinities of protein to nanomaterials in single molecular level.[48,74,75] Here FCS study has been done to figure out the adsorption behavior of BSA on the surface of these three CuNCs by monitoring translational diffusion time (τ_D) and calculating hydrodynamic radius (R_H) of these CuNCs in absence and presence of BSA. Figure 3.2 shows the normalized autocorrelation curves of CuNCs with increasing concentration of BSA. It has been observed from the figure that with increasing concentration of BSA, diffusion time (τ_D) increases which indicates the adsorption of protein molecules onto the surface of MNCs. The shift of the autocorrelation curves towards right in Figure 3.2 indicates the increasing hydrodynamic radius of CuNCs in presence of BSA.[76] Relevant parameters, obtained from FCS study are tabulated in Table APX3.2. The hydrodynamic radius of TA-CuNCs, Chitosan-CuNCs and Cys-CuNCs are estimated to be 0.61 nm, 0.66 nm and 0.63 nm respectively but in presence of BSA the hydrodynamic radii of these systems are found to increase to 1.26 nm, 1.24 nm and 1.18 nm respectively. Therefore, increment of hydrodynamic radius of the CuNCs in presence of BSA is observed to be much less than the thickness of a single BSA protein (~3.3 nm).[77] This observation clearly suggests that even though protein is adsorbed on the CuNCs surface but criterion for the "protein-corona" is not fulfilled.[72] Therefore the present data conclusively suggest that the CuNCs-BSA interaction does not proceeds through "protein-corona" formation. The observation is quite interesting in a sense that previously in case of CuNCs with different surface ligand (glutathione), protein-NCs interaction is observed to be mediated through "protein-corona" like structure.[34] The observation

of different features for the CuNCs that are used in this study also indicates the role of surface ligands in protein-NCs interaction.

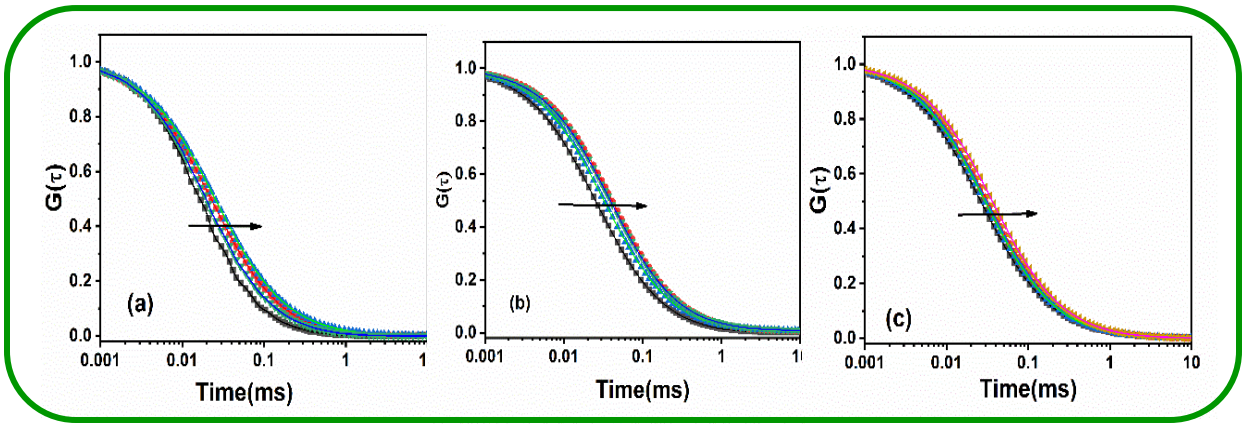

Figure 3.2. Normalized autocorrelation curves for (a) TA-CuNCs (b) Chitosan-CuNCs and (c) Cys-CuNCs with increasing concentrations of BSA. (Concentration of CuNCs are 30 nM and concentration of BSA is from 0 to 150 nM).

Hence, from the above studies it can be said that one BSA could bind with 1~3 TA-CuNCs and Chit-CuNCs separately and one BSA could bind with 2~4 Cys-CuNCs. This observation demonstrates that either CuNCs could target specific epitopes on the surface of BSA in a 1:1 ratio or multiple CuNCs can bind to one protein. Therefore, the present observation is very different from the conventional model of "protein-corona" and is also suggestive of the fact that the protein-CuNCs interaction goes through different route. Infect, the observation suggests that binding happens through "protein-complex" like structure formation. In the "protein complex" few to even more ultra-small NCs are adsorbed onto the surface of a single protein molecule which is in contrast to the larger size NPs where a few to tens (sometimes hundreds) of protein molecules are adsorbed onto a single NPs forming "protein corona", which has been shown schematically (scheme 3.2). We would also like to note that a recent study on gold NCs has shown that the protein-ligand interaction may not necessarily be mediated through the

formation of "protein-corona" like structure.[17] In this context, the current findings for the CuNCs are new and interesting. The present result highlights the importance of understanding the interaction of protein-NCs because biological outcomes can be affected by the changes in the interaction event. However, present observation also demands further investigations which can provide more information on binding pathways, thermodynamics of binding and conformation of protein structure in presence of CuNCs.

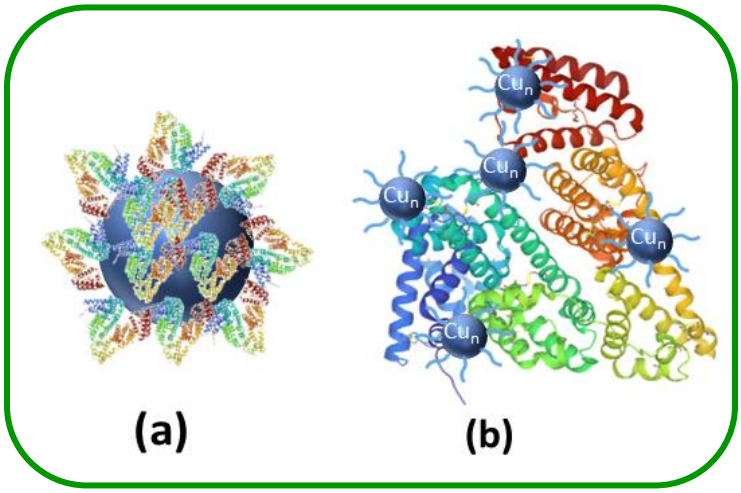

Scheme 3.2. Structures of (a) "protein-corona" and (b) protein complex. (This does not represent the real pictures)

Further investigations on the interaction of BSA with CuNCs have been carried out by monitoring the intrinsic fluorescence of BSA in absence and presence of the concerned CuNCs. It is to be noted here that the intrinsic fluorescence of BSA protein arises from the presence of three fluorescent amino acids namely tryptophan (Trp), tyrosine (Tyr) and phenylalanine (Phe) in the polypeptide chain. The fluorescence of Phe is negligible when compared to that of Tyr and Trp when excited at 280 nm. Therefore, the contribution of Phe to the fluorescence of BSA can be neglected in this studies.[78] Here, in the steady state experiment

we have studied the fluorescence response of BSA upon gradual addition of the three CuNCs separately.

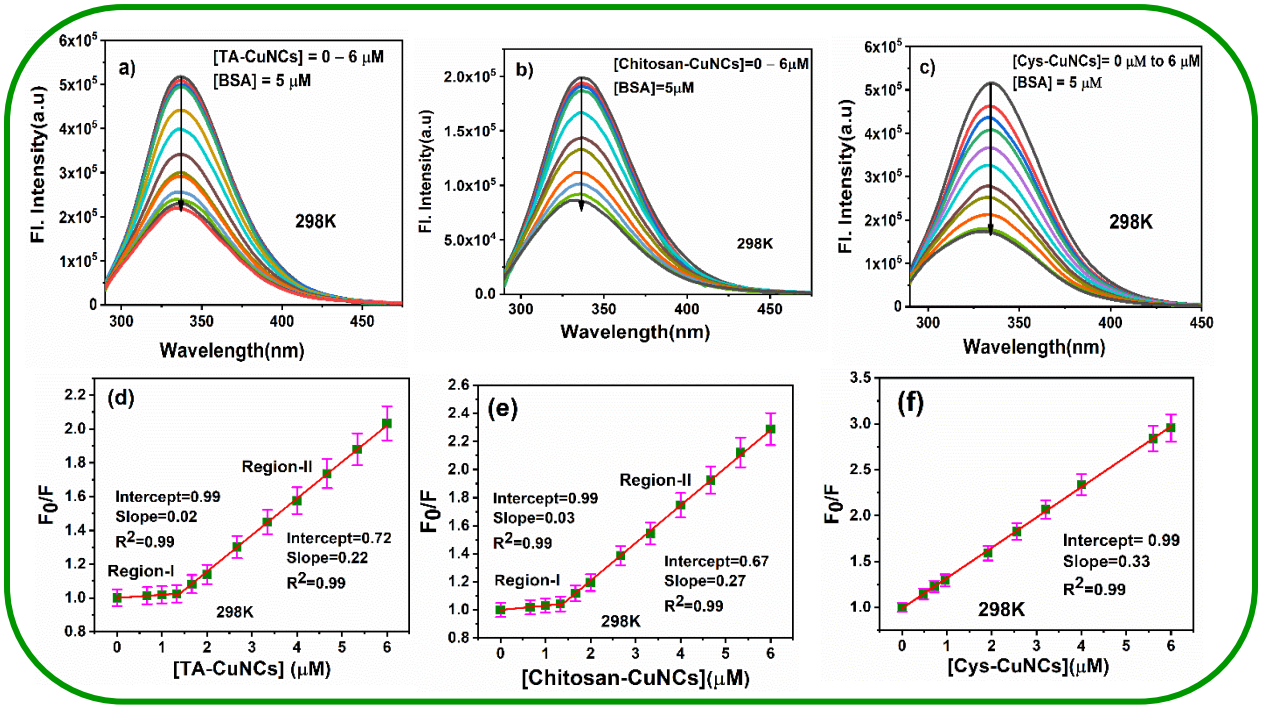

Figure 3.3. (a,b,c) Fluorescence emission spectra of BSA protein upon gradual addition of TA-CuNCs, chitosan-CuNCs and Cys-CuNCs CuNCs (λ_{ex}= 280nm). **(d,e,f)** Stern-Volmer plots of the quenching of BSA protein by TA-CuNCs, Chitosan-CuNCs and Cys capped CuNCs at pH 7.4 respectively.

The emission spectra of BSA at 298K in the presence of increasing concentration of TA-CuNCs, Chitosan-CuNCs and Cys-CuNCs are shown in Figure 3.3a,b and c. The data corresponding to fluorescence behavior of BSA in presence of CuNCs at various temperatures are also provided in Figure APX3.8a,b and c. The absorption spectra of BSA in absence and presence of the CuNCs are also shown in Figure APX3.7 separately. Except slight change in the optical density, no significant change in the absorption spectral profiles of BSA in presence of CuNCs has been observed. Interestingly, it can be seen from the Figure 3.3a,b and c that the

fluorescence of BSA is significantly quenched upon gradual addition of the CuNCs indicating the strong interaction between CuNCs and BSA protein molecules. However, upon a careful look at Figure 3.3a,b and c, one can also find out that the extent of fluorescence quenching of BSA is different for different CuNCs. For example, the percentage of fluorescence quenching of BSA with TA-CuNCs, Chitosan-CuNCs and Cys-CuNCs are estimated to be 56%, 60% and 65% respectively. This different extent of fluorescence quenching of BSA in the presence of CuNCs having various surface ligands is caused due to the difference in the surface chemical properties of various CuNCs employed in the study. No significant shift of the emission peaks position of the BSA upon addition of the CuNCs in all cases indicates that the polarity of the surrounding environments of amino acid residues of the BSA protein has not been affected by CuNCs in this measurements. Please note that, in the present study, prior to data analysis, all fluorescence intensities are corrected from inner filter effect[79] by using equation (3.7)

$$F_{corr} = F_{obs}\, antilog(\frac{OD_{ex}+OD_{em}}{2}) \qquad (3.7)$$

where F_{corr} is the corrected fluorescence intensity, F_{obs} is the observed fluorescence intensity, OD_{ex} and OD_{em} are the optical density at excitation and emission wavelength respectively. We note that the fluorescence quenching in emission spectrum can be caused due to various phenomenon such as formation of ground state complex with the quencher (static quenching), collision between the excited fluorophore and quencher molecule (dynamic quenching), excited state reaction and energy transfer phenomena, etc.[78-81] We have resorted to Stern Volmer analysis in the present study to understand the mechanism of fluorescence quenching of BSA by CuNCs. The Stern Volmer relation is given by equation (3.8),

$$\frac{F_0}{F} = 1 + K_{SV}[Q] \qquad (3.8)$$

where F_0 and F are the fluorescence intensities of BSA in the absence and presence of CuNCs, respectively, and K_{SV} is the Stern-Volmer constant. The plot of F_0/F vs quencher concentration ([Q]) for several CuNCs at 298K are shown in Figure 3.3d,e and f. Similar plots of F_0/F vs quencher (CuNCs) concentrations for other experimental temperatures are also provided in the Figure APX3.9a, b and c. As can be seen, from Figure 3.3d and e, in the case of TA-CuNCs and Chitosan-CuNCs, two distinct regions (region-I and region-II) in the SV plots have been observed. Region-I has been observed at relatively lower quencher concentration (upto 1.33 μM) and region-II has been observed at relatively higher quencher concentration (beyond 1.33 μm). Moreover, in both region-I and region-II of the said plots, F_0/F is found to vary linearly with increase in the concentration of CuNCs, however, having different slopes for region-I and region-II. Interestingly, Figure 3.3f reveals that in case of Cys-CuNCs the plot of F_0/F vs [Cys-CuNCs] provides a linear plot with only one region. The observed overall bimolecular quenching constants (k_q) estimated from the fluorescence quenching data are 3.1×10^{13} $M^{-1}s^{-1}$, 4.13×10^{13} $M^{-1}s^{-1}$, and 5.7×10^{13} $M^{-1}s^{-1}$ for TA-CuNCs, Chitosan-CuNCs, and Cys-CuNCs respectively. The k_q values in all these cases suggest that the overall quenching mechanism is predominantly static in nature.[82,83] Interestingly, when SV analysis is also done by using equation (3.9) in terms of change in the lifetimes of BSA and concentrations of various CuNCs, pattern of the SV plots (Figure APX3.11) of BSA against [CuNCs] has been observed to be similar to that has been observed for steady state fluorescence data (Figure 3.3d,e and f). The decay profiles of BSA in absence and presence of TA-CuNCs, Chitosan-CuNCs and Cys-CuNCs are shown in Figure APX3.10 and the relevant decay parameters are also collected in Table APX3.3. The decrease in the lifetime of BSA in presence of CuNCs in all cases also highlight the involvement of dynamic quenching process. The equation (9) can be represented by the following relation

$$\tau_0/\tau = 1 + K_D[Q] \qquad (3.9)$$

where τ_0 is the fluorescence lifetime in the absence of quencher and τ is the same in the presence of quencher. Therefore, upon careful look at the nature of the SV plots which are obtained from both steady state and time resolved fluorescence data one can clearly see that from the very beginning of titration, slope (~10^5 M^{-1}) of SV plots (Figure 3.3f/S11C) for Cys-CuNCs is found to be very similar (~10^5 M^{-1}) to that of region-II in the SV plots for TA-CuNCs (Figure 3d/S11a) and Chitosan-CuNCs (Figure 3.3e/S11b). It essentially means that for Cys-CuNCs, the protein fluorescence quenching has begun to follow a certain pattern at relatively lower quencher (Cys-CuNCs) concentration which is otherwise observed at relatively higher concentration for TA-CuNCs and Chitosan-CuNCs. All the above discussions, not only point out that binding of TA-CuNCs and Chitosan-CuNCs with BSA follow two types of binding modes and binding of Cys-CuNCs with BSA goes through one type of binding mode but more importantly the data also indicates that the binding of Cys-CuNCs with BSA is relatively stronger than that of other two CuNCs.

The current result is very interesting in a sense that this type of binding mode of CuNCs with BSA has not been observed before. The behavior of NCs towards protein can be very different as compared to the binding of relatively larger NPs. The present observation of various binding mode of various CuNCs stabilized by various ligands also indicates that the surface ligands play important role in protein-ligand binding interaction. Observation of similar profiles of SV plots in both steady state and time resolved fluorescence experiment in case of TA-CuNCs and Chitosan-CuNCs arises due to the fact that both of the CuNCs contain polyhydroxy groups, whereas, different profile of SV plot in case of Cys-CuNCs could arise due to presence of different functional group (thiol group) in the surface ligand.

3.3.3. Binding Nature and Thermodynamic Parameters of Interaction between CuNCs and BSA Protein

It is important to understand the thermodynamics of the binding event between NCs and protein as it provides valuable information on the feasibility of the process, nature of interaction, forces of binding etc.[28,32] Several types of interactions such as electrostatic interaction, hydrogen bonding, Van der Waals force of attraction, hydrophobic interaction, etc. are responsible for the binding interaction between protein and quencher molecules.[84,85] These types of interactions can be realized by analyzing the thermodynamic parameters such as enthalpy (ΔH) and entropy (ΔS) with proper sign.[85] Initially, fluorescence data that are obtained during the quenching of BSA against various CuNCs are analyzed further by constructing double logarithmic plot with the help of equation (3.10)[87-89]

$$\log[(F_0 - F)/F] = \log K_a + n\log[Q] \qquad (3.10)$$

where F_0 is the fluorescence intensity in the absence of quencher and F is the same in the presence of quencher, [Q] is the quencher concentration, K_a is the equilibrium binding constant and n is the number of binding sites in the protein. Double logarithm curves for the binding events corresponding to BSA with TA-CuNCs, Chitosan-CuNCs and Cys-CuNCs are shown in Figure 3.4a, b and c respectively. From the Figure 3.4a and b, it can be observed that the binding of TA-CuNCs and Chitosan-CuNCs with BSA take place in two stages (indicated by blue and red colored fitted lines) whereas, from the Figure 3.4c, it can be seen that the binding of Cys-CuNCs with BSA takes place in only one region. In this context we would like to mention that Mukherjee and co-workers[90] have previously shown that double logarithmic plot is quite effective in determining the sequential binding of a protein-surfactant assembly. They have

shown that the binding of sodium dodecyl sulfate (SDS) to human serum albumin (HSA) take place in four distinct stages depending upon the concentration. Similarly, in a separate work Panda and co-workers[91] have demonstrated the stepwise addition and sequential unfolding of HSA in presence of guanidium hydrochloride (GdnHCl). In the present study, the binding constants obtained from double logarithm plot for the blue regions are 1.4×10^5 M^{-1} (Figure 3.4a), 2.2×10^4 M^{-1} (Figure 3.4b) and the same for red regions are 7.9×10^9 M^{-1} (Figure 3.4a), 1.5×10^{10} M^{-1} (Figure 3.4b) for TA-CuNCs and Chitosan- CuNCs respectively. In the case of Cys-CuNCs, the estimated binding constant obtained from only one region of the double logarithm plot (Figure 3.4c) is 6.34×10^5 M^{-1}. The double logarithmic plots for Cys-CuNCs at other temperatures are shown in Figure APX3.12. Therefore, the current data also substantiate the two modes of binding for TA-CuNCs and Chitosan-CuNCs and one mode of binding for Cys-CuNCs.

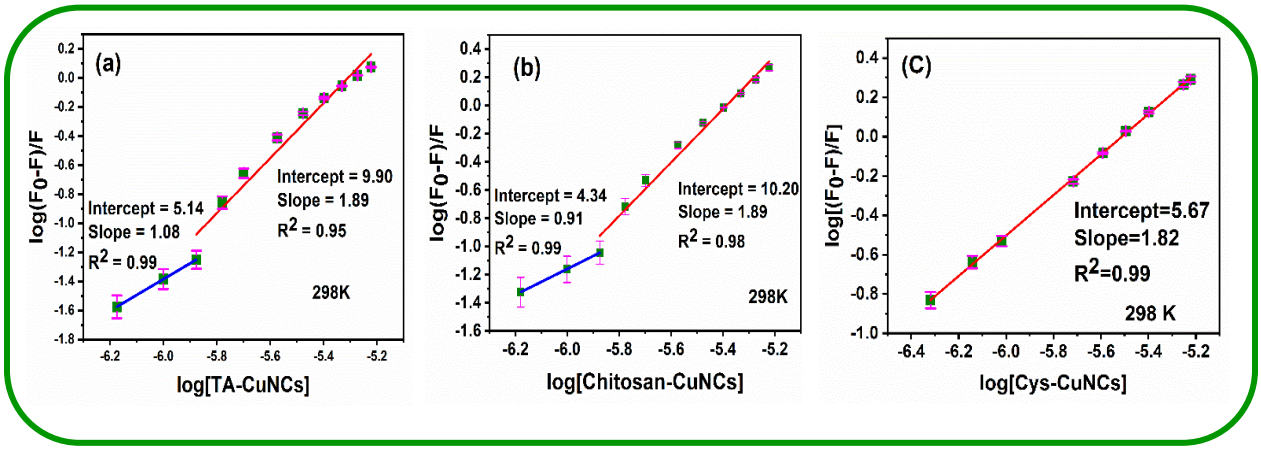

Figure 3.4. Double logarithm plot for the binding of (a) [TA-CuNCs], (b) [Chitosan-CuNCs] and (c) [Cys-CuNCs] with BSA at 298K temperature. The solid lines represent the simulated fitted line.

To get further insight into overall binding event and to get overall binding constants for the interaction of BSA with TA-CuNCs and Chitosan-CuNCs the quenching data of BSA are

analyzed by using hill equation (equation 3.11), from which the intrinsic dissociation constant (K_d) and by inversing it overall association constant (K_a) for the binding event has been calculated,[92,93]

$$\frac{\Delta F}{F_0} = \frac{(\Delta F_{max}/F_0)[Q]^n}{K_d + [Q]^n} \qquad (3.11)$$

where K_d is the dissociative binding constant, K_a is the associative binding constant, [Q] is the quencher concentration and n is the hill coefficient. The hill plots for the quenching of BSA with TA-CuNCs and Chitosan-CuNCs at various temperatures have been given in Figure APX3.13a and b. From the hill plots the obtained hill coefficients (n >1) indicate the cooperativity in the binding events for both the CuNCs while interacting with BSA. After getting the associated binding constants of BSA with TA-CuNCs and Chitosan-CuNCs systems from the hill plots and the same with Cys-CuNCs from the double logarithm plots, the enthalpy change (*ΔH*) and entropy change (*ΔS*) are estimated basically to understand the type of forces that are involved in binding of BSA with above mentioned CuNCs. For calculating these thermodynamic parameters Van't Hoff equation[32,85] has been used assuming that the *ΔH* and *ΔS* are remain constant with variation of temperature which is given by equation (3.12)

$$\ln K_a = -\left(\frac{\Delta H}{R}\right)\frac{1}{T} + \frac{\Delta S}{R} \qquad (3.12)$$

The Van't Hoff plot of those three systems is given in Figure APX3.14 and from slope and intercept of the fitted lines, *ΔH* and *ΔS* of those systems has been calculated. The free energy change (*ΔG*) is determined with the help of equation (3.13) by using the calculated associated binding constants of those systems at various temperatures.

$$\Delta G = -RT\ln K_a \qquad (3.13)$$

The estimated parameters i.e. binding constants (K_a), enthalpy change (ΔH), entropy change (ΔS), and free energy change (ΔG) are all organized in Table 3.1.

Table 3.1. Associative binding constant (K_a), and other relevant thermodynamic parameters for the interaction of TA-CuNCs, Chitosan-CuNCs and Cys-CuNCs with BSA protein.

Systems	**Temp (K)**	***K_a*** **(10^5 L mol^{-1})**	***ΔH*** **(KJ mol^{-1})**	***ΔS*** **(J $K^{-1}mol^{-1}$)**	***ΔG*** **(KJ mol^{-1})**
TA-CuNCs – BSA	298	3.11±0.05	4.10±0.29	118.89±0.36	-31.34 ±0.22
	303	3.22±0.07			-31.95±0.25
	308	3.32±0.06			-32.55±0.19
	313	3.39±0.07			-33.14±0.16
	318	3.45±0.09			-33.71±0.21
Chitosan-CuNCs-BSA	298	3.24±0.07	2.86±0.65	115.06±0.54	-31.44±0.16
	303	3.29±0.09			-32.00±0.20
	308	3.35±0.08			-32.58±0.23
	313	3.42±0.06			-33.16±0.18
	318	3.48±0.07			-33.74±0.21
Cys-CuNCs-BSA	298	6.32±0.05	-51.74±0.23	-62.44±0.87	-33.09±0.11
	303	4.36±0.05			-32.17±0.19
	308	3.62±0.06			-31.71±0.16
	313	2.45±0.07			-30.75±0.16

	318	1.62±0.08	-29.73±0.21

From the Table 3.1, it can be observed that the free energy changes (*ΔG*) for all the systems are negative which indicates that the binding of BSA with various CuNCs is a spontaneous process. It is known from the study of protein-ligand interaction, by Ross and Subramanian, [86] that both positive values for *ΔH* and *ΔS* are often indicative of the hydrophobic interaction whereas negative values for *ΔH* and *ΔS* are often indicative of both hydrogen binding and van der Waals interactions. "Ross theory" has been developed based on the interaction between small molecules and protein. Though CuNCs are involved in the interaction with BSA but interactions are mainly governed by the surface ligands of CuNCs, so "Ross theory" might be applicable to our systems. Keeping the sign convention in mind and the data that are obtained during the current investigations one can conclude that the interaction of BSA with TA-CuNCs and Chitosan-CuNCs might be mediated through hydrophobic interaction whereas the same with Cys-CuNCs might be mediated through hydrogen binding and van der Waals interactions. The conclusion is not surprising considering the chemical nature (TA and Chitosan have long carbon back bone which may responsible for creating hydrophobic atmosphere but Cysteine does not) (TA-CuNCs contains polyhydroxy group, Chitosan-CuNCs contains polyhydroxy and amine groups and Cys-CuNCs contains amine, carboxyl and thiol group) of surface ligands over CuNCs that are employed in the study. Therefore, this observation is clearly an indicative of the fact the surface ligands over nanoclusters play an important role in determining the intermolecular force of attraction between nanocluster and protein. The observation also highlights that one should also be careful in choosing the surface ligands while fabricating the nanocluster and subsequent studies on the interaction of protein with them. Additionally it is also known that, ITC is used as an effective tool to characterize the binding of small molecules, drugs

etc. to macromolecules thermodynamically.[94,96] To shed light into the interaction mechanism of CuNCs with BSA, ITC experiment has also been performed at 298K. The ITC thermographs presented in Figure 3.5 indicate that the titration of both TA-CuNCs and Chitosan-CuNCs individually to BSA has caused positive heat deflection which signifies that both the CuNCs interact to the protein in an endothermic manner but for the case of Cys-CuNCs negative heat deflection has been observed which indicates the exothermic process of binding event. The thermodynamic parameters (*ΔH, ΔS, ΔG, Ka*) obtained from ITC experiments are tabulated in Table APX3.4. The data obtained from ITC experiment for TA-CuNCs-BSA and Chitosan-CuNCs-BSA systems are fitted by two step "sequential binding model" which gives two values for each thermodynamic parameters (*ΔH, ΔS, ΔG, Ka*) which again confirms the two step binding process but the data obtained fron Cys-CuNCs-BSA system gives the best fit when the corresponding data are fitted by "one set of sites" binding model which gives only one value for each thermodynamic parameters. In this context, it is relevant to mention that though currently we do not know about the exact type of binding mode, however keeping in mind the outcomes of the work by Jiang and coworkers,[36] perhaps similar type of binding process taking place for TA-CuNCs-BSA and Chitosan-CuNCs-BSA systems. ITC experiment also support the conclusion that has been obtained from steady state fluorescence quenching of BSA by CuNCs.

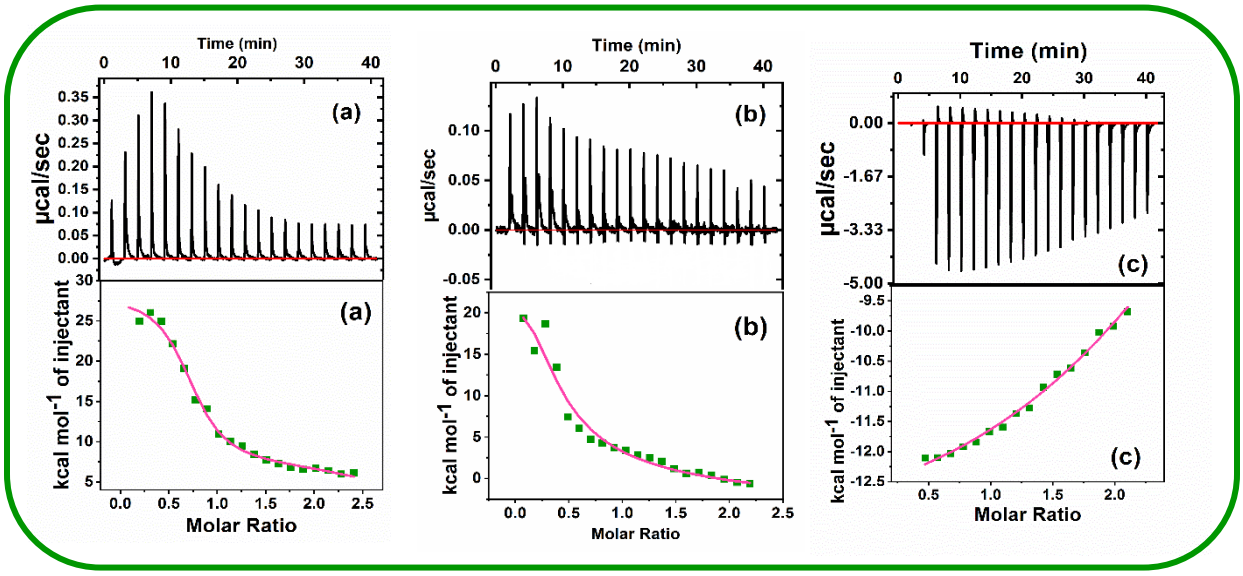

Figure 3.5. ITC titration profile of (a) TA-CuNCs (b) Chitosan-CuNCs and (c) Cys-CuNCs into BSA at 298 K in phosphate buffer of pH 7.4. Upper panels represent the raw data obtained from the titrations and bottom panels represent the integrated heats of each peak (green dots) with a corresponding nonlinear regression plot (pink line).

3.3.4. Conformational Studies

3.3.4.1. Synchronous Fluorescence

In order to investigate whether there is any conformational change or not in protein molecule during the interacting with CuNCs, synchronous fluorescence study has been performed. Synchronous fluorescence spectroscopy is a widely used tool to study the microenvironment of fluorophore component of protein molecules by monitoring the shifting of emission wavelength due to change of polarity in the vicinity of fluorophore moiety.[97,98] When offset wavelength ($\Delta\lambda$) are stabilized at 15 and 60 nm, the synchronous fluorescence spectra give the characteristic information about tyr and trp residue of protein molecule respectively.[32,99]The synchronous fluorescence spectra of BSA protein upon gradual addition of TA-CuNCs, Chitosan-CuNCs and Cys-CuNCs are shown in Figure 3.6. From the Figure 3.6 it can be observed that the

synchronous fluorescence of BSA is getting quenched with increasing the concentration of the above said nanoclusters at both the offset wavelengths i,e. at Δλ= 15 and 60 nm, indicating the interaction of BSA with CuNCs occurs through both trp and tyr residues. Almost, no change in the emission maxima of BSA (Figure 3.6) with increasing concentration for various CuNCs suggest that the microenvironment of tryptophan and tyrosine residues of BSA protein remain almost unperturbed in presence of CuNCs.

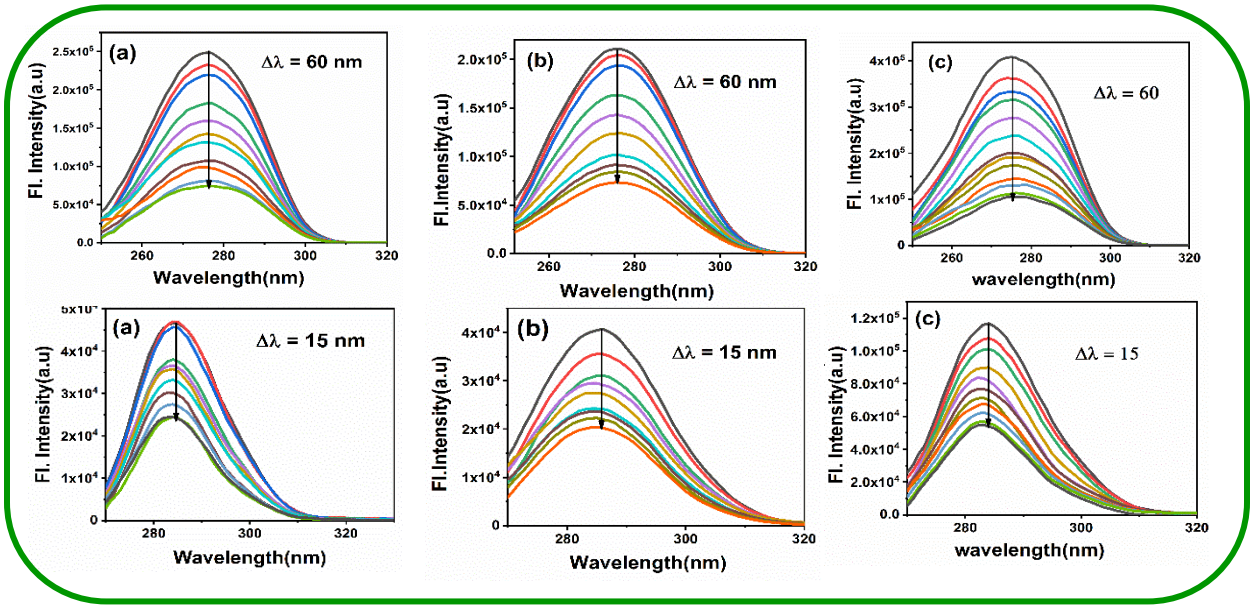

Figure 3.6. Synchronous fluorescence spectra of BSA with increasing concentration of (a) TA-CuNCs (b) Chitosan-CuNCs and (c) Cys-CuNCs at 298 K. The top panel shows the spectra with offset wavelength 60 nm, and the bottom panel shows the same with offset wavelength of 15 nm. (Concentration of BSA is 5 μM and concentration range of CuNCs is from 0 to 6μM).

3.3.4.2. Circular Dichroism (CD)

CD spectroscopy has been employed to reveal the possible influence of CuNCs capped with various ligand on the secondary structure of BSA. CD spectra of native BSA protein in presence of different CuNCs concentrations are shown in Figure 3.7. It can be observed from

Figure 3.7 that native BSA shows two negative peaks at 208 nm and 222 nm corresponding to the characteristic peaks of α-helical structure of BSA for π - π* and n - π* transition respectively.[85,100,101] The percentage of α-helical contents of BSA in absence and presence of various concentration of CuNCs has been estimated quantitatively by using equation (3.14) and equation (3.15)

$$MRE = \frac{\theta \text{obs (mdeg)}}{10ncl} \qquad (3.14)$$

where MRE is the mean residue ellipticity, θ_{obs} is the observed ellipticity in mill degrees, n is the number of amino acid residues (583 for BSA), l is the path length of the cell (0.2 cm), and C is the concentration of protein in mol dm^{-3}.

$$\alpha - helix(\%) = \frac{(-MRE_{208} - 4000)}{(33000 - 4000)} \times 100 \qquad (3.15)$$

where MRE_{208} is the calculated MRE value at 208 nm, 4000 is the MRE value of the β-form and random coil conformation, and 33 000 is the MRE value of a pure α-helix. The relevant data for this study are summarized in Table APX3.5. Analysis of data that are present in Table APX3.5 reveals that BSA in native form exhibits 56.5% α-helical structure, which is very close to the literature-reported value for α-helical structure of BSA.[102,103] Additionally it has been observed that percentage of α-helical form increases upon gradual addition of CuNCs for various CuNCs but with different extents (Figure 3.7). In particular, the change of α-helical form of BSA has been occurred to a greater extent in presence of TA-CuNCs and chitosan-CuNCs than in presence of Cys-CuNCs. However, the changes in the percentage of α-helical form of protein in presence of NCs are found to be very small. But, more importantly, comparison of the shapes and the peak positions corresponding to CD spectra (Figure 3.7) of BSA in absence and presence of CuNCs clearly indicate that the basic structure of the protein remains almost unaltered even

after binding with CuNCs.[104] This is an interesting result in a sense that though fluorescence of BSA is quenched by CuNCs but the native structure of BSA remains almost unchanged. This data indicates that the present CuNCs are bio compatible and can safely be used in various biological application.

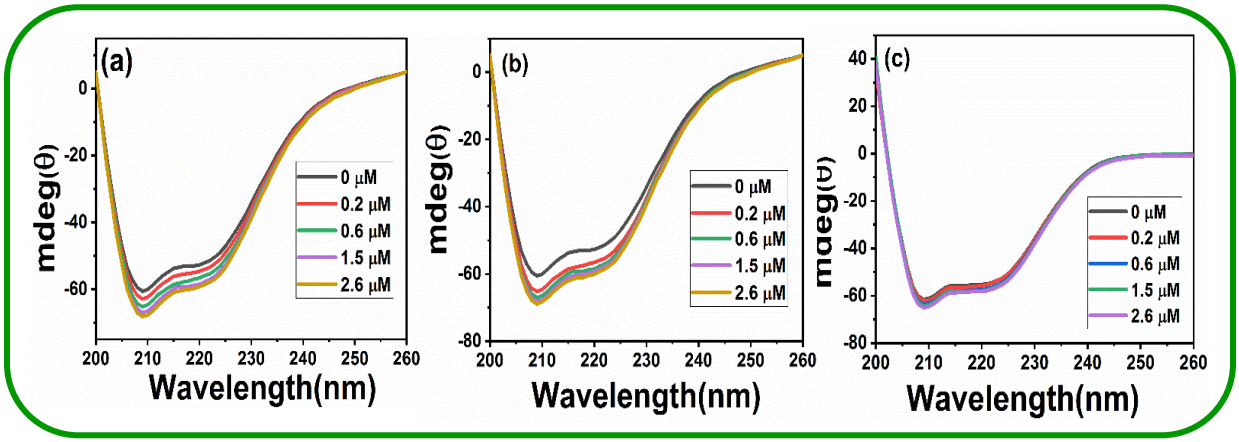

Figure 3.7. Far-UV CD spectra of 2 μM BSA (in 10 mM phosphate buffer of pH 7.4) in the absence and presence of increasing concentration of (a)TA-CuNCs (b) Chitosan-CuNCs and (c) Cys-CuNCs.

3.4. Conclusion

In this work, we report the study of interaction of BSA with CuNCs, modified with various surface ligands (tannic acid, chitosan and cysteine), with an aim to understand the mechanism of interaction between them. In particular, the current investigation is focused on to find out whether the protein-CuNC interaction goes through in a new pathway without forming the "protein-corona" which is otherwise observed in relatively larger sized nanoparticles when they are exposed to biological fluids. The current study also aims to unravel the role of surface ligand in controlling the protein-CuNC interaction mechanism. The investigations are carried out at both ensemble average and single molecule level. From the current investigations, several

interesting aspects in relation to protein-NCs interaction have emerged. The investigations have revealed that observation of fluorescence enhancement of nanoclusters in presence of protein may not necessarily indicate the "protein-corona" like structures during the event. In fact, analysis of data obtained from steady and time resolved fluorescence, ITC and zeta potential measurements have indicated that BSA protein in presence of CuNCs does not attain the required stoichiometry (BSA/CuNCs >1) to form "protein-corona" during the overall interaction event. Moreover, FCS studies have further shown that the thickness of BSA that is adsorbed onto CuNC is estimated to be less than the thickness of a single layer of protein. Essentially, our current investigations based on both ensemble average measurements and single molecule fluorescence measurements (FCS study) have clearly indicated that the interaction of various CuNCs that are employed in the present study with the BSA does not go through the formation of a "protein-corona" like structure. Further analysis of fluorescence data based on double logarithmic equations and estimation of the relevant thermodynamic parameters from both fluorescence and ITC measurements have revealed that the surface ligands of the CuNCs play important role in the protein-NCs binding events, and they can alter the mode and thermodynamics of the process. In particular, the analysis of the current data obtained from both steady state and time resolve fluorescence study of BSA in absence and presence of CuNCs have demonstrated that binding of BSA with TA-CuNCs and Chitosan-CuNCs follow two types of binding modes but the same with Cys-CuNCs goes through only one type of binding mode. Temperature-dependent fluorescence titration experiments and ITC experiments have indicated that the spontaneous interaction of BSA with TA-CuNCs and Chitosan-CuNCs is driven by hydrophobic forces, whereas the same with Cys-CuNCs is driven by hydrogen binding and van der Waals forces. The synchronous fluorescence and CD spectroscopic study have revealed that

CuNCs have insignificant effect on the native structure of BSA indicating the overall 3D structure of protein remains almost unaltered in presence of. CD spectroscopic study has revealed that TA-CuNCs, Chitosan-CuNCs have noticeable effect on the secondary structure of BSA but Cys-CuNCs has insignificant effect on it. The observation of new interaction pathway, different to that of "protein-corona", during the interaction of relatively cheaper and biocompatible CuNCs and BSA is an interesting finding of the current study in a sense that the outcome of the study is expected to encourage better design and application of NCs in various biological studies.

3.5. Appendix

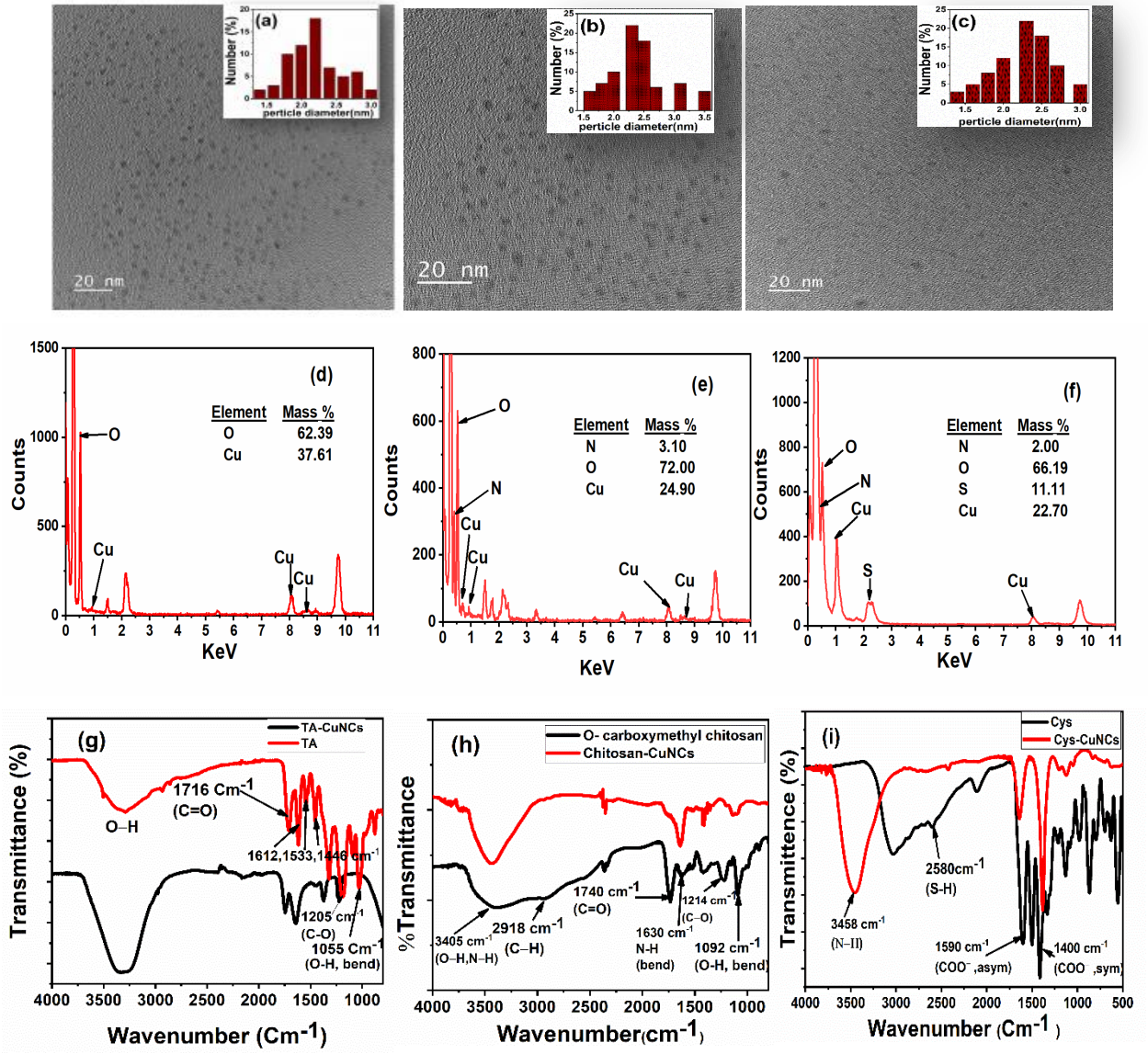

Figure APX3.1. (a,b,c)TEM images (inset shows particle size distribution plot), (d,e,f) EDAX spectra and (g,h,i) FTIR spectra of (a) TA-CuNCs (b) Chitosan-CuNCs and (c) Cys-CuNCs along with their corresponding ligand.

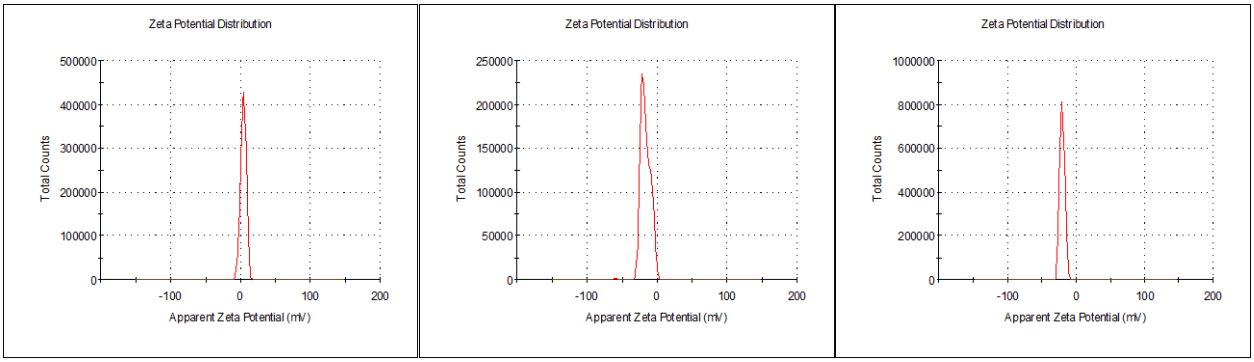

Figure APX3.2. Zeta potential graphs for the (a) TA-CuNCs, (b) Chitosan-CuNCs and (c) Cys-CuNCs in aqueous solution.

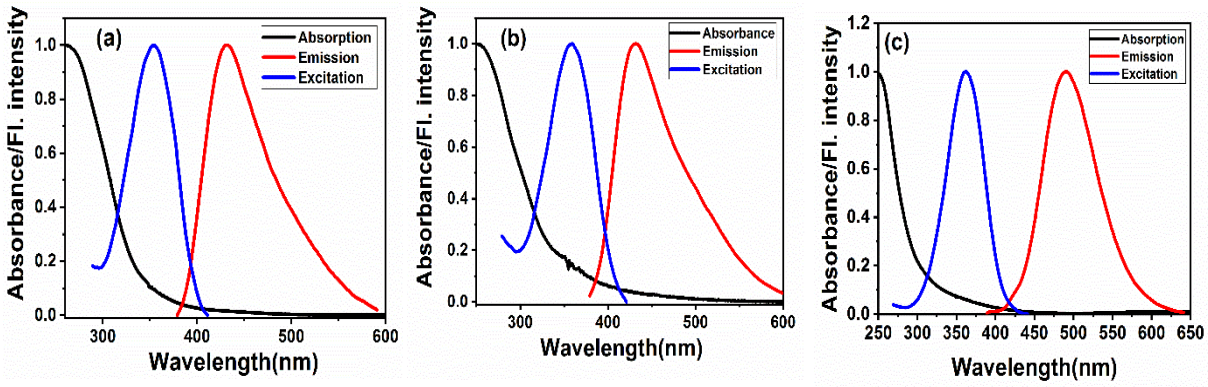

Figure APX3.3. Normalized absorption (black curve), emission (red curve) and excitation spectra (blue curve) of aqueous solution (a) TA-CuNCs (b) Chitosan-CuNCs and (c) Cys-CuNCs

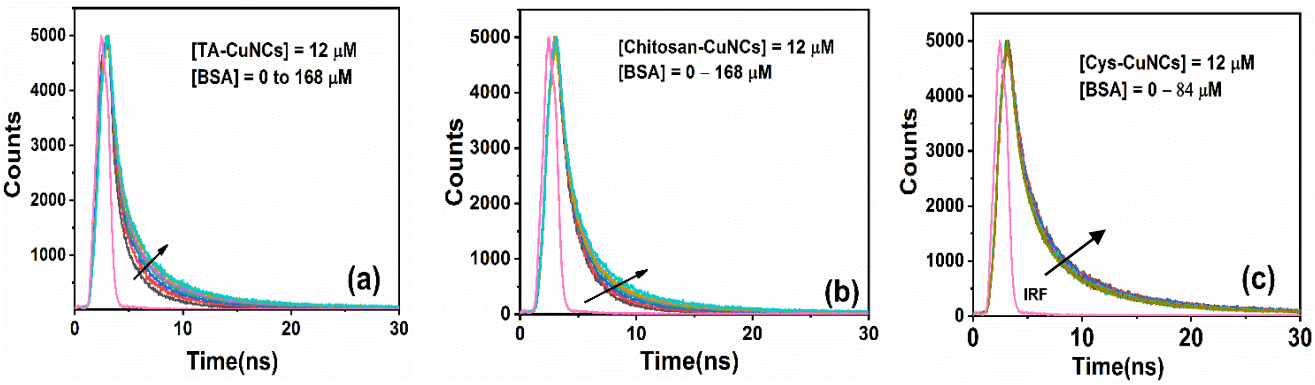

Figure APX3.4. Time resolved fluorescence decay curve of (a) TA-CuNCs (b) Chitosan-CuNCs and (c) Cys-CuNCs in absence and presence of BSA. The excitation wavelength is 375 nm.

Table APX3.1. Fluorescence decay parameters of CuNCs in phosphate buffer of PH = 7.4 with gradual addition of BSA.[a] (The excitation wavelength is 375 nm)

TA-CuNCs							
[BSA](μM)	α_1	τ_1	α_2	τ_2	α_3	τ_3	$\langle\tau_{avg}\rangle$
0	84	0.18	13	1.33	3	3.30	0.48
12	78	0.26	19	1.67	4	5.08	0.69
24	78	0.32	20	1.94	2	6.56	0.79
48	74	0.40	21	2.33	4	7.40	1.09
72	72	0.45	23	2.45	4	8.15	1.25
120	71	0.46	24	2.56	4	8.55	1.33
156	69	0.49	26	2.63	5	8.58	1.43
Chitosan CuNCs							
[BSA](μM)	α_1	τ_1	α_2	τ_2	α_3	τ_3	$\langle\tau_{avg}\rangle$
0	61	0.34	34	1.65	4	3.63	0.93
12	64	0.34	31	1.68	5	4.26	0.96
24	66	0.49	31	2.12	3	6.66	1.20
48	65	0.52	31	2.26	3	7.43	1.31
72	61	0.54	34	2.15	5	6.93	1.42
120	68	0.69	28	2.67	4	8.69	1.57
156	65	0.58	30	2.61	5	8.90	1.62
Cys-CuNCs							
[BSA](μM)	α_1	τ_1	α_2	τ_2	α_3	τ_3	$\langle\tau_{avg}\rangle$
0	62	0.86	31	3.52	6	10.9	2.32
2.4	52	0.73	39	2.79	9	9.19	2.34
4.8	62	0.89	37	3.41	6	11.46	2.44
12	55	0.83	35	3.01	9	9.96	2.49
24	57	0.9	34	3.2	8	11.18	2.53
48	53	0.98	38	3.45	9	11.57	2.83

[a]concentration of CuNCs are in μM, α are expressed in % scale and τ values (±5 %) are in ns unit

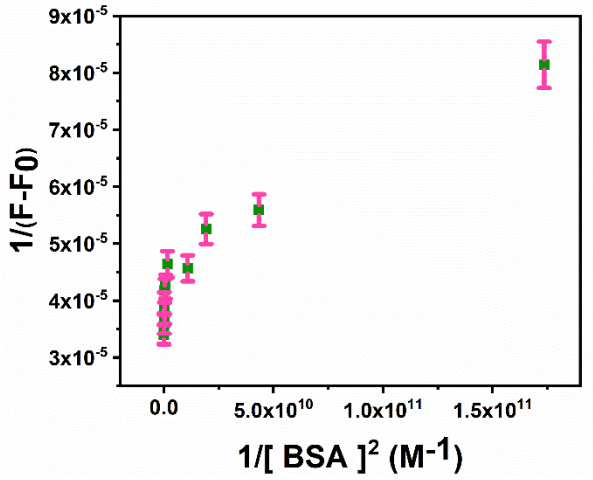

Figure APX3.5. Benesi-Hildebrand double reciprocal plot to determine the stoichiometric association of Cys-CuNCs to BSA for 2:1 (BSA: CuNCs) binding.

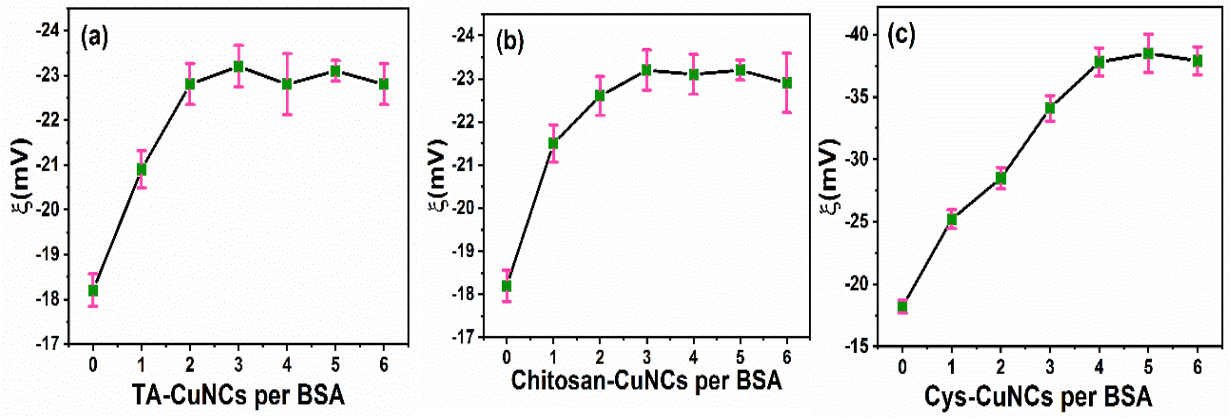

Figure APX3.6. Zeta potential of (a)TA-CuNCs-BSA system (b) Chitosan- CuNCs-BSA system and (c) Cys-CuNCs-BSA system at different ratios of CuNCsNCs to protein.

Table APX3.2. The associated diffusion parameters[a] of (CuNCs+BSA) systems with increasing concentration of BSA as obtained from FCS study.[a]

CuNCs (30 nM)	BSA (nM)	τ_D(μs)	R_H(nm)
TA-CuNCs	0	39.7	0.61
	30	48.5	0.80
	60	71.9	1.19
	100	73.9	1.23
	150	75.8	1.26
	0	36.8	0.66

Chitosan-CuNCs	30	46.4	0.77
	60	56.0	0.93
	100	73.8	1.22
	150	75.3	1.24
Cys-CuNCs	0	38	0.63
	30	47	0.79
	60	53.6	0.89
	100	66.9	1.11
	150	68.7	1.18

a ± 5%

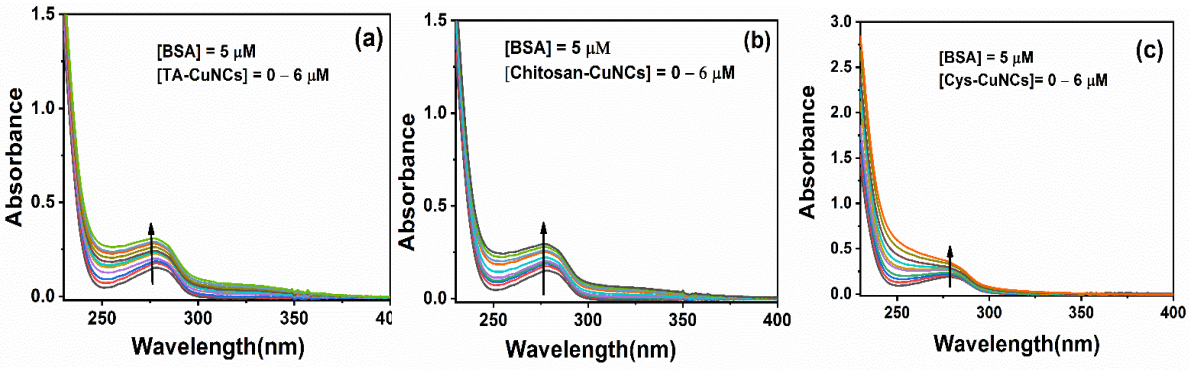

Figure APX3.7. UV-vis absorption spectra of BSA upon gradual addition of (a) TA-CuNCs (b) Chitosan-CuNCs and (c) Cys-CuNCs.

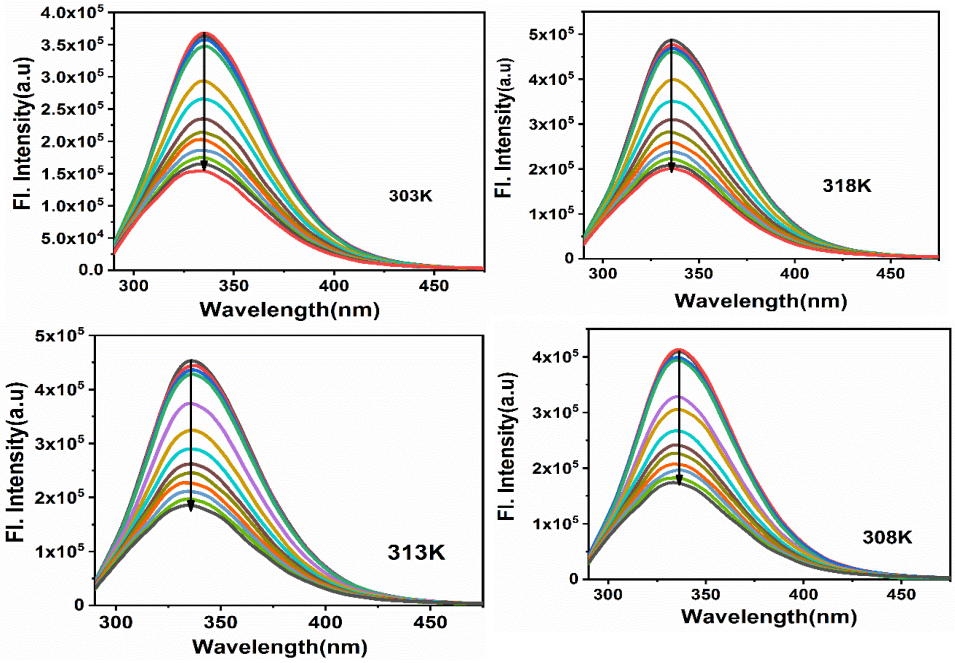

Figure APX3.8a. Fluorescence emission spectra of BSA with gradual addition of TA-CuNCs (λ_{ex} = 280 nm). Temperature has been mentioned in each cases.

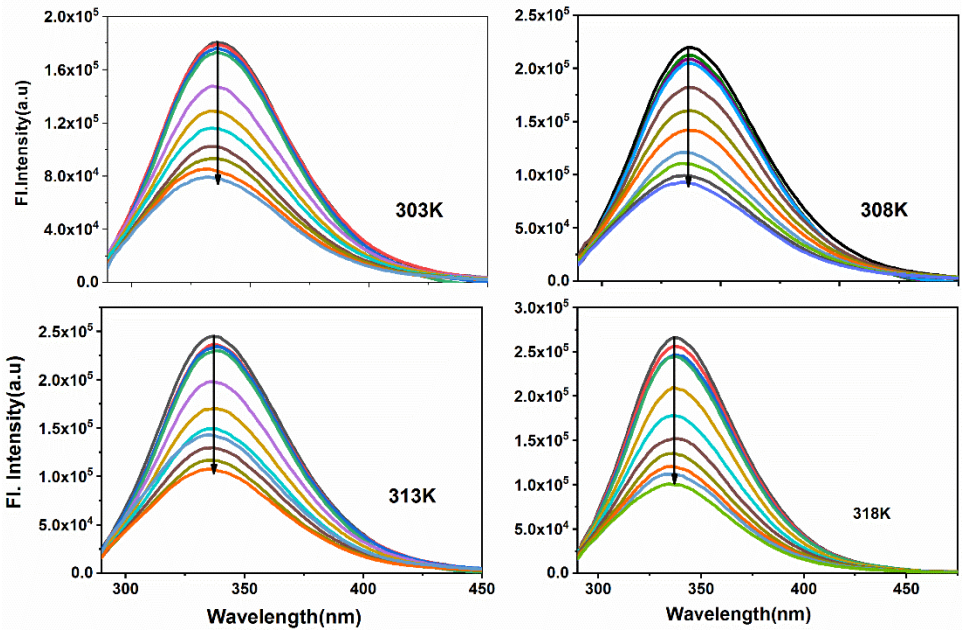

Figure APX3.8b. Fluorescence emission spectra of BSA (5 μM) with gradual addition of chitosan-CuNCs (0 – 6 μM) (λex = 280 nm). Temperature has been mentioned in each cases.

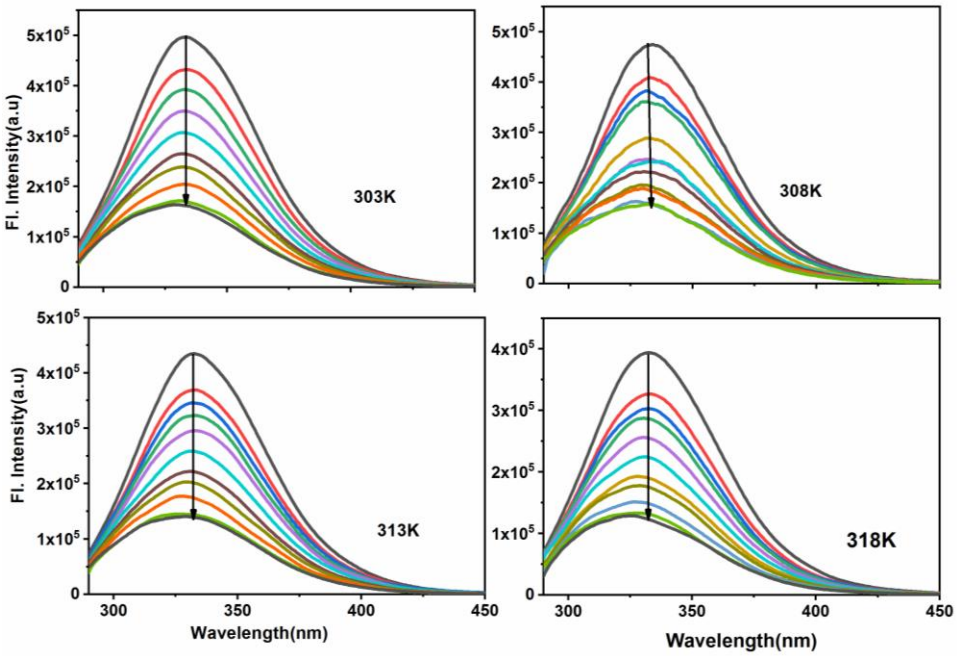

Figure APX3.8c. Fluorescence emission spectra of BSA (5 μM) with gradual addition of Cys-CuNCs (0 – 6 μM) (λ_{ex} = 280 nm). Temperature has been mentioned in each cases.

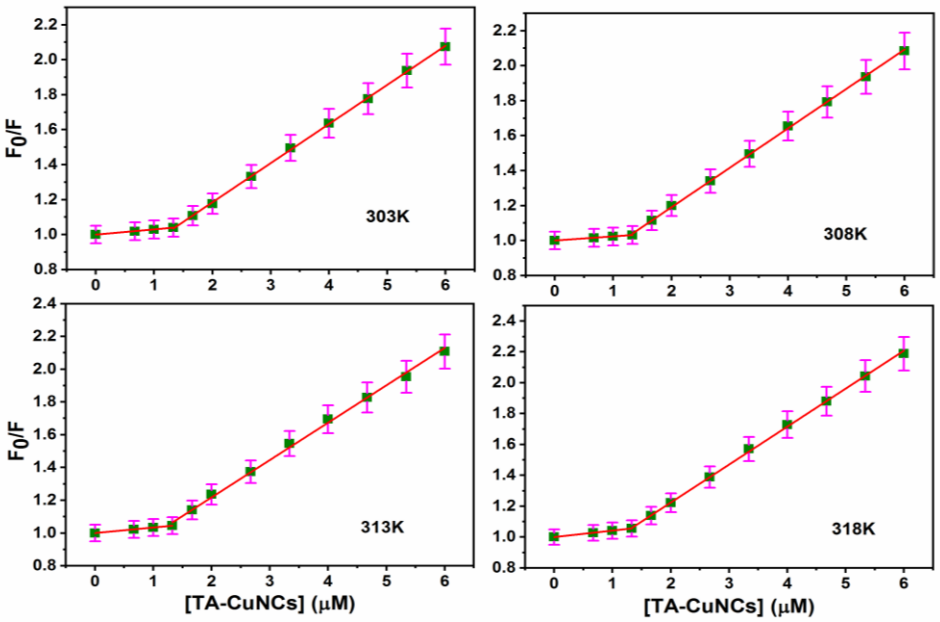

Figure APX3.9a. Stern-Volmer plots for quenching of BSA fluorescence by TA-CuNCs at different temperature marked at each figure.

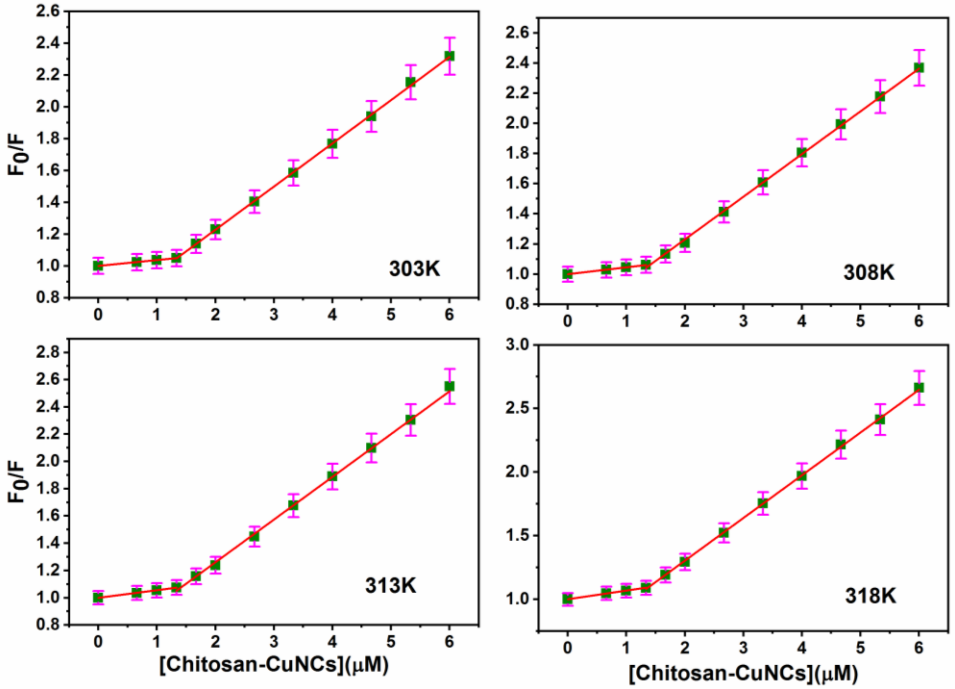

Figure APX3.9b. Stern-Volmer plots for quenching of BSA fluorescence by Chitosan-CuNCs at different temperature marked at each figure.

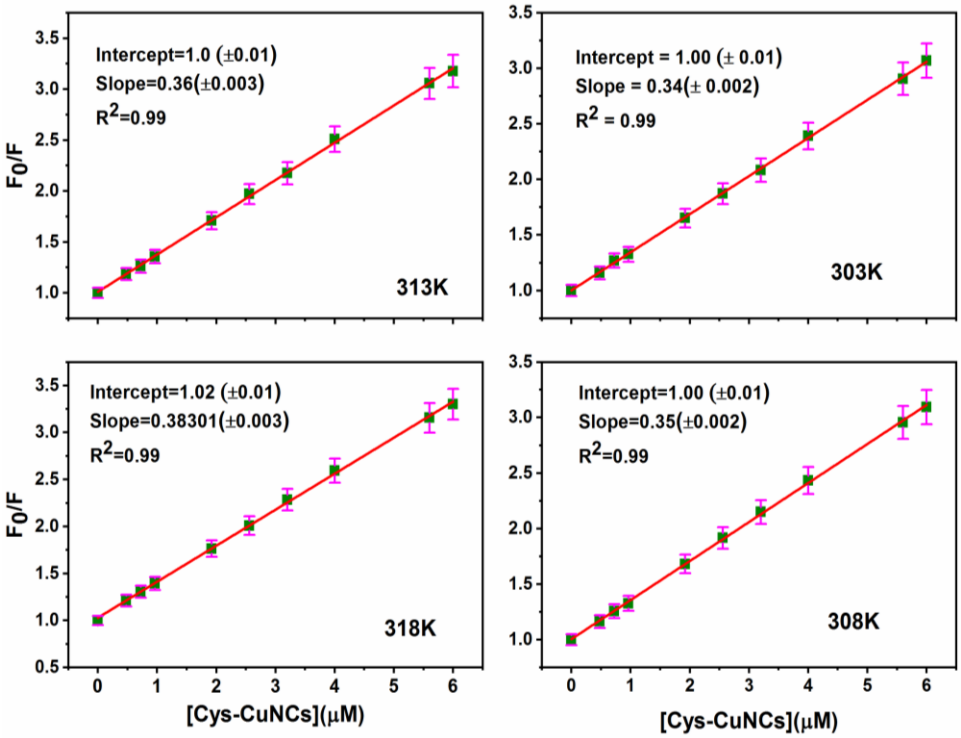

Figure APX3.9c. Stern-Volmer plots for quenching of BSA fluorescence by Cystein-CuNCs at different temperature marked at each figure.

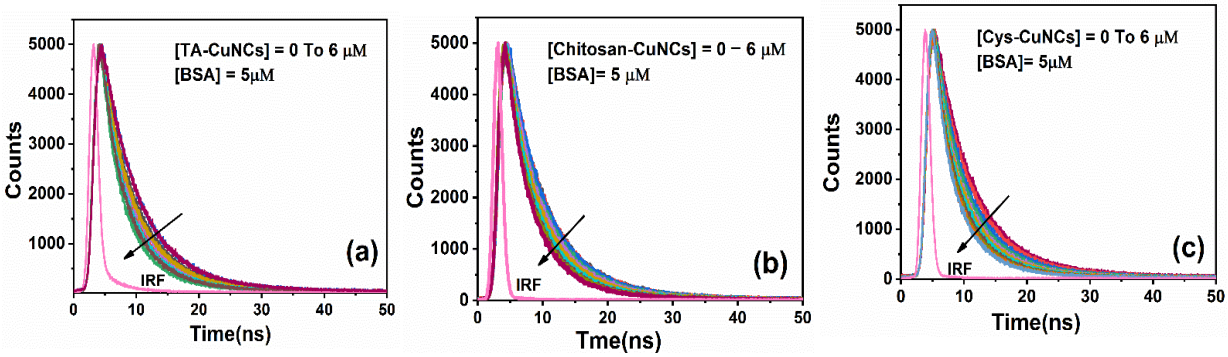

Figure APX3.10. Time resolved fluorescence decay curve of BSA in absence and presence of (a) TA-CuNCs (b) Chitosan-CuNCs and (c) Cys-CuNCs, recorded using excitation wavelength of 280 nm.

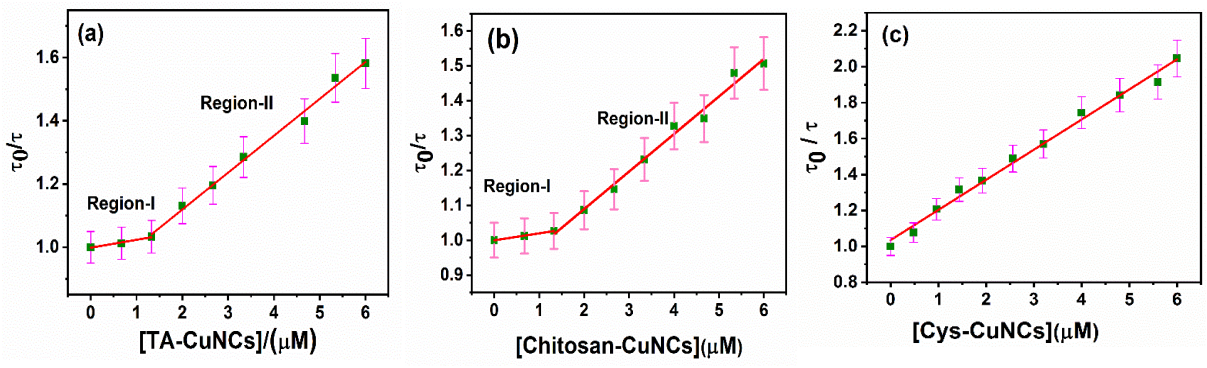

Figure APX3.11. Stern-Volmer plots for lifetime quenching of BSA protein by (a) [TA-CuNCs] (b) [Chitosan- CuNCs] and (c) [Cys-CuNCs].

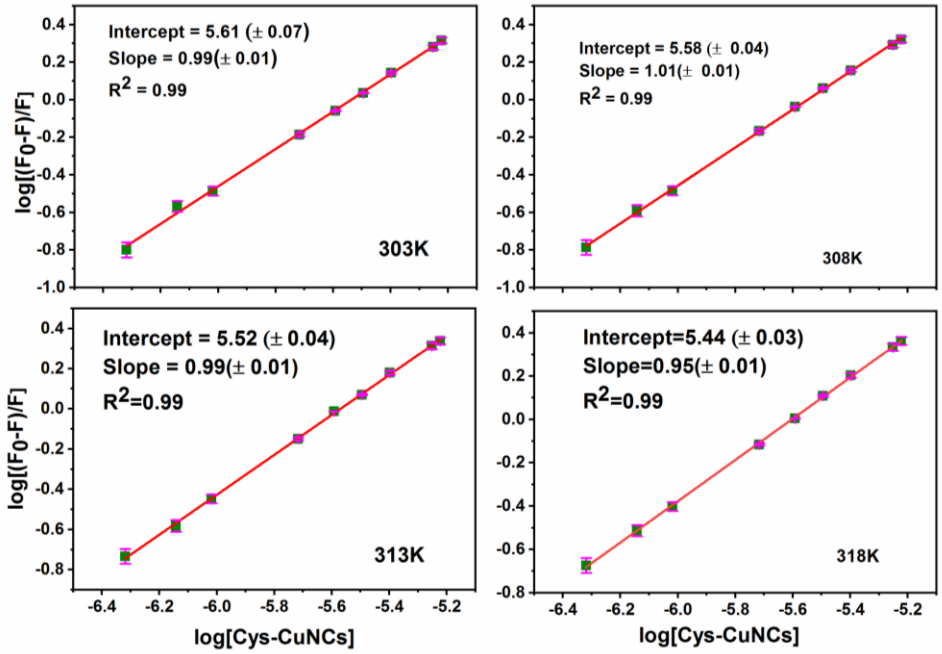

Figure APX3.12. Double logarithm plot for the binding of Cys-CuNCs with BSA at various temperature marked at each figure.

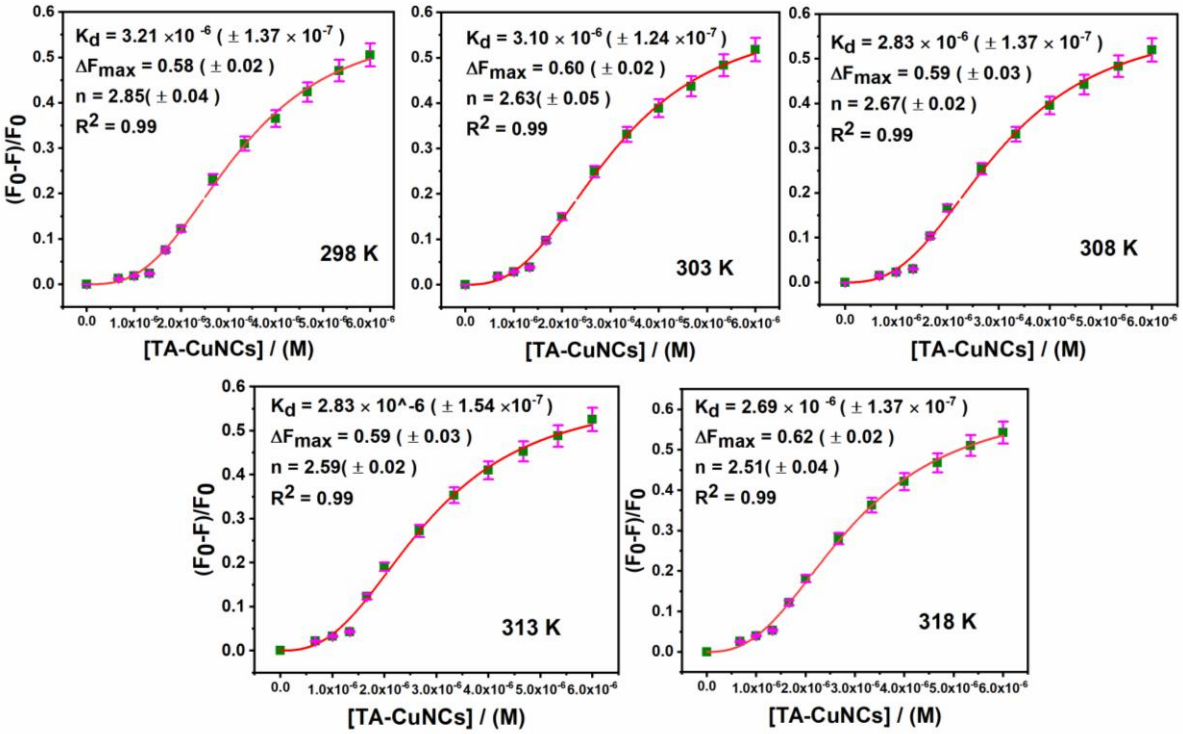

Figure APX3.13a. Hill plot for the fluorescence quenching of BSA with TA- CuNCs at various temperature marked at each figure.

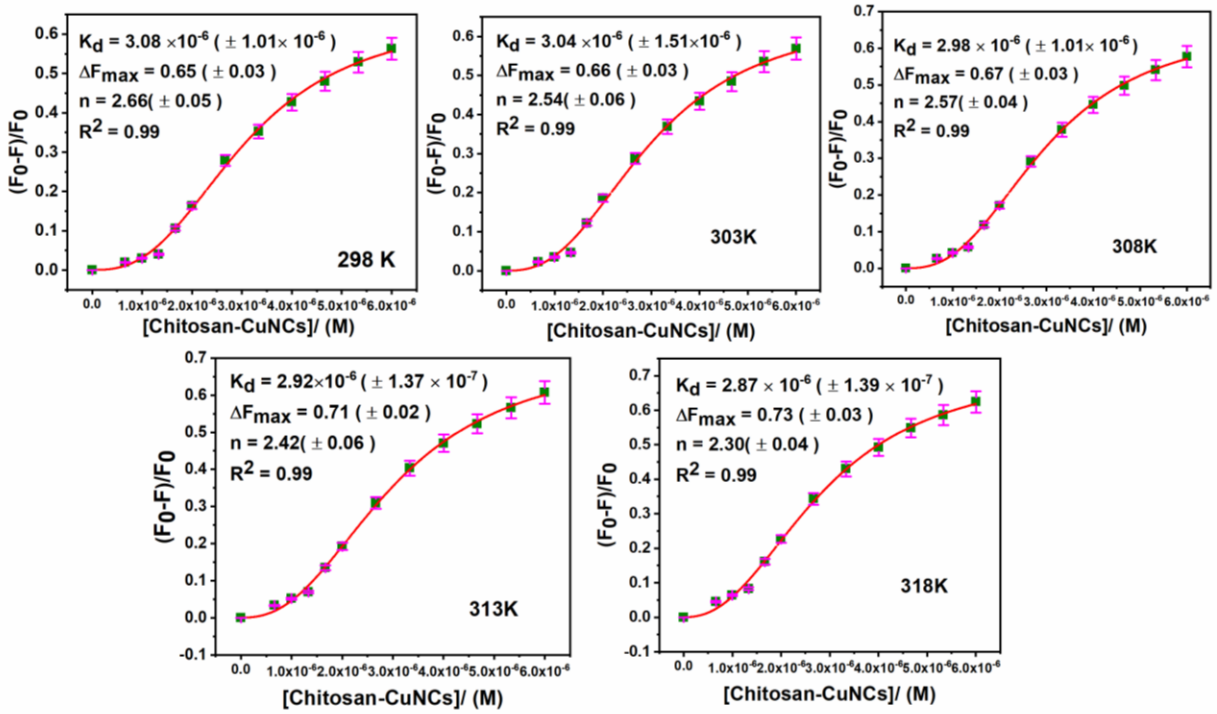

Figure APX3.13b. Hill plot for the fluorescence quenching of BSA with Chitosan- CuNCs at various temperature marked at each figure.

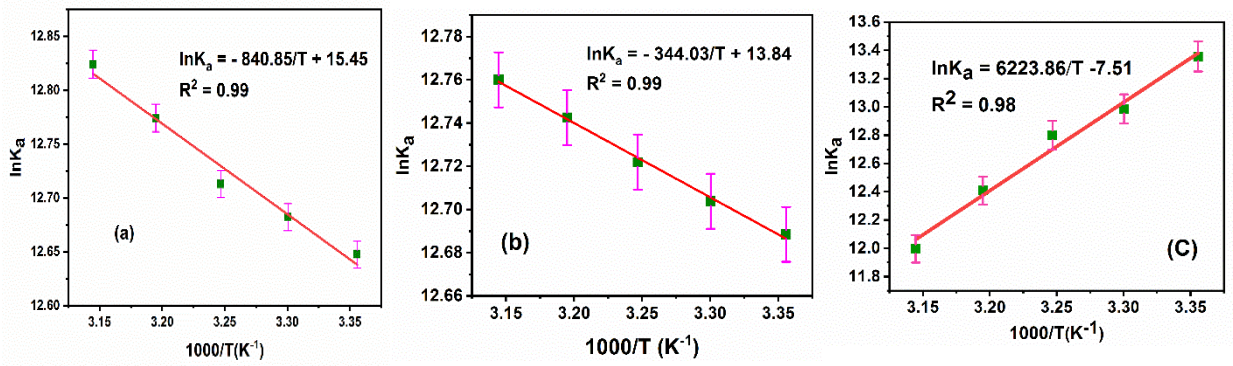

Figure APX3.14. van't Hoff plots of Cu NCs-BSA system: (a) TA-CuNCs BSA system (b) Chitosan-CuNCs BSA system and (c) Cys-CuNCs BSA system.

Table APX3.3. Fluorescence decay parameters of BSA in phosphate buffer of PH = 7.4 with gradual addition of (a) TA-CuNCs (b) Chitosan-CuNCs and (c) Cys-cuNCs to the solution (The excitation wavelength is 280 nm) [a]

[TA-CuNCs]	α_1	τ_1	α_2	τ_2	$\langle\tau\rangle$
0	35	3.65	65	6.90	5.76
0.67	36	3.51	64	6.85	5.65
1.33	26	2.81	74	6.63	5.64
2.00	33	3.52	67	6.84	5.57
2.67	33	3.27	67	6.83	5.52
3.34	30	2.63	70	6.64	5.44
4.00	32	2.45	68	6.45	5.17
4.67	38	2.20	62	6.26	4.70
5.34	46	2.10	54	5.92	4.17
6.00	55	2.24	44	5.86	3.84
[Chitosan-CuNCs]	α_1	τ_1	α_2	τ_2	$\langle\tau\rangle$
0	74	4.80	26	8.64	5.80
0.67	82	5.09	18	9.52	5.76
1.33	76	4.86	24	8.83	5.80

2.00	57	3.40	43	7.43	5.48
2.67	62	3.79	38	7.41	5.18
3.34	58	3.36	42	7.02	4.91
4.00	61	3.05	39	6.79	4.49
4.67	70	3.25	30	7.08	4.40
5.34	71	3.07	29	6.93	4.17
6.00	73	2.93	27	6.81	3.97
[Cys-CuNCS]	α_1	τ_1	α_2	τ_2	$<\tau>$
0	39	3.90	61	7.02	5.80
0.48	21	2.27	79	6.22	5.39
0.96	30	2.14	70	5.95	4.81
1.44	35	1.99	65	5.71	4.41
1.92	35	1.85	65	5.54	4.25
2.56	38	1.65	62	5.29	3.90
3.20	41	1.61	59	5.15	3.70
4.00	45	1.43	55	4.91	3.33
4.80	48	1.36	52	4.79	3.15
5.60	52	1.44	48	4.77	3.03
6.00	54	1.32	46	4.63	2.84

[a] concentration of CuNCs are in μM, α are expressed in % scale and τ values (±5 %) are in ns unit

Table APX3.4. Binding Constant (K_a) and Thermodynamic Parameters and no. of binding sites (N) for the Binding of TA-CuNCs, Chitosan-CuNCs and Cys-CuNCs with BSA at 298 K Obtained by ITC Experiment. [a]

CuNCs	*Ka* (10^6) (M^{-1})	*ΔH* (kJ mol^{-1})	*ΔS* (JK^{-1} mol^{-1})	*ΔG* (kJ mol^{-1})	N
TA-CuNCs	K_1 = 5.89 ± 0.46	ΔH_1 = 116.34±3.40	ΔS_1 = 520.80	ΔG = -38.85	2
	K_2 = 1.47 ± 0.16	ΔH_2 = 90.72± 2.58	ΔS_2 = 424.20	ΔG = -35.69	
Chitosan-CuNCs	K_1 = 1.90 ±0.35	ΔH_1 = 92.61± 1.09	ΔS_1 = 432.60	ΔG = -36.30	2
	K_2 = 9.20±0.48	ΔH_2 = 65.94 ± 3.65	ΔS_2 = 362.88	ΔG = -42.19	
Cys-CuNCs	9.16 ± 2.71	-102.06 ± 1.32	-211.60	ΔG = -39.15	4

[a] ± 5%

Table APX3.5. Variation in the Secondary Structure (α-Helical) of BSA with increasing Amount of CuNCs.

[CuNCs]/μM	TA-CuNCs	Chitosan-CuNCs	Cys-CuNCs
0	56.5	56.5	57.3
0.2	58.4	60.0	57.9
0.6	60.1	63.9	60.3
1.5	63.3	64.8	62.1
2.6	64.5	65.2	59.8

References

1. Zhang, L.; Wang, E. *Nano Today* **2014**, 9, 132–157.
2. Jin, R. C.; Zeng, C.; Zhou, M.; Chen, Y. *Chem. Rev.* **2016**, 116, 10346-10413.
3. Goswami, N.; Zheng, K.Y.; Xie, J.P. *Nanoscale* **2014**, 6, 13328–13347.
4. Choi, S.; Dickson, R.M.; Yu, J. *Chem. Soc. Rev.* **2012**, 41,1867–1891.
5. Guo, Y.; Cao, F.; Lei, X.; Mang, L.; Cheng, S.; Song, J. *Nanoscale* **2016**, 8, 4852–4863.
6. Chuang, C-H.; Porel, M.; Choudhury, R.; Burda, C.; Ramamurthy, V. *J. Phys. Chem. B*, **2018,** 122, 328−337.
7. Chen, L.Y.; Wang, W.C.; Yuan, H.; Chang, H.T. *Anal. Chem.* **2015**, 87, 216-229.
8. Yan, M.; Zhang, Y.; Xu, K.; Fu, T.; Qin, H. *Toxicology* **2011,** 282, 94-103.
9. Derfus, A.M.; Chan, W.C.W.; Bhatia, S.N. *Nano Lett.* **2004,** 4, 11-18.
10. Morteza, M.; L. Iseult, L.; Mohammad, R.E.; Marco, P.M.; Francesca, B.B.; Sophie, L. *Chem. Rev.* **2011**, 111, 5610–5637.
11. Casals, E.; Pfaller, T.; Duschl, A.; Oostingh, G.J.; Puntes, V. *ACS Nano* **2010**,4, 3623-3632.
12. Huang, R.X.; Carney, R.P.; Ikuma, K.; Stellacci, F.; B. L. T. Lau, B.L.T. *ACS Nano* **2014**, 8, 5402-5412.
13. Cui, M.H.; Liu, R.X.; Deng, Z.Y.; Ge, G.L.; Y. Liu,Y.; Xie, L. M. *Nano Res.* **2014**, 7, 345-352.
14. Lynch, I.; Dawson, K.A. *Nano Today* **2008**, 3, 40-47.
15. Ge, C.C.; Tian, J.; Zhao, Y.L.; Chen, C.Y.; Zhou, R.H.; Chai, Z. F. *Arch.Toxicol.* **2015**, 89, 519-539.
16. Lundqvist, M.; Stigler, J.; Elia, G.; Lynch,I.; Cedervall, T.; Dawson, K. A. *PNAS* **2008**, 105, 14265–14270.

17. Yin, M.M.; Chen, W.Q.; Lu, Y.Q.; Han, J.Y.; Liu, Y.; Jiang, F.L. *Nanoscale* **2020**, 12, 4573–4585.
18. Kopp, M.; Kollenda, S.; Epple, M. *Acc. Chem. Res.* **2017**, 50, 1383-1390.
19. Boselli, L.; Polo, E.; Castagnola, V.; K. A. Dawson, K. A. *Angew. Chem. Int. Ed.* **2017**, 56, 4215–4218.
20. Piella, J.; Bastus, G.N.; Puntes, V. *Bioconjugate Chem.* **2017**, 28, 88-97.
21. Huang, S.; Qiu, H.N.; Liu, Y.; Huang, C.S.; Sheng, J.R.; Su, W.; Xiao, Q. *Colloids and Surfaces B: Biointerfaces* **2015**, 136, 955-962.
22. Lai, L.; J.C.; Xu, Z.Q.; Ge, Y.S.; Jiang, F.L.; Liu, Y. *J. Membr. Biol.* **2015**, 248, 727-740.
23. Elward, J.M.; Irudayanathan, F.J.; Nangia, S.; Chakraborty, A. *J. Chem. Theory Comput.* **2014**, 10, 5224-5228.
24. Lai, L.; Lin, C.; Xu, Z.Q.; Han, X.L.; Tian, F.F.; Mei, P.; Li, D.W.; Jiang, F.L.; Ge, Y.S.; Zhang, Y.Z.; Liu, Y. *Spectrochim. Acta Part A*, **2012**, 97, 366-376.
25. Ashraf, S.; Park, J.; Bichelberger, M.A.; Kantner, K.; Hartmann, R.; Maffre, P.; A. H. Said, A.H.; Feliu, N.; Lee, J.; Lee, D.; Nienhaus, G.U.; S. Kim, S.; Parak, W.J. *Nanoscale* **2016**, 8, 17794-17800.
26. Wang, H.; Shang, L.; Maffre, P.; Hohmann, S.; Kirschhöfer, F.; Brenner-Weiβ, G.; Nienhaus, G. U. *Small* **2016**, *12*, 5836-5844.
27. Idowu, M.; Lamprecht, E.; Nyokong, T. *J. Photochem. Photobio. A*, **2008**, *198*, 7-12.
28. Zhang, W.; Zhang, Q.; Wang, F.; Yuan, L.; Xu, Z.; Jiang, F.; Liu, Y. *Luminescence* **2015**, *30*, 397-404.
29. Prasanth, S.; Raj, R. D.; Vineeshkumar, T. V.; Thomas, R. K.; Sudarsanakumar, C. *RSC Adv.* **2016**, *6*, 58288–58295.
30. Mahmoudi, M.; Lyunch, I.; Ejtehadi, M. R.; Monopoli, M. P.; Bombelli, F, B.; Laurent, S. *Chem. Rev.* **2011**, *111*, 5610–5637.
31. Sasidharan, A.; Riviere. J. E.; Monteiro-Riviere, N. A. *J. Mater. Chem. B.* **2015,** *3*, 2075-2082.
32. Yin, M. M.; Dong, P.; Chen, W. Q.; Xu, S. P.; Yang, L.Y.; Jiang, F.L.; Liu, Y. *Langmuir* **2017**, *33*, 5108-5116.
33. Shang, L.; Dörlich, R. M.; Trouillet, V.; Bruns, M.; Nienhaus, G. U. *Nano Research* **2012**, *5*, 531-542.
34. Das, N. K.; Chakraborty, S.; Mukherjee. M.; Mukherjee, S. *ChemPhysChem*. **2018**, *19*, 2218– 2223.
35. Muraca, F.; Boselli, L.; Castagnola, V.; Dawson, K. A. *ACS Appl. Bio Mater*. **2020**, 3, 3800−3808.
36. Chen, W. Q .; Yin, M. M.; Song, P. J .; He, X. H.; Liu, Y.; Jiang, F. L. *Langmuir* **2020**, 36, 6447−6457.
37. Huang, S.; Qiu, H.; Lu, S.; Zhu, F.; Xiao, Q. *J. Hazard. Mater*. **2015**, *285*, 18-26.
38. Xu, Z. Q.; Yang, Q. Q.; Lan, J. Y.; Zhang, J. Q.; Peng, W.; Jin, J. C.; Jiang, F. L.; Liu, Y. *J. Hazard. Mater*. **2016**, *301*, 242-249.

39. Zuo, G.; Kang, S. G.; Xiu, P.; Zhao, Y.; Zhou, R. *Small* **2013,** *9*, 1546-1556.
40. Moriyama, Y.; Watanabe, E.; Kobayashi, K.; Harano, H.; Inui, E.; Takeda, K. *J. Phys. Chem. B.* **2008**, *112*, 16585-16589.
41. Dutta, P.; Sen, P.; Halder, A.; Mukherjee, S.; Sen, S.; Bhattacharyya, K. Solvation dynamics in a protein–surfactant complex. *Chem. Phys. Lett*. **2003**, *377*, 229-235.
42. Chakraborty, A.; Seth, D.; Setua, P.; Sarkar, N. *J. Phys. Chem. B.* **2006**, 110, 16607-16617.
43. Duggan, E. L.; Luck, J. M. *J. Biol. Chem*. **1948**, *172*, 205-20.
44. Jiao, M.; Li, H. T.; Chen, J.; Minton, A. P.; Liang, Y. *J. Biophys*. **2010**, *99*, 914-923.
45. Sakata, S.; Inoue, Y.; Ishihara, K. *Langmuir* **2014**, *30*, 2745-2751.
46. Guo, Y.; Cao, F.; Lei, X.; Mang, L.; Cheng, S.; Song, J. *Nanoscale* **2016,** *8*, 4852-4863.
47. Shi, Y.; Luo, S.; Ji, X.; Liu, F.; Chen, X.; Huang, Y.; Dong. L.; Wang, L. *Dalton Trans*. **2017**, *46*, 14251-14255.
48. Patra, S.; Santosh, K.; Pabbathi, A.; Samanta, A. *RSC Adv*. **2012**, *2*, 6079-6086.
49. Pramanik, S.; Banerjee, P.; Sarkar, A.; Bhattacharya, S. C. *Luminescence* **2008**, *128*, 1969-1974.
50. Zhao, X.; Sheng, F.; Zheng, J.; Liu, R. *J. Agric. Food Chem*. **2011**, *59*, 7902-7909.
51. Jhonsi, M. A.; Kathiravan, A.; Renganathan, R. *Colloids Surf B Bioterfaces* **2009**, *72*, 167-172.
52. Cao, H.; Chen, Z.; Zheng, H.; Huang, Y. *Biosens Bioelectron.* **2014**, *62*, 189–195.
53. Cheng, L. C.; Huang, J. H.; Chen, H. M.; Lai, T.C.; Yang, K.Y.; Liu, R. S.; Hsiao, M.; Chen, C.H.; Her, L.J.; Tsai, D. P. *J. Mater. Chem.* **2012**, *22*, 2244-2253.
54. Zhou, T.; Xu, W.; Yao, Q.; Zhao, T.; Chen, X. *Appl. Fluoresc*. **2015**, 3, 044002.
55. Sahu, D. K.; Sahu, K. *J. Photochem. Photobiol. A* **2017**, 347, 17-25.
56. Lin, Z.; Slee, T. Mingos, D. M. P. *Chem. Phys*. 1990, **142**, 321−334.
57. Wei, W.; Lu, Y.; Chen, W.; Chen, S. *J. Am. Chem. Soc*. **2011,** 133, 2060-2063.
58. Negishi, Y.; Nobusada, K.; Tsukuda, T. *J. Am. Chem*. Soc. **2005**,127, 5261−5270.
59. Link, S.; Beeby, A.; FitzGerald, S.; El-Sayed, M. A.; Schaaff, T. G.; Whetten, R. L. *J. Phys. Chem. B* **2002**, 106, 3410−3415.
60. Stamplecoskie, K. G.; Kamat, P. V. *J. Am. Chem. Soc*. **2014**, 136,11093−11099.
61. Wu, Z.; Jin, R. *Nano Lett.* **2010**, 10, 2568-2573.
62. Lin, Y.; Charchar, P.; Christofferson, A. J.; Thomas, M. R.; Todorova, N.; Mazo, M. M.; Chen, Q.; Doutch, J.; Richardson,R.; Yarovsky, I.; Stevens, M. M. *J. Am. Chem. Soc*. **2018**, 140, 18217-18226.
63. Shang, L.; Brandholt, S.; Stockmar, F.; Trouillet, V.; Bruns, M.; Nienhaus, G. U. *Small* **2012**, 8, 661–665.
64. Gomez, S.; Philippot, K.; Colliere, V.; Chaudret, B.; Senocq, F.; Lecante, P. *Chem. Commun*. **2000**, 1945–1946.
65. Daniel, M. C.; Tsvetkova, I. B.; Quinkert, Z. T.; Murali, A.; De, M.; Rotello, V. M.; Kao, C. C.; Dragnea, B. *ACS Nano* **2010**, 4, 3853–3860.
66. Paramanik, B.; Kundu, A.; Chattopadhyay, K.; Patra, A. *RSC Adv*. **2014**, 4, 35059-35066.

67. Shang, L.; Nienhaus, G. U. *International Journal of Biochemistry & Cell Biology* **2016**, 75, 175-179.
68. Cedervall, T.; Lynch, I.; Lindman, S.; Berggård, T.; Thulin, E.; Nilsson, H.; Dawson, K. A.; Linse, S. *Proc. Natl. Acad. Sci. U. S. A.* **2007**, 104, 2050-2055.
69. Bhunia, S.; Kumar, S.; Purkayastha, P. *ACS Omega* **2019**, 4, 2523-2532.
70. Kundu, P.; Chattopadhyay, N. *Biophys. Chem.* **2018**, 240, 70-81.
71. McLendon, G. *Acc. Chem. Res.* **1998**, 21, 160-167.
72. Röcker, C.; Pötzl, M.; Zhang, F.; Parak, W. J.; Nienhaus, G. U. *Nat. Nanotechnol* **2009**, 4, 577-580.
73. Treuel, L.; Brandholt, S.; Maffre, P.; Wiegele, S.; Shang, L.; Nienhaus, G. U. *ACS Nano* **2014**, 8, 503-513.
74. Yadav, R.; Sengupta, B.; Sen, P. *J. Phys. Chem. B* **2014**, 118, 5428-5438.
75. Bussian, D. A.; Malko, A. V.; Htoon, H.; Chen, Y.; Hollingsworth, J. A.; Klimov, V. I. *J. Phys. Chem. C* **2009**, 113, 2241–2246.
76. Wang, J.; Mal, S.; Ren, J.; Yang1, J.; Qu,Y.; Ding, Zhang, D. M.; Yang, G. *Sensors and Actuators B: Chemical* **2018**, 267, 342-350.
77. Valstar, A.; Almgren, M.; Brown, W.; Vesilescu, M. *Langmuir* **2000**, 16, 922-927.
78. Shu, Y.; Liu, M.; Chen, S.; Chen, X.; Wang, J. *J. Phys. Chem. B* **2011**, 115, 12306-12314.
79. Lakowicz, J. R. *Principles of Fluorescence Spectroscopy*. Springer, *USA* **2006**; pp 55-472.
80. Valeur, B. *Molecular fluorescence: Principles and applications*. Wiley-VCH, Weinheim **2002.**
81. Das, A.; Roy, D.; De, C. K.; Mandal, P. K. *Phys. Chem. Chem. Phys.* **2018**, 20, 2251-2259.
82. Devatha, G.; Roy, S.; Rao, A.; Mallick, A.; Basu, S.; Pillai, P. P. *Chem. Sci*. **2017**, 8, 3879–3884.
83. Saha, S.; Majhi, D.; Bhattacharyya, K.; Preeyanka, N.; Datta, A.; Sarkar, M. *Phys. Chem. Chem. Phys*. **2018**, 20, 9523-9535.
84. Leckband, D. *Annu. Rev. Biophys. Biomol. Struct.* **2000**, 29, 1-26.
85. Islam, M. M.; Barik, S.; Sarkar, M. *J. Phys. Chem. B.* **2019,** 123 , 1512-1526.
86. Ross, P. D.; Subramanian, S. *Biochemistry* **1981**, 20, 3096-3102.
87. Connors, K. A. Wiley: New York, **1987;** pp 21-102.
88. Abou-Zied, O. K.; Al-Shihi, O. I. K. *J. Am.Chem. Soc.* **2008**, 130, 10793−10801.
89. Lasanta, T.; Lopez-de-Luzuriaga, J. M. L.; Monge, M.; Olmos, M. E.; Pascual, D. *Chem.Eur. J.* **2013**, 19, 4754−4766.
90. Anand, U.; Jash, C.; Mukherjee, S. *J. Phys. Chem. B* **2010**, 114, 15839–15845.
91. Santra, M. K.; Banerjee, A.; Rahaman, O.; Panda, D. *Int. J. Biol. Macromol*. **2005**, 37, 200-204.
92. Andrade, S. M.; Costa, S. M. B *Chem. Eur. J.* **2006**, 12, 1046 – 1057.
93. Lacerda, S. H. D. P.; Park, J. J.; Meuse, C.; Pristinski, D.; Becker, M. L.; Karim, A.; Douglas, J. F. *ACS Nano* **2010**, 4, 365-379.

94. De, M.; You, C. C.; Srivastava, S.; Rotello, V. M.; *J. Am. Chem. Soc.* **2007**, 129, 10747-10753.
95. Huang, R.; Lau, B. L.T. *Biochimica et Biophysica Acta*. **2016**, 1860, 945–956.
96. Ghosh, S.; Chakrabarty, S.; Bhowmik, D.; Kumar, G. S.; Chattopadhyay, N. *J. Phys. Chem. B* **2015**, 119, 2090-2102.
97. Sahoo, B. K.; Ghosh, K. S.; Bera, R .; Dasgupta, S. *Biopolymers* **2009**, 91, 108−119.
98. Paul, B. K.; Ray, D.; Guchhait, N. *Phys. Chem.Chem.Phys.* **2013**, 15, 1275-1287.
99. Chi, Z.; Liu, R. *Biomacromolecules* **2011**, 12, 203-209.
100. Ghosh, D.; Mondal, S.; Ghosh, S.; Saha, A. *J. Mater. Chem*. **2012**, 22, 699–706.
101. Wang, C.; Wang, C.; Xu, L.; Cheng, H.; Lin, Q.; Zhang, C. *Nanoscale* **2014**, 6, 1775–1781.
102. Yue, Y.; Li, H. W.; Liu, T.Y.; Wu, Y. *Vibrational Spectroscopy* **2014**, 74, 137–141.
103. Gospodarczyk, W.; Szutkowski, K.; Kozak, M. *J. Phys. Chem. B* **2014**, 118, 8652-8661.
104. Bhogale, A.; Patel, N.; Mariam, J.; Dongre, P.M.; Miotello, A.; Kothari, D.C. *Colloids and Surfaces B: Biointerfaces* **2014**, 113, 276–284.

CHAPTER 4

Copper Nanoclusters as an Effective Enzyme Inhibitor on the Activity Modulation of α-Chymotrypsin

The present work is undertaken with an objective to find out the suitability of CuNCs on the activity modulation of a model enzyme, α chymotrypsin (α-ChT). This work also aims to highlight the role of surface chemistry corresponding to CuNCs in modulating the activity of α-ChT. For this purpose, two different types of CuNCs having chemically different surface ligands, namely, cysteine (Cys) and tannic acid (TA), have been synthesized. Subsequently, the interaction of these CuNCs with α-ChT has been investigated by employing various spectroscopic techniques at both ensemble average and single molecule level. Results obtained from enzyme kinetics studies have revealed that both the CuNCs act as good enzyme inhibitors. While Cys-CuNCs almost completely diminish the activity of α-ChT through a competitive inhibition mechanism, TACuNCs partially reduce the enzyme activity through a noncompetetive inhibition mechanism indicating the vital role of surface ligand in the regulation of α-ChT activity. To gain a molecular level understanding of the enzyme−inhibitor interaction event, fluorescence spectroscopy, ITC measurements, fluorescence correlation spectroscopy (FCS), agarose gel electrophoresis, and circular dichroism (CD) spectroscopy are conducted. Thermodynamics results obtained from fluorescence titration experiment and ITC measurements have indicated that Cys-CuNCs follow a one-step binding process, whereas TA-CuNCs follow a two-step binding process. Moreover, FCS studies have provided evidence for the interaction of CuNCs with α-ChT at the single molecule level. Importantly, circular dichroism (CD) measurements have demonstrated that the basic structure of α-ChT remains almost unaltered in the presence of CuNCs. The outcome of the present study is expected to open up a possibility of using CuNCs as an effective nanoscale enzyme regulator for various biological applications.

4.1. Introduction

Life depends on a well-coordinated series of chemical reactions that are controlled by an important class of biomolecules, called enzymes. The activity of enzyme to an appropriate level offers an effective worth over several important physiological processes such as DNA replication, signal transduction, metabolism etc.[1-2] On the other hand, unusual activities of some enzymes can lead to a series of disorders.[3-5] So, it becomes extremely important to regulate the enzyme activity in therapeutics and pharmaceutics. This has encouraged the

scientific community to develop suitable regulators for the modulation of enzyme activity and to investigate the proper mechanism of inhibition. The regulation of enzyme activity can be done either by covalent modification or regulator binding which may be irreversible or reversible.[6] Irreversible regulators bind to the enzyme permanently through covalent bond whereas reversible regulators bind enzyme through hydrophobic interactions, electrostatic forces, hydrogen bonds, or van der Waals forces. Mainly the regulation type is classified as competitive inhibition, where binding of the inhibitor prevents binding of the substrate, non-competitive inhibition, where the inhibitor does not affect the binding of the substrate to the enzyme and uncompetitive inhibition, where inhibitor binding increases the affinity of the enzyme for the substrate.[6-8] The activity of enzymes can be tuned by controlling various factors such as sizes, shapes, and surface charges of both enzymes and regulators, as well as pH, temperature, and ionic strength of the environment.[9-11] It has been observed that there are several reports where synthetic small organic molecules have been used to inhibit the enzyme activity[12-15]. But these types of organic inhibitors face some limitations because of their complexity in synthesis, unstable nature and degradation in presence of some enzymes.[16-17] In recent time, researchers have made attempted to design and develop nano-regulators which offer a new pathway for regulating enzyme activity.[16, 18-33] These nano-regulators shows several advantages over small molecule ligands in terms of increasing photostability, a larger surface-to-volume ratio, presence of multivalent functionalities which can be attached on the materials to meet the structural complexity of proteins and so on. It is to be noted here that among these nano-regulators, carbon nanomaterials and metal nanoparticles are widely used as inhibitor for the regulation of enzyme activity. However, ultra-small (< 2nm) fluorescence metal nanoclusters (MNCs) has been less studied as nano-regulator although they have potential advantages over bigger size nanomaterial.[34] Due to having larger specific surface area and larger curvature the ultra-small MNCs are expected to be more effective nano-

regulator as compared to the aforementioned candidates. Moreover, these MNCs offer good fluorescence property and by exploiting their environment sensitive fluorescence behaviour one would be able to extract several useful information regarding MNC-enzyme interaction events.[34-39]

In this context it is relevant to mention here that recently, Jiang and co-workers [34] have demonstrated the allosteric inhibition of α-chymotrypsin (α-ChT) by gold nanoclusters (AuNCs). Recently, Zhou and co-workers[28] have demonstrated that 2-D Cu-MOF nanosheets can act as an effective enzyme inhibitor through competitive irreversible binding of the active site of α-ChT. In another work, Zhou and co-workers[27] have shown the effect of surface functional group density of carbon nanotube (CNTs) on the α-Chymotrypsin structure and activity alterations. De and co-workers[20] have investigated the efficiency of grapheme oxide in the modulation of activity of α-Chymotrypsin. In another work, Rotello and co-workers[25] have demonstrated that AuNPs tailored with various surface functionalities exhibit different inhibition ability on α-ChT activity. It is evident from the above discussion that most of the studies are done based on larger size metal nanoparticles and carbon nanoparticles but studies on ultra-small (< 2nm) fluorescence metal nanoclusters (MNCs) are limited. Therefore, investigating the potential of inexpensive, water soluble, biocompatible copper nanoclusters (CuNCs) as effective nano-regulator would be quite interesting. Since surface ligand is known to play vital role in modulating enzyme activity, the role of surface ligand over CuNCs for the same would be a worthwhile objective to pursue. To the best of our knowledge such studies on CuNCs are elusive. Again, it is known that the behaviour of nanoparticles in biological media is quiet complex and the ensuing interaction between nanoparticles and biomolecules does not happen in a straight forward manner. Therefore, it becomes a formidable challenge to understand the nitty-gritty of the nanoparticles-biomolecules interaction mechanism. Unless otherwise these issues are addressed, the

development of an effective nano-regulator for a target specific job will be difficult to conceptualise for the real time application.

Keeping in mind the above facts, we have synthesised two different CuNCs capped with two chemically different surface ligands i.e., Cys and TA and investigated the interaction of these CuNCs with of bovine α-chymotrypsin (α-ChT) at both ensemble average and single molecule level. α-ChT is an important digestive enzyme which is widely used as model enzyme for studying the activation inhibition of enzyme by nanomaterials due to having clear structure and catalytic mechanism[40-41]. Initially, results obtained from activity assays and inhibition kinetics studies have revealed that both the CuNCs can act as good enzyme inhibitor. As the information regarding the mechanistic aspect of CuNCs-enzyme interaction event is very less, we have focused our attention to comprehend this issue. So, to gain molecular level understanding of the enzyme-CuNCs interaction event, various techniques such as fluorescence spectroscopy, ITC measurements, fluorescence correlation spectroscopy (FCS), agarose gel electrophoresis and circular dichroism (CD) spectroscopy have been employed. Several interesting results have been emerged from the above studies which are expected to open up a new direction for the design and development of nano-inhibitor for the better application in biological systems. The structure of α-ChT in folded form, the chemical structure of the ligands used for synthesizing those CuNCs and the synthesis protocol of Cys-CuNCs and TA-CuNCS that are used in the present study are given in Scheme 4.1.

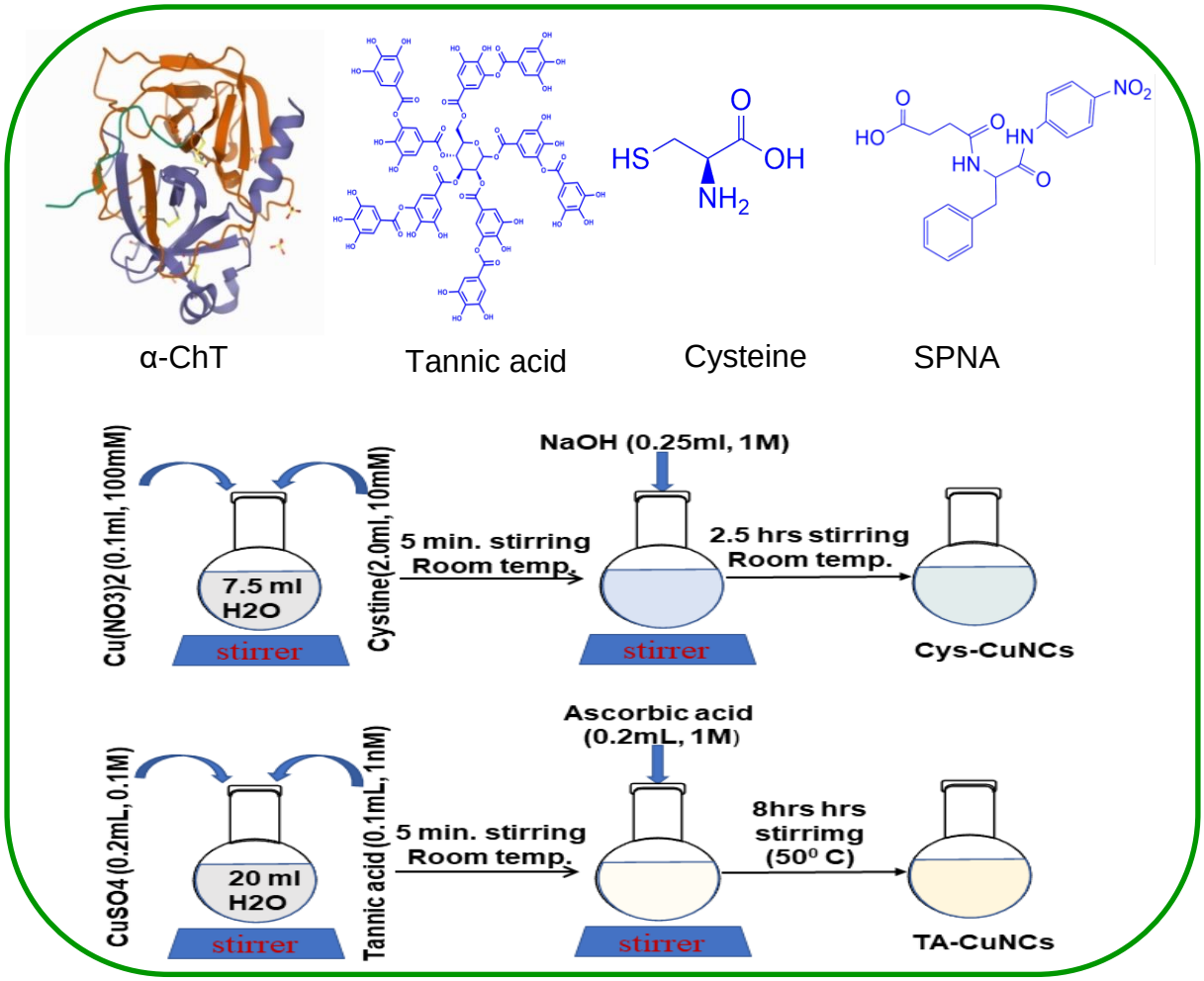

Scheme 4.1. Schematic representation of α-ChT in folded form (Taken from Protein Data Bank), chemical structures of the ligands (Tannic acid and Cysteine), substrate for enzymatic reaction (SPNA) and the synthesis protocol for Cys-CuNCs and TA-CuNCs.

4.2. Characterization of CuNCs

These synthesised CuNCs have been characterized by employing transmission electron microscopy (TEM), energy-dispersive X-ray analysis (EDAX), Fourier transform infrared (FTIR) spectroscopy, and steady-state absorption and emission spectroscopy. The sizes of the CuNCs were determined from TEM images (Figure 4.1a,b) and it was estimated to be 2.3 ± 0.5 and 2.2 ± 0.5 for Cys-CuNCs and TA-CuNCs respectively. The TEM images also reveal that the synthesized CuNCs were spherical in shape. Moreover, the high resolution TEM

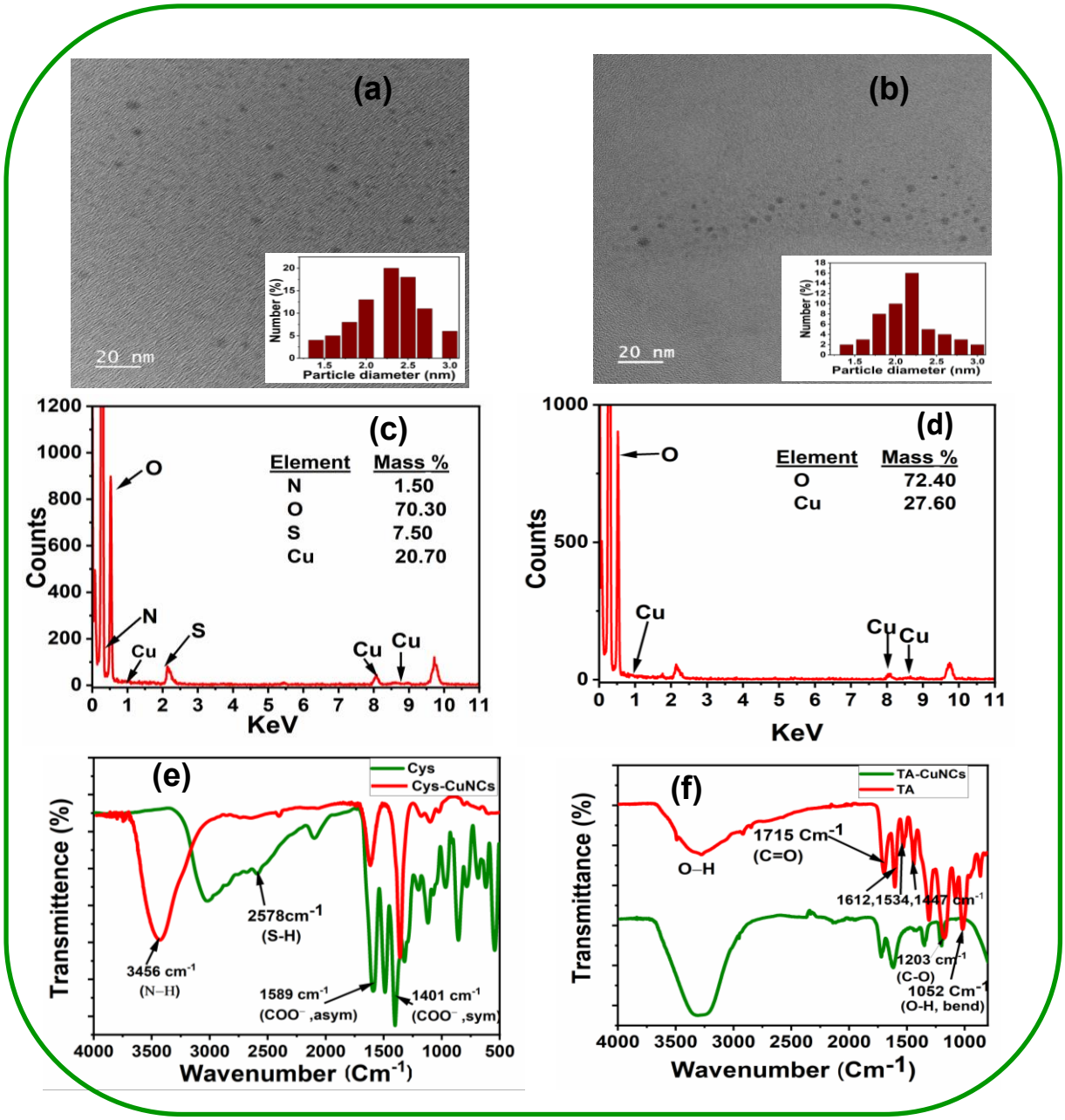

Figure 4.1. (a,b) TEM images (inset shows particle size distribution plot), (c,d) EDAX spectra and (e,f) FTIR spectra of Cys-CuNCs and TA-CuNCs respectively.

(HRTEM) images of these systems are provided in the Figure APX4.1. For elemental analysis of those systems EDAX measurement had been done (Figure 4.1a,b). As carbon coated gold grid had been used, a saturation peak corresponding to carbon had been observed in the EDAX spectra. FTIR study has been done to confirm the successful introduction of the ligand onto the surface of CuNCs. Figure 4.1e shows the FTIR spectra of Cys-CuNCs and

cysteine. It has been observed from the figure that the characteristic S−H stretching band (2578 cm^{-1}) is disappeared but the characteristic peaks of the −COOH group (asymmetric and symmetric stretching at 1589 and 1401 cm^{-1}, respectively) and $-NH_2$ (3000−3800 cm^{-1}, stretching) group remain unaltered in the FTIR spectrum of Cys-CuNCs, which confirms that cysteine ligands are attached onto the surface of CuNCs by the thiol moieties. The FTIR spectra of the TA and TA-CuNCs have been shown in the Figure 4.1f. Some specific major bands of TA are at 3300 cm^{-1} (O−H, stretching), 1715 cm^{-1} (C=O, stretching), 1203 cm^{-1} (C−O, stretching), and 1052 cm^{-1} (O−H, bending). It can be seen from the FTIR spectrum of TA-CuNCs that the O−H bending and C−OH stretching vibration of tannic acid are disrupted due to the attachment of TA on the surface of CuNCs as evidenced from the reduced intensity and shifting of the bands. The absorption and emission spectra of the synthesized CuNCs are provided in Figure APX4.2 Powder X-ray diffraction (PXRD) data for those CuNCs have been shown in the Figure APX4.3 and we have matched these data with the existing data file (JCPDS file) of CuO. Any major peak corresponding to CuO has not been found for those CuNCs suggesting the absence of CuO in the synthesised CuNCs. The zeta potential graphs of the CuNCs are provided in the Figure APX4.4 which has revealed the negative surface charges of those systems. For determining the number of Cu atoms in the metal core (Cu_n) of those nanoclusters have been determined by using Jellium model, which is discussed in the Supporting Information.[44-45]

4.3. Activity Assays

N-succinyl-L-phenylalanine p-nitroanilide (SPNA) has been taken as substrate. To determine the activity of α-ChT, the enzymatic hydrolytic product (p-nitro aniline) formation is evaluated by monitoring the absorption peak at 410 nm every 5 min interval. All the experiments were performed in 5 mM phosphate buffer of pH 7.4. For the inhibition kinetic study, the α-ChT (2.5 μM) was first incubated with CuNCs of different concentration for 2

hr. and then different concentration of SPNA was added from a stock solution of 3 mM in ethanol. To determine the amount of product formation, molar extinction coefficient (ε) of 8750 M^{-1} cm^{-1} at λ=410 nm for p-nitro aniline has been used. To check the reversibility, NaCl (0 to 1M) was added to the mixture of α-ChT and CuNCs before and after the incubation.

4.4. Preparation of Gel Electrophoresis

Gel electrophoresis was performed with a horizontal electrophoresis system (BIO-RAD, PowerPac Basic). For this study, 1% agarose gel was prepared in 5 mM sodium phosphate buffer. Suitably sized wells of 30 µL were created by placing a comb in the gel. Samples of different α-ChT:CuNCs ratios were prepared by keeping the concentration of α-ChT (30 µM) fixed and varying the concentration of CuNCs and incubated for 2 hr. Then 5 µL of 50% glycerol was added to 30 µL aliquot of the incubated solution to ensure the proper well loading and a constant voltage (100 V) was applied for 50 min for Cys-CuNCs and 120 min for TA-CuNCs for sufficient separation. After the experiment, the gels was placed in staining solution (0.5% Coomassie blue, 40% methanol, 10% acetic acid aqueous solution) for 2 h, followed by extensive destaining (40% methanol, 10% acetic acid aqueous solution) until protein bands were clear.

4.5. Result and Discussion

4.5.1. α-ChT Activity Assays and it's Inhibition by CuNCs

The extent of enzyme activity is determined by calculating the rate of the catalytic reaction.[6] Here, the enzymatic activity of α-ChT has been monitored by estimating the p-nitroaniline production from the hydrolysis of SPNA with the help of UV-Vis spectroscopic technique. Specifically, to investigate the influence of CuNCs on the enzyme activity of α-ChT, the α-ChT catalyzed reaction is first monitored in the presence of various concentrations of CuNCs

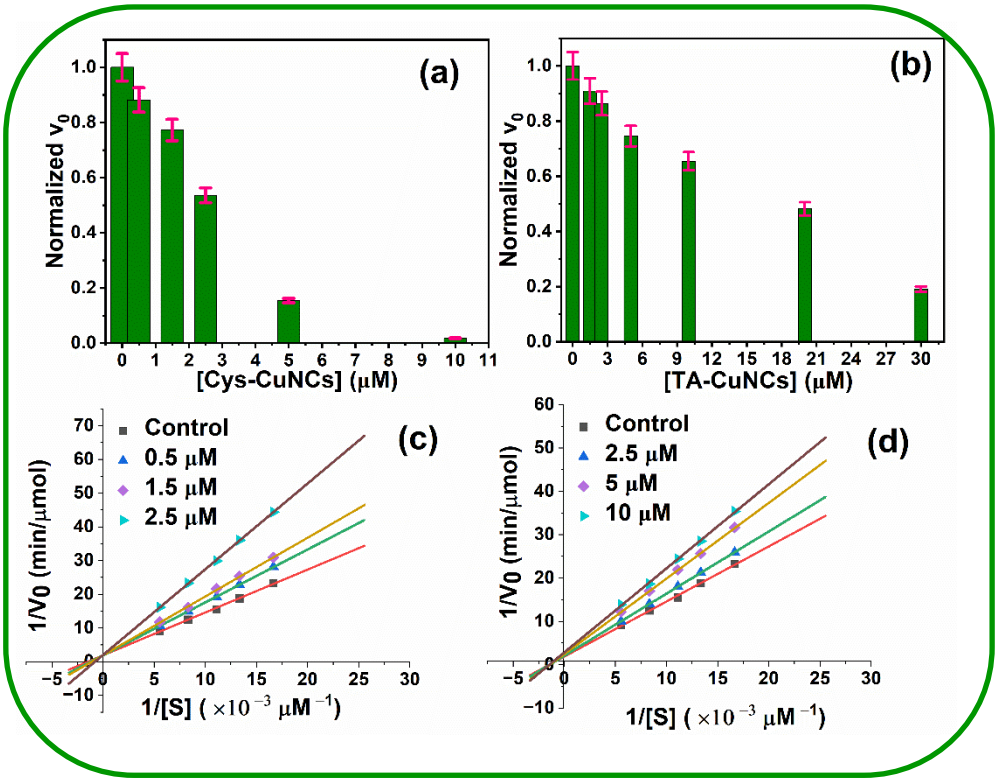

Figure 4.2. Normalized rates (v_0) of α-ChT catalyzed reactions under different concentrations of (a) Cys-CuNCs and (b) TA-CuNCs using SPNA as a substrate. Lineweaver−Burk plots of α-ChT in the absence and presence of different concentrations of (c) Cys-CuNCs and (d) TA-CuNCs.

capped with two different types of surface ligands e.g., cysteine (Cys) and tannic acid (TA). The activity of α-ChT in the absence of CuNCs is considered as unity (100%), thereby the activities of α-ChT in the presence of CuNCs are normalized to that of free α-ChT. The outcome of the investigation is illustrated in the bar diagrams (Fig 1a,b). From these figures, it can be seen that the enzyme activity of α-ChT is decreased with increasing concentration of both Cys-CuNCs (Fig 1a) and TA-CuNCs (Fig 1b). In case of Cys-CuNCs, the enzyme activity of α-ChT is decreased almost completely (99%), but in case of TA-CuNCs, the enzyme activity of α-ChT is reduced to maximum 81%. The effect of the two free ligands, (Cys and TA) on the enzyme activity has also been checked (Figure APX4.5). No change in the enzyme activity of α-ChT indicates that bare ligands can't affect the enzyme activity.

Interestingly, Cys-CuNCs are found to reduce the activity of α-ChT almost completely at very low concentrations of Cys-CuNCs. This observation is the signature of competitive inhibitor as these type of inhibitors binds to the active site of enzymes and blocks the pathway for the substrate.[34] On the contrary, TA-CuNCs is found to reduce the activity of α-ChT partially (to an upper limit of 81%) at a relatively higher concentration (than Cys-CuNCs), indicating the noncompetitive nature of the interaction event.[8, 21, 30] Therefore, these results have suggested that surface ligands of CuNCs may play a crucial role in modulating the activity of α-ChT.

4.5.2. CuNCs− α-ChT Inhibition Kinetics

To understand the binding sites of α-ChT for CuNCs, it is imperative to investigate the mode of inhibition by employing kinetics studies.[12, 20, 27] For this purpose, Michaelis–Menten and mixed model inhibition kinetics are invoked. To calculate the relevant kinetics parameters such as maximum reaction rate (v_{max}), and Michaelis−Menten constant (K_m), the double reciprocal form of the Michaelis−Menten equation called Lineweaver−Burk (LB) equation[34] (eq 4.2) is used, which is given by

$$\frac{1}{v_0} = \frac{K_M^{app}}{v_{max}^{app}} \times \frac{1}{[S]} + \frac{1}{v_{max}^{app}} \qquad (4.2)$$

where v_{max}^{app} is the apparent maximum rate and K_M^{app} is the apparent Michaelis constant, v_0 represents the initial reaction rate and [S] represents the concentration of substrate. The reciprocal of the substrate (S) concentration against the reciprocal of the initial reaction rates (v_0) in the absence and presence of different fixed concentrations of Cys-CuNCs and TA-CuNCs are plotted, and the plots are provided in Figure 4.2c and Figure 4.2d, respectively. The kinetics parameters extracted from these plots are listed in Table 4.1. It is to be noted that

LB plot and the associated kinetics parameters are the most widely used straightforward method for diagnosing inhibitor modality.

Table 4.1. The Apparent Michaelis Constant and Apparent Maximum Rate under Different Concentrations of Cys-CuNCs and TA-CuNCs

[Cys-CuNCs] (μM)	**0**	**0.5**	**1.5**	**2.5**
K_M^{app}**(μM)**	680.00	831.76	888.85	1322.49
v_{max}^{app} **(μM/min)**	0.54	0.53	0.51	0.52
[TA-CuNCs] (μM)	**0**	**2.5**	**5**	**10**
K_M^{app}**(μM)**	680.00	702.48	706.82	690.61
v_{max}^{app}**(μM/min)**	0.54	0.49	0.40	0.35

From these plots, (v_{max}^{app} and K_M^{app}) are extracted.[6] It is known that, in competitive inhibition, there is competition between the inhibitor and substrate for the active site of the free enzyme. Because of this competition, more substrate is required to reach the half-maximum value v_{max}^{app} and this type of inhibition can be overcome at high substrate concentrations.[34] Hence, in case of competitive inhibition, the enzyme sample has the kinetic effect in raising the K_M^{app} for its substrate without affecting the value of v_{max}^{app}. In noncompetitive inhibition, inhibitors bind to the enzyme distinct from the active site and reduce the enzyme activity without affecting the binding of the substrate to the enzyme. Therefore, increasing substrate concentration can't overcome this type of inhibition. So, the effect of noncompetitive inhibitors is the decrease of v_{max}^{app} without affecting K_M^{app} for the substrate. For uncompetitive inhibition, inhibitors bind exclusively to the enzyme-substrate complex and thereby affect product formation. Therefore, the kinetics effect of uncompetitive inhibitors is the decrease of

v_{max}^{app} with the decrease in activated ES complex and the decrease of K_M^{app} due to the increase in the affinity of the enzyme for its substrate. From the Figure 4.2c, it can be observed that for the different fixed concentrations of Cys-CuNCs, the extended fitted lines intersect at the same point on the y-axis as an uninhibited enzyme. The data that are collected in Table 4.1 indicates that v_{max}^{app} is almost unaffected with increasing the value of K_M^{app}, suggesting that Cys-CuNCs inhibit ChT activity with a competitive mechanism. Interestingly, in case of TA-CuNCs, it has been found that the extended fitted lines (Figure 4.2d) meet at the same point on the X-axis. The data in table 4.1 shows that v_{max}^{app} is decreased while K_M^{app} remained almost constant with the increase of TA-CuNCs concentration. This observation clearly demonstrates the noncompetitive inhibition mode of α-ChT activity caused by TA-CuNCs.

Again to get more insight into the inhibition mechanism, inhibition constants (K_i and α) are determined by using mix model inhibition equation which is given as

$$\frac{1}{v} = \frac{1+[I]/(\alpha K_i)}{v_{max}} + \frac{K_m(1+[I]/K_i)}{v_{max}[S]} \qquad (4.3)$$

In eq 4.3, the factor α reflects the effect of the inhibitor on the affinity of the enzyme for the substrate, and likewise the substrate effect on the affinity of the enzyme for the inhibitor. It is an important parameter which is used to describe the type of inhibition[8, 28]. When α = 1, it indicates the noncompetitive inhibition. When $\alpha \gg 1$, it means the competitive inhibition and $\alpha \ll 1$ tells uncompetitive inhibition. In the present study, from the slope and intercept of the L-B plot, we have determined K_M = 680 μM and v_{max} = 0.54 μM/min for α-ChT in the absence of inhibitor. From the mixed model inhibition equation, we have obtained α = 18.64 for 2.5 μM Cys-CuNCs indicating a competitive mode of inhibition and α = 1.02 (~ 1) for 10 μM TA-CuNCs indicating a non-competitive mode of inhibition. The findings of two types of inhibition modes for the two different CuNCs can be rationalised by considering the following facts. It has been demonstrated that if there is a structural similarity between the

inhibitor and the substrate or the enzymatic reaction takes place via a similar transition state, then the inhibition mechanism goes through via competitive mode.[6] In the present study, in case of cys-CuNCs, the surface of Cys-CuNCs show some structural similarity with the substrate (SPNA) as they have same functional group on their surface and thus this could be one of the possible reason for the exhibition of competitive binding mode of cys-CuNCs. Additionally, the enzymatic reaction may follow the same transition state, which allows the Cys-CuNCs to proceed via a competitive mode of inhibition. On the other hand, due to the presence of bulky tannic acid and polyhydroxy moieties, it becomes difficult for TA-CuNCs to make closer approach towards the active centre of α-ChT, thereby facilitating it's binding to the allosteric sites.

4.5.3. Effect of Ionic Strength on the Activity Inhibition of α-ChT

It is imperative to monitor the enzymatic activity by altering the ionic strength of the medium because ionic strength in biological systems can vary from 5 mM (bile) to 250 mM (red blood cells).[46-47] Previously, it has been reported by many researchers that the interaction between α-ChT and inhibitors can be diminished by increasing the ionic strength of the medium and subsequently reversing the activity, which indicates the electrostatic interaction of the binding event.[20, 28] So, to investigate the extent of reversibility of the interaction between α-ChT and CuNCs, the enzyme activity tests have been performed with the variation of ionic strength of the solution in two different approaches. First, α-ChT and CuNCs are incubated for two hours, and then various concentrations of NaCl (0 to 1M) has been added to the incubated system, and in the second experiment, the varied concentration of NaCl has been added to the solution of α-ChT and CuNCs before incubation. The activity of α-ChT in the presence of various concentrations of NaCl added after and before incubation to those CuNCs are normalized by the α-ChT activity without inhibitor at the same salt concentration, and the representative bar plots are provided in Figure 4.3a,b and Figure 4.3c,d respectively.

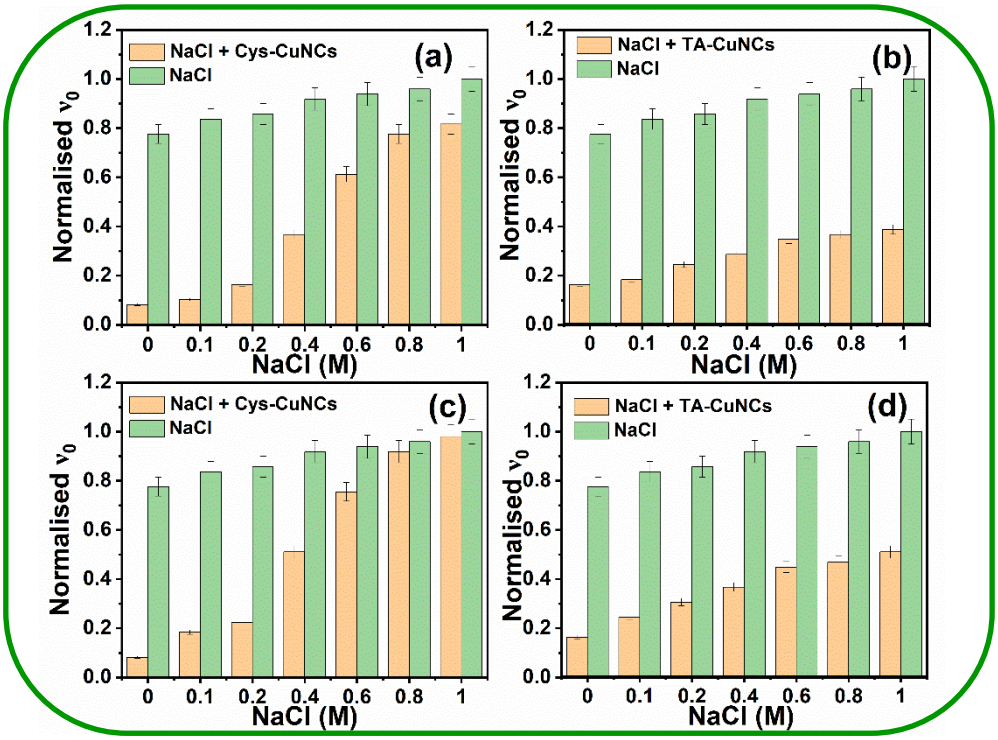

Figure 4.3. Normalized activities of α-ChT in the presence various concentrations of NaCl added after incubation with (a) 2.5 μM of Cys-CuNCs and (b) 10 μM of TA-CuNCs and before incubation with (c) 2.5 μM of Cys-CuNCs and (d) 10 μM of TA-CuNCs.

From bar plots, it can be seen that for both cases, the α-ChT activity can be restored with increasing salt concentrations, but the extent of recovery is different for those two systems. From the first experiment (Figure3a,b), it is observed that in the case of Cys-CuNCs, 80% of the activity is recovered at 1M salt concentration, but in the case of TA-CuNCs, the α-ChT activity is recovered to only ~18 %. This partial restoration of enzyme activity indicates that the added NaCl could not completely release the CuNCs from α-ChT binding and restore their activities at 100%. This observation can be rationalised by considering the following: (i) during incubation of α-ChT and CuNCs, a few amounts of α-ChT may irreversibly bound to the CuNCs (ii) it is also possible that two steps binding processes are happening during the binding events and among these two steps, one may be irreversible, and another one may be reversible and (iii) may be due to the partial denaturation of α-ChT and consequent loss of activity.[20, 27]

From the second experiment (Figure 4.3c,d), it is observed that in case of Cys-CuNCs the restoration of enzyme activity is ~100%, whereas in case of TA-CuNCs, it is ~30%. This result demonstrates that the electrostatic attraction between the α-ChT and Cys-CuNCs can be weakened in the presence of competitive ions. The high ionic strength in the solution might have blocked the α-ChT from binding with Cys-CuNCs and thus facilitating full protection of its enzymatic activity. Therefore, the outcomes of this study also demonstrate that electrostatic force is the dominant interaction mode for the binding between α-ChT Cys-CuNCs, and upon ionic strength mediation this interaction is largely reversible in nature. On the other hand, observations of 30% activity recovery in case of TA-CuNCs can be rationalized by considering the fact that other intermolecular interactions (hydrophobic interaction, H-bonding, Van der Waals force of attraction etc.) between α-ChT and TA-CuNCs might be playing predominant role (over electrostatic interaction).

4.5.4. CuNCs Induced Quenching of the Intrinsic Fluorescence of Chymotrypsin and Enzyme−CuNCs Bioconjugate Analysis

Along with the activity measurement study it is also very important to study, the nature of interactions and thermodynamics associated with the interaction between CuNCs and α-ChT. For this purpose, we have performed fluorescence titration study by monitoring the intrinsic fluorescence of α-ChT with the gradual addition of Cys-CuNCs and TA-CuNCs separately at various temperatures. We note here that among the three amino acids, namely, tryptophan (Trp), tyrosine (Tyr), and phenylalanine (Phe), the Phe residues have the lowest absorptivity and fluorescence quantum yield and the fluorescence of Tyr is almost complete quenched due to interaction with peptide chain or an efficient energy transfer to the Trp moiety.[34, 48-49] For this reason the contribution of Phe and Tyr to the fluorescence of α-ChT has been neglected in this study when excited at 280 nm. In the present study, as the possibility of inner filter effect[50] cannot be neglected, the emission spectra are corrected first prior to data analysis.

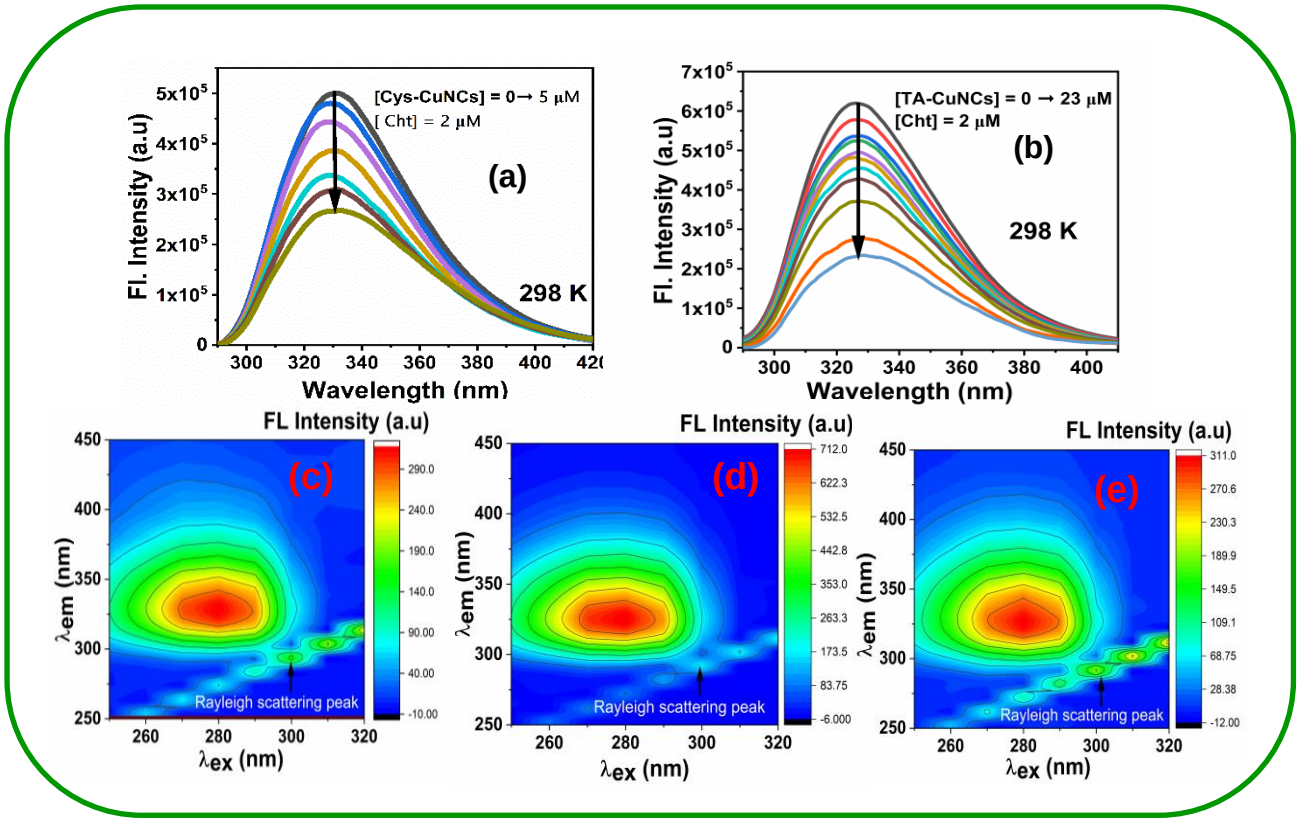

Figure 4.4. Fluorescence emission spectra of α-ChT protein upon gradual addition of (a) Cys-CuNCs, and (b) TA-CuNCs CuNCs (λex = 280 nm), respectively.3D fluorescence spectra of (c) α-ChT and α-ChT incubated with (d) Cys-CuNCs and (e) TA-CuNCs.

The correction of the emission spectra obtained from the fluorescence titration experiment are done by using the following eq 4.4

$$F_{corr} = F_{obs}\, antilog\left(\frac{OD_{ex}+OD_{em}}{2}\right) \qquad (4.4)$$

where F_{corr} represents the corrected fluorescence intensity, F_{obs} represents the observed fluorescence intensity, and OD_{ex} and OD_{em} are the optical densities at excitation and emission wavelengths, respectively. The absorption spectra of α-ChT in the absence and presence of CuNCs are shown in the Figure APX4.9a,b. The corrected emission spectra of α-ChT at 298 K in the absence and presence of an increasing concentration of Cys-CuNCs and TA-CuNCs are given in the Figure 4.4a,b. It can be seen from the Figure 4.4a,b that there is a

significant quenching of α-ChT in the presence of both CuNCs, which indicates the strong interaction between CuNCs and α-ChT molecules. The data corresponding to the fluorescence behaviour of α-ChT in the presence of Cys-CuNCs and TA-CuNCs at various temperatures are also provided in Figure APX4.7 and Figure APX4.8, respectively. It is to be noted here that at higher concentration of Cys-CuNCs (> 5μM) the emission maximum (λ_{max}=330 nm) of α-ChT gets red-shifted up to a maximum of 350 nm which is the characteristic peak of denatured ChT.[20] The corresponding fluorescence data of α-ChT at higher concentrations of Cys-CuNCs are shown in the supporting information (Figure APX4.10). From the normalised fluorescence spectra (inset of the Figure APX4.10) one can observed the red shifting of emission maxima due to denaturation at higher concentration. As the denaturation process of α-ChT has been found to start beyond 5μM concentration of Cys-CuNCs, the fluorescence data up to 5μM concentration have been taken for further analysis. Moreover, Three-dimensional fluorescence spectra (Figure 4.4c,d,e) of α-ChT in the absence and presence of those CuNCs have also been captured to verify the interaction of α-ChT with CuNCs. Figure 4.4c,d,e, have demonstrated that the Rayleigh scattering peak of α-ChT is increased with the addition of CuNCs, indicating that α-ChT is bound to CuNCs to form a complex.[34, 51] Please note here that there are several reasons for a fluorophore to be quenched such as the collision between the excited fluorophore and quencher molecule (dynamic quenching), formation of a ground-state complex with the quencher (static quenching), excited-state reaction and energy transfer phenomena, etc[50, 52-53]. Therefore, it becomes essential to understand the mechanism of fluorescence quenching of α-ChT by CuNCs with the help of Stern−Volmer (SV) equation (eq 4.5)

$$\frac{F_0}{F} = 1 + K_{SV}[\mathrm{Q}] \qquad (5)$$

Where F_0 and F are the fluorescence intensities of α-ChT in the absence and presence of

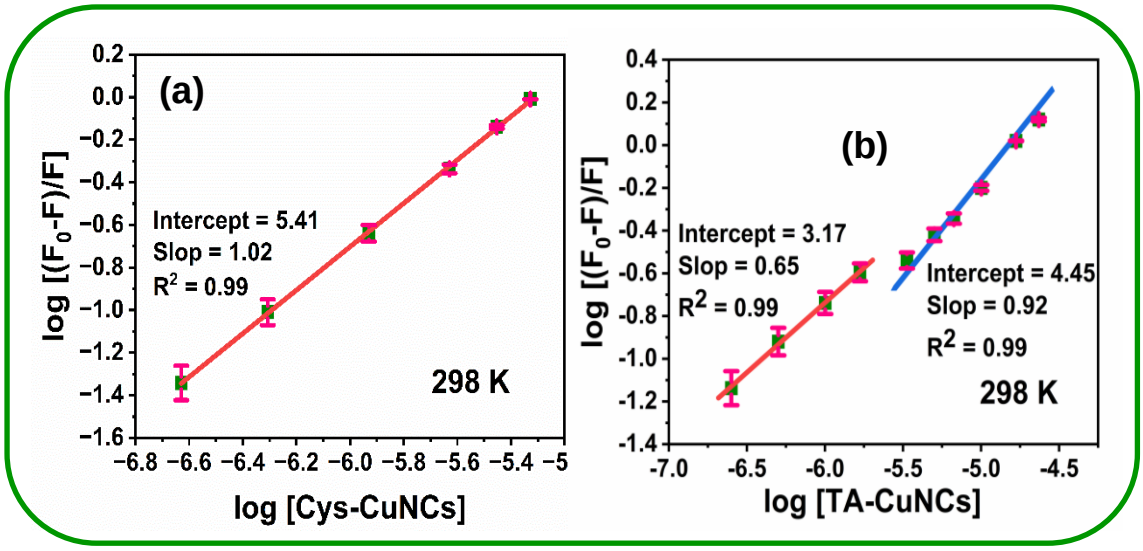

Figure 4.5. Stern−Volmer plots of the quenching of α-ChT protein by (a) Cys-CuNCs and (b) TA-CuNCs.

CuNCs, respectively, and K_{SV} is the Stern−Volmer constant. The corresponding SV plots at 298 K are shown in Figure 4.5a,b and that of other temperatures are provided in Figure APX4.11 and Figure APX4.12. Interestingly, from the Figure 4.5a, it can be seen that in the case of Cys-CuNCs, the SV plot provides a linear plot with only one region, but in the cases of TA-CuNCs, Figure 4.5b reveals two distinct regions (region-I and region-II) of different slope in the SV plots and both of the regions vary linearly with increasing the concentration of TA-CuNCs. While the Region-I for TA-CuNCs has been observed at a relatively lower quencher concentration (up to 1.6 μM), region-II has been observed at a relatively higher quencher concentration (beyond 1.6 μm). From the SV plots, it can be opined that Cys-CuNCs may follow one step of binding and TA-CuNCs may follow two steps of binding with α-ChT. These outcomes suggest that surface ligands of CuNCs can alter the nature of binding modes when interacting with α-ChT. The quenching constant (kq) value for Cys-CuNCs is estimated to be 1.14×10^{13} $M^{-1}s^{-1}$, and the same for TA-CuNCs is estimated to be 9.69×10^{13} $M^{-1}s^{-1}$ and 4.19×10^{13} $M^{-1}s^{-1}$ for Region-I and Region-II, respectively. The estimated kq values in all of these cases are greater than the largest possible values of bimolecular

quenching constant ($2 \times 10^{10}\ M^{-1}\ s^{-1}$) in the aqueous medium, suggesting that the quenching mechanism is predominantly static in nature[54-55]. Further, time-resolved fluorescence study has been performed to investigate whether the dynamic component in the quenching event is present or not. The decay profile of α-ChT (Figure APX4.13a,b) in the absence and presence of CuNCs and the corresponding time constants (Table APX4.1) demonstrate that the lifetime of α-ChT is decreased with increasing the concentration of both Cys-CuNCS and TA-CuNCs separately, confirming the involvement of the dynamic quenching process also during the interaction event. Further, we have also deeply investigated whether energy transfer is responsible or not for the quenching of α-ChT in the presence of CuNCs. For this purpose, the individual systems as well as the composite systems are excited at 280 nm and the emission of acceptors (CuNCs) has been monitored to investigate whether any characteristic peak of CuNCs (~488 nm for Cys-CuNCs and ~430 nm for TA-CuNCs nm) are appeared or not in longer wavelength due to energy transfer (Figure APX4.14). When the composite system (α-ChT-CuNCs) is excited at 280 nm, no emission peak is observed for α-ChT-Cys-CuNCs systems which rule out the energy transfer from α-ChT to Cys-CuNCs. Whereas, for the α-ChT-TA-CuNCs systems, a very less intense shoulder peak is observed at ~435 nm (Figure APX4.14b) but this peak is basically due to TA-CuNCs, not due to energy transfer.

4.5.5. Effect of α-ChT on the Photoluminescent Property of CuNCs

Binding behaviour of α-ChT with CuNCs can also be monitored by investigating the effect of α-ChT on the photoluminescent property of CuNCs. For this purpose, steady-state (Figure APX4.15a,b) and time resolve fluorescence measurements (Figure APX4.16a,b) have been carried out by monitoring the fluorescence intensity of those CuNCs in the absence and presence of α-ChT. The excitation wavelength for steady state measurement was 390 nm and for time resolve measurement the excitation laser source was 375 nm. From these measurements, it can be seen that both the fluorescence intensity and lifetime of CuNCs are

enhanced with increasing the concentration of α-ChT but in different extent due to different surface chemical nature of those CuNCs. The enhancement of fluorescence intensity and lifetime of CuNCs is attributed due to the adsorption of α-ChT over the surface of CuNCs.[56-57] The increment of the fluorescence intensity of both CuNCs in presence of α-ChT can be rationalised by the fact that a large number of amine and carboxylic groups of α-ChT may interact with CuNCs, which can give stability of those systems.[56, 58] It is also expected that the α-ChT molecules surrounding the CuNCs surface prevent the contact of water molecules from CuNCs surface and cause the reduction in the nonradiative relaxation process, which may also responsible for the enhancement of both fluorescence intensity as well as lifetime.[57, 59] Again, it is well reported that when protein molecules are adsorbed on the surface of nanomaterials, it can form either "protein-corona' or protein-complex".[60-61] Stoichiometry ratios for the binding of protein to CuNCs is important parameters to define a stable "protein corona". Many researchers have shown that for an effective protein corona formation, the protein/nanoparticle ratio is predicted to be always >1.[35, 62] Herein, to know the adsorption nature of α-ChT over CuNCs surface, the binding stoichiometry ratio (α-ChT:CuNCs) has been determined by utilising the fluorescence enhancement data on the basis of Benesi−Hildebrand (B−H) doublereciprocal plot[63] (eq 4.6).

$$\frac{1}{F-F_0} = \frac{1}{F_m - F_0} + \frac{1}{(F_m - F_0)K[\alpha-ChT]^n} \qquad (4.6)$$

where F and F_m are the fluorescence intensities of CuNCs with successive addition of α-ChT and maximum α-ChT concentrations, respectively, F_0 is the fluorescence intensity in the absence of α-ChT, and K is the equilibrium constant related to CuNCs and α-ChT association. From the B-H plot (Figure APX4.17a,b) it can be observed that for both the systems, the data points are linearly fitted when $1/(F - F_0)$ is plotted against 1/[α-ChT], which indicates a 1:1 (α-ChT:CuNCs) stoichiometry for the α-ChT-CuNCs binding events.

Along with this result, previously, the gel electrophoresis and ITC experiments have also demonstrated that the stoichiometric ratio of α-ChT to CuNCs is ≤ 1 which rule out the formation of protein-corona.

4.5.6. Binding Nature and Thermodynamic Parameters of the Interaction between CuNCs and α-ChT.

In order to establish the nature of interaction, the feasibility of the process, binding forces, the relevant thermodynamic parameters such as enthalpy change (ΔH), entropy change (ΔS) and free energy change (ΔG) have been estimated for the binding event. Essentially hydrogen bonding, van der Waals force of attraction, electrostatic interaction, hydrophobic interaction, etc., play important role for the binding interaction between protein and quencher molecules[64-65]. Initially, the fluorescence data obtained from the steady state titration study of α-ChT in the absence and presence of CuNCs has been utilised to construct double logarithm plot[66] (eq 4.7) for the determination of associated binding constant (K_a) value for the α-ChT-CuNCs interaction.

$$\log\left[\frac{F_0 - F}{F}\right] = \log K_a + n\log[Q] \qquad (4.7)$$

where F_0 and F represent the fluorescence intensity of α-ChT in the absence and presence of quencher concentration [Q] respectively, K_a is the equilibrium binding constant, and n is the number of binding sites in the enzyme. The representative double logarithmic plots at 298 K are given in Figure 4.6a,b and at various temperatures in Figure APX4.18 and Figure APX4.19. It can be seen from the Figure 4.6a that for the case of Cys-CuNCs, the data points are fitted by single line, whereas for the case of TA-CuNCs, the data points are fitted by two distinct fitted lines (indicated by red and blue fitted lines). As double-logarithmic plot is quite

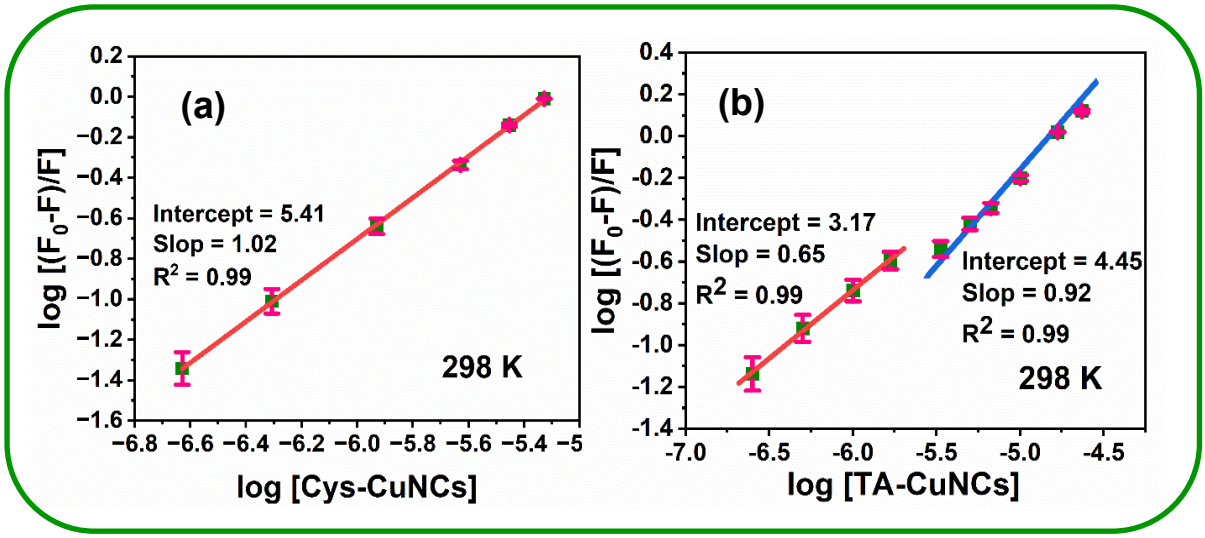

Figue 4.6. Double-logarithmic plot for the binding of (a) Cys-CuNCs and (b) TA-CuNCs, with α-ChT at 298 K. The solid lines represent the simulated fitted line.

effective in determining the stepwise binding of a protein−ligand assembly,[66-67] it can be concluded from the plots that the interaction of α-ChT with Cys-CuNCs takes place via a single step. In contrast, the same with TA-CuNCs takes place in two steps processes which is in agreement with the results obtained from SV plots. In the present study, the binding constant for the interaction of α-ChT with Cys-CuNCs is measured to be 2.57 x 10^5 M^{-1}, whereas the same with TA-CuNCs is estimated to be 1.48 x 10^3 M^{-1} for the first step (red region) and 8.23 x 10^3 M^{-1} for the second step (blue region). The binding constants for the above two systems at various temperatures (Table 4.1) are used to construct Van't Hoff plot[34] to estimate the enthalpy (ΔH) and entropy (ΔS) changes. It is pertinent to mention here that the value of ΔH and ΔS corresponding to particular interaction can help to understand the type of forces involved for the same interaction event. The Van't Hoff equation is given by the eq 4.8 and the corresponding plots for those two systems are given in the Figure 4.7

$$\ln K_a = -\left(\frac{\Delta H}{R}\right)\frac{1}{T} + \frac{\Delta S}{R} \qquad (4.8)$$

From the slope and intercept of the fitted lines, ΔH and ΔS of those systems have been

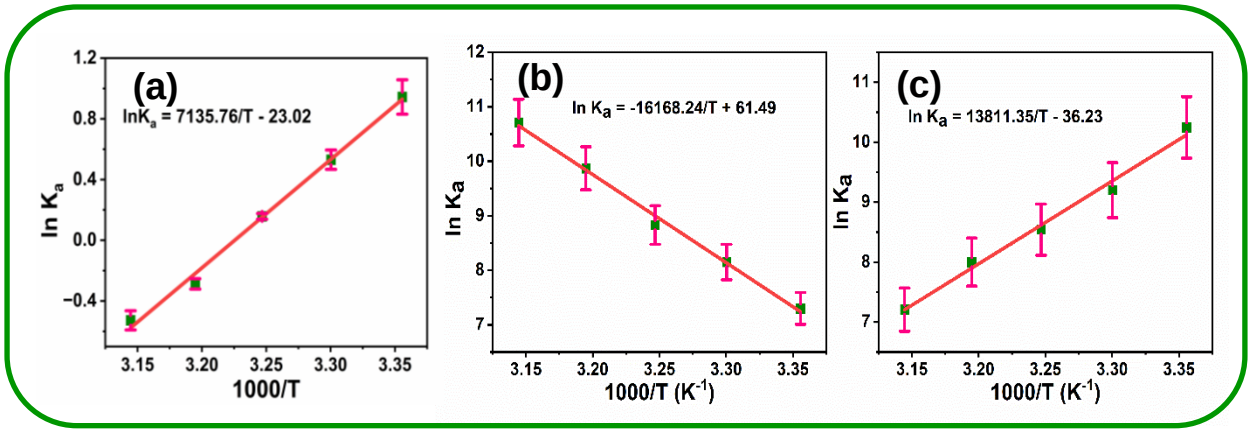

Figure 4.7. Van't Hoff plots of Cu NCs- α-ChT system: (a) Cys-CuNCs- α-ChT system (b) TA-CuNCs- α-ChT system for 1st step of binding and (c) TA-CuNCs- α-ChT system for 2nd step of binding.

calculated. It can be seen from the Figure 4.7a that in the case of Cys-CuNCs, there is a positive slope (Figure 4.7a) which indicates the exothermic process but in the case of TA-CuNCs, for the first step of binding, it gives a negative slope (Figure 4.7b) indicating endothermic process whereas for the second step, it gives positive slope (Figure 4.7c) indicating exothermic process. The free-energy change ($\Delta G = -RT\ln K_a$) is determined by using the calculated associated binding constants of those systems at various temperatures. It is to be noted here that Ross and Subramanian[68] have studied the protein-ligand interaction and have said that positive values for both ΔH and ΔS indicate the hydrophobic interaction, whereas negative values for ΔH and ΔS indicate both hydrogen bonding and van der Waals interactions. By looking at the sign convention of the thermodynamic parameters, one can predict the type of forces involved in the interaction event. From the Table 4.2, it can be seen that in case of Cys-CuNCs, both ΔH and ΔS are negative which is indicative of both hydrogen bonding and van der Waals interactions. It is to be noted here that the electrostatic interaction is also responsible for the binding event, as it is the primary step of hydrogen bonding.[69] In the case of TA-CuNCs, the first step of the interaction event is associated with

positive values of ΔH and ΔS, indicating the involvement of hydrophobic interaction, whereas the negative values of ΔH and ΔS for the second step indicate the involvement of the hydrogen bonding, van der Waals and electrostatic interactions. The above studies have revealed that the association constant (K_a) for the interaction of α-ChT with Cys-CuNCs is higher than TA-CuNCs. Moreover, it can also be observed that at lower concentration, Cys-CuNCs shows relatively higher fluorescence quenching of ChT than that is exhibited by TA-CuNCs. These results suggest that Cys-CuNCs can act as a stronger and higher potent inhibitor than TA-CuNCs. These different types of results for the above two systems also point out the role of different surface ligands of the CuNCs and eventually modulate the binding interaction with the enzyme.

The binding events are also studied by isothermal titration calorimetric (ITC) study[70] that directly provide a heat change signal for the progression of interaction event.

Table 4.2. Associative binding constant (K_a), and other relevant thermodynamic parameters for the interaction of Cys-CuNCs and TA-CuNCs with α-ChT enzyme.

Systems	**Temp (K)**	**K_a (10^5 M^{-1})**	**ΔH (KJ mol^{-1})**	**ΔS (J $K^{-1}mol^{-1}$)**	**ΔG (KJ mol^{-1})**
Cys-CuNCs- α-ChT	298	2.57±0.04	-59.33±0.28	-190 ±0.33	-30.86
	303	1.70±0.05			-30.34
	308	1.17±0.06			-29.88
	313	0.95±0.08			-29.82
	318	30.59±0.10			-29.04
Systems		**K_a**	**ΔH**	**ΔS**	**ΔG**

		(10^3 L mol^{-1})	(KJ mol^{-1})	(J $K^{-1}mol^{-1}$)	(KJ mol^{-1})
TA-CuNCs- α-ChT (First step)	298	1.48±0.10	134.42±0.61	510.12±0.69	-18.09
	303	3.46±0.15			-20.52
	308	6.84±0.10			-22.61
	313	19.34±0.10			-25.68
	318	44.80±0.07			-28.31
TA-CuNCs- α-ChT (Second step)	298	8.20±0.07	-114.82±0.33	-300.21±0.81	-22.33
	303	7.60±0.08			-22.51
	308	5.13±0.09			-21.87
	313	3.80±0.05			-21.45
	318	1.35±0.09			-19.05

The representative ITC thermographs for the binding events of α-ChT with Cys-CuNCs and TA-CuNCs are given in the Figure APX4.20 and relevant thermodynamic parameters (ΔH, ΔS, ΔG, Ka) obtained from ITC experiments are tabulated in Table APX4.2. The data obtained from the interaction of α-ChT with Cys-CuNCs are fitted with one set of sites binding model whereas that of with TA-CuNCs are fitted by two steps sequential binding model, which again confirms the two-step binding process supporting the conclusion obtained from steady-state fluorescence titration study of α-ChT in presence CuNCs. It is relevant to mention here that in our previous work, it was demonstrated that the interaction of bovine serum albumin (BSA) with CuNCs with specific surface ligands follow a sequential binding mode.[37] Recently, Jiang and co-workers[34] have also demonstrated the two-step binding process during NC−protein interaction. Based on the thermodynamic parameters obtained from both steady state fluorescence and ITC measurements and keeping in mind the sign convention as obtained from Ross model, a schematic diagram of the interaction event is

provided in the scheme 4.2. These results have clearly demonstrated the importance of surface chemistry associated with CuNCs, binding modes of the surface ligands and the interacting forces between the enzyme and nano inhibitors during the interaction of MNCs with biomolecules. The outcome of this study is expected to be helpful in engineering various nano-regulator that can be utilised in tuning the enzyme activity for various target oriented biological applications.

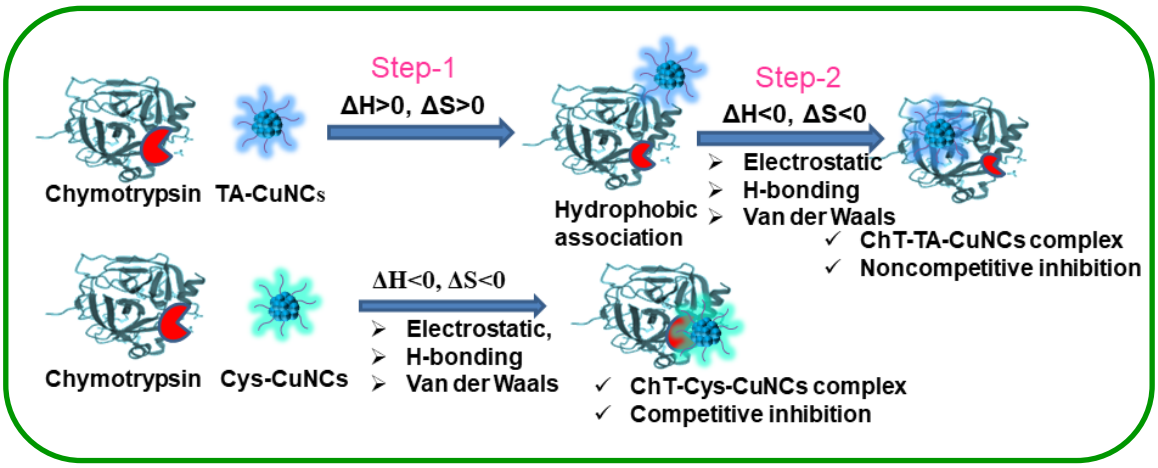

Scheme 4.2. Schematic representation of the binding event between α-ChT and CuNCs.

4.5.7. Gel Electrophoresis Study

Gel electrophoresis is an important technique to determine the binding ratio between protein and nanomaterials.[20, 25, 34] Herein, agarose gel electrophoresis has been carried out to estimate the binding stoichiometries of α-ChT with TA-CuNCs and Cys-CuNCs separately. The representative gels are provided in Figure APX4.21a,b. As can be seen from the Figure APX4.21a,b, α-ChT-CuNCs complex move relatively faster than free α-ChT towards anode due to negatively charged CuNCs providing more negative charges over α-ChT. It has also been observed that the intensity of the bands gets diminished with increasing the concentration of both CuNCs, This might have happened due to the unavailability of the binding site of α-ChT towards coomasie blue G250 after interacting with those CuNCs.

Figure APX4.21a,b show the saturation of electrophoresis rate at ~1:2 and ~1:3, respectively which indicates that the binding ratio of α-ChT and Cys-CuNCs is ~1:2 and that of α-ChT and TA-CuNCs is ~1:3. It is to be noted here that to form a stable "protein-corona" the protein/nanoparticle ratio is should be greater than 1.[35] Therefore, the results obtained from the present gel electrophoresis study does not provide evidence in favour of protein-corona formation rather it suggests that the interaction event goes through the formation of α-ChT-CuNCs complex.

4.5.8. Binding Interaction at Single Molecular Level (FCS)

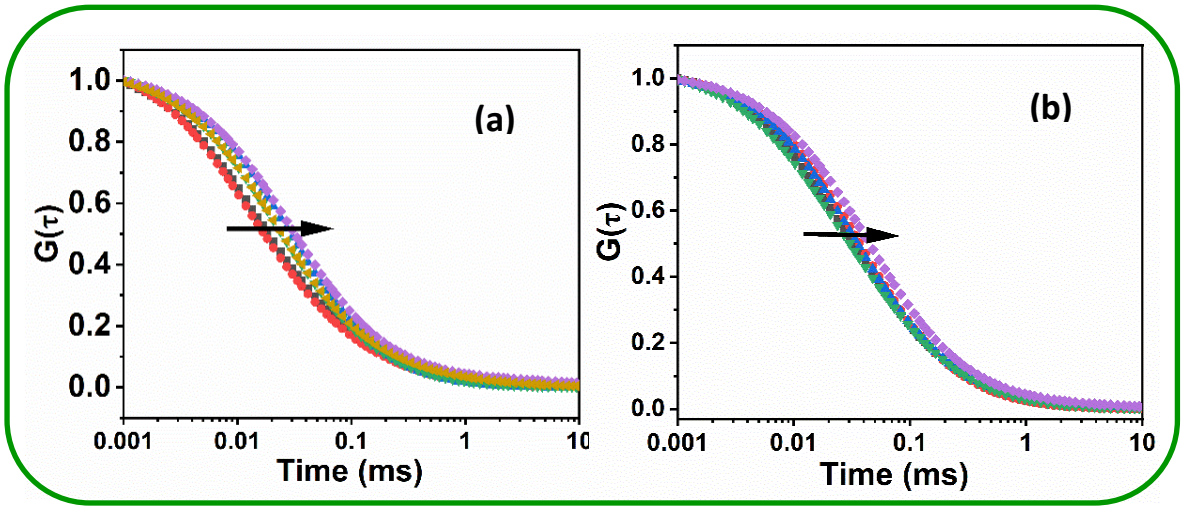

Figure 4.8. Normalized autocorrelation curves for (a) Cys-CuNCs, and (b) TA-CuNCs, with increasing concentrations of α-ChT.

FCS is extensively used as a highly sensitive and elegant technique for the study of molecular diffusion, binding affinities and kinetics of biomolecules and nanomaterials in single-molecule level.[50] Herein, to investigate the adsorption behaviour of α-ChT over the surface of CuNCs at single molecule level, FCS study has been performed by monitoring translational diffusion time (τ_D) of these CuNCs in the absence and presence of α-ChT and thereby calculating hydrodynamic radius (R_H) of those systems. The normalised cross-correlation

curves are given in Figure 4.8. It has been shown from the figure that the normalised curves are shifted towards right hand side with increasing the concentration of α-ChT which indicates the increment of diffusion time(τ_D) and hydrodynamic radius(R_H) of CuNCs in the presence of α-ChT, indicating the adsorption of α-ChT on the surface of CuNCs. The estimated relevant parameters obtained from the FCS study are provided in the Table APX4.3.

4.5.9. Investigation of α-ChT Secondary Structure Changes Induced by CuNCs

4.2.9.1. Synchronous Fluorescence: To investigate the effect of CuNCs on the conformational changes of α-ChT, synchronous fluorescence measurements are performed. This method provide several information about the microenvironment in the vicinity of fluorophore moiety of a protein molecule by monitoring the shifting of emission wavelength due to change of polarity in that environment.[37] Herein, when the offset wavelength (Δλ) is stabilized at 60 and 15 nm, the corresponding synchronous spectra reflect the characteristic fluorescence of trp and tyr residues of the protein molecule, respectively. From the Figure APX4.22, it is observed that the fluorescence of both trp and tyr residue of α-ChT are quenched with increasing the concentration of CuNCs, which indicates that these both residues of α-ChT are involved in the interaction event with CuNCs. Upon a careful look at Figure APX4.22, no significant change in the emission maxima of α-ChT with increasing concentration for various CuNCs has been observed which suggests that the microenvironment of trp and tyr residues of α-ChT remains almost unperturbed in the presence of those CuNCs.

4.5.9.2. Circular Dichroism (CD)

CD spectroscopy is a widely used important tool to monitor the secondary structure of protein molecules.[20, 28, 34] Herein, CD spectroscopy has been employed to investigate the effect of

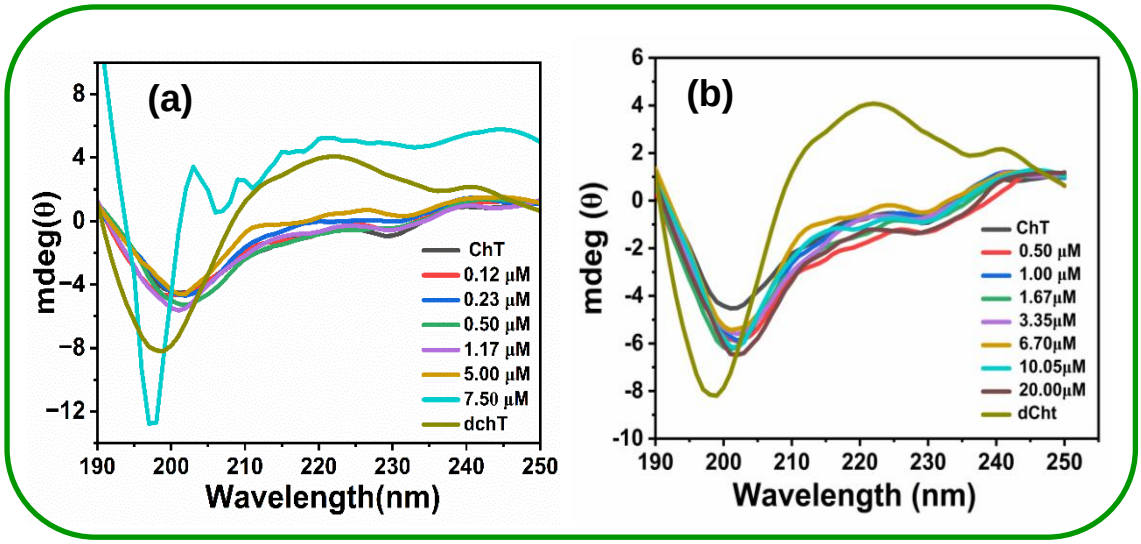

Figure 4.9. Far-UV CD spectra of 2 µM α-ChT (in 5 mM phosphate buffer of pH 7.4) in the absence and presence of increasing concentration of (a) Cys-CuNCs and (b) TA-CuNCs.

CuNCs on the secondary structure of α-ChT. From the Figure 4.9a,b it can be seen that the natural α-ChT has two characteristic peaks at 202 nm and 230 nm, while denatured α-ChT has one distinctive minimum at 200 nm. The CD spectra of α-chT in the presence of CuNCs have been compared with those of natural α-ChT and thermally denatured α-ChT (dchT). In the case of Cys-CuNCs, the change of the minimum at 202 nm is insignificant up to the concentration range of 0 to 5 µM, whereas in the case of TA-CuNCs, the minimum at 202 nm is little bit decreased, indicating the changes in the secondary structure of α-ChT by TA-CuNCs to some extent. Moreover, Figure 4.9 reveals that the shape and band position of incubated α-ChT with Cys-CuNCs (up to 5.00 µM) and TA-CuNCs remain same as natural α-ChT and nothing at all like that of DchT which suggest that the α-ChT is not denatured in the presence of CuNCs. Upon a careful look at the Figure 4.9a, it can be seen that at a higher concentration of Cys-CuNCs (8.00 µM) the CD spectrum shows structural similarity with that of dchT. This result indicates that α-ChT is denatured in the presence of a higher concentration of Cys-CuNCs (>5 µM) which corroborates the result obtained from steady state fluorescence study. These outcomes is interesting in a sense that though CuNCs quench

fluorescence of α-ChT, the native structure of α-ChT remains almost unchanged in presence of those concentration of CuNCs at which α-ChT is significantly inhibited. These data indicate that CuNCs can safely be used in various biological applications.

4.6. Conclusion

In summary, the interaction of α-ChT with two different CuNCs capped with two chemically different surface ligands namely, Cys and TA, has been investigated at both ensemble average and single molecule level. This study is also done to unreveal the role of surface chemistry of CuNCs in modulating the activity of α-ChT. Initially, results obtained from activity assays and inhibition kinetics measurements have revealed that both the CuNCs can act as a good enzyme inhibitors. Interestingly, kinetic measurements have shown that Cys-CuNCs almost completely diminish the activity of α-ChT through a competitive inhibition mechanism whereas TA-CuNCs partially reduce the enzyme activity through a non-competitive inhibition mechanism. Therefore, these results clearly demonstrate the crucial role of surface ligand in the regulation of α-ChT activity. In order to gain a molecular level understanding on the fundamentals behind the interaction events, both CuNCs in absence and presence of α-ChT are investigated by employing fluorescence spectroscopy, ITC measurements, FCS, agarose gel electrophoresis and circular dichroism (CD) spectroscopy. From the above studies, several interesting results in terms of getting an effective nano-regulator (CuNCs) as well as obtaining new insights towards understanding the role of surface chemistry in the modulation of enzyme activity have emerged. Thermodynamic results obtained from temperature-dependent fluorescence titration experiments and ITC measurements have indicated that Cys-CuNCs follow one-step binding process, whereas TA-CuNCs follow two-step binding process. Further analysis of thermodynamics data has also revealed that the one-step binding mechanism for Cys-CuNCs is mainly associated with electrostatic interaction, whereas the two-step binding mechanism for TA-CuNCs arises due

to involvement of hydrophobic interaction at first, followed by other interacting forces such as electrostatic, hydrogen bonding and van der Waals interactions. Again, the binding stoichiometry ratio of α-ChT for both CuNCs obtained from gel electrophoresis, B-H plot and ITC measurement is estimated to be <1, which support that the binding event goes through the formation of protein-complex rather than protein-corona. Moreover, FCS studies have demonstrated the interaction of CuNCs with α-ChT at the single molecule levels. Interestingly, circular dichroism (CD) measurements have revealed that the basic structure of chT remains almost unaltered in the presence of CuNCs. The above results demonstrate that both CuNCs can act as effective nano-regulator for enzyme activity, however in terms of potency and strong binding ability, Cys-CuNCs is found to be more effective than TA-CuNCs. The outcome of the present study is expected to be helpful for the design and development of ultra-small Cu-nanoparticle based suitable nano-regulator for various biological applications. The study also demonstrates the surface chemistry associated with CuNCs can play important role in regulating the enzyme activity.

4.7. Appendix

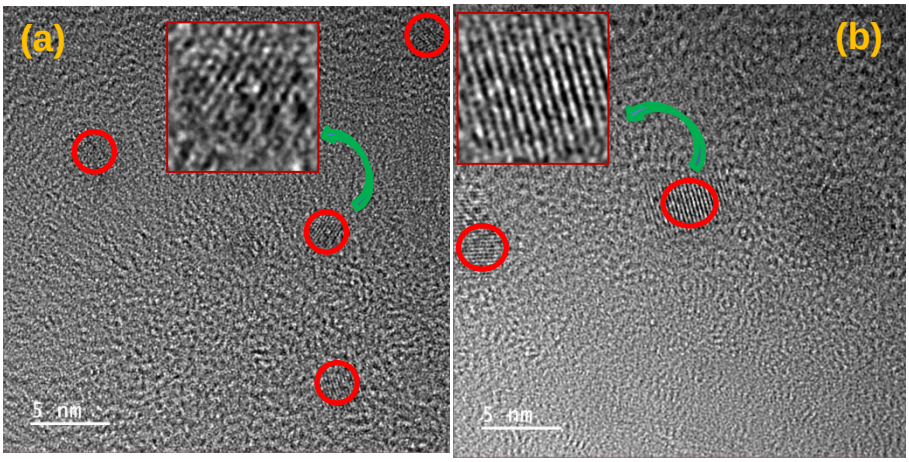

Figure APX4.1. HRTEM images of (a) Cys-CuNCs and (b) TA-CuNCs.

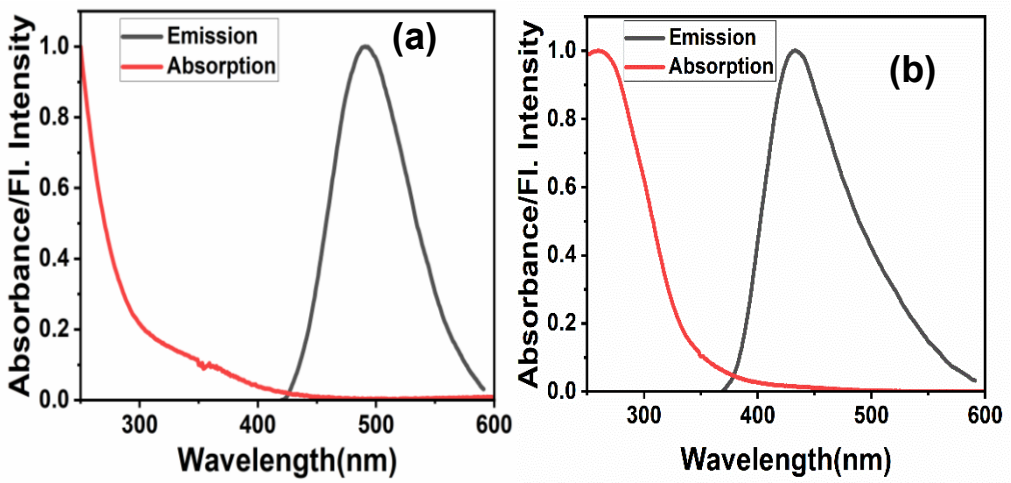

Figure APX4.2. Normalized absorption (red curve) and emission (black curve) of (a) Cys-CuNCs (b) TA-CuNCs.

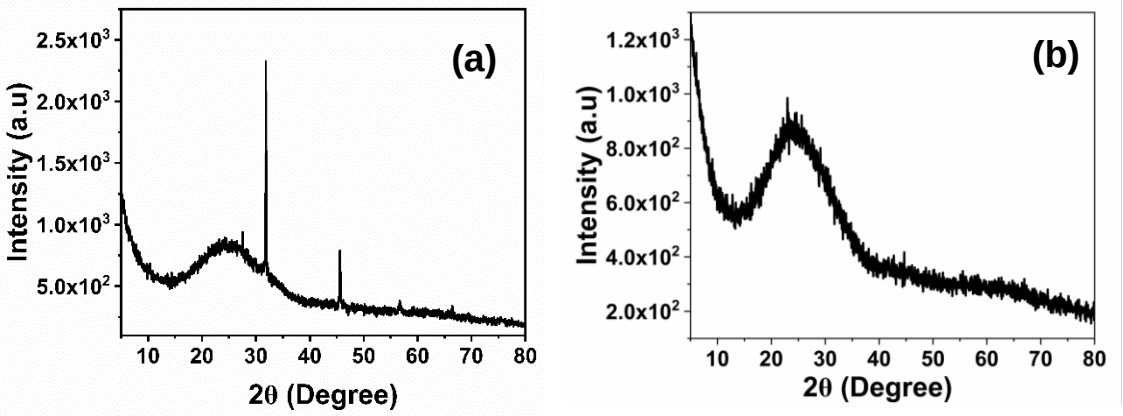

Figure APX4.3.. Powder XRD pattern of (a) Cys-CuNCs and (b) TA-CuNCs.

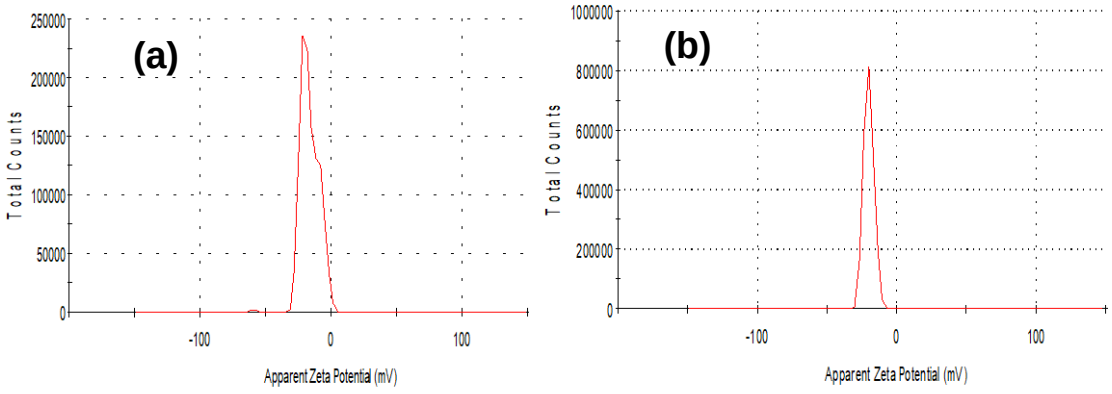

Figure APX4.4. Zeta potential graphs for the (a) TA-CuNCs, and (b) Cys-CuNCs in aqueous solution.

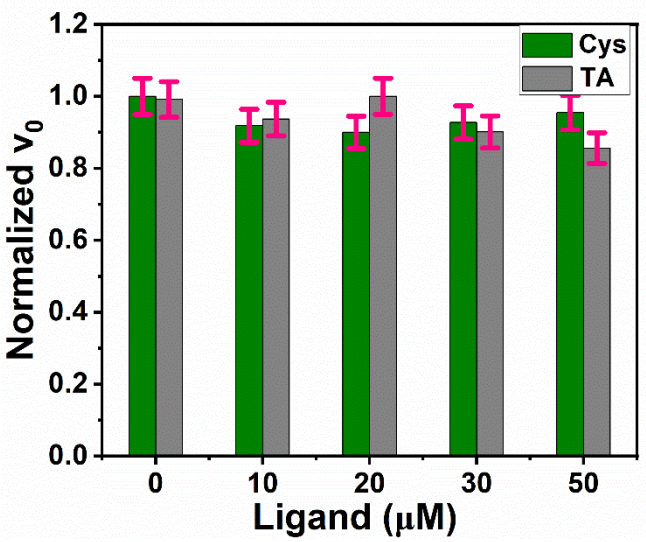

Figure APX4.5. Normalized rates (v_0) of ChT catalyzed reactions under different concentrations of Cysteine (green color) and Tannic acid (gray color) using SPNA as a substrate.

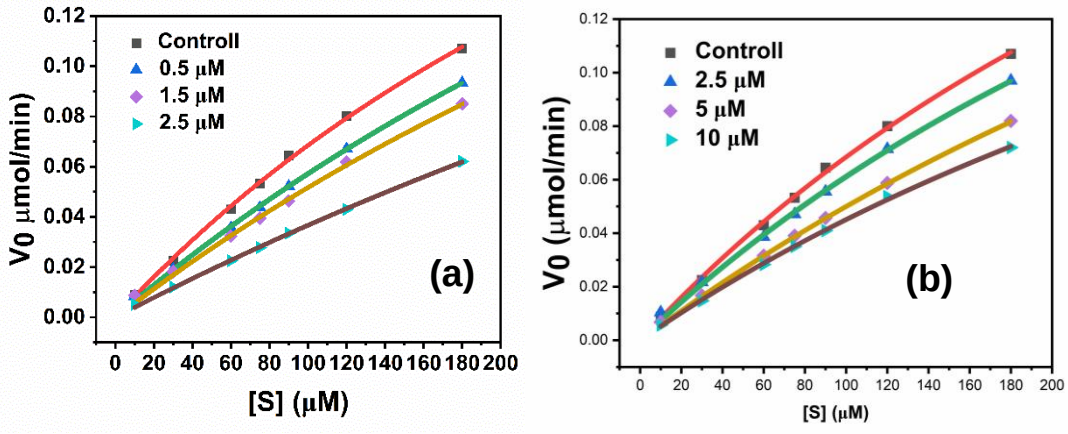

Figure APX4.6. Michaelis−Menten plots of α-ChT in the absence and presence of different concentrations of (a) Cys-CuNCs and (b) TA-CuNCs.

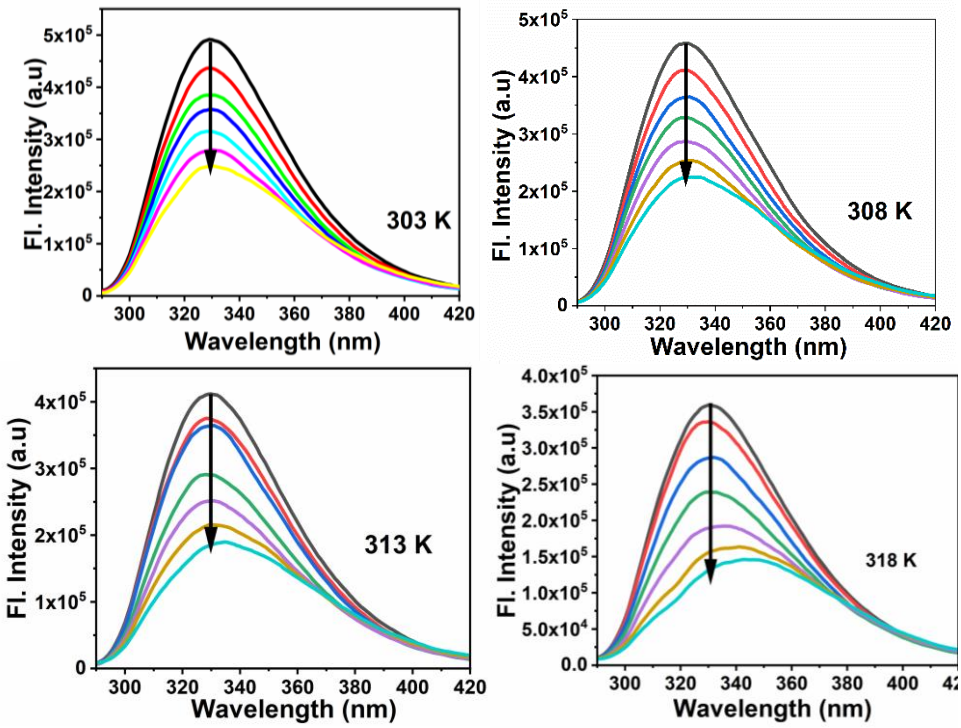

Figure APX4.7. Fluorescence emission spectra of α-ChT with gradual addition of Cys-CuNCs (λex = 280 nm). Temperature has been mentioned in each case.

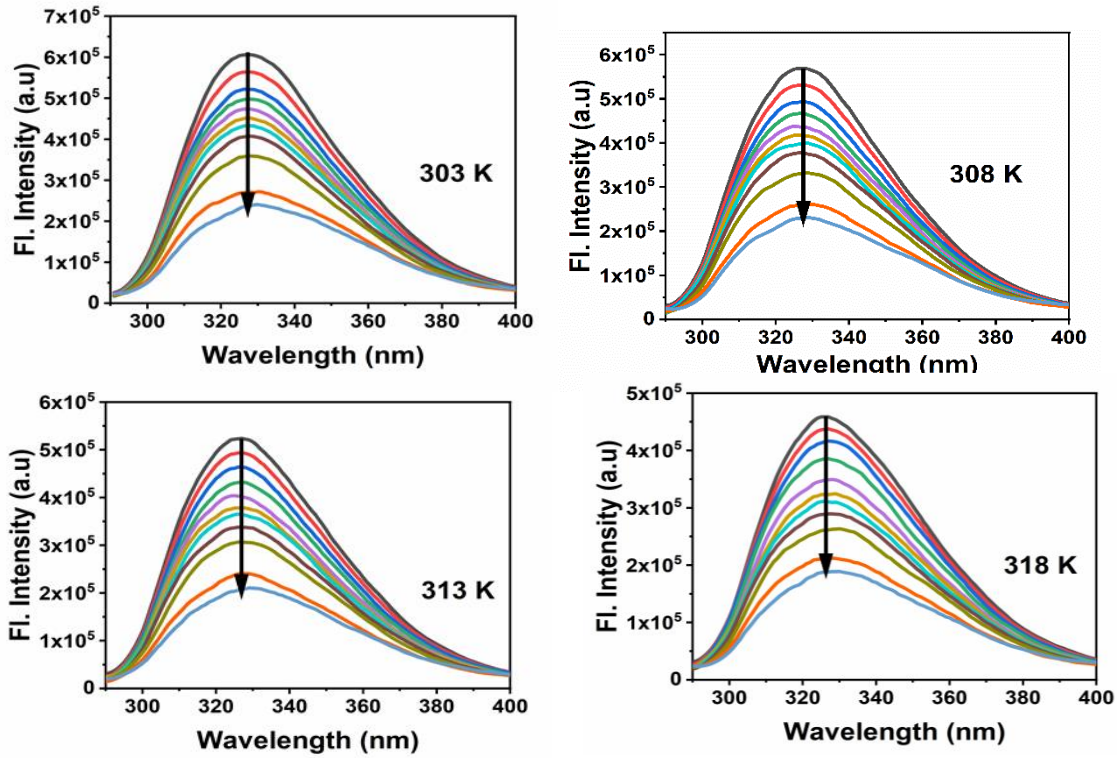

Figure APX4.8. Fluorescence emission spectra of α-ChT with gradual addition of TA-CuNCs (λex = 280 nm). Temperature has been mentioned in each case.

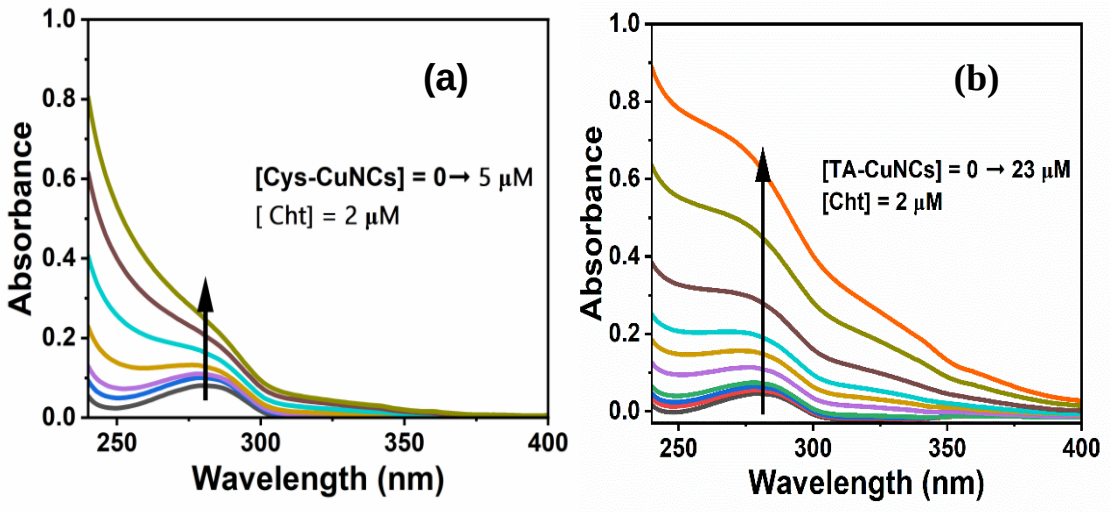

Figure APX4.9. UV-vis absorption spectra of α-ChT upon gradual addition of (a) Cys-CuNCs (b) TA-CuNCs.

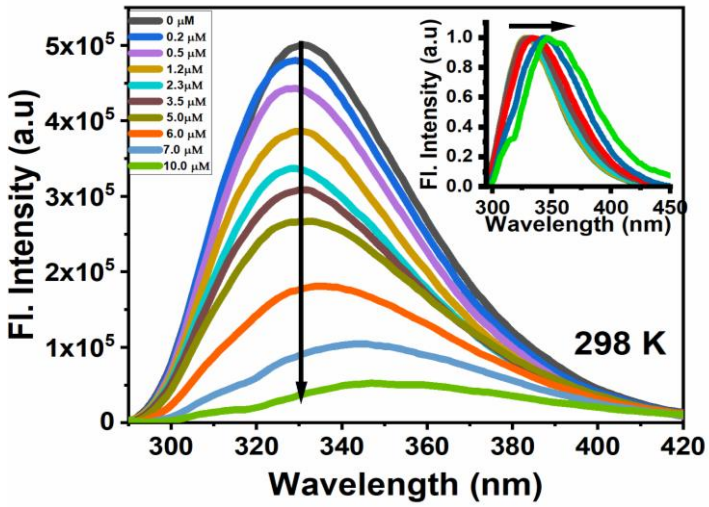

Figure APX4.10. Fluorescence spectra of α-ChT with the increasing concentration of Cys-CuNCs. (Inset : normalised fluorescence spectra).

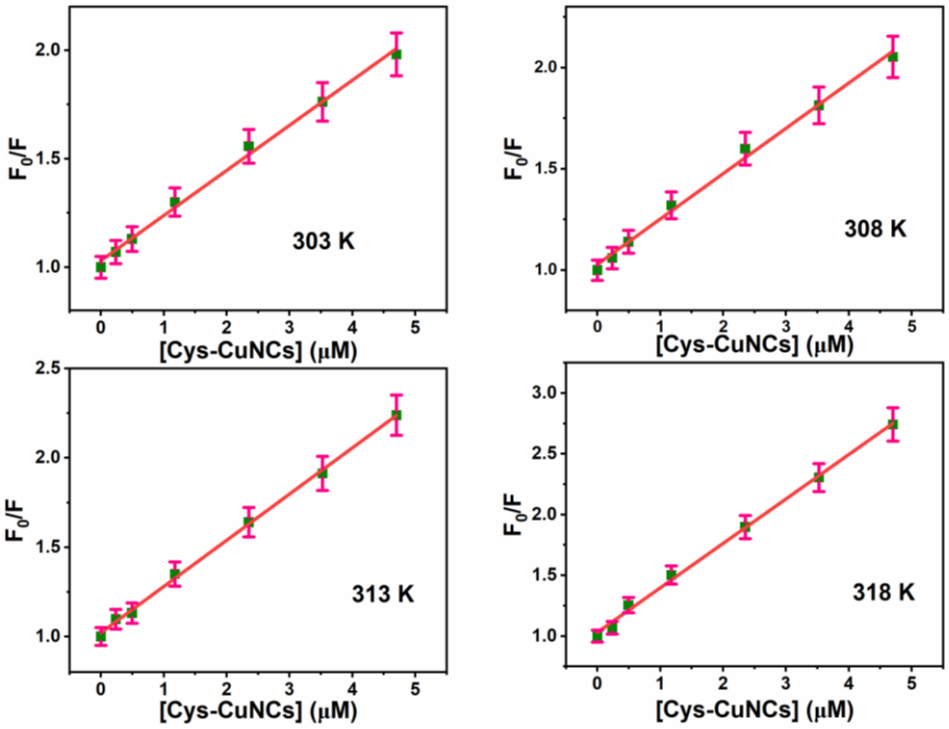

Figure APX4.11. Stern-Volmer plots for quenching of α-ChT fluorescence by Cys-CuNCs at different temperature marked at each figure.

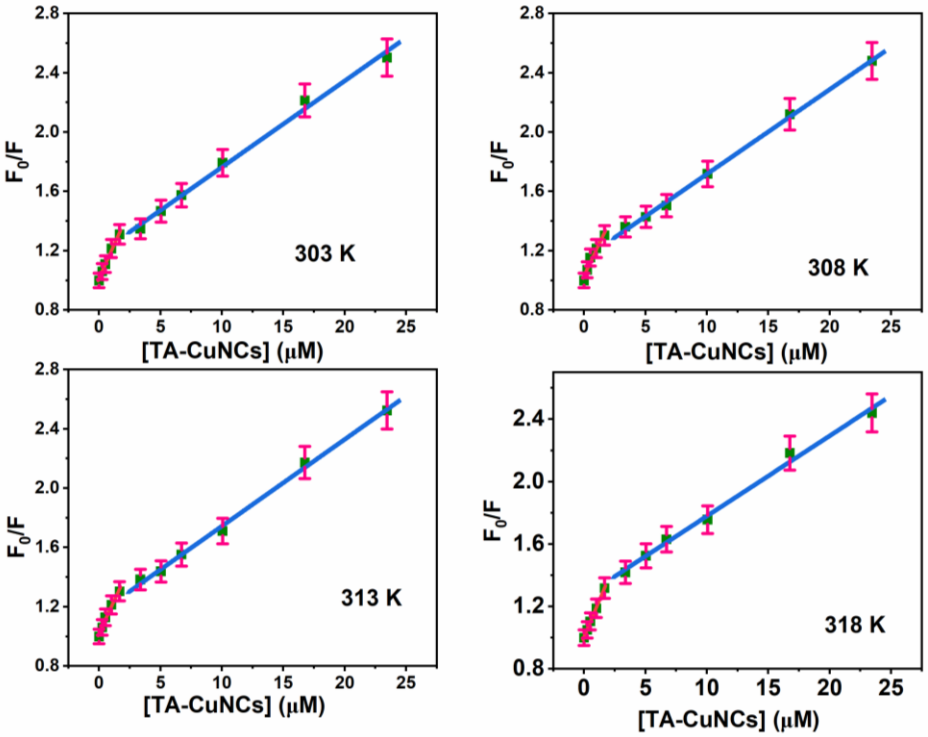

Figure APX4.12. Stern-Volmer plots for quenching of α-ChT fluorescence by TA-CuNCs at different temperature marked at each figure.

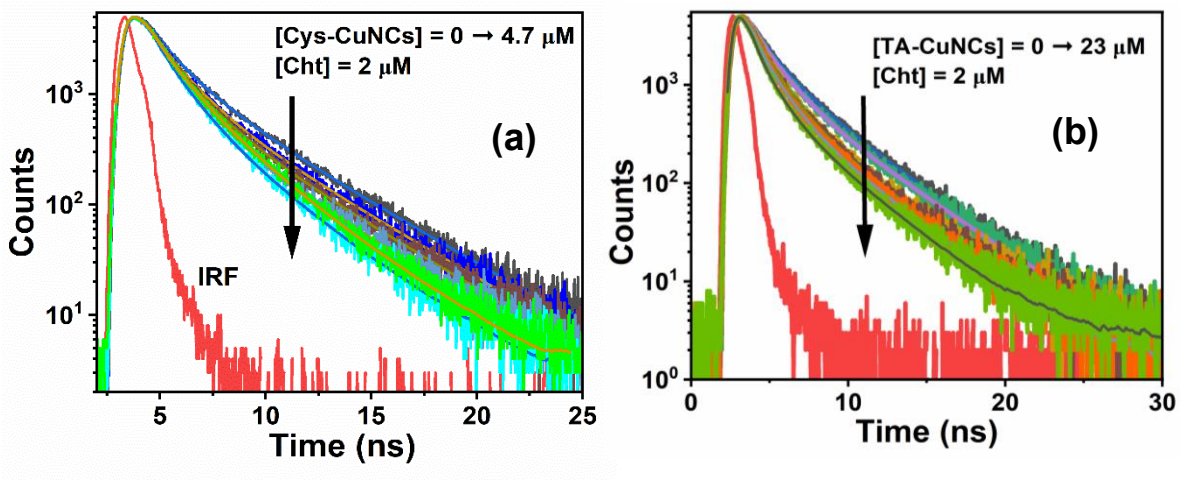

Figure APX4.13. Time resolved fluorescence decay curve of α-ChT in absence and presence of (a) Cys-CuNCs ans (b) TA-CuNCs, recorded using excitation wavelength of 280 nm.

Table APX4.1. Fluorescence decay parameters of α-ChT in phosphate buffer of PH = 7.4 with gradual addition of (a) Cys-CuNCs and (b) TA-CuNCs. [a]

[Cys-CuNCs]	α_1	τ_1	α_2	τ_2	α_3	τ_3	$\langle\tau\rangle$
0.00	40	0.54	40	1.54	20	3.89	1.61
0.12	40	0.43	45	1.33	15	3.77	1.34
0.24	40	0.39	47	1.25	13	3.59	1.20
5.00	43	0.47	47	1.29	9	3.19	1.11
[TA-CuNCs]	**α_1**	**τ_1**	**α_2**	**τ_2**	**α_3**	**τ_3**	**$\langle\tau\rangle$**
0.00	40	0.54	40	1.54	20	3.89	1.61
3.35	50	0.44	33.3	1.31	16.7	3.64	1.26
10.05	50	0.39	33.3	1.26	16.7	3.55	1.21
23.00	57.14	0.33	28.57	1.09	14.28	3.29	0.97

[a] concentration of CuNCs are in μM, α are expressed in % scale and τ values (±5 %) are in ns unit

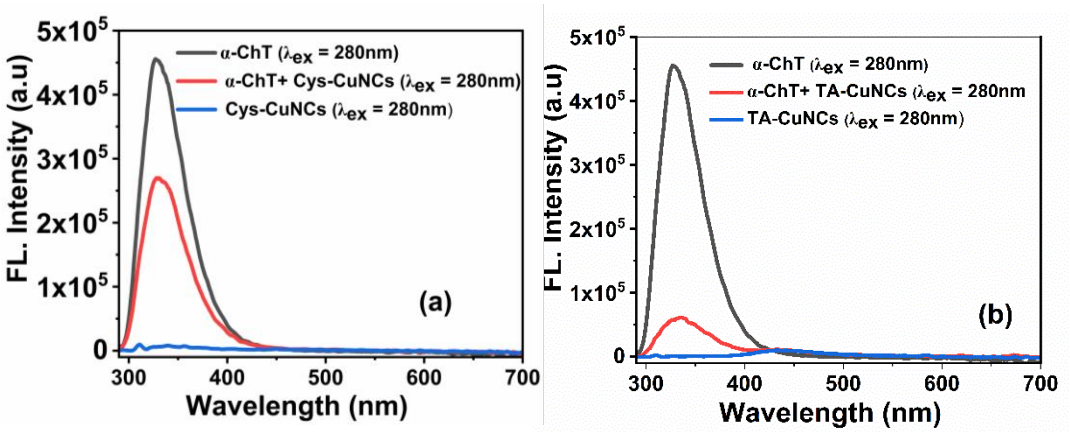

Figure APX4.14. Emission spectra of (a) α-ChT, α-ChT-Cys-CuNCs composite system, Cys-CuNCs and (b) α-ChT, α-ChT-TA-CuNCs composite system, TA-CuNCs (λ_{ex}=280 nm).

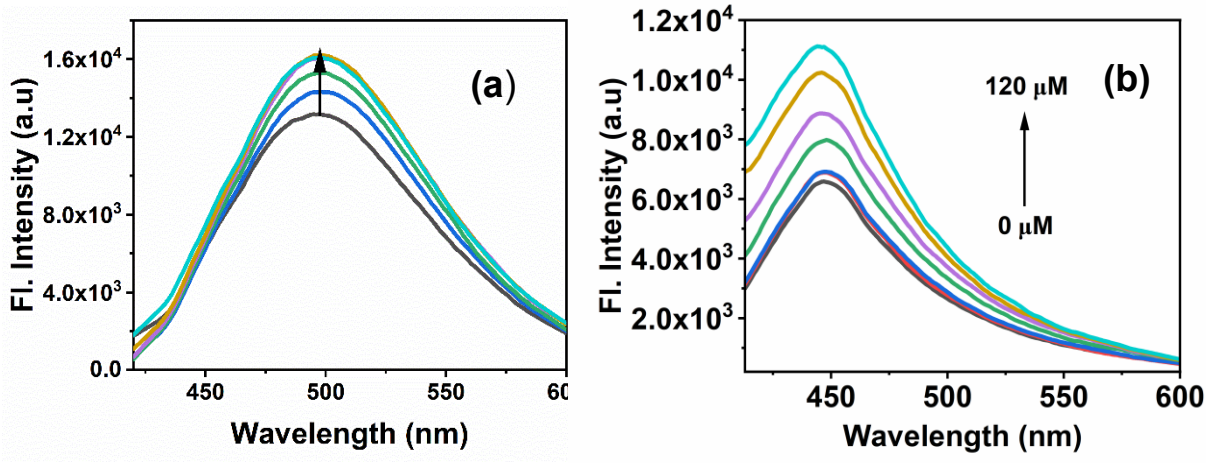

Figure APX4.15. Emission spectra of (a) Cys-CuNCs and (b) TA-CuNCs with gradual addition of α-ChT. (λex = 390 nm).

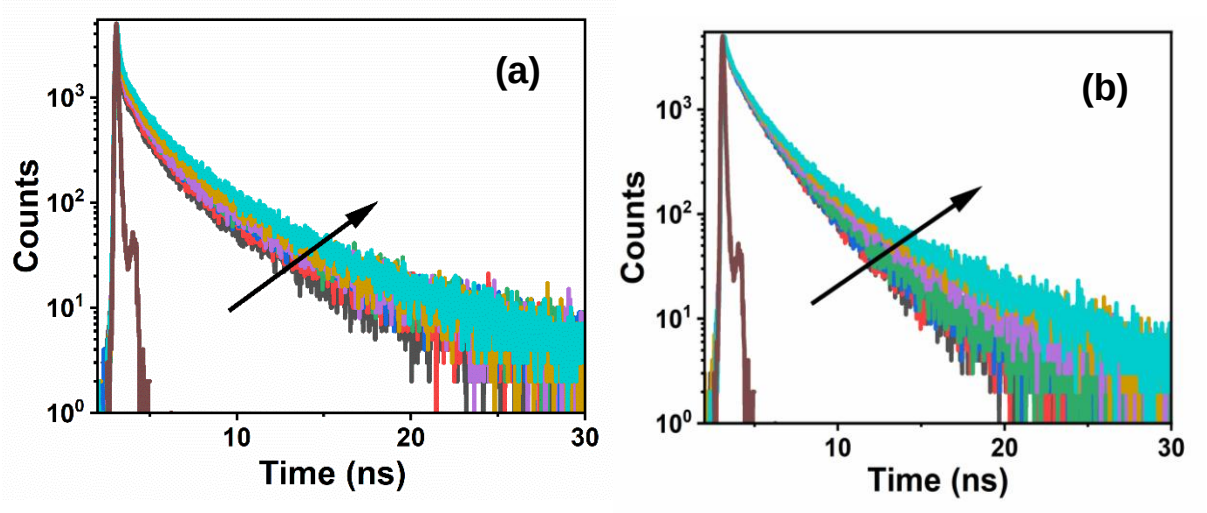

Figure APX4.16. Time resolved fluorescence decay curve of (a) Cys-CuNCs and (b) TA-CuNCs with gradual addition of α-ChT. (Concentration of these CuNCs are 10μM).

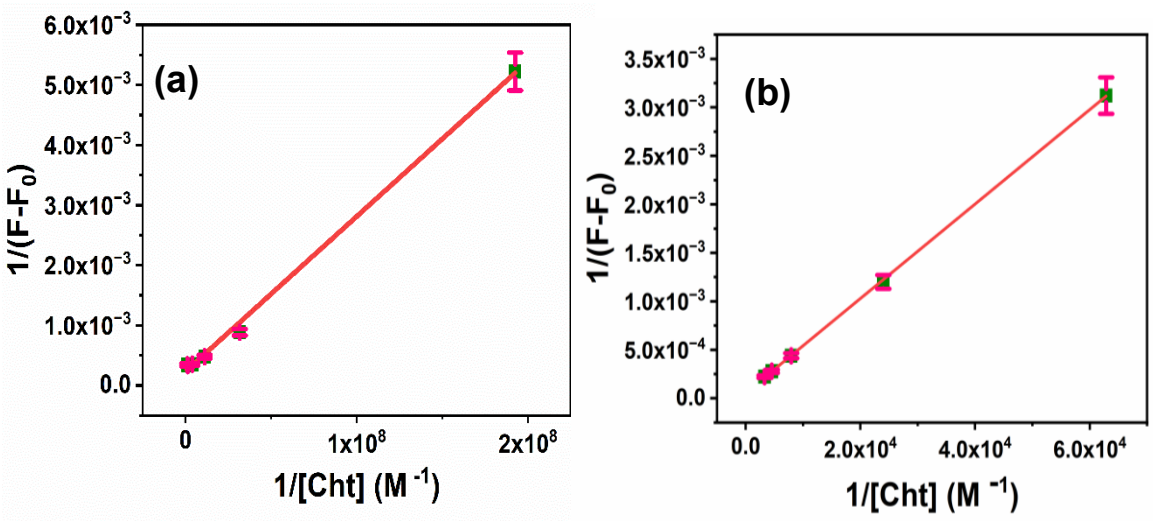

Figure APX4.17. Benesi-Hildebrand double reciprocal plot to determine the stoichiometric association of (a) Cys-CuNCs and (b) TA-CuNCs to α-ChT.

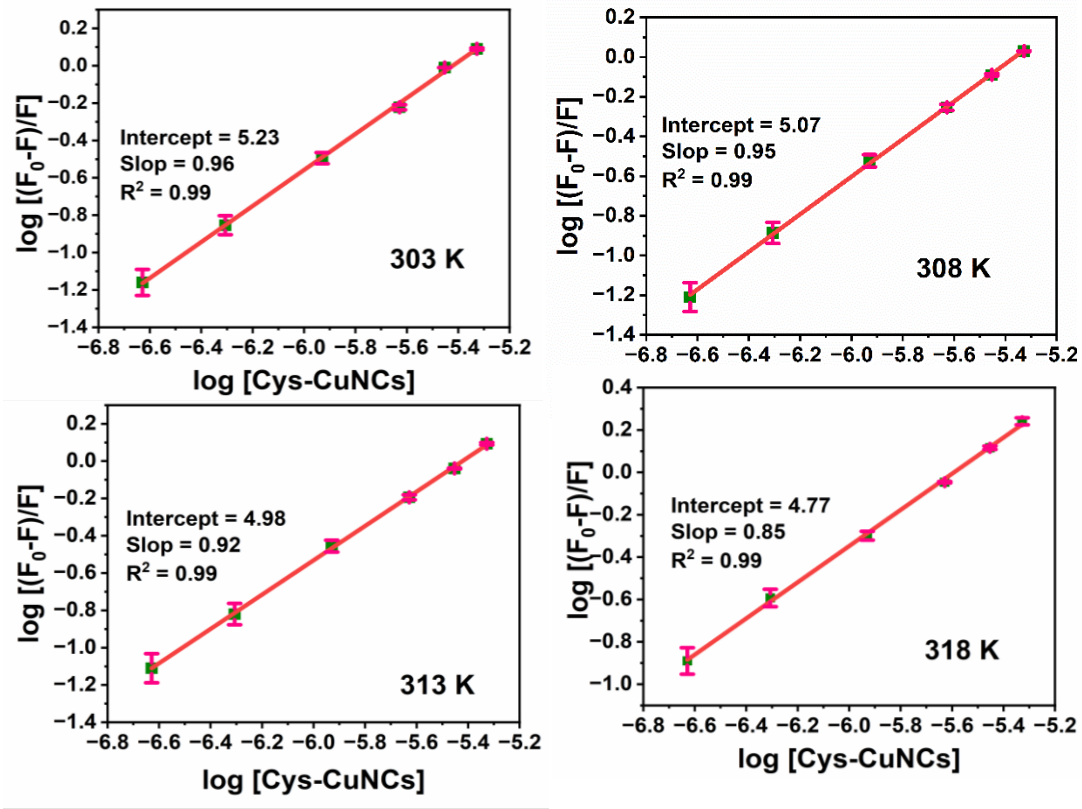

Figure APX4.18. Double logarithm plot for the binding of Cys-CuNCs with α-ChT at various temperatures marked at each figure.

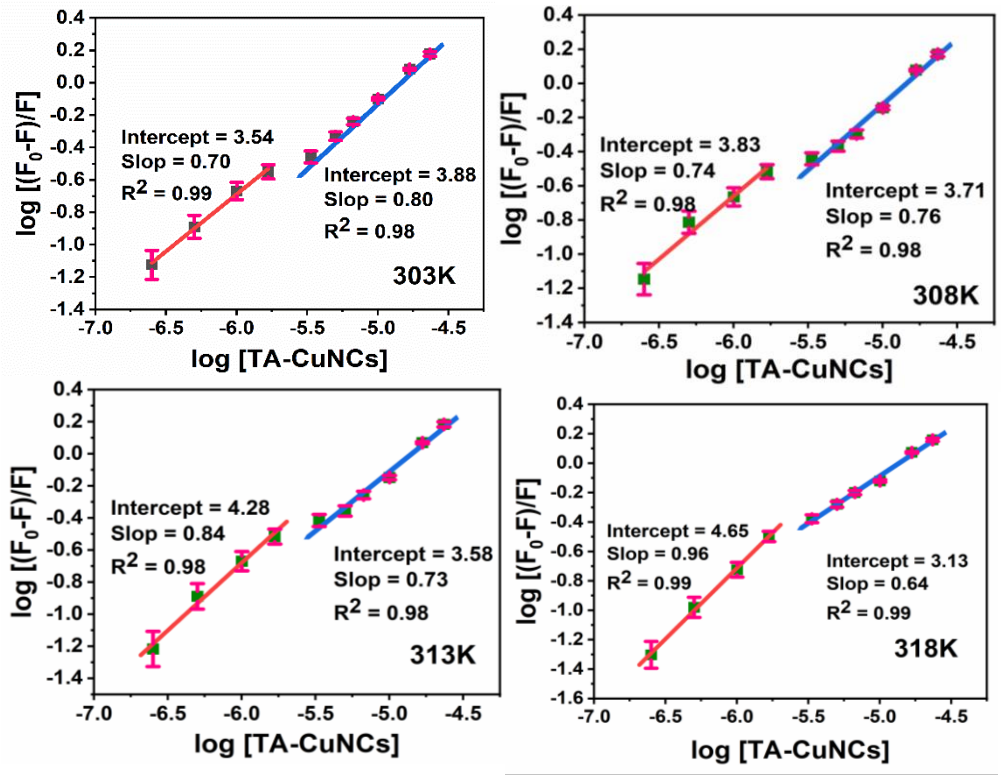

Figure APX4.19. Double logarithm plot for the binding of TA-CuNCs with α-ChT at various temperature marked at each figure.

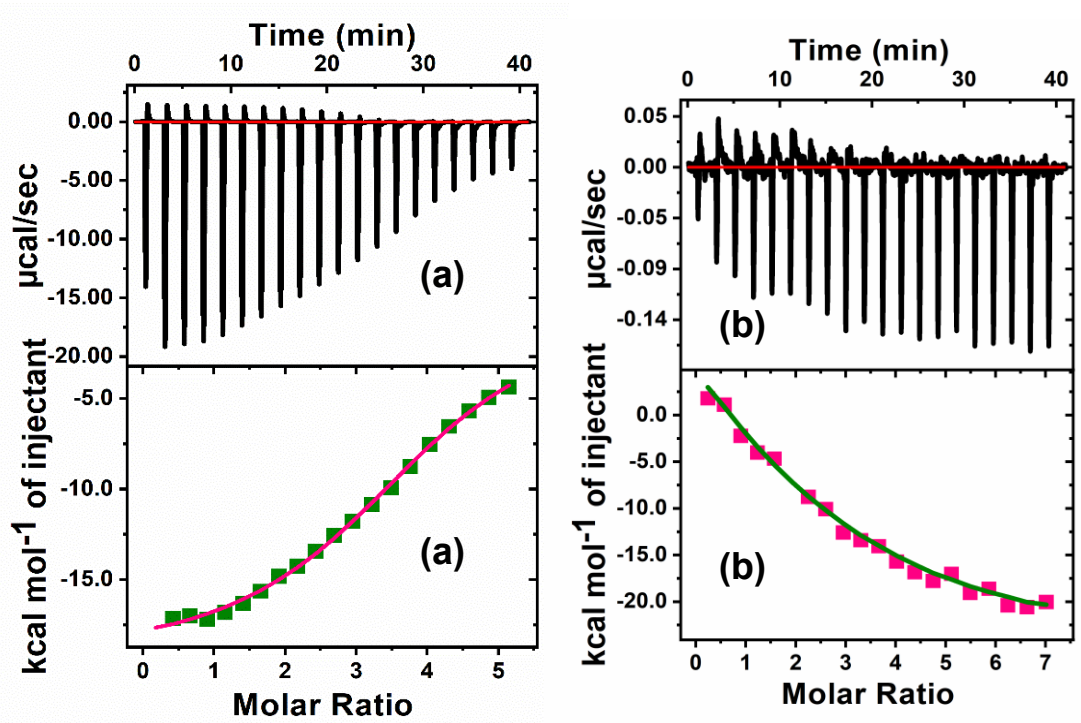

Figure APX4.20. ITC titration profile of (a) Cys-CuNCs, and (b) TA-CuNCs into α-ChT at 298 K in phosphate buffer of pH 7.4. (Top) Raw data obtained from the titrations and

(bottom) integrated heats of each peak (green dots) with a corresponding nonlinear regression plot (pink line).

Table APX4.2. Binding Constant (K_a) and Thermodynamic Parameters and for the Binding of Cys-CuNCs, and TA-CuNCs with α-ChT at 298 K Obtained by ITC Experiment. [a]

CuNCs	*Ka* (10^4) (M^{-1})	*ΔH* (kJ mol^{-1})	*ΔS* (JK^{-1} mol^{-1})	*ΔG* (kJ mol^{-1})
Cys-CuNCs	K_1 = 1.30 ±1.6	ΔH_1 = -76.57±3.40	ΔS_1 = -177.66	ΔG = -23.47
TA-CuNCs	K_1= 2.92 ± 4.6	ΔH_1 = 298.2 ±3.40	ΔS_1 = 874.21	ΔG_1= -25.47
	K_2= 15.7±1.6	ΔH_1 = -512.20±3.85	ΔS_2 = -630	ΔG_1= -29.64

[a] ± 5

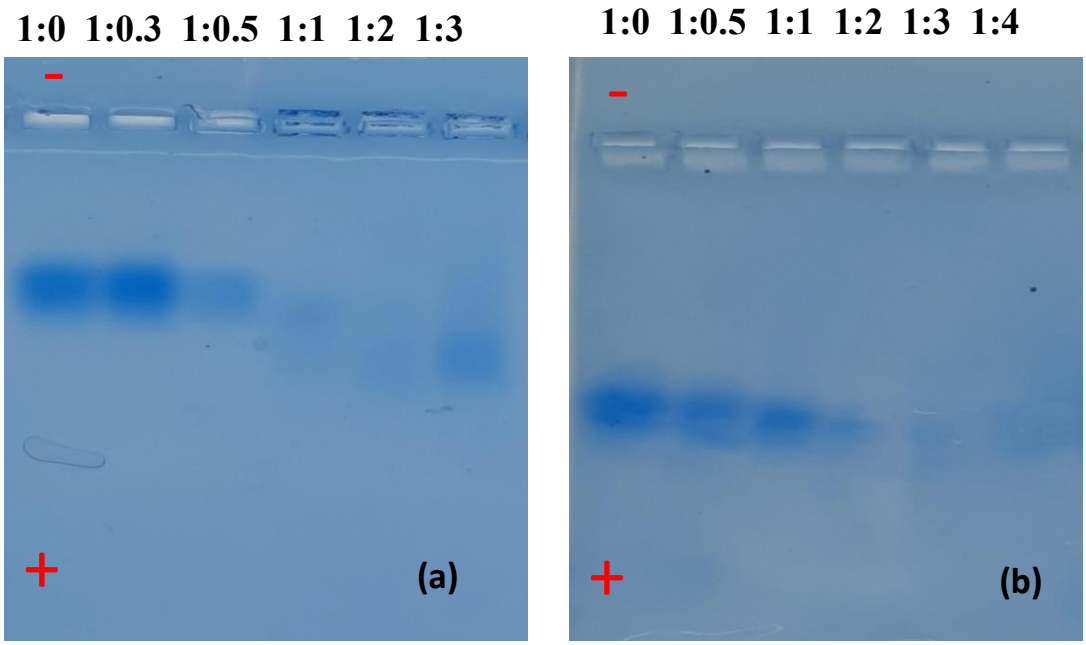

Figure APX4.21. Agarose gel electrophoresis of (a) α-ChT and Cys-CuNCs and (b) α-ChT and TA-CuNCs at various ratio. CuNCs concentrations are varied at a constant ChT concentration (30 μM)**.**

Fluorescence Correlation Spectroscopy (FCS)

FCS experiments were done by using a time resolved confocal microscope (MicroTime 200, PicoQuant) equipped with a water immersion objective (60 × /1.2 NA). The excitation source was a pulsed diode laser (λ_{Ex} = 403 nm, full width at half-maximum (FWHM) = 144 ps). A pinhole having a diameter of 50 μm was used for the spatial filtration of the signal and focused through a 50/50 beam splitter before entering the two single-photon avalanche diodes (SPADs). For the calibration of the FCS setup, rhodamine-6G solution in water medium has been used. All FCS curves were analyzed using SymPhoTime software (PicoQuant) by applying pure diffusion model to obtain the corresponding values of τ_d for CuNCs with increasing concentration of α-ChT. The correlation function, G(τ), for fluorescence and intensity fluctuation is given by eq APX4.1

$$G(\tau) = \frac{(<\delta F(t)\delta F(t+\tau)>}{<F(t)>^2} \qquad \text{(APX4.1)}$$

where F(t) is the average fluorescence intensity and δF(t) and δF(t + τ) are the fluctuations from the average fluorescence intensity at time t and t + τ, respectively.

From the Stokes−Einstein equation, the hydrodynamic radii of CuNCs and CuNCs with α-ChT systems are determined, which is given by using eq APX4.2

$$R_H = \frac{KT}{6\pi\eta D} \qquad \text{(APX4.2)}$$

Table APX4.3. The associated diffusion parameters of CuNCs systems with increasing concentration of α-ChT as obtained from FCS study

CuNCs (100 nM)	α-ChT (μM)	τ_D(μs)	R_H(nm)
	0	34.4	0.62
	0.28	40.6	0.73
Cys-CuNCs	1.00	104.3	1.89

	1.50	167.2	3.03
	2.50	170.4	3.09
TA-CuNCs	0	41.0	0.74
	0.28	67.5	1.22
	1.00	96.2	1.74
	1.50	150.3	2.72
	2.50	156.1	2.83

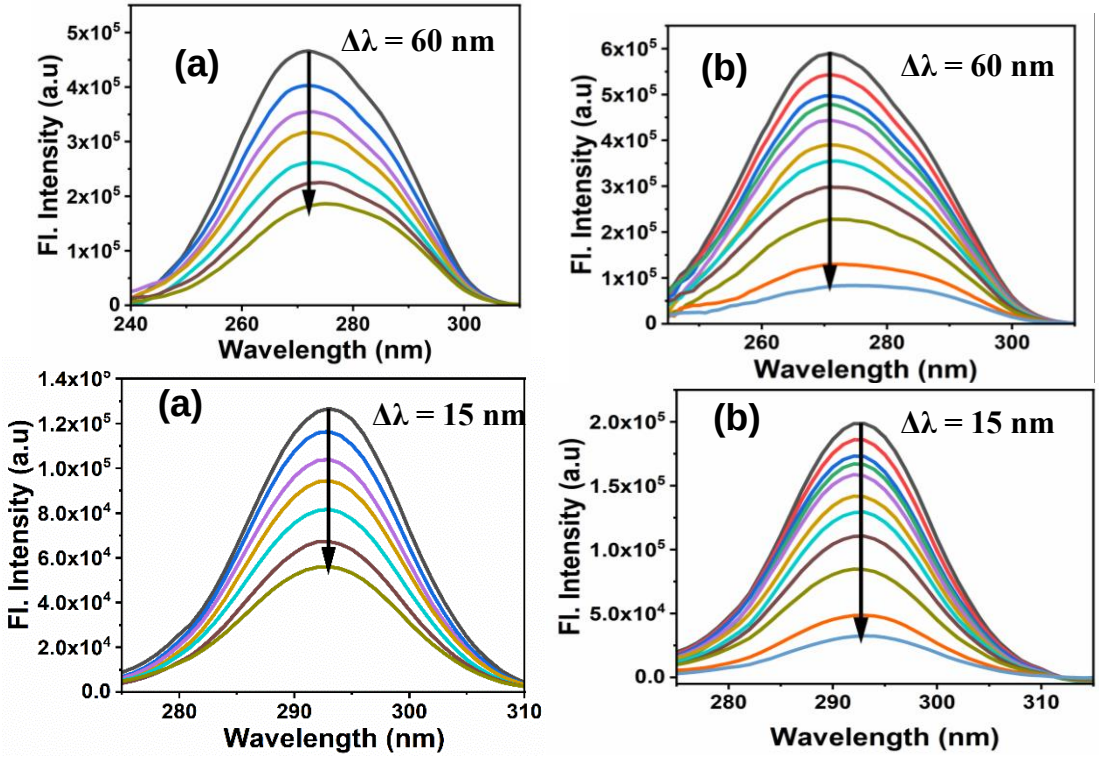

Figure APX4.22. Synchronous fluorescence spectra of α-ChT with the increasing concentration of (a) Cys-CuNCs, and (b) TA-CuNCs at 298 K. (Top) Spectra with offset wavelength 60 nm and (bottom) spectra with offset wavelength of 15 nm.

References

1. Fowkes, F. M. *Ind. Eng. Chem.* **1964**, *56*, 40-52.
2. Saha, B.; Saikia, J.; Das, G. *Analyst* **2015**, *140*, 532-542.
3. Ribatti, D. *Leuk. Res.* **2009**, *33*, 638-644.
4. Roskoski, R. *Pharmacol. Res.* **2016**, *111*, 784-803.
5. Denton, R. M., *Biochim. Biophys. Acta Bioenerg.* **2009**, *1787*, 1309-1316.
6. Copeland, R., Enzymes, A. Wiley-VCH: New York **2000**.
7. Schwab, A.; Illarionov, B.; Frank, A.; Kunfermann, A.; Seet, M.; Bacher, A.; Witschel, M. C.; Fischer, M.; Groll, M.; Diederich, F. *ACS Chem. Biol.* **2017**, *12*, 2132-2138.
8. Sarkar, K.; Dastidar, P., *Chem. Eur. J.* **2018**, *24*, 11297-11302.
9. Stayton, P. S.; Shimoboji, T.; Long, C.; Chilkoti, A.; Ghen, G.; Harris, J. M.; Hoffman, A. S. *Nature* **1995**, *378*, 472-474.
10. Ding, Z.; Fong, R. B.; Long, C. J.; Stayton, P. S.; Hoffman, A. S. *Nature* **2001**, *411*, 59-62.
11. Chen, M.; Zeng, G.; Xu, P.; Lai, C.; Tang, L. *Trends Biochem. Sci.* **2017**, *42*, 914-930.
12. Yin, F.; Cao, R.; Goddard, A.; Zhang, Y.; Oldfield, E. *J. Am.Chem. Soc.* **2006**, *128*, 3524-3525.
13. Tan, Z.; Bruzik, K. S.; Shears, S. B. *J. Bio. Chem.* **1997**, *272*, 2285-2290.
14. Ding, K.; Lu, Y.; Coleska, Z. N.; Qiu, S.; Ding, Y.; Gao, W,; Stuckey, J.; Krajewski, K,; Roller, P. P.; Tomita, Y.; Parrish, D. A.; Deschamps, J. R.; Wang, S. *J. Am.Chem.Soc.* **2005**, *127*, 10130-10131.
15. Kozikowski, A. P.; Sun, H.; Brognard, J.; Dennis, P. A. *J. Am.Chem.Soc.* **2003**, *125*, 1144-1145.
16. Cha, S.-H.; Hong, J.; McGuffie, M.; Yeom, B.; VanEpps, J. S.; Kotov, N. A. *ACS Nano* **2015**, *9*, 9097-9105.
17. Martino, S.; Tiribuzi, R.; Tortori, A.; Conti, D.; Visigalli, I.; Lattanzi, A.; Biffi, A.; Gritti, A.; Orlacchio, A. *Clin. Chem.* **2009**, *55*, 541-548.
18. Chou, S. S.; Kaehr, B.; Kim, J.; Foley, B. M.; De, M.; Hopkins, P. E.; Huang, J.; Brinker, C. J.; Dravid, V. P. *Angew. Chem. Int. Ed.* **2013**, *52*, 4160-4164.
19. Hong, R.; Fischer, N. O.; Verma, A.; Goodman, C. M.; Emrick, T.; Rotello, V. M. *J. Am.Chem. Soc.* **2004**, *126*, 739-743.
20. De, M.; Chou, S. S.; Dravid, V. P. *J. Am.Chem. Soc.* **2011**, *133*, 17524-17527.
21. Zhang, B.; Xing, Y.; Li, Z.; Zhou, H.; Mu, Q.; Yan, B. *Nano Lett.* **2009**, *9*, 2280-2284.
22. Fischer, N. O.; McIntosh, C. M.; Simard, J. M.; Rotello, V. M. *PNAS* **2002**, *99*, 5018-5023.
23. Fischer, N. O.; Verma, A.; Goodman, C. M.; Simard, J. M.; Rotello, V. M. *J. Am. Chem. Soc.* **2003**, *125*, 13387-13391.
24. Hong, R.; Emrick, T.; Rotello, V. M. *J. Am. Chem. Soc.* **2004**, *126*, 13572-13573.

25. You, C.-C.; De, M.; Han, G.; Rotello, V. M. *J. Am. Chem. Soc.* **2005**, *127*, 12873-12881.
26. You, C.-C.; Agasti, S. S.; De, M.; Knapp, M. J.; Rotello, V. M. *J. Am.Chem. Soc.***2006**, *128*, 14612-14618.
27. Zhao, X.; Hao, F.; Lu, D.; Liu, W.; Zhou, Q.; Jiang, G. *ACS Appl. Mater. Interfaces* **2015**, *7*, 18880-18890.
28. Xu, M.; Yuan, S.; Chen, X.-Y.; Chang, Y.-J.; Day, G.; Gu, Z.-Y.; Zhou, H.-C. *J. Am. Chem. Soc.* **2017**, *139*, 8312-8319.
29. Ellappan, V.; Kesavan, M.; Ramalingam, P.; Kulandaivel, J.; Rajalingam, R. *Luminescence* **2015**, *30*, 978-989.
30. Li, H.; Kong, W.; Liu, J.; Yang, M.; Huang, H.; Liu, Y.; Kang, Z. *J. Mater. Chem. B* **2014**, *2*, 5652-5658.
31. Sun, X.; Feng, Z.; Hou, T.; Li, Y. *ACS Appl. Mater. Interfaces* **2014**, *6*, 7153-7163.
32. Liu, Y.; Yan, B.; Winkler, D. A.; Fu, J.; Zhang, A. A*CS Appl. Mater. Interfaces* **2017**, *9*, 18626-18638.
33. Peng, J.; Liu, S.; Yan, S.; Fan, X.; He, Y. *Colloids Surf. A: Physicochem. Eng. Asp.* **2010**, *359*, 13-17.
34. Chen, W.-Q.; Yin, M.-M.; Song, P.-J.; He, X.-H.; Liu, Y.; Jiang, F.-L. *Langmuir* **2020**, *36*, 6447-6457.
35. Yin, M.-M.; Chen, W.-Q.; Lu, Y.-Q.; Han, J.-Y.; Liu, Y.; Jiang, F.-L. *Nanoscale* **2020**, *12*, 4573-4585.
36. Yin, M.-M.; Chen, W.-Q.; Liu, Y.; Jiang, F.-L. *ACS Appl. Nano Mater.* **2019**, *2*, 408-417.
37. Akhuli, A.; Chakraborty, D.; Agrawal, A. K.; Sarkar, M. *Langmuir* **2021**, *37*, 1823-1837.
38. Akhuli, A.; Preeyanka, N.; Chakraborty, D.; Sarkar, M. *ACS Appl. Nano Mater.* **2022**, *5*, 5826-5837.
39. Palmal, S.; Basiruddin, S. K.; Maity, A. R.; Ray, S. C.; Jana, N. R. *Chem. Eur. J.* **2013**, *19*, 943-949.
40. Blow, D. M. *Acc. Chem. Res.* **1976**, *9*, 145-152.
41. Hedstrom, L. *Chem. Rev.* **2002**, *102*, 4501-4524.
42. Zhou, T.; Xu, W.; Yao, Q.; Zhao, T.; Chen, X. *Methods Appl. Fluoresc.* **2015**, *3*, 044002.
43. Cao, H.; Chen, Z.; Zheng, H.; Huang, Y. *Biosens. Bioelectron.* **2014**, *62*, 189-195.
44. Sahu, D. K.; Sahu, K. *J. Photochem. Photobiol. A* **2017**, *347*, 17-25.
45. Lin, Z.; Slee, T.; Mingos, D. M. P. *Chem. Phys.* **1990**, *142*, 321-334.
46. Mithani, S. D.; Bakatselou, V.; TenHoor, C. N.; Dressman, J. B. *Pharm Res* **1996**, *13*, 163-7.
47. Mouat, M. F.; Manchester, K. L. *Comp. Haematol. Int.* **1998**, *8*, 58-60.
48. Abou-Zied, O. K.; Al-Shihi, O. I. K. *J. Am. Chem. Soc.* **2008**, *130*, 10793-10801.
49. Paul, B. K.; Ray, D.; Guchhait, N. *Phys. Chem. Chem. Phys.* **2013**, *15*, 1275-1287.
50. Lakowicz, J. R., *S. pringer: USA*, **2006**, pp 55−472.

51. Ellappan, V.; Kesavan, M.; Ramalingam, P.; Kulandaivel, J.; Rajalingam, R. *Luminescence* **2015**, *30*, 978-89.
52. Valeur, B., *Wiley-VCH: Weinheim, **2002***.
53. Li, S.; Aphale, A. N.; Macwan, I. G.; Patra, P. K.; Gonzalez, W. G.; Miksovska, J.; Leblanc, R. M. *ACS Appl. Mater. Interfaces* **2012**, *4*, 7069-7075.
54. Devatha, G.; Roy, S.; Rao, A.; Mallick, A.; Basu, S.; Pillai, P. P. *Chem. Sci.* **2017**, *8*, 3879-3884.
55. Saha, S.; Majhi, D.; Bhattacharyya, K.; Preeyanka, N.; Datta, A.; Sarkar, M. *Phys. Chem. Chem. Phys.* **2018**, *20*, 9523-9535.
56. Wu, Z.; Jin, R. *Nano Lett.* **2010**, *10*, 2568-2573.
57. Daniel, M.-C.; Tsvetkova, I. B.; Quinkert, Z. T.; Murali, A.; De, M.; Rotello, V. M.; Kao, C. C.; Dragnea, B. *ACS Nano* **2010**, *4*, 3853-3860.
58. Gomez, S.; Philippot, K.; Collière, V.; Chaudret, B.; Senocq, F.; Lecante, P. *Chem. Comm.* **2000**, 1945-1946.
59. Paramanik, B.; Kundu, A.; Chattopadhyay, K.; Patra, A. *RSC Adv.* **2014**, *4*, 35059-35066.
60. Cedervall, T.; Lynch, I.; Lindman, S.; Berggård, T.; Thulin, E.; Nilsson, H.; Dawson, K. A.; Linse, S. *PNAS* **2007**, *104*, 2050-2055.
61. Shang, L.; Nienhaus, G. U. *Int. J. Biochem. Cell Biol.* **2016**, *75*, 175-179.
62. Casals, E.; Pfaller, T.; Duschl, A.; Oostingh, G. J.; Puntes, V. *ACS Nano* **2010**, *4*, 3623-3632.
63. Mallick, A.; Haldar, B.; Chattopadhyay, N. *J. Photochem. Photobiol. B, Biol.* **2005**, *78*, 215-221.
64. Nepal, D.; Geckeler, K. E. *Small* **2007**, *3*, 1259-1265.
65. Mu, Q.; Liu, W.; Xing, Y.; Zhou, H.; Li, Z.; Zhang, Y.; Ji, L.; Wang, F.; Si, Z.; Zhang, B.; Yan, B. *J. Phys. Chem. C* **2008**, *112*, 3300-3307.
66. Anand, U.; Jash, C.; Mukherjee, S. *J. Phys. Chem. B* **2010**, *114*, 15839-15845.
67. Santra, M. K.; Banerjee, A.; Rahaman, O.; Panda, D. *Int. J. Biol. Macromol.* **2005**, *37*, 200-204.
68. Ross, P. D.; Subramanian, S. *Biochemistry* **1981**, *20*, 3096-3102.
69. Islam, M. M.; Barik, S.; Sarkar, M. *J. Phys. Chem. B* **2019**, *123*, 1512-1526.
70. Huang, R.; Lau, B. L. T. *Biochim. Biophys. Acta - Gen. Subj.* **2016**, *1860*, 945-956.

CHAPTER 5

Turn-Off Detection of Reactive Oxidative Species and Turn-On Detection of Antioxidants Using Fluorescent Copper Nanoclusters

The present work has been undertaken with an aim to design and develop a material-based nanoscale fluorescence sensory system for the selective and sensitive detection of both highly reactive oxidative species (hROS) and antioxidants in a single chemical entity by exploiting two optically distinguishable useful signals. For this purpose, water-soluble, chitosan-capped fluorescent copper nanoclusters (CuNCs) have been synthesized and characterized by using conventional methods. The sensory action of the CuNCs for several analytes of interest has been investigated at both ensemble-averaged and single-particle levels by exploiting spectroscopic and microscopic techniques. The steady-state fluorescence studies have revealed that CuNCs can act as a very efficient turnoff sensor for hROS (• OH and ClO−) and also a turn-on sensor for antioxidants (ascorbic acid and glutathione). Interestingly, it has been demonstrated that the present sensory system is quite effective in detecting antioxidants in commercial fruit juice and human blood samples at low concentration levels. The feasibility of the hROS sensing ability of CuNCs at single-particle levels is also demonstrated with the help of fluorescence correlation spectroscopy (FCS). Analysis of the data obtained from X-ray photoelectron spectroscopy (XPS) has clearly indicated that the mechanism of turn-off sensing is due to the oxidation of Cu(0)NCs to Cu(II) by hROS. On the other hand, fluorescence studies have revealed that the turn-on sensing mechanism is due to the presence of antioxidants, which prevents the oxidation of CuNCs by hROS. More interestingly, investigation has also demonstrated that the optical output signals of the probe−analyte interaction during the hROS/antioxidant signaling can successfully be exploited to construct NAND and IMPLICATION logic gates. Essentially, the outcome of the present investigation demonstrates that CuNCs not only can be effectively used as a nanoscale sensor for both hROS and antioxidants but also have the potential to be used for electronics and medical diagnostics purposes.

5.1. Introduction

In recent times, the development of fluorescent probes for detecting reactive oxygen species (ROS), such as superoxide (O^{2-}), hydrogen peroxide (H_2O_2), hydroxyl radical (•OH), hypochlorite (ClO^-), peroxynitrite ($ONOO^-$), etc. have drawn immense attention from the scientific community because of their essential roles in the physiological events such as

aging, cancer, inflammation, regulatory functions, signaling, and so on.[1-3] It is known that an appropriate level of ROS generated in metabolic processes acts as important signaling molecules, and thus, several physiological functions have been regulated by this class of species.[4,5] In the human body, the burden of ROS production is balanced by a complex antioxidant defense system, including the enzymatic scavenger's superoxide dismutase (SOD), catalase, and glutathione peroxidase. [6,7] Among these ROS, •OH, ClO^- and $ONOO^-$ are known to be highly reactive due to their substantial oxidant property, and for that, these species are also called highly reactive oxidative species (hROS). Therefore, it can be easily realized that excessive intracellular accumulation of hROS, as well as a defective antioxidant system, can directly oxidize nucleic acids, lipids, and proteins, leading to potentially serious damage in living cells.[8,9] Moreover, factors such as stress, excessive alcohol intake, and smoking, along with other environmental factors, such as radiation and toxins, are also known to be causing an increase in ROS levels in the human body system.[1,10,11] Therefore, the detection of these ROS is crucial for our well-being. We note here that antioxidants such as ascorbic acid (AA), glutathione (GSH), etc., play a crucial role in fighting oxidative stress by counteracting and regulating overall ROS levels to maintain physiological homeostasis that is essential for cell growth and function.[12-14] It is also noted that the intake of antioxidants through fruits and vegetables helps in maintaining adequate antioxidant levels in the human body.[15] Therefore, it is also crucial to detect the presence of antioxidants in various sample types, e.g., pharmaceutical, food, cell biology, etc, and their detection is also important for the diagnosis of some diseases and their therapy in clinical chemistry.[16-19] Therefore, the detection of ROS along with antioxidants can be a worthwhile objective to pursue. Several methods have been developed for the detection of ROS and antioxidants by exploiting fluorescence spectroscopy,[16,17,20-23] chemiluminescence derived methods,[24,25] chromatography method,[26-28] electrochemical biosensors,[19,29,30] electron spin resonance method[31,32,] etc.

Among these methods, fluorescence-based techniques have significant advantages because of their simplicity, high sensitivity, and non-destructive nature.[33] It has been observed that commonly molecular-based organic fluorescent probes have been designed for the detection of ROS and antioxidants. However, subsequent research works have revealed that these organic probes have some limitations in terms of their use in real applications as these probes suffer from their low solubility in aqueous medium, susceptibility to photobleaching, spontaneous autoxidation, complex chemical synthesis, and biotoxicity.[34-36] Moreover, while detecting the above-mentioned analytes, in most of the cases, two different types of molecular-based probes have been used separately. So, it will be interesting to detect these two types of analytes by using a singular chemical entity. In recent times, people have attempted to design and develop material-based sensory systems by miniaturizing to the nanoscale level, which gives several advantages over molecular-based sensors, such as photostability, large surface-to-volume ratio, lowering available detection limits, reducing the amount of the involved sensing chemicals, etc.[37-43] The development of nanomaterials provides a new direction in sensor development for detecting biologically and environmentally important analytes.[40-43] Therefore, it is desirable to have a material-based nanosensor that can overcome the above- mentioned limitations of the molecular-based organic probes and is capable of detecting both ROS as well as antioxidants through two distinguishable optical output signals.

In this perspective, we note that metal nanoclusters (MNCs) have drawn a great deal of attention from researchers due to their ultra-small size (< 2nm), low toxicity, useful optical properties, and good water solubility, which make them ideal candidates for sensing, bio-analysis, labeling, and bio-imaging application.[37,38,44,45] Among these MNCs, gold and silver nanoclusters have been widely studied for a wide variety of biochemical applications, such as sensing, in vitro and in vivo imaging, and cancer therapy.[40-43,46-51] In this context, it is

relevant to mention here that Chu and coworkers have shown that the fluorescence of Au-NCs has been quenched by highly reactive oxygen species (hROS), including •OH, ClO^-, and $ONOO^-$ and live-cell imaging of hROS has been developed by using AuNCs decorated silica nanoparticles as a fluorescent probe. Recently, Kashab and co-workers[41] have reported a quantitative spectroscopic method for the detection of antioxidant such as ascorbic acid through "light on" mechanism using AuNCs and hydroxyl radical (•OH). In another work, Changqing and co-workers [42] have shown turn-on sensing of GSH based on the recovered fluorescence of the Au NC−Hg(II) system. Recently, Sachdev and co-workers[43] have reported the detection of hydroxyl and superoxide anion radicals using copper nanoclusters as ratiometric fluorescence probes. It may be noted here that even though several sensing studies of ROS and antioxidants have been done widely using AuNCs and AgNCs as fluorescence probes individually, fluorescence material-based nanoscale signaling systems that is designed and developed to detect both ROS and antioxidants are rather limited. To the best of our knowledge, only AuNCs have been used as a singular chemical entity by Kashab and co-workers[41] for the detection of both ROS and antioxidants. Similar studies based on CuNCs are elusive even though copper has biological importance and favorable properties like good biocompatibility, low cost, high water solubility, and ready availability.[53] The cost-effectiveness of CuNCs is its biggest advantage over other metal nanoclusters. These properties make the CuNCs better candidates for simpler applications. In particular, detection of •OH and ClO^- through the turn-off mechanism and antioxidants through the turn-on mechanism by using CuNCs as singular material-based nanoprobe is elusive. So, it will be of paramount importance if a copper-based nanosensor for the detection of both ROS and antioxidants is designed and developed. Moreover, it will also be interesting if the optical output signals of the probe-analyte interaction event can successfully be exploited to construct molecular logic gate. This can act as an added advantage as multiple logic gates

constructed from different molecules, and molecular-like materials have drawn considerable attention from researchers due to their potential application in electronics as well as chemical and biological computers.[54,55]

Keeping the above facts in mind, water-soluble, chitosan-capped copper nanoclusters have been synthesized. The present work is carried out to address two-fold objectives; firstly, to fabricate CuNCs that can be used for sensitive and selective detection of hROS such as •OH, ClO^- and also to detect important antioxidants in various real samples by exploiting two optically distinguishable output signals and secondly, to construct molecular logic gates by exploiting outcome of the probe-analytes interaction events. Steady-state absorbance and emission, time-resolved fluorescence study, X-ray photoelectron spectroscopy (XPS), and fluorescence correlation spectroscopy (FCS) have been carried out to investigate the sensory action of the probe in the absence and presence of the analytes at ensemble-average and single-particle level. Essentially, the outcome of the present investigation demonstrates that CuNCs can not only be effectively used as nanoscale sensor for both hROS and antioxidants but also it has the potential to be used in electronics and medical diagnostics purposes. A schematic diagram demonstrating the strategy for the detection of hROS and antioxidants by CuNCs is shown in scheme 5.1.

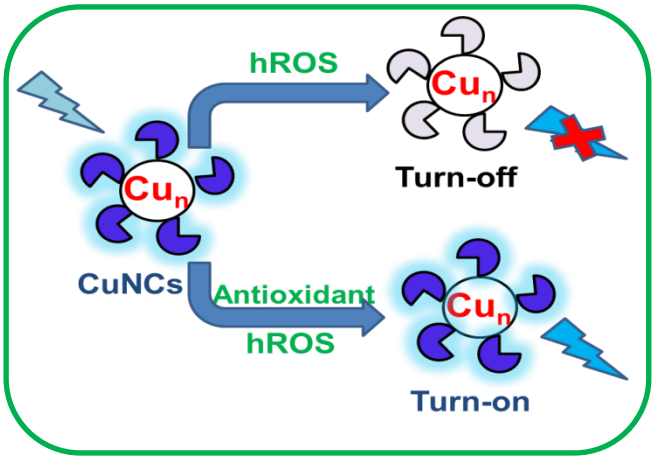

Scheme 5.1. Sensing Strategy for the detection of hROS and Antioxidants by CuNCs

5.2. In Vitro Generation of ROS and Sensing Analytes

Various ROS were generated by using documented protocols [40,58]. The aqueous NaOCl and H_2O_2 were freshly prepared in mili-Q water and their concentrations were determined from the UV absorption at 292 nm (ε = 350 M^{-1} cm^{-1}) and 240 nm (ε = 43.6 M^{-1} cm^{-1}) respectively. Hydroxyl radical (•OH) was generated on the basis of Fenton reaction by immediately mixing Fe^{2+} in H_2O_2 at a molar ratio of 1:10 in an acidic medium. Tert-butyl peroxyl radical (TBO•) was generated immediately by adding Fe^{2+} in the aqueous solution of TBHP. The concentration of both •OH and TBO• were equalled to the concentration of Fe^{2+} solution added. For the generation of superoxide anion radical ($O2^{\bullet-}$), KO_2 was dissolved in DMSO solution, and the solution was sonicated, and then molecular sieves were added to the solution to remove traces of water. Solutions of other analytes were prepared in mili-Q water. The Fluorescence property of CuNCs had been utilized for the detection of ROS. In brief, 300µL of CuNCs (stack solution) was added into 1.7 mL of phosphate buffer (pH 7.4), and then fluorescence titration study was performed with the addition of various concentrations of analytes. Each fluorescence data was collected after 10 minutes of incubation.

5.3. Antioxidant Sensing

For the detection of ascorbic acid (AA), 300 µL of as-prepared CuNCs was mixed with 1.7 mL of different concentrations of AA in phosphate buffer (pH 7.4) followed by an addition of 12.5 µM •OH. Similarly, for the detection of GSH, 300 µL of CuNCs was mixed with 1.7 mL of different concentrations of GSH in phosphate buffer (pH 7.4) followed by the addition of 36 µM ClO^-. After incubation for 10 min, the fluorescence spectra were taken at an excitation wavelength of 360 nm. Linear curves were obtained from the fluorescence data, which were used as a working curve for real sample analysis (*vide infra*). For the determination of ascorbic acid in commercial juice samples, the samples were centrifuged,

the supernatant was filtered through a 0.22 μm pore size filter membrane, and the samples were tested by following the procedure for AA detection. In brief, diluted fruit juice had been added to the fluorescence cuvette containing 300 μL of CuNCs, maintaining the total volume of 2ml. From the fluorescence data, we have determined the initial amount of ascorbic acid in that 2ml solution, i.e., the working cuvette concentration, by using the linear curve as a working curve (vide infra). The human blood samples were collected by venepuncture in EDTA-containing tube from the NISER health centre. The blood samples were treated according to the reported procedure.[59] In brief, to inhibit γ-glutamyltranspeptidase (GGT) activity, 40 μL of 100 mM serine−borate complex was added into 2 mL of human whole blood. Then, the sample was centrifuged at 12,000 rpm for 15 minutes at room temperature to remove hemocytes. The resultant supernatant was diluted and used for further analysis.

5.4. Result and Discussion

5.4.1. Responsiveness of CuNCs to hROS

The responsiveness of an ideal probe is characterized by its sensitivity to selectively identify analytes in the presence of interfering analytes. So, we have performed fluorescence titration experiments of CuNCs upon gradual addition of hROS (•OH and ClO^- separately) to determine the sensitivity of the probe for quantitative estimation of hROS. Representative fluorescence spectra of CuNCs in the absence and presence of various concentrations of •OH and ClO^- are provided in Figure 5.1a,b. Interestingly, from Figure 5.1 a,b, it can be seen that the fluorescence intensity of the probe has been significantly quenched by 91% and 90% in the presence of 12.5 μM •OH and 36 μM ClO^- respectively. Remarkably, a linear response of the change in the fluorescence intensity quenching of the probes against the concentration of hROS has been observed (Figure 5.1 c,d). The linear correlation between $(F_0\text{-}F)/F_0$ with the concentration of •OH has been observed in the concentration range of 0 to 7.5 μM (Figure 5.1

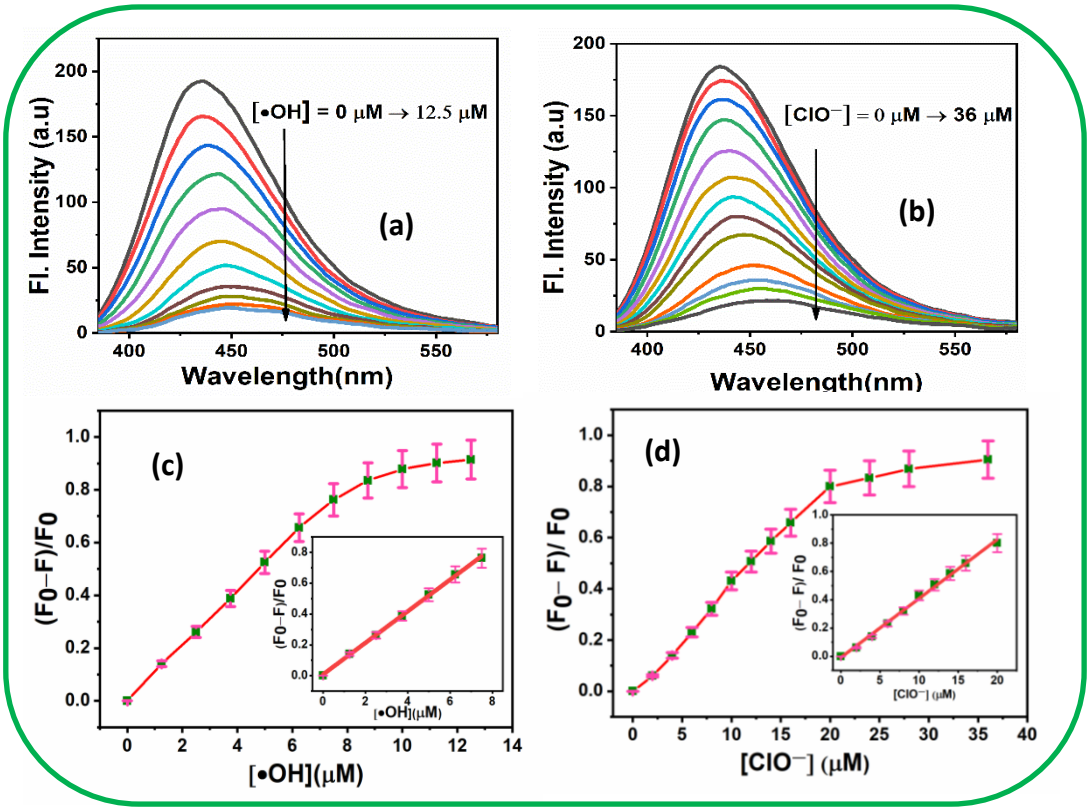

Figure 5.1. Fluorescence response of CuNCs upon addition of various concentrations of (a) •OH and (b) ClO^-; (c) plots of intensity ratio $(F_0\text{-}F)/F_0$ vs the concentrations of •OH and (d) plots of intensity ratio (F0-F)/F0 vs the concentrations of ClO^-; (Inset: linear fit of fluorescence intensity ratio versus concentration of analytes)

c), whereas for ClO^- the same linear correlation is observed in the concentration range of 0 to 20 μM (Figure 5.1d). More fascinatingly, the detection limits of this sensory system, estimated by '3σ' standard deviation rule [43] are found to be 0.1 μM, and 0.2 μM for •OH and ClO^- respectively, which fall well within the physiological concentration ranges for the detection of hROS.[40,60,61] This result is very exciting in the sense that the CuNCs have an excellent potential for the sensitive detection of hROS. Interestingly, when an aqueous solution of •OH and ClO− have been used as ink to write the symbols •OH and ClO−, respectively, on filter paper which is entirely covered with CuNCs, the symbols are found to be visible under UV-light but are found to be invisible under day-light (Figure 5.2). This

observation is fascinating in the sense that the CuNCs may also be used to develop security ink for confidential data encryption, anti-counterfeiting, and other innovative applications.

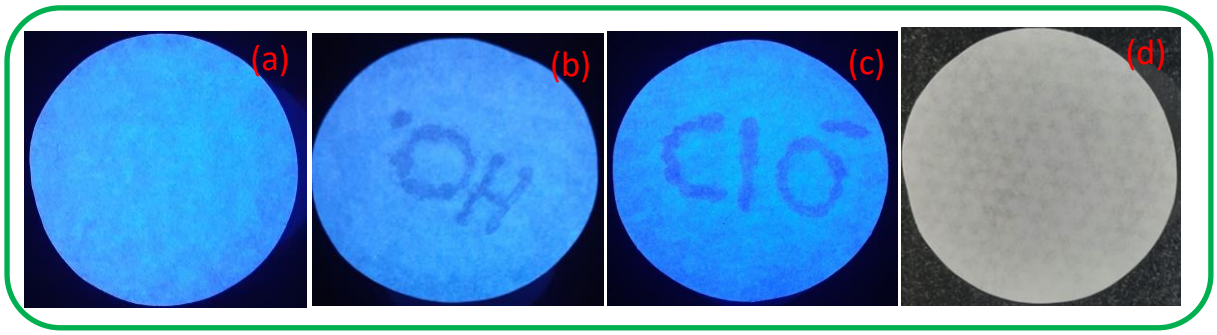

Figure 5.2. The photographs of (a) filter paper entirely covered with CuNCs (b) CuNCs covered filter paper with symbol •OH by using aqueous •OH as ink (c) CuNCs covered filter paper with symbol ClO^- by using aqueous ClO^- as ink under UV-light and (d) CuNCs covered filter paper with symbol •OH by using aqueous •OH as ink under day-light.

We have further resorted to the Stern-Volmer plot to understand the nature of fluorescence quenching of CuNCs in presence of hROS which is given by the eq (5.1)

$$\frac{F_0}{F} = 1 + K_{SV}[Q] \qquad (5.1)$$

where F_0 and F are the fluorescence intensities of CuNCs in the absence and presence of quencher, respectively and K_{SV} is the Stern−Volmer constant. The plots of F_0/F Vs quenchers are shown in Figure 5.3a,b. As seen from Figures 5.3a,b, both the SV plots for the analytes •OH and ClO^- follow upward curvature suggesting the feasibility of both static and dynamic quenching.[33] We have further performed time-resolved fluorescence study to confirm the dynamic component in the quenching event. The decay profiles of CuNCs in the absence and presence of hROS have been shown in Figure APX5.4, and the corresponding decay parameters are collected in Table APX5.1. It can be observed from the data obtained from the time-resolved fluorescence studies that the lifetime of CuNCs is decreased in the

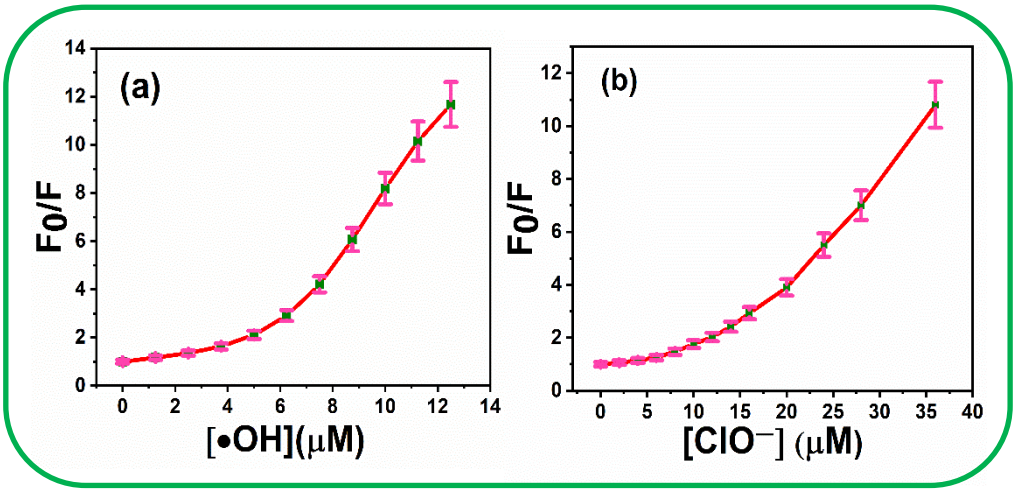

Figure 5.3. Stern−Volmer plots of CuNCs in the presence of (a) •OH and (b) ClO^- respectively.

presence of hROS, which confirms the involvement of the dynamic quenching process during the sensing event.

To gain deeper insight into the mechanistic aspect of the fluorescence quenching of CuNCs in the presence of hROS, we have analyzed the oxidation state of CuNCs in the absence and presence of hROS by X-ray photoelectron spectroscopy (XPS) and the corresponding deconvoluted XPS spectra are given in Figure 5.4. From Figure 5.4a, it can be seen that in the absence of hROS, the CuNCs show two peaks at 932.3 eV and 952.3 eV corresponding to the Cu 2p3/2 peak and Cu 2p1/2 peak, respectively, which indicates the presence of reduced copper rather than Cu (II) in CuNCs. Again, in the presence of hROS, the XPS spectra of CuNCs (Figure 5.4b,c) exhibit an additional peak at around 943 eV, which can be assigned to the characteristic peak of Cu(II). These results clearly indicate that the fluorescence quenching of CuNCs is due to the oxidation of Cu(0)NCs to Cu(II) by hROS. A similar explanation has been provided by other researchers while explaining the radical-induced oxidation of metal nanoclusters.[40,41,58,62] In this context, we also note that Wang and

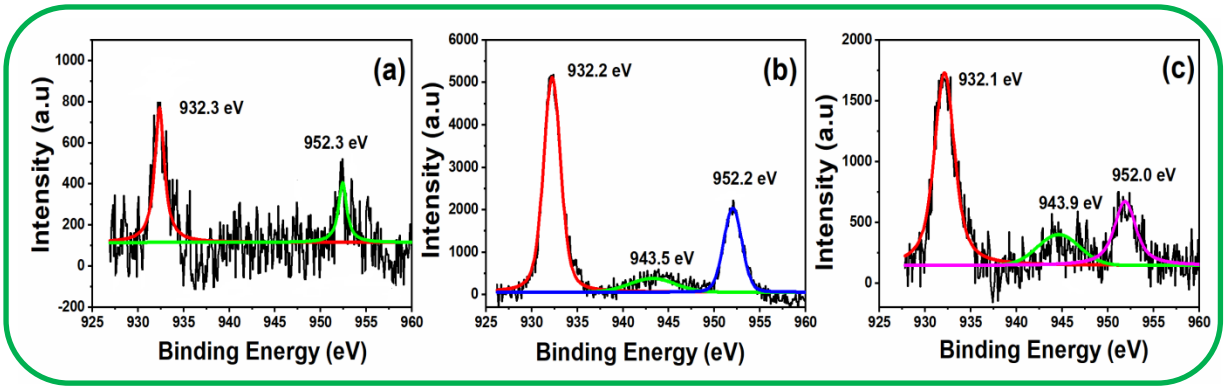

Figure 5.4. High-resolution Cu (2P) XPS spectra of (a) CuNCs (b) CuNCs in presence of •OH and (c) CuNCs in presence of ClO^-.

co-workers [57] have developed a sensory system based on CuNCs to detect HClO, and the mechanism of fluorescence quenching of the probe was attributed to the oxidation of reduced Cu on the surface of CuNCs by HClO. In another work, Jiang and co-workers [61] have synthesized GSH capped AuNCs for the detection of hROS and shown that hROS-mediated fluorescence quenching is due to the oxidation of AuNCs by hROS. In order to prove that the oxidation process is predominantly involved during the sensory action, we have taken UV-Vis spectra (Figure APX5.5) of CuNCs in the absence and presence of •OH and ClO^- separately. From Figure APX5.5, it has been observed that there is no surface plasmon resonance (SPR) peak, suggesting that larger Cu nanoparticles are not formed after the addition of those analytes. Again, from the TEM images (Figure APX5.6) of CuNCs, no noticeable change in the morphology of CuNCs, before and after the treatment of the sample with •OH and ClO^-, could be found. This result also suggests that the fluorescence quenching of CuNCs is predominantly due to the oxidation of CuNCs by •OH and ClO^-.

5.4.2. Selectivity of the Sensing System

In order to validate the selectivity of CuNCs for detecting hROS in practical applications, the fluorescence response of CuNCs has been monitored in the presence of other ROS and

species commonly present in biological matrices. The said response is depicted in a bar diagram (Figure 5.5a). From Figure 5.5a, it can be observed that non-oxidants, reductants and weak oxidants in the system have minimal effect with respect to hROS on the fluorescence responses of CuNCs which is in accordance with the oxidation based quenching mechanism.[40,41] Therefore, these results essentially indicate that CuNCs act as superior sensitive and selective nanosensor that can directly be utilized as a fluorescence sensory system for selective detection of hROS.

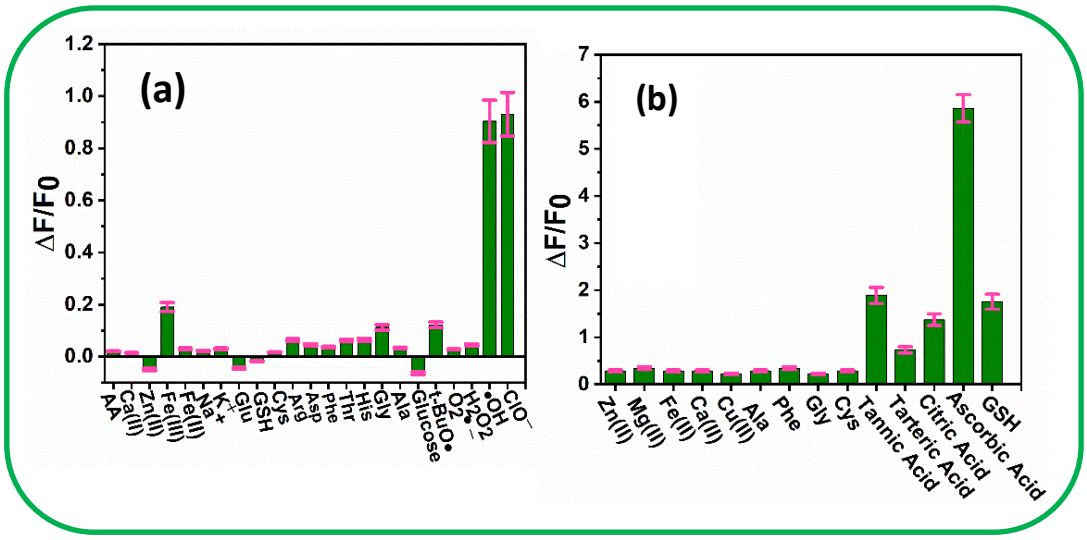

Figure 5.5. Fluorescence response of (a) CuNCs sensor in the presence of hROS (12.5 μM •OH and 36 μM ClO^-) and different coexistents (500 μM) and (b) CuNCs/•OH system in the presence of AA and different coexistents (350 μM).

5.4.3. Sensing of hROS at the Single-Particle Level

To shed light on the hROS sensing by CuNCs at the single-particle level, we have performed fluorescence correlation spectroscopy studies. This technique is widely used as an extremely sensitive and highly precise single-molecule technique that can monitor the small change in the fluorescence behavior of the probe at the nanomolar or sub-nanomolar regime. In this context, we note that Mukherjee and co-workers,[43] in their recent work, have demonstrated

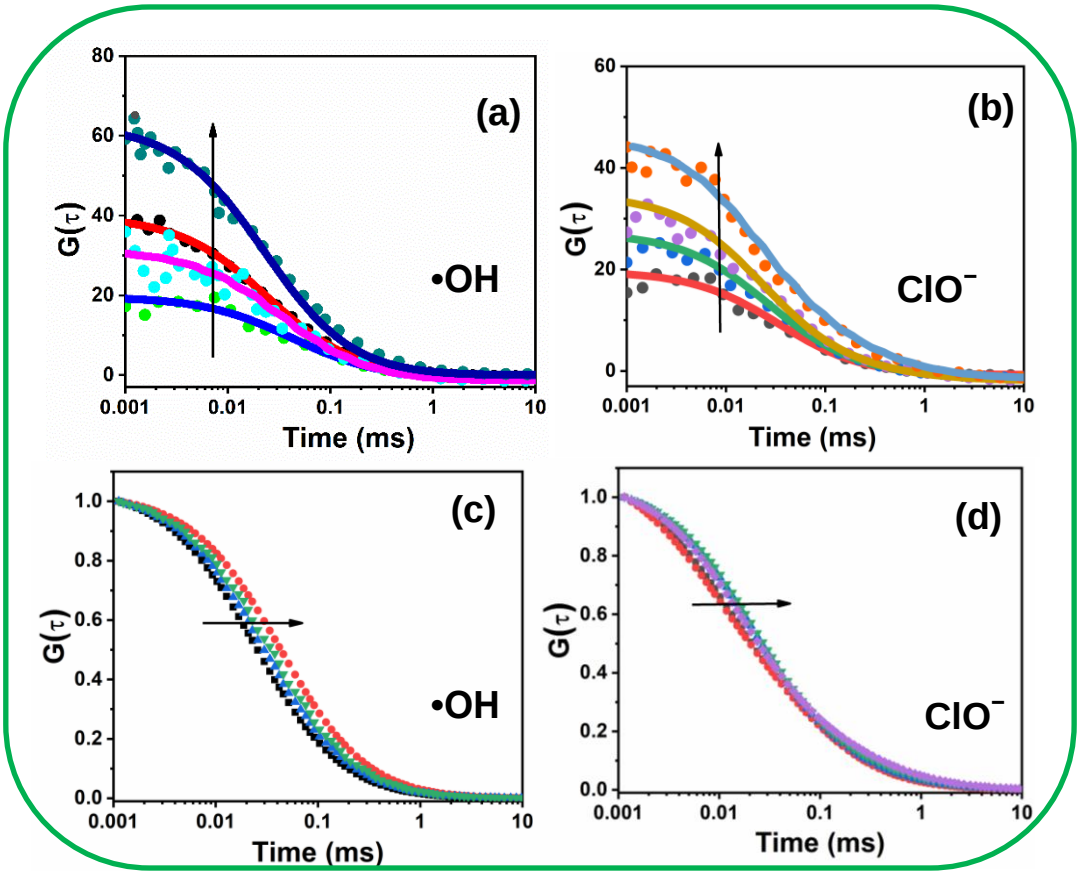

Figure 5.6. (a,b) Fluorescence correlation curves and (c,d) normalized fluorescence correlation curves of CuNCs with increasing concentrations of •OH and ClO^- (concentrations of CuNCs and analytes are 50 nM and 0−600 nM, respectively).

that the FCS technique can successfully be employed to monitor the fluorescence signaling of Hg(II) by AuNCs at the single-molecule level. Here, FCS study has been performed to understand the translational diffusion behaviour of CuNCs in the absence and presence of the analytes. As a slight perturbation can cause an appreciable change in their diffusion characteristics, we have monitored the translation diffusion time (τ_D) of CuNCs when subjected to increasing concentration of hROS and subsequently calculating hydrodynamic radius (R_H). Figure 5.6 shows the fluorescence correlation curves (Figure 5.6a,b) and their corresponding normalized correlation curves (Figure 5.6c,d) of CuNCs with the gradual addition of hROS. The right shift of normalized correlation curve (Figure 5.6c,d) of CuNCs

in the presence of hROS implies slower diffusion of the fluorophore, i.e. CuNCs, which results in the increase of diffusion time (τ_D) and hydrodynamic radius (R_H). Relevant parameters are tabulated in Table APX5.2. The τ_D and R_H of CuNCs are estimated to be 39.70 μs and 0.70 nm respectively but in the presence of •OH, the τ_D and R_H are found to increase to 66.44 μs and 1.20 nm respectively and in the presence of ClO^-, the τ_D and R_H are found to increase to 67.76 μs and 1.22 nm respectively. The increment of both τ_D and R_H of CuNCs after the addition of those analytes suggests there is some binding between CuNCs and the analytes. In agreement with the steady-state fluorescence studies, the FCS analysis of our CuNCs sensory system also reveals that this system can detect hROS at single-particle level in nanomolar regime.

5.4.4. Response of CuNCs to Various Antioxidants

As antioxidants play a vital role in maintaining the homeostasis of ROS in our body, it is very important to determine antioxidants in body fluids as well as in food items such as fruit juices. However, before going to real samples such as body fluids and fruit juices, we have investigated the response of the CuNCs system in the absence and presence of various commercially available well-known chemical antioxidants in order to have a proper understanding of the CuNCs−antioxidants interaction. The fluorescence intensity of CuNCs is found to be significantly quenched in the presence of •OH (Figure 5.1a); however, interestingly, the fluorescence intensity of CuNCs is observed to be almost constant even in the presence of •OH if ascorbic acid (AA) is added before addition of •OH (Figure APX5.7a). The observation of insignificant change in the fluorescence intensity of CuNCs by •OH in the presence of AA can be rationalized by considering the excellent antioxidant and efficient scavenger properties of •OH. During the course of the study, we have also tried to look at the fluorescence response of CuNCs in the presence of Fe (II) and H_2O_2 separately as they are used in Fenton reaction to produce •OH. It is observed from Figure APX5.7b that there is an

insignificant effect of fluorescent intensity of CuNCs in the presence of Fe (II) and H2O2 separately, but in the presence of both Fe (II) and H2O2, the fluorescence intensity is quenched ~ 91% , which also demonstrate the formation of •OH. To check the reversibility of the fluorescence quenching, we have added AA to the CuNCs, which is already quenched by •OH, but the fluorescence is found not to be recovered even after the addition of excess amount of AA, suggesting the irreversible oxidation of CuNCs by •OH.

To determine the sensitivity of the probe to AA, we have performed fluorescence titration measurements of CuNCs with increasing concentrations of AA in the presence of a fixed amount of •OH (12.5 μM). As shown in Figure 5.7a, the fluorescence intensity of CuNCs increases with the increasing concentration of AA. The correlation between $(F-F_0)/F_0$ with AA concentration shows linearity in the concentration range of 17.5-175 μM (Figure 5.7c) where F_0 is the fluorescence intensity of CuNCs/•OH system and F is the same of CuNCs/•OH system in the presence of AA. The limit of detection (LOD) [43] of AA is found to be 5 μM (3σ). The selectivity of the probe to AA in the presence of common biological species and different antioxidants has been investigated, and its corresponding data is shown in the bar diagram (Figure 5.5b). From Figure 5.5b, it can be observed that common biological ions and amino acids have a negligible effect on the fluorescence intensity of the sensory system, whereas for AA the effect (fluorescence increase) is found to be significant. The bar diagram also shows that other antioxidants have very little effect on the sensory system when the same is compared with AA. So, from this observation, one can infer that the antioxidant nature and •OH scavenging capacity of AA are mainly responsible for the increase in fluorescence intensity of CuNCs. Moreover, this outcome also suggests that CuNCs can effectively be used as a reliable and straightforward fluorescent probe for the turn-on detection of AA with negligible interference from other non-antioxidant molecules.

Additionally, we have also checked the detection of antioxidants by taking CuNCs in the presence of a fixed amount of ClO^- The fluorescence responsiveness of this system to different antioxidants with the coexistence of various common biological species has been shown in the bar diagram (Figure APX5.8). From Figure APX5.8, it can be seen that this sensory system is highly sensitive to selectively detecting GSH in the presence of other coexistence. For the quantitative determination of GSH, we have performed steady-state fluorescence measurement, which is given in Figure 5.7b. It has been seen from Figure 5.7b that the fluorescence intensity of CuNCs increases with the increasing concentration of GSH in the presence of a fixed amount of ClO^- (36 μM). The correlation between $(F-F_0)/F_0$ with the concentration of ClO^- shows linearity in the concentration range of 17.5-175μM (Figure 5.7d) where F_0 is the fluorescence intensity of CuNCs/ ClO^- system and F is the same of CuNCs/ ClO^- system in the presence of GSH. The LOD of GSH is found to be 4.5 μM (3σ). It is to be noted here that different hROS species added to the CuNCs can affect the response of the probe in term of estimating antioxidant for the following possible reasons: (a) Different nature of interactions between various antioxidants and CuNCs, (b) Different radical scavenging properties of various antioxidants towards various ROS and (c) Different antioxidant power of various antioxidants.

To shed more light on the CuNCs-antioxidant interaction event, we have tried to determine the binding stoichiometry ratio of CuNCs to AA and GSH separately. For this purpose, the fluorescence data have been analyzed based on the modified Benesi−Hildebrand (B−H) double reciprocal plots (Figure APX5.9a,b) by using eq 5.2 for 1:1 (AA : CuNCs) complexation and eq 5.3 for 3:2 (GSH : CuNCs) complexation [63] independently

$$\frac{1}{F-F_0} = \frac{1}{F_m - F_0} + \frac{1}{(F_m - F_0)K[AA]} \qquad (5.2)$$

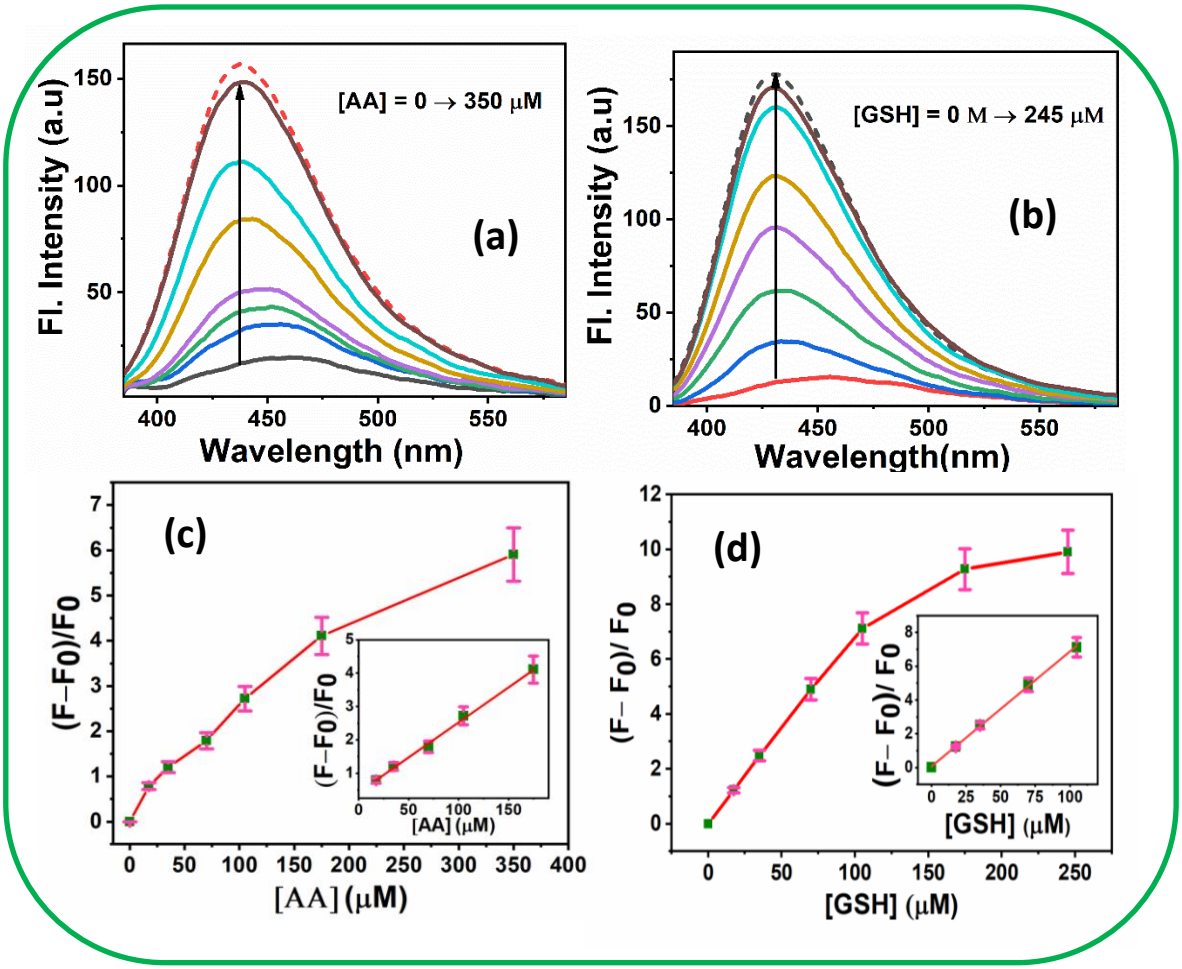

Figure 5.7. Fluorescence spectra of (a) CuNCs/•OH system in the presence of AA and (b) CuNCs/ClO^- system in the presence of GSH. Plots of intensity ratio $(F-F_0)/F_0$ vs the concentrations of (c)AA and (d) GSH (Inset: linear fit of fluorescence intensity ratio versus concentration of the analytes). The dashed line represents the emission of the CuNCs alone.

$$\frac{1}{F-F_0} = \frac{1}{F_m - F_0} + \frac{1}{(F_m - F_0)K[GSH]^{1.5}} \qquad (5.3)$$

where F and F_m are the fluorescence intensities of CuNCs with successive addition of analytes (AA or GSH), and at maximum analytes concentrations respectively, F_0 is the fluorescence intensity of CuNCs/•OH or CuNCs/ClO^- in the absence of analytes, and K is the equilibrium constant related to CuNCs and analytes association. From the plots, it is evident that a good linear correlation is obtained when $1/(F-F_0)$ is plotted against 1/[AA] and

$1/[GSH]^{1.5}$ for AA and GSH, respectively, which indicates a 1:1 (AA : CuNCs) and 3:2 (GSH : CuNCs) stoichiometric ratio for CuNCs to AA and GSH respectively. Moreover, we have performed fluorescence correlation spectroscopy (FCS) study to get insight into the interaction event between CuNCs and the antioxidants (AA and GSH) at single-molecule level. The normalized fluorescence correlation curves of CuNCs in the absence and presence of the analytes (AA and GSH) are given in Figure APX5.10a,b separately. From Figure APX5.10a,b, it has been observed that there occurs a shift in the normalized curves towards the right side with increasing concentration of the analytes, which suggests the increments of both the diffusion time (τ_D) and hydrodynamic radius (R_H) of CuNCs. The relevant parameters obtained from the FCS study are collected in Table APX5.2. The increase of diffusion time (τ_D) and hydrodynamic radius (R_H) of CuNCs upon the addition of the analytes substantiates the adsorption of the analytes onto the surface of CuNCs.

5.4.5. Analytical Applications

5.4.5.1. Application in Commercial Fruit Juices and Human Blood Samples.

Encouraged by the initial fluorescence response of CuNCs with antioxidants, we have also shown the practical application of the sensory system in real fruit juices and human blood samples. So, the CuNCs system is first applied to detect AA in various commercial fruit juices and GSH in human blood samples. The reliability of the proposed sensor has been checked by spiking the real samples with known amount of standard analytes and subsequently calculating its recovery using the following eq 5.4

$$Recovery\ (\%) = \frac{(C_{Total} - C_{Real})}{C_{Spiked}} \times 100 \qquad (5.4)$$

where C_{Total} is the concentration of analyte found in the spiked sample, C_{Real} is the concentration of analyte in the original real sample, and C_{spiked} is the concentration of the standard analyte spiked in the real sample. Recoveries of the added known amount of AA are

Table 5.1. Determination of AA in Commercial Fruit Juice Samples.[a]

Fruit Juices	Initial amount of AA (µM) (taken for volumetric titration) by DCPIP method	Initial amount of AA (µM) (Working Cuvette concentration) by fluorescence method	The added amount of AA (µM)	AA found (µM)	AA recovery (%)
Apple	74 ± 2.50	80.82 ± 2.00	50.00	133.00 ± 3.74	106.00 ± 3.15
Mango	125 ± 2.00	132.70 ± 4.15	20.00	152.51 ± 3.50	99.00 ± 4.00
Pomegranate	96 ± 2.00	101.00 ± 4.00	20.00	120.00 ± 2.50	95.00 ± 2.50

[a] Data presented are in means ± standard deviation (n = 3).

estimated to be in the range of 95% to 106 % , and that of GSH is estimated to be 97.4% to 104 %. This data is very interesting as it shows analytical recovery greater than 95 %, which indicates the practicability and reliability of the present method. According to the working curve and dilution ratio, AA concentrations in apple, mango, and pomegranate juices are estimated to be 16.16 mM, 53.10 mM, and 40.40 mM, respectively. These data are consistent with the standard DCPIP method[64,65], which has been discussed in the supporting information. In the case of blood samples, the concentration of GSH are estimated to be 849.20 µM And 900 µM for two healthy volunteers, which are in agreement with the reported standard methods.[66-69] The results that are obtained from the spike recovery method for

concentration of AA determination is tabulated in Table 5.1, and that of for GSH is given in Table APX5.3. These results confirm that the proposed method has great potential application in the determination of antioxidants in commercial fruit juices as well as human blood samples.

5.4.5.2. Application in Tap Water Sample

The significant responsiveness of the CuNCs towards ClO^- encourages us to show the practical applicability of the CuNCs for monitoring ClO^- in tap water samples. For this purpose, we have taken tap water from our laboratory without any pre-treatment. The change of fluorescence intensity of the CuNCs is insignificant in the presence of a small amount of tap water. So the presence of ClO^- in the blank sample could be ignored. The reliability of the proposed sensor has been checked by spiking the real samples with known amount of standard analytes (ClO^-) and subsequently calculating its recovery, which has been given in Table APX5.4, and these data are verified with the standard N,N-diethyl-p-phenylenediamine (DPD) method[57,70]. The UV-Vis spectra of DPD with increasing concentration of ClO^- and the standard curve of the DPD calorimetric method have been given in Figure APX5.11a and Figure APX5.11b, respectively. This result suggests that the CuNCs can be used as a probe for the quantitative determination of ClO^- in the real sample.

5.4.5.3. Molecular Logic Gate Construction of the Proposed Sensory System

Since molecular logic gates of various Boolean logic operations, constructed with biological and chemical molecules, have great potential for application in biosensor and bioimaging,[54,55] the optical outcomes of the current sensory events have been exploited to construct molecular logic gates. Here, specifically, the observed fluorescence response of CuNCs to hROS (•OH) and to hROS in the presence of antioxidants have inspired us to construct NAND and IMPLICATION molecular logic gates, respectively for its future practical applications. First,

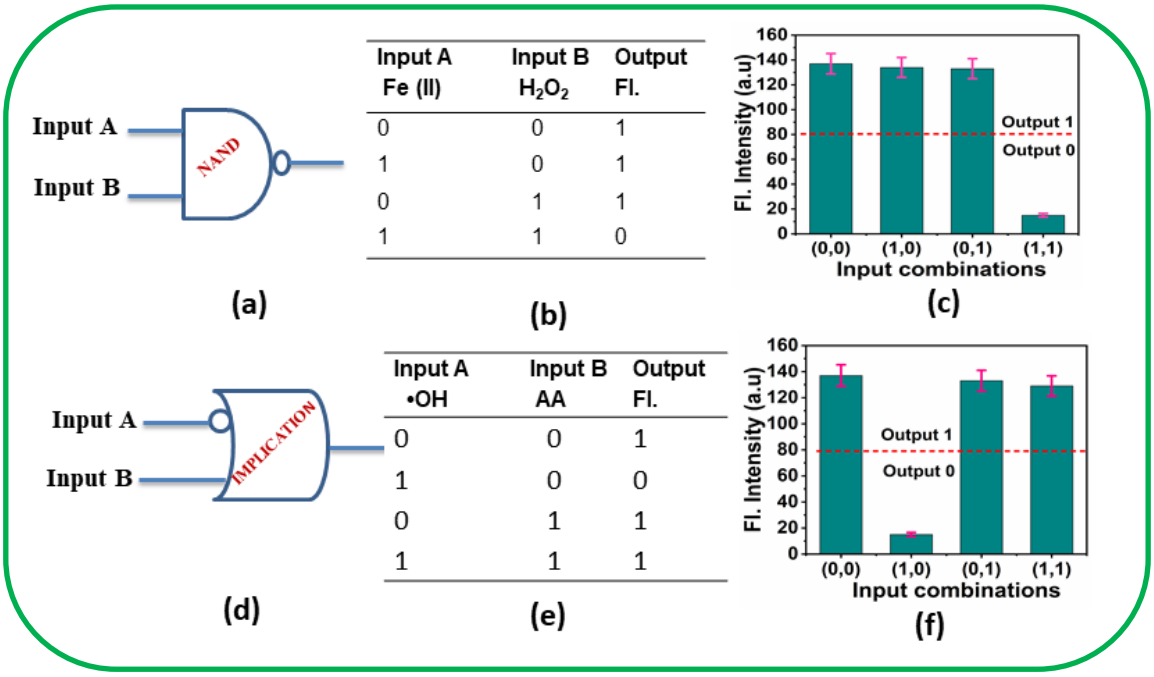

Figure 5.8. (a,d) Symbol, (b,e) truth table and (C,f) bar representation of the fluorescence intensities at λ_{ex}=360 nm (λ_{ex}=430) nm of NAND and IMPLICATION logic gate respectively.(The red dashed line shows the threshold of those logic gates).

the fluorescence response of CuNCs to •OH, which is generated from the Fenton reaction (mixing of ferrous ions with H_2O_2), has been employed to develop the NAND logic gate. The layout of this logic operation, truth table and corresponding fluorescence response of the interaction events are shown in Figure 5.8a,b,c. Please note that Fe (II) and H_2O_2 are taken as input A and input B, respectively and fluorescence intensity of CuNCs is taken as output for the NAND logic gate. In the truth table of the NAND logic gate (Figure 5.8b), the presence of Fe(II) or H_2O_2 is considered as 1, and their absence is considered as 0, and in the output, 1 is considered for the maximum fluorescence intensity and 0 for the corresponding quenched fluorescence intensity. As can be seen from Figure 5.8b, when both inputs are absent (0/0) or in the presence of either input (1/0, 0/1), the sensory system provides output 1. Please also note that, only the presence of both inputs (1/1) results a significant fluorescence quenching which gives output signal 0 in the NAND logic gate. Again, from the fluorescence response

of CuNCs with •OH and AA, a two-input IMPLICATION logic gate can be obtained. In the IMPLICATION logic gate operation, •OH and AA are considered as input A and input B, respectively. The layout of this logic operation, truth table, and corresponding fluorescence response of the interaction events are depicted in Figure 5.8d,e,f. We note here that the presence and absence of these inputs are taken as 1 and 0, respectively and for output, the maximum fluorescence intensity of CuNCs is taken as 1, and the corresponding quenched fluorescence intensity is taken as 0. One can see in the truth table of Figure 5.8e that four different states are developed due to the presence and/or absence of •OH and AA eg; (0, 0), (1, 0), (0, 1), and (1, 1). As can be seen in Figure 5.8e, only in the presence of •OH and in the absence of AA (1/0) the fluorescence of CuNCs gets quenched, and the output becomes 0, but in all other cases, the outputs remain as 1 and thus giving overall outcomes as IMPLICATION operation. The fluorescence spectra of the NAND and the IMPLICATION logic gates of all the systems are shown in Figure APX5.12.

5.5. Conclusion

In summary, we have designed and developed a material-based nanoscale fluorescent sensory system for the purpose of detecting both highly reactive oxidative species (hROS) as well as antioxidants in a single chemical entity by exploiting two optically distinguishable useful signals. To achieve this goal, water-soluble, chitosan capped fluorescent copper nanoclusters (CuNCs) has been synthesized and characterized by using conventional spectroscopic and microscopic methods. Steady-state absorption and fluorescence measurements, time-resolved fluorescence study, X-ray photoelectron spectroscopy (XPS) and fluorescence correlation spectroscopy (FCS) have been employed to investigate the sensory action of the probe in the absence and presence of several analytes of interest at both ensemble-averaged and single-particle level. Several interesting aspects in terms of CuNCs-analyte interaction events have been emerged from the current study. The results obtained from the steady-state fluorescence

studies have demonstrated that the CuNCs can act as a promising turn-off sensor for hROS (•OH and ClO^-) while the same system can act as turn-on sensor for antioxidants (AA and GSH) with high sensitivity and selectivity in the presence of other foreign substances. Quite interestingly, the nanoscale sensory system is found to be effective in determining GSH content in human blood samples and also AA content in different real fruit juice samples, which demonstrate the usefulness of the current sensory system for real practical application. Moreover, FCS studies have revealed the hROS sensing ability of CuNCs can also be achieved at single-particle level. The translational diffusion time (τ_D) and hydrodynamic radius (R_H) of the CuNCs increase significantly upon addition of the analytes indicating the probe-analytes interaction at single-particle level. Interestingly, XPS data have revealed that the fluorescence quenching of CuNCs in the presence of hROS can be rationalized in terms of the oxidation of Cu(0)NCs to Cu(II) by hROS. On the other hand, fluorescence Studies have revealed that the ability of antioxidants to protect the fluorescence intensity of CuNCs against quenching by hROS is primarily responsible for the turn-on sensing mechanism of the antioxidants. Additionally, the investigations have depicted that optical output signals obtained from the fluorescence response of CuNCs in presence of hROS and antioxidant can successfully be exploited to construct NAND and IMPLICATION logic gate. Overall, the outcome of the present investigations have demonstrated that CuNCs can not only be effectively used as nanoscale sensor for the detection of both hROS and antioxidants but also the system has the potential to be used in electronics and medical diagnostics purposes.

5.6. Appendix

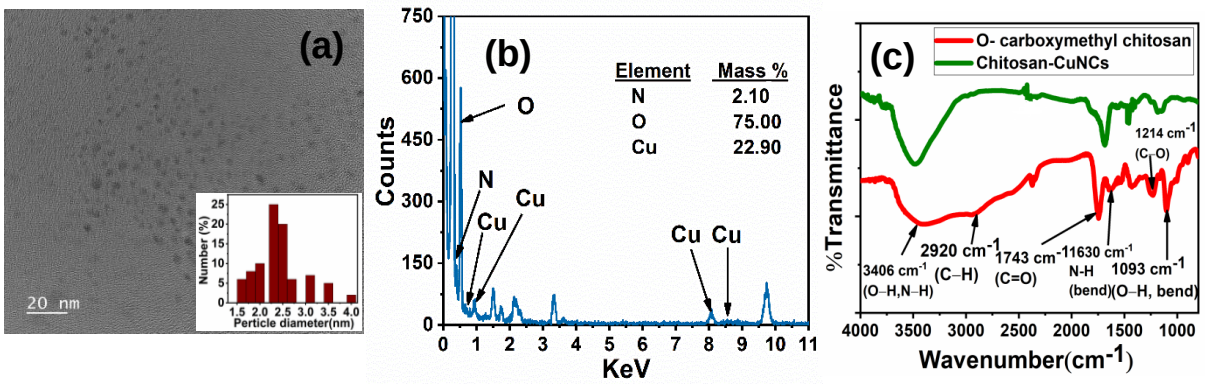

Figure APX5.1. (a) TEM images (inset: particle size distribution plot), (b) EDAX spectra and (c) FTIR spectra of CuNCs.

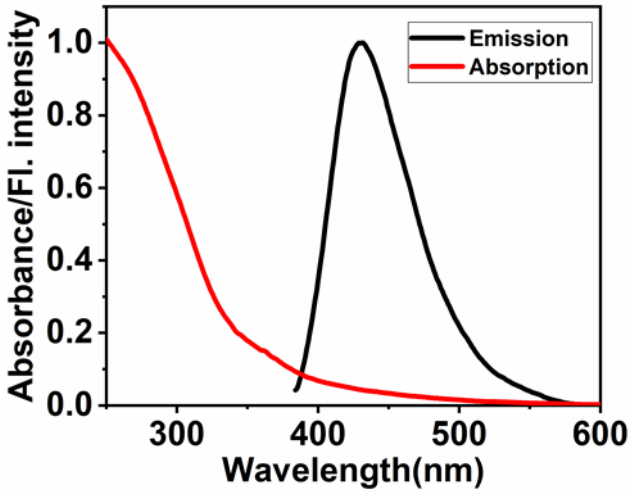

Figure APX5.2. Normalized absorption (red curve) and emission (black curve) of CuNCs in aqueous solution.

Stability of the CuNCs.

The stability the CuNCs in aqueous medium has been checked by monitoring the fluorescence intensity of CuNCs for a period of 30 days and the corresponding bar plot is provided in Figure APX5.3a. From the Figure APX5.3a, it can be clearly seen that the fluorescence intensity remain almost intact even after 30 days confirming the highly stable nature of the CuNCs in aqueous medium. This also suggests that the system may be usable for longer period of time. The stability of the CuNCs with the variation of pH value has also

been given in the Figure APX5.3b which demonstrates that the system is comparatively stable with the pH value from 5 to 8. Moreover, the stability of the CuNCs to ionic strength has been checked by monitoring the fluorescence intensity of CuNCs with the addition of various concentration of NaCl solution which has been given in the Figure APX5.3c. From the Figure APX5.3c, it can be seen that at higher NaCl concentration the fluorescence intensity of CuNCs has been affected to a little extent. All these experiments suggest that the synthesised CuNCs is highly stable.

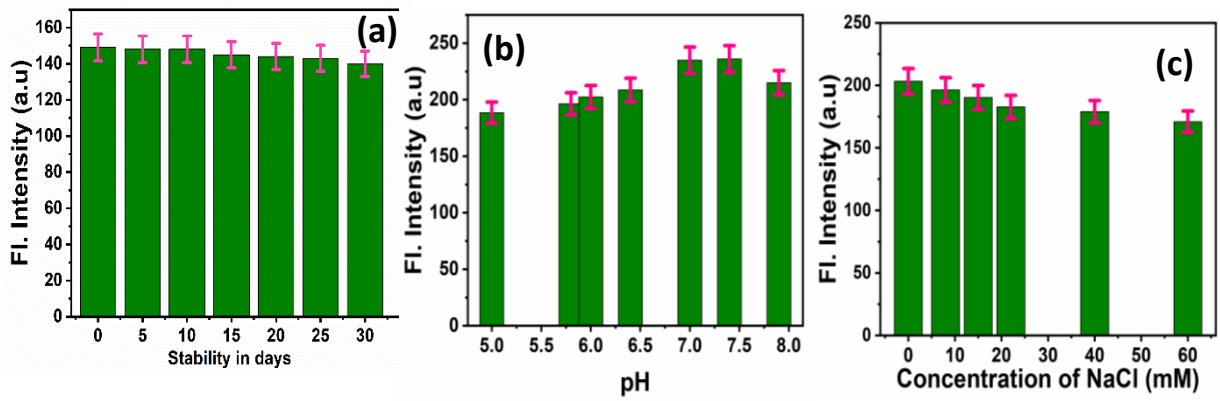

Figure APX5.3. The fluorescence stability of the CuNCs showed (a) in 30 days (b) with the variation of pH value (c) with the increasing concentration of NaCl.

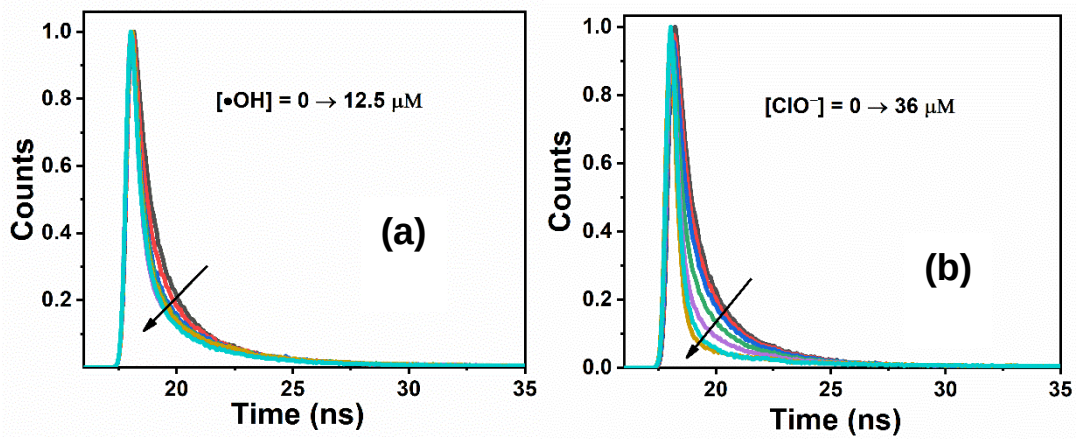

Figure APX5.4. Time resolved fluorescence decay curve of CuNCs in the absence and presence of (a) •OH and (b) ClO^-. The excitation wavelength is 375 nm.

Table APX5.1. Fluorescence decay parameters of CuNCs with the gradual addition of •OH and ClO^-. [a](The excitation wavelength is 375 nm)

[•OH](μM)	α_1	τ_1(ns)	α_2	τ_2(ns)	α_3	τ_3(ns)	$\langle\tau_{avg}\rangle$(ns)
0.00	68	0.63	31	2.09	1	13.12	1.16
2.50	76	0.37	22	1.92	1	8.98	0.85
5.00	81	0.34	18	2.15	2	12.9	0.80
7.50	80	0.36	19	2.03	2	10.57	0.79
10.00	80	0.33	19	1.77	2	9.34	0.75
12.50	83	0.31	15	2.06	1	12.13	0.71
[ClO^-](μM)	α_1	τ_1(ns)	α_2	τ_2(ns)	α_3	τ_3(ns)	$\langle\tau_{avg}\rangle$(ns)
0.00	68	0.63	31	2.09	1	13.12	1.16
4.00	67	0.58	32	2.01	1	12.18	1.12
10.00	68	0.53	32	1.93	1	11.33	1.05
16.00	72	0.41	28	1.78	1	10.53	0.87
30.00	82	0.32	17	1.74	1	11.65	0.66

[a] α are expressed in % scale and τ values (± 5 %) are in ns unit

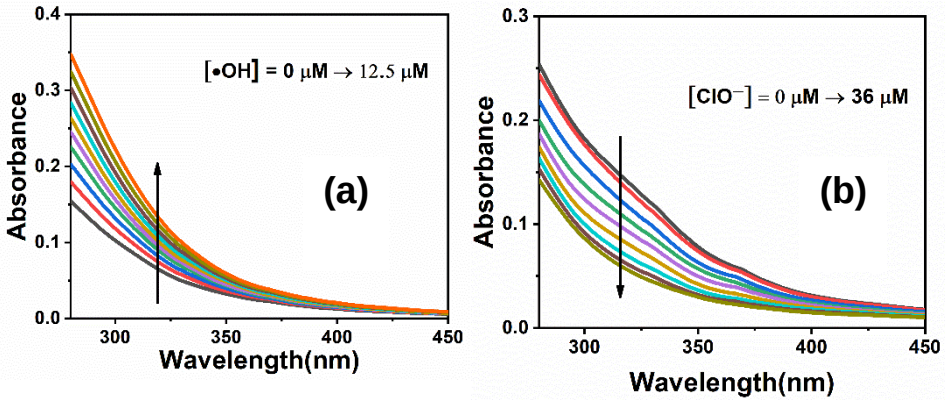

Figure APX5.5. UV-vis absorption spectra of Chitosan-CuNCs upon gradual addition of (a) •OH and (b) ClO^-

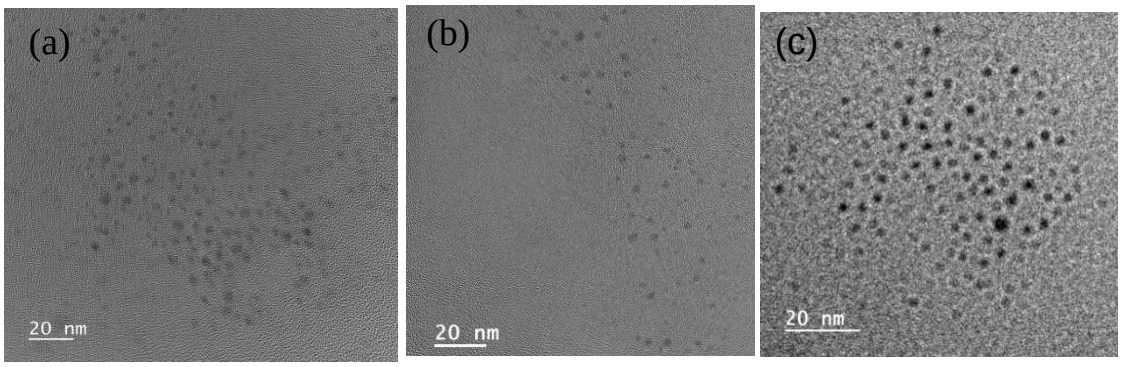

Figure APX5.6. TEM images of (a) CuNCs (b) CuNCs in presence of •OH and (c) CuNCs in presence of ClO^-.

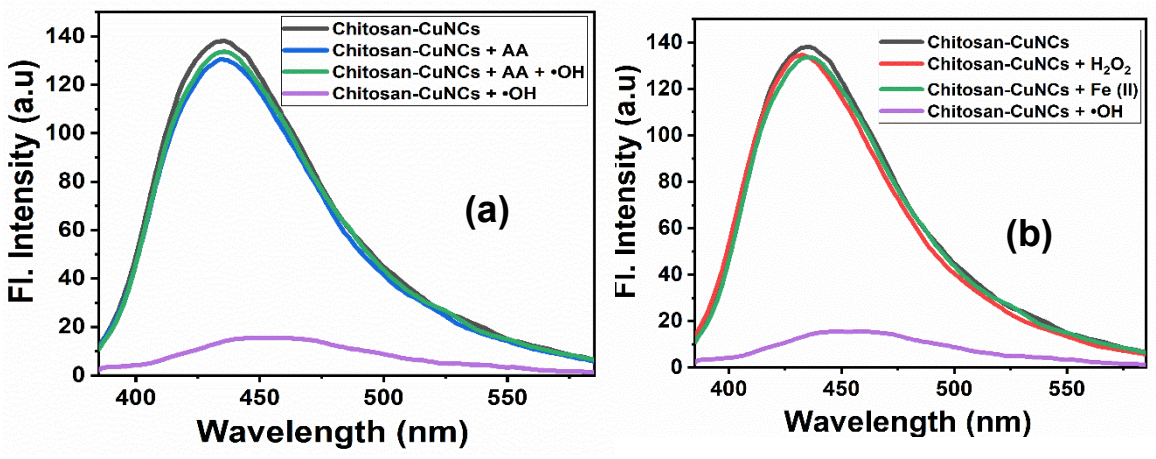

Figure APX5.7. (a) Fluorescence intensity of CuNCs in the absence and presence of AA, •OH separately and in the presence of both AA and •OH. (b) Fluorescence intensity of CuNCs in absence and presence of H_2O_2 and Fe (II) separately and in presence of both H_2O_2 and Fe (II). Colour of the legends represents the corresponding spectra.

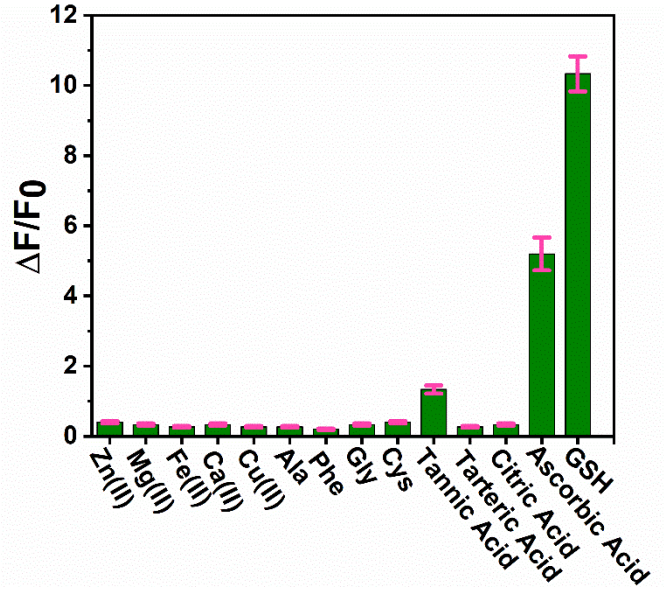

Figure APX5.8. Fluorescence response of CuNCs/ ClO^- system in the presence of GSH and different coexistent (350 μM).

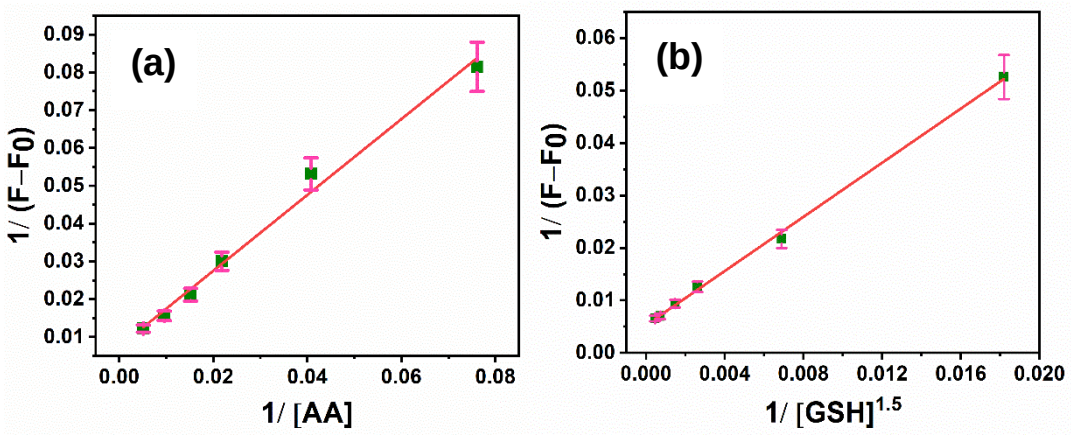

Figure APX5.9. Benesi-Hildebrand double reciprocal plot to determine the stoichiometric association of Chitosan-CuNCs to (a) AA and (b) GSH.

Fluorescence Correlation Spectroscopy Study-

FCS experiment was done by using a time resolved confocal microscope which has been discussed in the supporting information. (Micro Time 200, PicoQuant) with an excitation source of a pulsed diode laser (λ_{Ex} = 403 nm, full width at half-maximum (FWHM) = 144 ps). The sample was placed on a coverslip, and excitation laser beam was focused onto the sample using a water immersion objective (60 × /1.2 NA) and the fluorescence light from the

sample was directed through a dichroic mirror. A pinhole having a diameter of 50 μm was used for the spatial filtration of the signal and focused through a 50/50 beam splitter before entering the two single-photon avalanche diodes (SPADs). The FCS setup was calibrated by using Rhodamine-6G solution in water medium. All FCS curves were analyzed by using SymPhoTime software (PicoQuant) to obtain the corresponding values of τ_d for CuNCs with increasing concentration of analytes. The correlation curves for all systems were fitted by using eq. APX5.1

$$G(\tau) = \left\{1 + \sum_{j=0}^{n_{Trip}-1} T[j] \left[exp\left(\frac{\tau}{\tau_{Trip}[j]}\right) - 1\right]\right\} \sum_{i=0}^{n_{Diff}=1} \frac{\rho[i]}{\left[1+\left[\frac{\tau}{\tau_{Diff}[i]}\right]^{\alpha[i]}\right]\left[1+\frac{\left[\frac{\tau}{\tau_{Diff}[i]}\right]^{\alpha[i]}}{\kappa^2}\right]^{0.5}} + G_{Inf}$$

(eq. APX5.1)

where, τ and τ_D represent the lag time and the diffusion time respectively, $\kappa = \omega z/\omega xy$, where ωz and ωxy are the longitudinal and transverse radii of the observation 3D Gaussian confocal volume, respectively, T is the Dark (triplet) fraction of molecules and n_{Trip} is the number of triplet state which has been taken zero for smooth and clear fitting of the chosen systems, ρ is the contribution of the i^{th} diffusing species, n_{Diff} is the number of independently diffusing species, and G_{inf} is the correlation offset. From the Stokes−Einstein equation, the hydrodynamic radii (R_H) of CuNCs in absence and presence of analytes were determined using eq. APX5.2

$$R_H = \frac{KT}{6\pi\eta D} \qquad \text{(eq. APX5.2)}$$

where k is the Boltzmann constant, T is the absolute temperature, η is the viscosity of the solvent and D is the diffusion coefficient of the fluorophore (CuNCs).

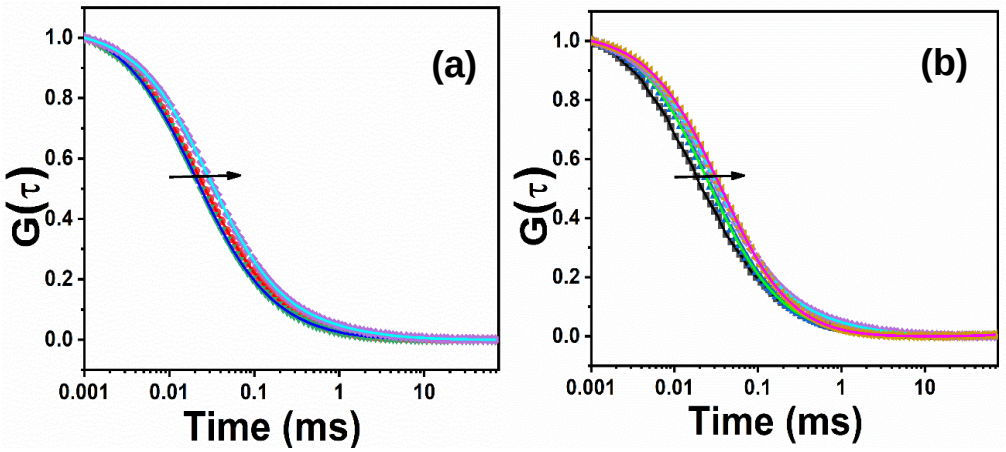

Figure APX5.10. Normalized fluorescence correlation curves of CuNCs with increasing concentrations of (a) AA and (b) GSH.

Table APX5.2. The associated diffusion parameters[a] of CuNCs systems with increasing conc entration of analytes as obtained from FCS study.[a]

Systems	Conc. of analytes (nM)	Diffusion time (µs)	Hydrodynamic radius (R_H) (nm)
•OH	0	39.70	0.70
	25	51.50	0.92
	75	58.18	1.04
	500	66.44	1.20
ClO^-	0	39.70	0.70
	50	46.14	0.84
	150	61.96	1.12
	1000	67.76	1.22
AA	0	39.70	0.70
	250	45	0.83
	625	57	1.02
	1250	111	1.98
GSH	0	39.70	0.70
	625	53.5	0.96
	2500	70	1.26
	5000	93.00	1.66

a± 5%

Table APX5.3. Determination of GSH in human blood samples.[a]

Samples	Initial amount of GSH (µM) (Working Cuvette concentration)	Added amount of GSH (µM)	GSH found (µM)	GSH recovery (%)
1	19.30 ± 1.52	11.00	30.84 ± 1.45	104.00 ± 2.20
2	20.45 ± 0.90	11.00	31.18 ± 1.50	97.50 ± 3.25

[a]Data presented are in means ± standard deviation (n = 3).

Volumetric method with standard dichlorophenol indophenol

The data obtained for the determination of ascorbic acid concentration in fruit juices through our fluorescence method have been compared with those obtained by the volumetric method with standard dichlorophenol indophenol. The procedure of the volumetric method is given below

1. 100 ml of 100 µM ascorbic acid and 100 ml of 20uM DCPIP solution had been prepared as standard solution.

2. 10 ml of the standard DCPIC solution was taken in a conical flask.

3. Burette was filled with the standard ascorbic acid solution.

4. Ascorbic acid solution was added drop by drop to the conical flux until the color changed from blue to colorless, and the consumed volume of ascorbic acid solution was recorded.

5. The procedure was repeated using various fruit juices. Please note that the intermediate pink color was ignored, and the addition was continued until a colorless solution appeared.

Calculation of AA concentration in fruit juices:

The concentration of AA in fruit juices was calculated by using standard AA solution by using following relation:

(vol. of standard) × (Conc. standard) = (vol. of unknown) × (Conc. unknown)

Table APX5.4. Recovery of ClO^- Spiked in Tap Water by standard addition method. [a]

Added amount of ClO^- (µM)	ClO^- found (µM)	ClO^- recovery (%)
8	7.3 ± 1.70	91.25 ± 3.50
12	11.5 ± 1.50	96.00 ± 3.70
14	13.2 ± 2.10	94.00 ± 2.60

[a]Data presented are in means ± standard deviation (n = 3)

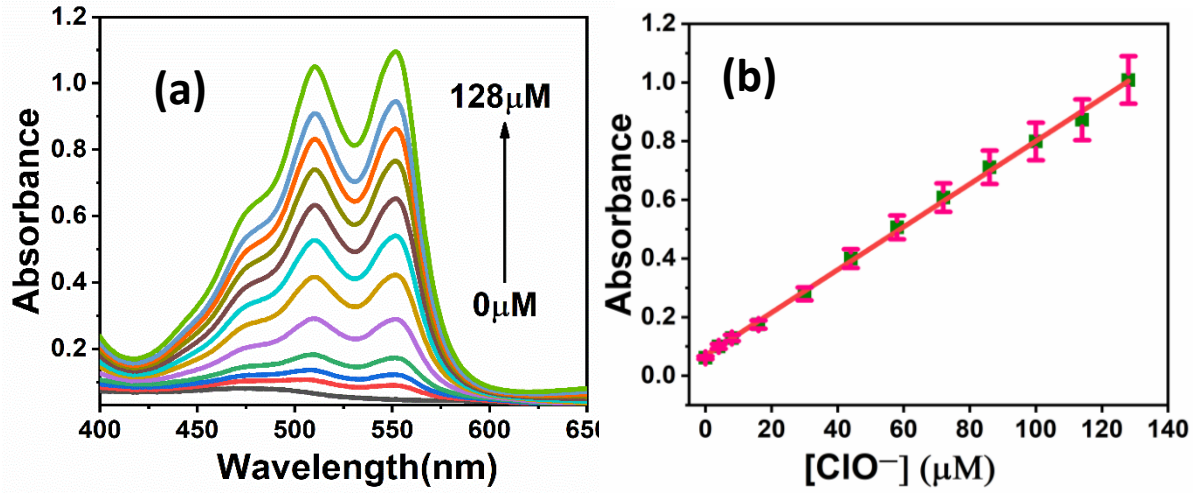

Figure APX5.11. (a) UV spectra of DPD with increasing concentration of ClO^- (b) Standard curve for the detection of ClO^- by DPD colorimetric method.

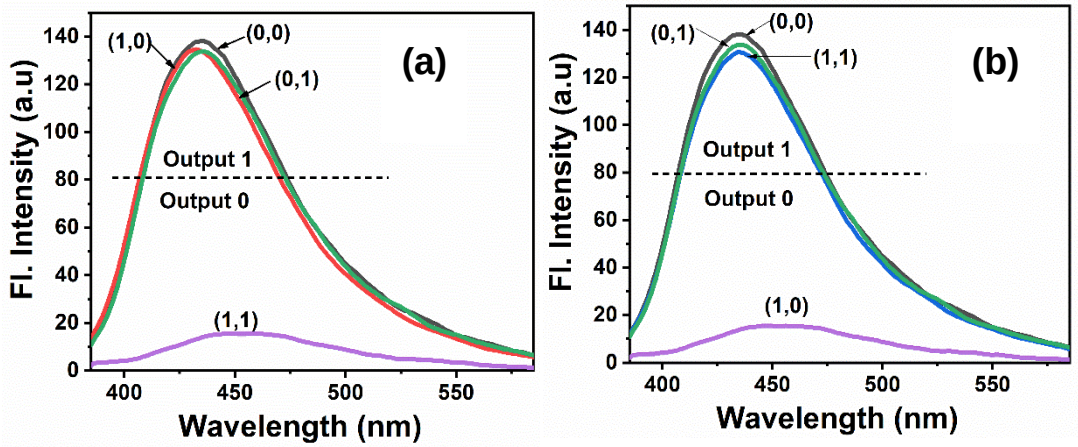

Figure APX5.12. The fluorescence spectra of CuNCs in the presence of different inputs: (a) NAND logic gate with Fe (II) and H_2O_2 as inputs; (b) IMPLICATION logic gate with •OH and AA as inputs.

Table APX5.5. Comparative table based on the performance of various nanosensors developed for the detection of ROS.

Fluorescence systems	hROS detection	Linear range (µM)	Detection limit (µM)	References
AuNCs@HPF	•OH	1-150	0.68	71
GSH-AuNCs	•OH	1-80	0.10	72
C-dots-AuNCs	ClO−	0.1-60	0.50	73
PCuNCs-BCuNCs	•OH	1.5-11.5	0.15	74
Dialdehyde bridged fluoresccenr probes	ClO−	5-5000	5.00	75
PVP-CuNCs	ClO−	1-30	0.10	76
PVP-capped CuNCs	ClO−	0.5–8 µM	0.019	77
CdSe-ZnS quantum dots	ClO−	0-0.83	0.25	78
Semiconducting conjugated polymer (SCP)	ClO−	2-6	0.50	79
FHAuNCs	•OH	1–20 µM	0.13	80
Chitosan-CuNCs	•OH ClO^-	0-7.5 0-20	0.10 0.20	Present work

References

1 Finkel, T.; Holbrook, N. J. *Nature* **2000**, *408*, 239−247.
2 Zhuang, M.; Ding, C.; Zhu, A.; Tian, Y. *Anal. Chem*. **2014**, *86*, 1829−1836.
3 Miller, E. W.; Tulyanthan, O. E.; Isaciff, Y.; Chang, C. J. Nat. *Chem. Biol*. **2007**, *3*, 263−267.
4 Rhee, S. G. *Science* **2006**, *312*, 1882–1883.
5 Gibellini, L.; Marcello, P.; Nasi, M.; Biasi, S.D.; Roat, E.; Bertoncelli, L.; Cossarizza, A. *Cancers* **2010**, *2*, 1288-1311.
6 McCord, J. M.; Fridovich, I. *J. Biol. Chem*. **1969**, *244*, 6049–6055.
7 Chae, H. Z., Kang, S. W.; Rhee, S. G. *Enzymol*. **1999**, *300*, 219–226.
8 Jiang, Q.; Xiao, N.; Shi, P.; Zhu, Y.; Guo, Z. Coord. Chem. Rev. **2007**, *251*, 1951−1972.

9 Cantuti-Castelvetri, I.; Shukitt-Hale,B.; Joseph, J. *Int. J. Dev. Neurosci*. **2000**, *18*, 367–381.

10 Valko, M.; Leibfritz, D.; Moncola, J.; Cronin, M. D.; Mazur, M.; Telser, J. *Int. J Biochem. Cell Biol.* **2007**, *39*, 44–84.

11 Pizzino,G.; Irrera,N.; Cucinotta,M.; Pallio,G.; Mannino,F.; Arcoraci,V.; Squadrito,F.; Altavilla,D.; Bitto, A. *Longev*. **2017**, *2017*, 8416763.

12 Menon, V.; Ram, M.; Dorn, J. *Diabetic Med*. **2004**, *21*, 1346−1352.

13 Jefferies, H.; Coster, J.; Khalil, A.; Bot, J.; Mccauley, R. D.; Hall, J. *ANZ J. Surg*. **2003,** *73*, 517–522.

14 Crawford, D.; Zbinden, I.; Moret, R.; Cerutti, P. *Cancer Res*. **1988**, *48*, 2132−2134.

15 Kendall, M.; Batterham, M.; Prenzler, P. D.; Ryan, D.; Robards, K. *Food. Chem*. **2008**, *108*, 425−438.

16 Guo, Y.; Yang, X.; Hakuna, L.; Barve, A.; Escobedo, J . O.; Lowry, M.; Strongin, R. M. *Sensors* **2012**, *12*, 5940-5950.

17 Hou, X .;Guo,X.; Chen, B.; Liu, C.;Fan Gao, F.; Zhao, J.; Wang, J. *Sensors and Actuators B: Chemical* **2015**, *209*, 838-845.

18 Guo, Q.; Ji, S.; Yue, Q.; Wang, L.; Liu, J.; Jia, J. *Anal. Chem*. **2009**, *81*, 5381−5389.

19 Oliveira, R.; Bento, F.; Sella, C.; Thouin, L.; Amatore, C. *Anal. Chem*. **2013**, *85*, 9057−9063.

20 Peterson, K. L.; Margherio, M. J.; Doan, P.; Wilke, K. T.; Pierre, C. *Inorg. Chem.* **2013**, *52*, 9390–9398.

21 Zhang, Z.; Fan, J.; Zhao, Y.; Kang, Y.; Du, J.; Peng, X. *ACS Sens.* **2018,** *3*,735– 741.

22 Zielonka, J.; Zhao, H.; Xu, Y.; Kalyanaraman, B. *Free Radical Biol*. *Med.* **2005**, *39*, 853–863.

23 Wang, H.; Joseph, J. A. *Free Radical Biol. Med*. **1999**, *27*, 612–616.

24 Goldstein, S.; Merenyi, G. *Methods Enzym*ol. **2008**, *436*, 49–61.

25 Li, Y.; Zhu, H.; Kuppusamy, P.; Roubaud, V.; Zweier, J. L.; Trush, M. L. *J. Biol. Chem.*, **1998**, *273*, 2015–2023.

26 Glod, B. K.; Czapski, G. A.; Haddad, P. R. *Trends Anal. Chem*., **2000**, *19*, 492–497.

27 Piszcz, P.; Zurawski, K.; Glod, B. K. *Journal of Chemistry*, **2014**, *2014*, 1–6.

28 García-Plazaola, J. I.; Becerril, J. M. *Phytochemical Analysis*,**1999**, *10*, 307-313.

29 Beissenhirtz, M. K.; Scheller, F. W.; Lisdat, F. *Anal. Chem*. **2004**, *76*, 4665–4671.

30 M. Ganesana, J. S. Erlichman and S. Andreescu. *Free Radical Biol. Med.* **2012**, *53*, 2240–2249.

31 T. Munzel, I. B. A. Ev, A. L. Kleschyov and D. G. Harrison, *Thromb. Vasc. Biol*. **2002**, *22*, 1761–1768.

32 Han, D.; Williams, E.; Cadenas, E. *Biochem. J*. **2001**, *353*, 411–416.

33 Lakowicz, J. R. Principles of Fluorescence Spectroscopy; Springer: USA, 2006; pp 55−472.

34 Cadenas, E.;Kelvin J.A.Davies, K. J. A. *Free Rad. Biol. Med*. **2000**, *29*, 222–230.

35 Zielonka, J.; Kalyanaraman, B. *Free Rad. Biol. Med*. **2008**, *45*, 1217–1219.

36 Folkes, L. K.; Patel, K. B.; Wardman,P.; Wrona,M. *Arch. Biochem. Biophys*. **2009**, *484*, 122–126.

37 Zhang, L.; Wang, E. *Nano Today* **2014**, *9*, 132−157.

38 Jin, R. C.; Zeng, C.; Zhou, M.; Chen, Y. *Chem. Rev*. **2016**, *116*, 10346−10413.
39 A. Wiseman, Handbook of Experimental Pharmacology XX/2, Part 2, Springer-Verlag, Berlin, 1970, pp. 48–97.
40 Chen, T.; Hu, Y.; Cen, Y.; Chu, X.; Lu, Y. *J. Am. Chem Soc*. **2013**, *135*, 11595−11602.
41 Hu, L.; Deng, L.; Alsaiari, S.; Zhang, D.; Khashab, N. M. *Anal. Chem*. **2014**, *86*, 4989−4994.
42 Tian, D.; Qian, Z.; Xia, Y.; Zhu, C. *Langmuir* **2012**, *28*, 3945−3951.
43 Chakraborty, S.; Nandy,A.; Ghosh, S.; Das,N. K.; Parveen, S.; Datta,S.; Mukherjee, S. *Analyst*, **2021**, *146*, 1455-1463.
44 Goswami, N.; Zheng, K. Y.; Xie, J. P. *Nanoscale* **2014**, *6*, 13328−13347.
45 Choi, S.; Dickson, R. M.; Yu, J. *Chem. Soc. Rev*. **2012**, *41*, 1867− 1891.
46 Xie, J.; Zheng, Y.; Ying, J. *Chem. Commun*. **2010**, *46*, 961−963.
47 Wu, Z.; Wang, M.; Yang, J.; Zheng, X.; Cai, W.; Meng, G.; Qian, H.; Wang, H.; Jin, R.. *Small* **2012**, *8*, 2028−2035.
48 Shang, L.; Azadfar, N.; Stockmar, F.; Send, W.; Trouillet, V.; Bruns, M.; Gerthsen, D.; Nienhaus, G. U. *small* **2011**, *7*, 2614–2620.
49 Liu, C.; Wu, H.; Hsiao, Y.; Lai, C.; Shih, C.; Peng, Y.; Tang, K.; Chang, H.; Chien, Y.; Hsiao, J.; Cheng, J.; Chou, P. T. *Angew. Chem., Int. Ed*. **2011**, *50*, 7056−7060.
50 Wang, Y.; Chen, J.; Irudayaraj, J. *ACS Nano* **2011**, *5*, 9718− 9725.
51 Chen, H.; Li, B.; Ren, X.; Li, S.; Ma, Y.; Cui, S.; Gu, Y. *Biomaterials* **2012**, *33*, 8461−8476.
52 Garima.; Jindal, S.; Garg, S.; Matai, I.; Packirisamy, G.; Sachdev,. *Microchim Acta* **2021**, *188*, 1-12.
53 Guo, Y.; Cao, F.; Lei, X.; Mang, L.; Cheng, S.; Song, J. *Nanoscale* **2016**, *8*, 4852−4863.
54 Li, T.; Wang, E.; Dong, S. *J. Am. Chem. Soc*. **2009**, *131*, 15082− 15083.
55 Silva, A. P. D.; Uchiyama, S. *Nat.Nanotechnology* **2007**, *2*, 399-410.
56 Akhuli, A.; Chakraborty, D.; Agrawal, A. K.; Sarkar, M. *Langmuir* **2021**, *37*, 1823−1837.
57 Cheng, L. C.; Huang, J. H.; Chen, H. M.; Lai, T. C.; Yang, K. Y.; Liu, R. S.; Hsiao, M.; Chen, C. H.; Her, L. J.; Tsai, D. P. *J. Mater. Chem*. **2012**, *22*, 2244−2253.
58 Dong, W.; Sun, C.; Sun, M.; Ge, H.; Asiri, A. M.; Marwani, H. M.; Ni, R.; Wang S. *ACS Appl. Nano Mater*. **2020**, *3*, 312−318.
59 Zhou, X.; Zhao, G.; Chen, M.; Gao, W.; Zhou, X.; Xie, X.; Yang, L.; Du, G. *ACS Sustainable Chem. Eng*. **2018**, *6*, 3948−3956.
60 Mancini, M. C.; Kairdolf, B. A.; Smith, A. M.; Nie, S. *J. Am. Chem. Soc*. **2008**, *130*, 10836−10837.
61 Korotkova, E. I.; Misini, B.; Dorozhko, E. V.; Bukkel, M. V.; Plotnikov, E. V.; Linert, W. *Int. J. Mol. Sci*. **2011**, *12*, 401−409.
62 Xie, Y.; Xianyu, Y.; Wang, N.; Yan, Z.; Liu, Y.; Zhu, K.; Hatzakis, N. S.; Jiang, X. *Adv. Funct. Mater*. **2018**, *28*, 1702026.
63 Bhunia, S.; Kumar, S.; Purkayastha, P. *ACS Omega* **2019**, *4*, 2523−2532.
64 Vitamin C Testing. *Flinn Scientific* **2016,** Publication No. 91358.

65 Pisoschi, A. M.; Danet, A. F.; Slawomir Kalinowski, S. *J. Autom. Methods Manage. Chem*. **2008**, *2008*, 1-8.
66 Michelet, F.; Gueguen, R.; Leroy, P.; Wellman, M.; Nicolas, A.; Siest, G. *Clin. Chem.* **1995,** *41/10*, 1509-1517.
67 Tietze, F. *Anal. Biochem.* **1969**, *27*, 502-522.
68 Araujo, A. R. T. S.; Saraiva, M. L. M. F. S.; Lima, J. L. F. C. *Talanta*, **2008**, *74*, 1511–1519.
69 Kong, X. J.; Wu, S.; Chen, T. T.; Yu, R. Q.; Chu, X. *Nanoscale* **2016**, *8*, 15604−15610.
70 Moberg, L.; Karlberg, B . *Anal. Chim. Acta* 2000, *407*, 127–133.
71 Zhuang, M.; Ding, C.; Zhu, A.; Tian, Y. *Anal. Chem.* **2014**, *86*, 1829−1836.
72 Xie, Y.; Xianyu, Y.; Wang, N.; Yan, Z.; Liu, Y.; Zhu, K.; Hatzakis, N. S.; Jiang, X. *Adv. Funct. Mater*. **2018**, *28*, 1702026.
73 Ju, E.; Liu, Z.; Du, Y.; Tao, Y.; Ren, J.; Qu, X. *ACS Nano*, **2014**, *8*, 6014–6023.
74 Garima.; Jindal,S.; Garg, S.; Matai, I.; Packirisamy, G.; Sachdev, A. *Microchim. Acta* **2021,** *188*, 13.
75 Yanga, Z.; Wanga, M.; She, M.; Yina, B.; Huang, Y.; Liu, P.; Li, J.; Zhang, S. *Sens. Actuators*, ***2014***, *202*, 656–662.
76 Tang, Q.; Yang, T.; Huang, Y. *Microchim Acta*, **2015**, *182*, 2337– 2343.
77 Dong, W.; Sun, C.; Sun, M.; Ge, H.; Asiri, A. M.; Marwani, H. M.; Ni, R.; Wang S. *ACS Appl. Nano Mater*. **2020**, *3*, 312−318.
78 Yan, Y.; Wang, S.; Liu, Z. *Anal. Chem.* **2010**, *82*, 9775-9781.
79 Wang, H.; Li, Y.; Chen, Y. *J. Mater. Chem. C*, **2015**, *3*, 5136-5140.
80 Ran, X.; Wang, Z.; Pu, F.; Liu, Z.; Ren, J.; Qu, X. *Chem. Commun*. **2019**, *55*, 15097-15100.

CHAPTER 6

Probing the role of Surface Ligands on Copper Nanoclusters in the reduction of 4-Nitrophenol to 4-Aminophenol: A Spectroscopic Investigation

We have investigated the impact of surface ligands of CuNCs in catalyzing the $NaBH_4$-mediated reduction of 4-nitrophenol to 4-aminophenol, thereby we have tried to understand some issues related to the reaction mechanism. For this purpose, tannic acid (TA-CuNCs) and cysteine-capped (Cys-CuNCs) CuNCs have been synthesized as nano-catalysts, and their catalytic performance has been compared with ligand-free CuNCs. Kinetic data obtained from absorption studies, have revealed that the rate constant for the reaction, catalyzed by these nano-catalysts, follows the order: $k_{TA-CuNCs} > k_{CuNCs} > k_{Cys-CuNCs}$. Cys-CuNCs and ligand-free CuNCs exhibit an induction time in catalytic reactions, unlike TA-CuNCs, indicating the crucial role of ligand-mediated surface modification. Furthermore, it has been found that elimination of dissolved oxygen from the reaction medium increases rate constants and eliminates induction time, suggesting its role in facilitating reverse oxidation. It has also been observed that the catalytic activity decreases with rising 4-NP concentration, suggesting a Langmuir-Hinshelwood mechanism for the event. Moreover, the fluorescence property of the nano-catalysts has also been employed to extract various important information regarding the catalytic reaction at both ensemble average and single particle level. Furthermore, it has been demonstrated that CuNCs-based nano-catalysts are not only limited to the conversion of 4-nitrophenol to 4-aminophenol but are quite useful in the conversion of various types of organic substrates.

6.1. Introduction

In recent years, there has been substantial global focus on the study and application of noble metal nanoparticles.[1-6] Researchers have been highly intrigued by metal nanoclusters (MNCs) due to their ultra-small size (<2 nm), minimal toxicity, advantageous optical characteristics, and excellent water solubility.[7-9] These attributes have made them suitable for a wide range of applications, including sensing, bio-analysis, labeling, bioimaging, etc.[7, 10-13] Over the last few years, catalysis by nanomaterials has drawn immense attention from the scientific community owing to the unique properties of NPs at nanometer length scale.[14-19] In fact, the majority of these studies are carried out by employing relatively larger size (>2nm), non-

fluorescent metal nanoparticles. However, fluorescent metal nanoclusters (MNCs) have been relatively understudied as nano-catalysts compared to larger nanoparticles (NPs).

Interestingly, MNCs can provide unique advantages in terms of inducing a catalytic reaction. For example, (i) MNCs can provide a distinct metal core, differing from conventional nanoparticles and bulk materials, exposing a larger surface-to-volume ratio (ii) by virtue of ultra-small size of MNCs, they can introduce quantized energy levels for reactant activation through electron excitation, (iii) their easily modifiable geometric and electronic characteristics are also expected to help lead a specific reaction pathways during reactions and (v) more importantly, as the MNCs are fluorescent in nature one would also be able to understand the finer details of the catalytic reaction by monitoring the fluorescence of these MNCs in the absence and presence of reagents [20-22] It is also pertinent to mention here that surface ligands of nanomaterials play a crucial role in colloidal chemistry, providing precise atomic control during nanostructure synthesis and contributing to long-term stability by preventing agglomeration and aggregation.[23-25] Moreover, ligands play a pivotal role in modulating the electronic energy states of the nanoclusters (NCs), thereby exerting control over various catalytic properties. While ligands are crucial for designing and preserving nanostructured catalysts, their impact on catalytic turnover in multiple reactions can be obscured by competing factors. At the surface of nanomaterials, ligands might be expected to hinder catalytic activity by barricading access to potentially active sites on the catalyst surface.[26-30] As anticipated, numerous studies have observed negative impacts on catalytic rates mainly due to that issue.[26, 28, 31-35] However, some studies have found no detrimental effects from capping ligands. In contrast, others have even reported increased selectivity towards specific reaction products.[36-40] These findings highlight the intricate nature of ligand interactions and their role in catalytic processes. Hence, a precise kinetic analysis is expected to be highly valuable to figure out the exact mechanistic pathway of a catalytic reaction. The

catalytic activity of nanomaterials in aqueous media is commonly assessed through the reduction of 4-nitrophenol (4-NP) to 4-aminophenol (4-AP) by borohydride (BH_4^-).[15, 17, 41-42] Furthermore, this 4-NP to 4-AP transformation holds significant implications for the human well-being and the environment. 4-NP and its derivatives are persistent pollutants found in industrial wastewater, originating from producing insecticides, synthetic dyes, and herbicides.[43-45] Again, 4-AP, derived from 4-NP, serves as a crucial intermediate for producing several drugs and is widely used as a photographic developer, hair-dyeing agent, anticorrosion–lubricating agent in fuels, etc.[46-48] Due to these reasons, conversion of nitrophenol to aminophenol is essential. However, the mechanism underlying the catalytic reduction of the reaction remains a subject of debate despite its widespread use for catalyst comparison. Particularly, understanding the influence of ligands of nanomaterials on the catalytic reduction of 4-NP to 4-AP is a complex topic due to the wide variety of ligands used with nanomaterials and the challenges in accurately characterizing their quantity and arrangement on catalytic surfaces. Consequently, the existing literature presents a complex and occasionally conflicting discussion on ligand effects.[17, 19, 23, 49-52] Hence, a molecular-level comprehension of the catalytic reduction of 4-NP to 4-AP employing MNCs as nano-catalysts and an exploration of the role of surface ligands over MNCs become imperative.

In this context, it is pertinent to mention here that recently, Neretina and co-workers[23] have demonstrated that surface ligands on NPs can significantly influence the reduction of 4-nitrophenol due to the displacement of the ligands on the catalytic surfaces of AuNP by BH_4^- during the reaction. Recently, Kitchens and co-workers[26] have investigated the impact of thiolated polyethylene glycol (HS-PEG) as a stabilizing ligand in the catalytic reduction of 4-NP by gold nanoparticles (AuNPs). They have found that the catalytic activity of AuNPs is influenced by the chain length and packing density of HS-PEG. Higher molecular weight and lower surface coverage of HS-PEG are found to be responsible for the increased rate

constants and shorter induction times. In this context, while working on nano-gold catalysts, Xie and co-workers[53] have observed that surface ligands cannot only influence the active sites of the catalysts but also can influence the pathway of the catalytic reaction. The above initial studies have essentially indicated that there is an opportunity to customize the ligand-protected metal NCs for selective catalytic reactions. However, it has been observed that despite several studies, the mechanism of surface ligands-mediated catalysis is still hazy. It is to be noted here that several reported studies have tracked the catalytic processes, utilizing absorption spectral changes of the systems or relying on spectrographic signals from additional chromogenic agents in the absence of absorbance changes. Additionally, some studies are done by using nuclear magnetic resonance (NMR). However, NMR is thought to be challenging for in situ, real-time, and fast-tracking measurements. Moreover, existing indicative methods, primarily relying on signals from substrates or products, fail to meet requirements for both strong catalytic performance and sensitive indication in catalytic reactions. As it is well known that fluorescence is more sensitive than most of the other techniques, a critical thought would be to consider whether the catalyst's fluorescence signals can serve as an effective indicator of the given catalytic reaction process.[54] Additionally, it's worth highlighting that there is a scarcity of comparable studies focusing on CuNCs despite the several biological significance and advantageous properties of CuNCs. It would be quite interesting to see if the fluorescence property of CuNCs can be utilized for a better understanding of the catalytic reduction of 4-NP to 4-AP in particular and MNCs-induced catalytic reaction in general.

Keeping in mind the above facts, we have investigated the role of surface ligands on copper nanoclusters (CuNCs) in catalyzing the $NaBH_4$-mediated reduction of 4-NP to 4-AP in aqueous medium. For this purpose, two types of CuNCs, one capped with tannic acid (TA-CuNCs) and the other with cysteine (Cys-CuNCs) have been synthesized and utilized as

nano-catalysts. We have compared the catalytic performance of these ligand-capped CuNCs with that of ligand-free CuNCs. To understand the catalytic mechanisms at a molecular level, we have utilized the absorption signals of reactants as well as the fluorescence signals of the CuNCs catalysts. Additionally, the fluorescence signals of the CuNCs have been utilized to investigate the potential of these nano-catalysts to conduct the said reaction at single-particle levels. Furthermore, it has been demonstrated that CuNCs-based nano-catalysts are not only limited to converting 4-NP to 4-AP but are quite useful in catalyzing various substrate scopes.

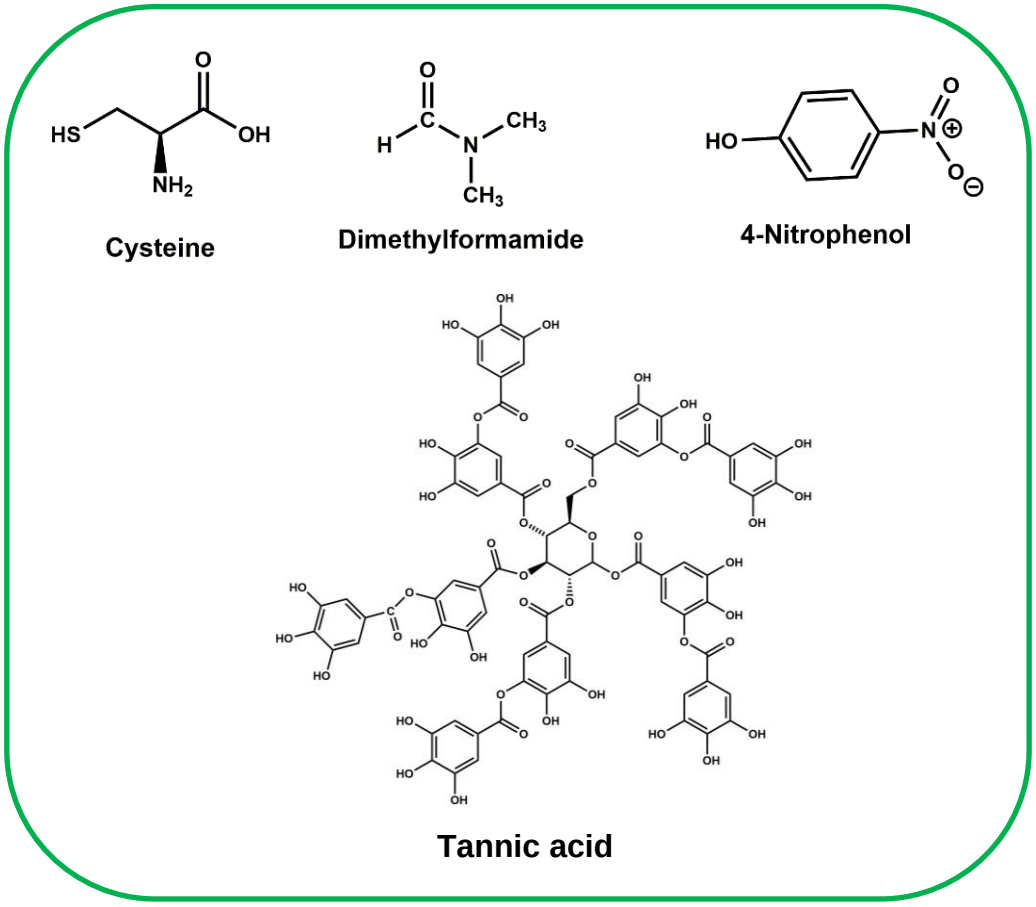

Scheme 6.1. Molecular structures of the some chemicals used in this study.

6.2. Kinetic Measurements

In evaluating the catalytic efficacy of various CuNCs, the catalytic reduction of 4-NP to 4-AP served as a model reaction. The experimental setup involved the utilization of UV-Vis

absorption spectroscopy and fluorescence emission spectroscopy. A standard quartz cuvette with a 1 cm path length was used for the kinetic measurements. In the case of UV-Vis absorption spectroscopic measurements, 2.5 ml aqueous solution of 0.1 mM 4-NP and 50 µL of 0.5 M freshly prepared $NaBH_4$ solutions were mixed together. Subsequently, 80 nM concentrations of various CuNCs solutions were introduced separately into the aforementioned mixture. The catalytic reduction process was continuously monitored by recording absorption spectra at 2-minute intervals within the wavelength range of 200–800 nm at a temperature of 25 °C.

6.3. Result and Discussion

6.3.1. Characterization of CuNCs

The synthesized copper nanoclusters (CuNCs) have been characterized by employing various analytical techniques, including steady-state absorption and emission spectroscopy, transmission electron microscopy (TEM), energy-dispersive X-ray analysis (EDAX), Fourier transform infrared (FTIR) spectroscopy and MALDI-TOF mass spectroscopy. The absorption and emission spectra of the CuNCs are provided in the Figure APX6.1. In the Figure APX6.1, the absorption spectra of all three CuNCs reveal robust absorption in the UV region and an extended absorption tail in the visible region. It is essential to note that these absorption profiles differ significantly from the characteristic surface plasmon resonance (SPR) band (ca. 560−600 nm) observed in relatively larger CuNPs.[55] The absorption profiles of the present CuNCs can be ascribed to the discrete electronic energy band structure of CuNCs rather than the SPR of CuNPs.[56] Figure APX6.1 also illustrates the excitation and emission spectra of the three CuNCs in an aqueous medium at room temperature. As can be seen, TA-CuNCs, Cys-CuNCs, and ligand-free CuNCs exhibit fluorescence maxima at 430, 431, and 489 nm, respectively, when excited at 360 nm. The sizes of the CuNCs are estimated to be 2.3 ± 0.5 and 2.2 ± 0.5 for TA-CuNCs and Cys-CuNCs, respectively through

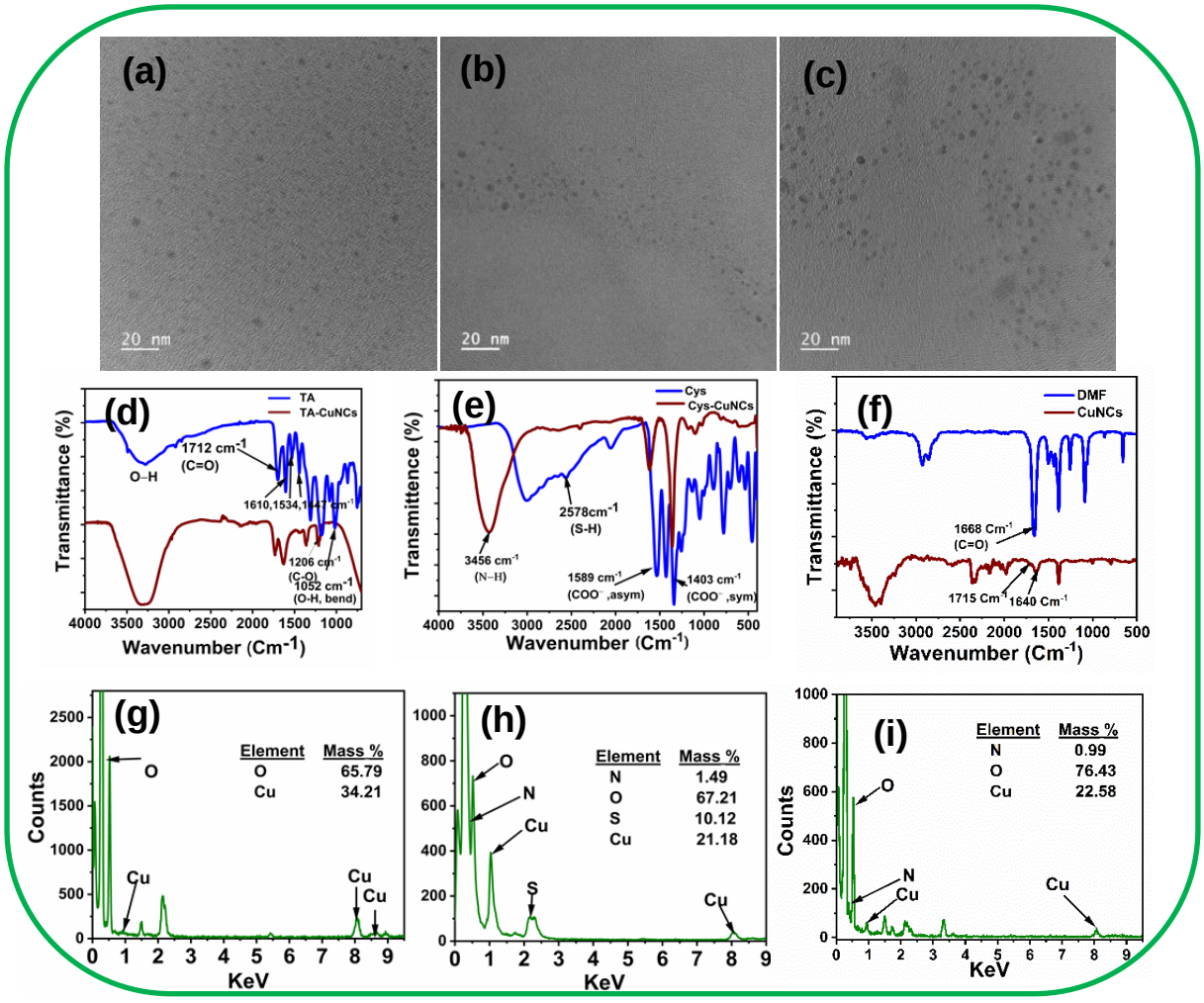

Figure 6.1. (a, b, c) TEM images, (d, e, f) FTIR spectra and (g, h, i) EDAX spectra of TA-CuNCs and Cys-CuNCs and DMF stabilized CuNCs, respectively**.**

TEM measurements (Figure 6.1a,b,c). For elemental analysis, EDAX measurements (Figure 6.1g,h,i) have been conducted. Further, to confirm the successful introduction of the ligands onto the surface of CuNCs, an FTIR study has been performed, and the obtained data are provided in Figure 6.1d,e,f. The FTIR spectra of tannic acid (TA) and TA-CuNCs are shown in the Figure 6.1d. In the vibrational spectra, specific major bands of TA are identified at 3300 cm^{-1} (O−H, stretching), 1716 cm^{-1} (C=O, stretching), 1205 cm^{-1} (C−O, stretching), and 1055 cm^{-1} (O−H, bending). Upon examining the FTIR spectrum of TA-CuNCs, it becomes evident that the C−OH stretching and O−H bending vibrations originating from tannic acid

undergo disruption after the capping process on the surface of CuNCs. This disruption is manifested by the reduced intensity and shifting of the aforementioned bands, indicating the attachment of the TA ligands to the CuNCs' surface. In Figure 6.1e, the FTIR spectra of cysteine and Cys-CuNCs are presented. Upon close examination of the figure, it becomes clear that the characteristic peaks of the −COOH group, represented by asymmetric and symmetric stretching at 1590 and 1400 cm−1, respectively, as well as the $-NH_2$ group stretching in the range of 3000−3800 cm−1, remain unaltered. Notably, the S−H stretching band is found to be absent in the FTIR spectrum of Cys-CuNCs. This observation serves as conclusive evidence that cysteine ligands are successfully attached to the surface of CuNCs through the thiol moieties. The FTIR analysis for ligand free CuNCs (Figure 6.1f) reveals a significant interaction between CuNCs and DMF, as evidenced by relatively broader CuNCs peak compared to neat DMF. Please note that the carbonyl peak of DMF shifts from 1668 cm^{-1} to 1640 cm^{-1} in CuNCs, indicating a strong interaction with the carbonyl group. The FTIR spectrum (Figure 6.1f) of ligand-free CuNCs implies two potential types of DMF-CuNCs interactions on the surface: one involving coordination through the C=O group and another possibly through the $N(Me)_2$ group, giving rise to distinct peaks at 1640 cm^{-1} and 1715 cm^{-1}, respectively.[57] For determining the number of Cu atoms in the metal core (Cu_n) of those nanoclusters, a well-known model called Jellium model has been used, which has been discussed in the chapter 2.[57-58] The precise atomic composition of the synthesized CuNCs are also ascertained through MALDI-TOF mass spectrometric analyses which has been discussed in the appendix (Figure APX6.8, 6.9, 6.10). Utilizing the molecular weight of the corresponding ligands and the atomic weight of copper, the most likely chemical composition of these monodispersed CuNCs can be rationalized as $[Cu_{16}\,TA_4\,K^+]$, $[(Cu)_{15}(Cys)_{24}\,Na^+]$ and $[(CuO)_8(Cu)14\ 6H^+]$ for TA-CuNCs, Cys-CuNCs and ligand-free CuNCs respectively.

6.3.2 Investigation of the Catalytic Reduction of 4-nitrophenol by CuNCs

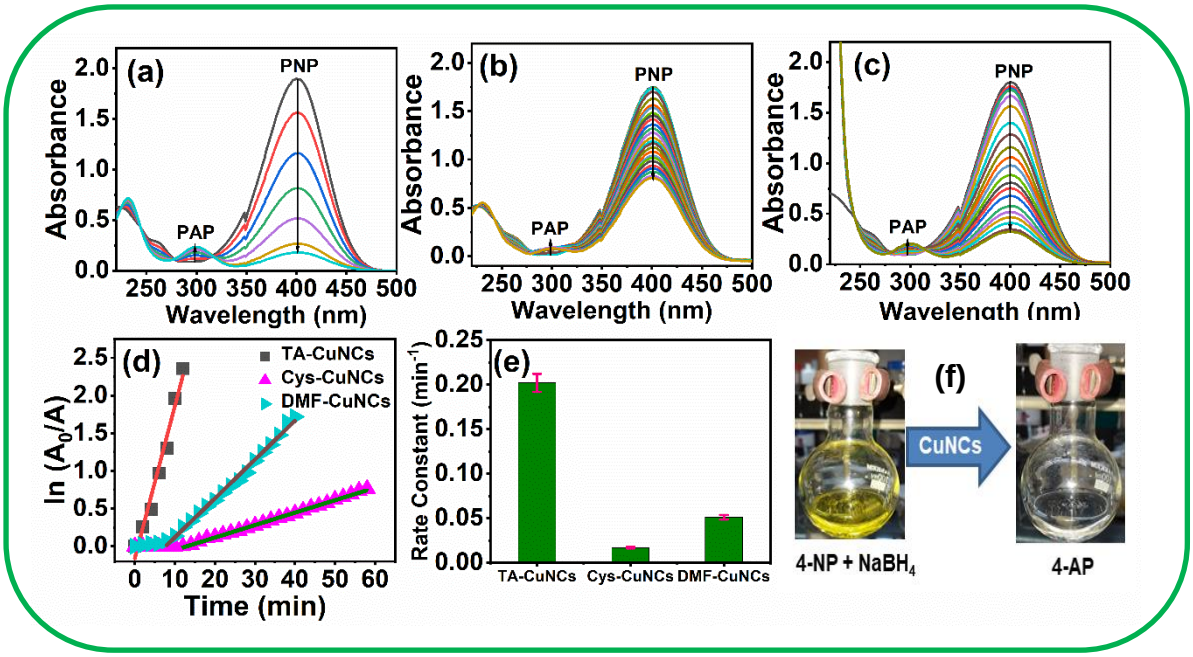

Figure 6.2. Absorption spectra of 4-nitrophenol reduced by $NaBH_4$ in the presence of (a) TA-CuNCs (b) Cys-CuNCs and (c) ligand-free CuNCs with 2 min time interval, (d) ln(Ao/At) vs. time plot for determination of rate constants; (e) Bar diagram of catalytic reaction rate constant vs various CuNCs; (f) Pictorial presentation for the conversion of 4-NP to 4-AP.

In the current study, the catalytic activity of the CuNCs has been investigated by monitoring the reduction of 4-nitrophenol (4-NP) to 4-aminophenol (4-AP) by $NaBH_4$ in aqueous medium. Primarily, the progress of the reaction has been examined by UV-vis spectroscopy, measuring the optical density of 4-NP and 4- AP as a function of time. Initially, it has been observed that absorption maxima of 4-NP (Figure APX6.2) are instantly changed from 318 to 400 nm (and the color of the solution changes from colorless to yellow) upon the addition of freshly prepared aqueous $NaBH_4$ solution, which is caused due to the formation of 4-nitrophenolate ion under the alkaline conditions.[41, 59] Prior discussing the catalytic activity of the synthesized CuNCs, it is to be noted here that the reduction of 4-NP in the presence of $NaBH_4$ is thermodynamically feasible (E_0 for 4-NP/4-AP = −0.76 V and H_3BO_3/BH_4^- =

−1.33 V versus NHE) process but it is kinetically restricted in the absence of a catalyst.[60-62] Metal nanoparticles are known to catalyze the reaction by enabling electron transfer from the donor BH_4^- to the acceptor 4-NP.[63] Moreover, it has been reported that electron transfer initially happens from the reducing agent to the nano catalyst, followed by electron transfer from the nano catalyst to the electron-acceptor oxidizing agent. Considering this aspect and to give an electrochemical viewpoint in the current study, the reduction potential of the CuNCs has been estimated through cyclic voltammetric measurements, and the representative I-V plots of those systems have been given in Figure APX6.3. The reduction potential of TA-CuNCs, Cys-CuNCs, and ligand-free CuNCs is estimated to be - 0.29 V, -0.26 V, and -0.29 V, respectively, indicating their ability to catalyze the conversion from 4-NP to 4-AP. Now coming to the discussion of kinetic aspects of the catalytic reduction of 4-NP to 4-AP by employing CuNCs as nano catalysts. For this purpose UV-vis absorption study has been performed and the representative absorption spectra of the reaction mixture containing 4-NP and $NaBH_4$ in absence and presence of two different types of CuNCs, one capped with tannic acid (TA-CuNCs) and the other with cysteine (Cys-CuNCs) at different time intervals have been provided in the Figure 6.2a,b. Alternatively, to explore the influence of surface ligands on the catalytic reaction, we have also employed unprotected CuNCs (Figure 6.2c) without stabilizing ligands, for the said catalytic reaction and the results are demonstrated through UV-Vis spectra. However, it's important to note that this unprotected CuNCs are not entirely bare but are stabilized by solvent molecules adsorbed onto their surfaces.[57, 64] From the Figure 6.2a,b,c it has been observed that with the addition of those CuNCs to the reaction mixture, a gradual decrease in the characteristic absorption peak of 4-nitrophenlate (~400 nm) and concomitant appearance of a new peak for 4-AP (~300 nm) has been observed. Moreover, as depicted in the Figure 6.2a,b,c, the presence of isosbestic points at 315, 282, and 246 nm can unequivocally be attributed to the formation of 4-AP as the reduction

product. Again, the products are thoroughly characterized by HRMS, ^{1}H NMR ^{13}C NMR techniques, which have been discussed in the appendix (Figure APX6.5, 6.6, 6.7). The % yield of the catalytic conversion has been estimated to be 94 %, 76%, and 89 % for TA-CuNCs, Cys-CuNCs, and ligand-free CuNCs, respectively. Given the large excess of $NaBH_4$ (as discussed in the experimental Section), the catalytic reaction can logically be treated as a pseudo-first-order reaction with respect to the concentration of 4-NP. Consequently, the reaction kinetics has been analyzed by using following pseudo first order rate equation (eq 2)

$$\ln({}^{A_0}/_{A}) = kt \qquad (2)$$

where k is the apparent first-rate constant (s^{-1}), t is the reaction time, A_0 and A are the absorbance of 4-NP at times 0 and t s, respectively. The appropriate linear relation plots of ln (A_0/A) vs. time (t) have been shown in the Figure 6.2d and the calculated rate constants for the catalytic reaction in presence of three different CuNCs are shown in the bar diagram (Figure 6.2e). From the bar diagram it can be visualised that the rate constant for the reaction, catalyzed by these nano-catalysts, follows the order: $k_{TA-CuNCs}(0.202\,min^{-1})$ > $k_{CuNCs}(0.051\,min^{-1})$ > $k_{Cys-CuNCs}(0.017\,min^{-1})$. Notably, Cys-CuNCs and ligand-free CuNCs have exhibited an induction time (~10 min) before the reaction commenced, whereas no induction time has been observed with TA-CuNCs. Please note that the induction time for a catalytic reaction is the initial period during which little or no observable reaction occurs, as certain conditions or species must be formed before the reaction proceeds at a noticeable rate. The observed induction time in the present case has suggested that surface modification of CuNCs by ligands play a crucial role in the catalytic reaction. It was supposed that ligand free CuNCs should provide highest rate constant and there should be no induction period as there is no barrier to prevent the reactant to access the surface of the catalyst. So, this phenomenon should be carefully investigated. Please note that the origin of the induction time is a highly

debating subject where numerous mechanisms have been proposed. In this context, early studies with AgNPs catalysts suggested that purging the aqueous reactants with N_2 gas could reduce or eliminate the induction time which is described by the fact that the induction time is required for BH_4^- to remove an oxide layer from the Ag surface.[41]But this hypothesis was ruled out when non-oxidizable catalysts like Au and Pt also exhibited induction times.[65-67] An alternative explanation proposed that dissolved oxygen competes with 4-NP for hydrogen species from BH_4^- until the dissolved oxygen is consumed.[66, 68] Nevertheless, this explanation failed to garner significant attention in the literature. Some studies, such as those involving Au-based nanocages, attributed the induction period to the time required for 4-NP to bind to the catalyst surface.[69] Ballauff and coworkers[17] have provided convincing arguments, based on reaction kinetics, suggesting that the reaction is not diffusion-limited to the catalyst surface but rather occurs on the catalyst surface itself. Despite this, numerous reports have argued in favour of a diffusion-limited mechanism, often citing a dependency of the induction time on surface ligands as justification.[64, 70-72] An alternative mechanism proposed by Ballauff and co-workers[17] have suggested that the induction period results from catalyst surface reconstruction caused by reactants attachment, while another suggests the time required for borohydride to inject electrons into the catalyst, lowering the reduction potential and enabling the reaction to proceed.[73-74] Since, in the present study, different CuNCs, each having unique surface ligands are involved and thus each ligand is expected to exhibit distinct binding affinities to the metal and varying ligand densities over NCs surface, contributing to differences in induction times. It has been demonstrated by FTIR spectra (*vide supra*) that TA ligands are incorporated with copper core by forming Cu-O linkage whereas Cys ligands are incorporated via forming Cu-S linkage. As Cu-S bond is stronger that Cu-O, it is expected that surface restructuring of TA-CuNCs will be easier that Cys-CuNCs. Moreover, the number of surface ligands per MNCs of these nano-catalysts are different as

discussed in the characterisation section. The ligand density of Cys-CuNCs may be greater than that of TA-CuNCs. Due to these reasons, Cys-CuNCs mediated catalytic reaction is expected to follow lower rate constant and certain induction time than that of TA-CuNCs mediated catalytic reaction. Surprisingly, it has been observed that ligand-free CuNCs catalysts have shown slower reaction kinetics as well as certain induction times than that of TA-CuNCs (Figure 6.2d). These observations can be explained by delving into the mechanism of the 4-nitrophenol (4-NP) reduction reaction. It has been reported[57, 64, 75-76] that even though no stabilizing ligand has been used, a layer of dimethylformamide (DMF) is formed over the surface of MNCs, which has been substantiated by FTIR spectroscopy in this study. Based on these findings it has been attributed that first, the DMF layers undergo restructuring, leading to partial desorption of DMF molecules from the surface of the CuNCs and then 4-NP permeates onto the CuNCs surface through diffusion. These processes contribute to the slower rate constant and lesser induction time of the catalytic reaction. To get more insight into this event, we have performed the same experiment by removing dissolved oxygen from the reaction medium by purging N_2 gas and the obtained absorption profile, kinetic rate plot and bar diagram of rate constant are provided in the Figure APX6.4. From the figure one can observe that the rate of the reaction is increased to a significant extent for all the CuNCs. Interestingly, no induction time has been observed for Cys-CuNCs and ligand-free CuNCs that had been observed in the presence of dissolved oxygen. It is to be noted here that Maschmeyer and co-workers[15] have provided compelling evidence indicating that the conversion of 4-nitrophenol to 4-aminophenol includes an intermediate step involving 4-nitrosophenol. This intermediate may undergo oxidation by dissolved oxygen, leading to the regeneration of 4-nitrophenol. Based on the literature report and our experimental findings, it has been opined that dissolved oxygen also plays another role in facilitating the reverse oxidation of 4-nitrosophenol (an intermediate) to 4-nitrophenol, and

the time required to consume the dissolved oxygen in the reaction medium has indicated the induction time.

6.3.3 Fluorescence Behaviour of CuNCs During Catalysis

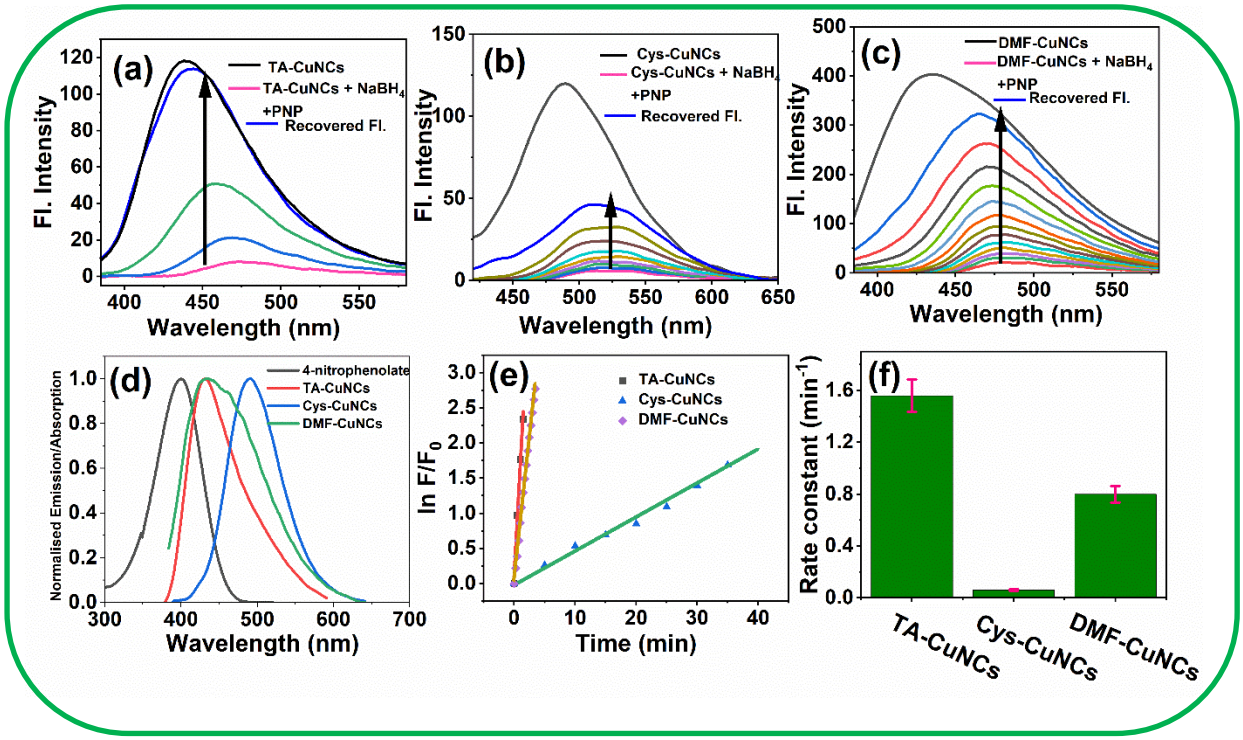

Figure 6.3. Fluorescence spectra of (a) TA-CuNCs (b) Cys-CuNCs and (c) ligand free CuNCs in the absence and presence of reactants (4-NP + $NaBH_4$); (d) Spectral overlap of the absorption spectrum of 4-nitro phenolate with the emission spectra of nano-catalysts; (e) Plot of the 1st order rate equation; (f) Bar diagram of the estimated rate constants.

Since the present NCs are fluorescent, we have also tried to follow the above catalytic reaction by examining the fluorescence behavior of the synthesized nano-catalysts during the catalytic reduction of 4-NP to 4-AP in the presence of $NaBH_4$ initially by employing steady-state fluorescence spectroscopy. It has been observed from the fluorescence study (Figure 6.3a,b,c) that upon addition of the as-prepared CuNCs to the mixture of p-nitrophenol and $NaBH_4$, the fluorescence intensities of the CuNCs are drastically reduced, accompanied by a dark blue color in the reaction mixture. Subsequently, as time passes, the fluorescence

intensities of the CuNCs are observed to increase gradually. This recovery of the fluorescence intensity corresponded to the decrease of the absorption peak at 400 nm (characteristic peak of 4-nitrophenolate ion) and the emergence of a new absorption peak at approximately 300 nm (characteristic peak of 4-AP) in the UV-vis absorption spectra, indicating the generation of 4-AP and the consumption of 4-NP. Therefore, the recovery of the fluorescence signal of the CuNCs can effectively be utilized as a quantitative indicator for monitoring the catalytic conversion of 4-NP 4-AP. To understand the mechanism

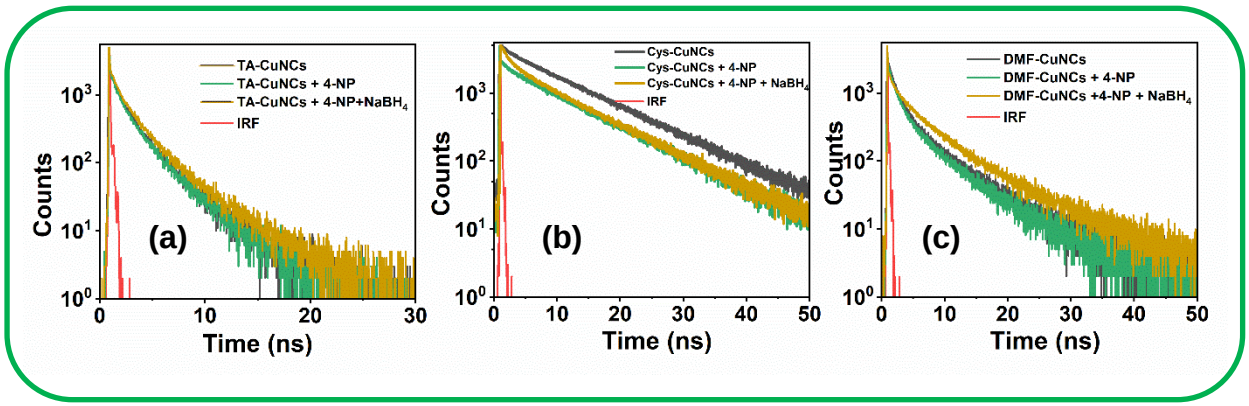

Figure 6.4. Fluorescence lifetime decay of (a) TA-CuNCs (b) Cys-CuNCs and (c) DMF-CuNCs before and after catalysis.

behind the fluorescence changes in CuNCs, we have observed that the emission spectra of CuNCs has overlapped with the absorption spectra of 4-NP in the presence of $NaBH_4$ (Figure 6.3d). The inner filter effect (IFE), arising from the absorption of emission light of CuNCs by absorbers (4-nitrophenolate) in the detection system, is identified as the cause of fluorescence changes. It has been observed that as the reduction of 4-NP progresses, its concentration gradually becomes diminished, leading to a reduction of IFE and the gradual recovery of the fluorescence of CuNCs becomes possible. Furthermore, the rate constants for the catalytic reactions are calculated based on the fluorescence spectra of the nano-catalysts. The plot of $\ln(F_t/F_0)$ versus time (t) is shown in Figure 6.3e (F_t/F_0 is the relative fluorescence intensity at maximum emission). The linear relationship observed in $\ln(F_t/F_0)$ versus time (t) plots allows

the determination of rate constants for the reaction of 4-NP reduction. The rate constants are estimated to be 1.56 min^{-1}, 0.06 min^{-1}, and 0.8 min-1 for TA-CuNCs, Cys-CuNCs, and ligand-free CuNCs, respectively (Figure 6.3f). Quite interestingly, the rate constants estimated from the fluorescence recovery data are found to follow a similar trend to those obtained from absorption data. Furthermore, upon close examination of the fluorescence spectra of these systems, it has been noted that the emission maxima of our nano catalysts experience a red shift in the presence of 4-NP and $NaBH_4$. The observed shift clearly indicates the surface restructuring of the nano catalysts during catalytic processes in the presence of reactants. Overall, these findings indicate that the catalytic process can effectively be monitored through the fluorescence behavior of the luminescent catalyst itself, providing a convenient approach for tracking reactions without the need for specific spectrophotometric characteristics of the substrates. Moreover, we have also monitored the fluorescence lifetime of all three CuNCs before and after the catalytic reaction. The decay profiles of TA-CuNCs, Cys-CuNCs, and ligand-free CuNCs before and after catalysis are provided in Figure 6.4, and the relevant decay parameters are also collected in Table APX6.1. From the Table APX6.1, it can be seen that before catalytic reaction, the average fluorescence lifetime of TA-CuNCs, Cys-CuNCs, and ligand-free CuNCs are 0.19 ns, 8.04 ns and 0.45 ns, respectively, which are changed to 0.16 ns, 4.40 ns and 0.33 ns after catalysis. The recovery of fluorescence lifetime of TA-CuNCs, Cys-CuNCs, and ligand-free CuNCs is ~84 %, ~50%, and ~73 %, respectively. From these fluorescence studies (both steady state and time resolved) it can be opined that as the photophysical properties of these CuNCs are not drastically changed after catalysis, these nano catalysts can be useful for various photocatalytic reaction also.

6.3.4. Catalysis at the Single Particle Level (FCS)

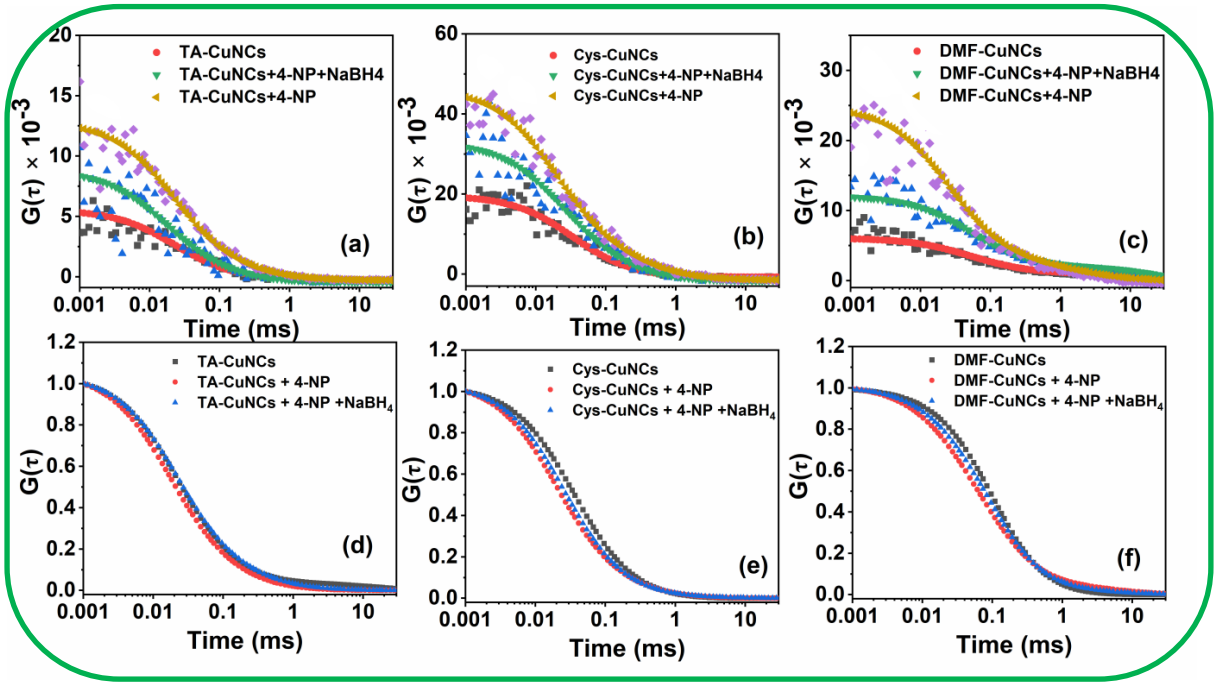

Figure 6.5. (a,b,c) Fluorescence correlation curves and (d,e,f) normalized fluorescence correlation curves of CuNCs in the presence of 4-NP and (4-NP + $NaBH_4$).

To shed light on the reduction of 4-NP to 4-AP by CuNCs at the single-particle level, we have performed FCS studies. This technique is widely used as an extremely sensitive and highly precise single molecule technique that can monitor a slight change in the fluorescence behaviour of the probe at the nanomolar or sub-nanomolar regime. Here, FCS study has been performed to understand the translational diffusion behavior of CuNCs in the absence and presence of the reactants. As a slight perturbation can cause an appreciable change in their diffusion characteristics, we have monitored the translation diffusion time (τD) of CuNCs when subjected to reactants and subsequently calculated the hydrodynamic radius (R_H). Figure 6.5 shows the fluorescence correlation curves (Figure 6.5a,b,c) and their corresponding normalized correlation curves (Figure 6.5d,e,f) of CuNCs in presence of reactants leading to the catalytic reduction. From the fluorescence correlation curve, it has been observed that the amplitude of the autocorrelation function (G(τ)) of CuNCs is increased in the presence of 4-NP, which is again decreased after the catalytic reaction in the presence

of $NaBH_4$. It is known that the amplitude of the G(τ) is inversely proportional to the number of fluorescent molecules under the observation volume. Hence, this phenomenon has been attributed to the decrease in the number of fluorophore moieties under the observation volume of the confocal microscope in the presence of 4-NP and successive increment of the number towards the initial value in the presence of $NaBH_4$. This observation is also supported by the quenching of the fluorescence intensity of CuNCs in presence of 4-NP followed by recovery of fluorescence intensity after the progression of the catalytic reaction that has been discussed in steady state fluorescence measurements study (*vide supra*). Again, the left shift of the normalized correlation curve (Figure 6.5d,e,f) of CuNCs in the presence of 4-NP implies faster diffusion of the fluorophore (CuNCs) which results in the decrease of diffusion time (τ_D) and hydrodynamic radius (R_H). After catalysis, a right shift of the normalization curve towards pure CuNCs has been observed. The relevant parameters are tabulated in Table APX6.2. The decreased value of τ_D and R_H in the presence of 4-NP is suggestive of the surface restructuring of CuNCs. Again, after addition of $NaBH_4$, the values of the parameters (τ_D, R_H) are increased, indicating the progress of the catalytic reaction at single particle level also.

6.3.5. Langmuir-Hinshelwood Mechanism for 4-NP Reduction with CuNCs

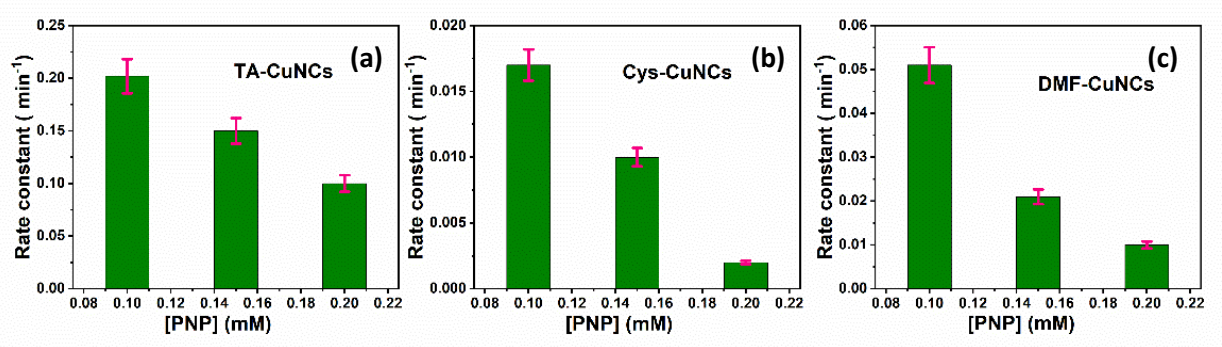

Figure 6.6. Variation of the catalytic rate constant with the increasing concentration of 4-NP in the presence of (a) TA-CuNCs, (b) Cys-CuNCs, and (c) ligand-free CuNCs.

To get more insight into the mechanistic aspect of the catalytic reaction, we have performed the same reaction with the increasing concentration of 4-NP in the presence of different nano-catalysts, and the estimated rate constants are provided in the bar diagram (Figure 6.6). From the bar diagram, it can be observed that the rate constant of the catalytic reaction decreases with the increasing concentration of 4-NP. This observation is suggestive of Langmuir-Hinshelwood mechanism.[65] It is known that in the Langmuir-Hinshelwood mechanism, BH_4^- reacts with nano-catalysts, leading to the adsorption of hydride ions on the catalyst

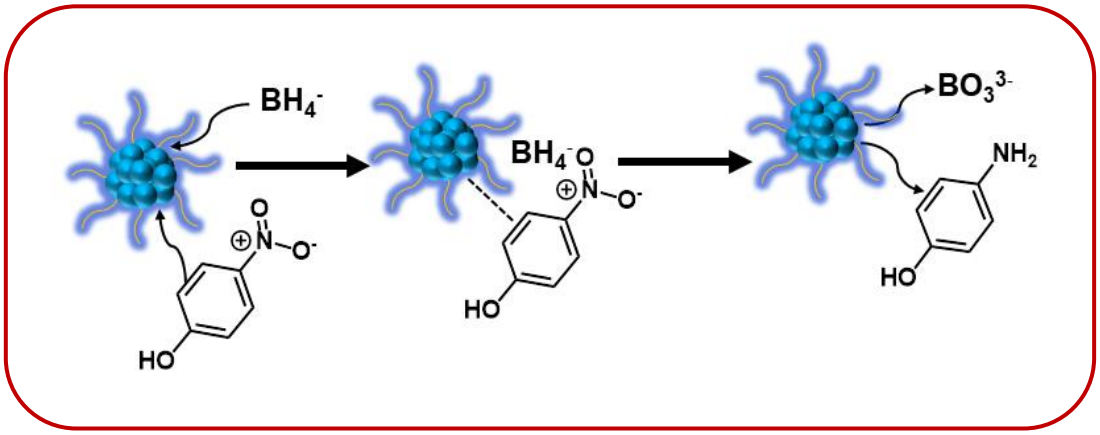

Scheme 6.2. Schematic representation of catalytic reduction of 4-NP to 4-AP.

surface. Simultaneously, PNP is also adsorbed on the catalyst surface.[65] Subsequent to these adsorption processes, the reduction of 4-NP to 4-AP occurs on the catalyst surface through electron transfer between surface-adsorbed hydride ions and 4-NP. The ensuing desorption of 4-AP creates a vacant active site on the NP surface, initiating the subsequent reduction cycle. It is pertinent to mention here that many researchers[26, 77] have demonstrated the validity of the Langmuir-Hinshelwood mechanism by conducting catalytic reductions as a function of 4-NP concentration. As the concentration of 4-NP increases, the catalytic activity is expected to decrease. This is because 4-NP has a higher adsorption constant than BH4-, resulting in the occupation of most active sites on the catalyst surface at higher 4-NP concentrations. Consequently, the interaction between the catalyst and BH_4^- slows down, leading to a

reduction in catalytic activity. The results obtained from this study substantiates that the 4-NP reduction by CuNCs adheres to the Langmuir-Hinshelwood mechanism. A schematic diagram of the catalytic reaction mechanism has been given in the Scheme 6.2.

6.3.6 Applications towards Various Substrate Scopes

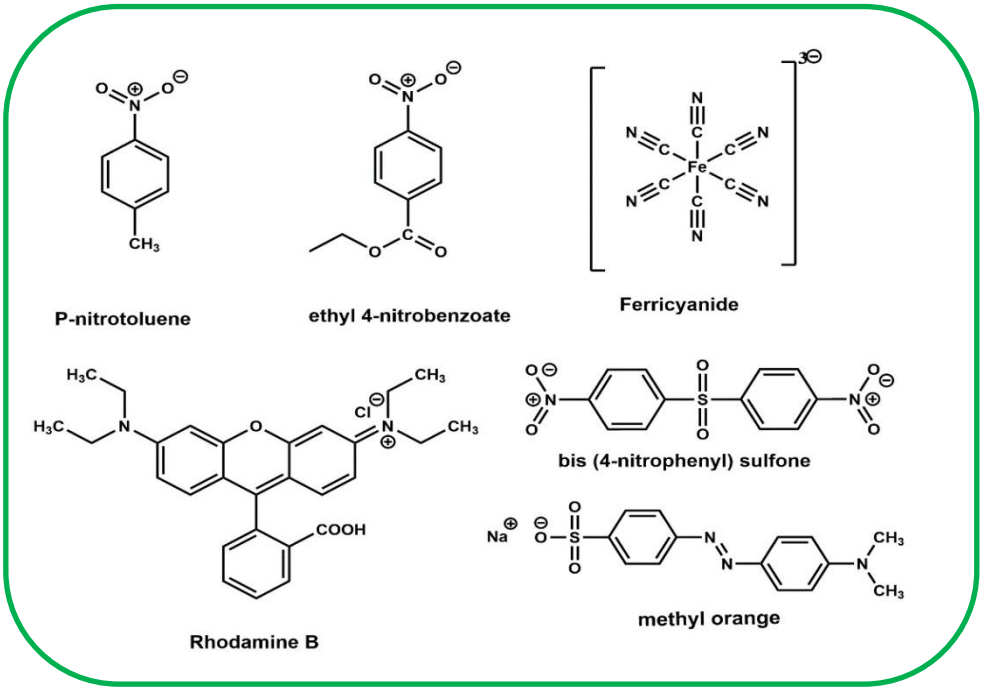

Scheme 6.3. Molecular structures of the substrate scope used in this study.

The reduction of nitro-arenes to aromatic amines holds paramount importance in organic synthesis, as aromatic amines serve as critical structural motifs in agrochemicals, pharmaceuticals, dyes, and biologically active compounds.[78-79] The resilience of our catalytic protocol involving copper-based nano-catalysts against nitro substrates prompted us to evaluate their applicability in the conversion of various essential drug molecules, industrially important analytes, as well as in dye degradation. During the attempts, using TA-CuNCs as nano-catalyst and following the same experimental protocols, we have found that Ethyl 4-Nitrobenzoate is converted to Benzocaine (Figure 6.7a), a topical pain reliever. Interestingly, it has also been observed that Dapsone, an antibiotic in the treatment of leprosy, can also be synthesized from 4,4-Sulfonylbis nitrobenzene by using this nano- catalyst (Figure 6.7b). The

use of this catalytic methodology for synthesizing these drug molecules is expected to be more effective than traditional methods that rely on the potentially hazardous $SnCl_2$/HCl. From the Figure 6.7c and Figure 6.7d it can be seen that

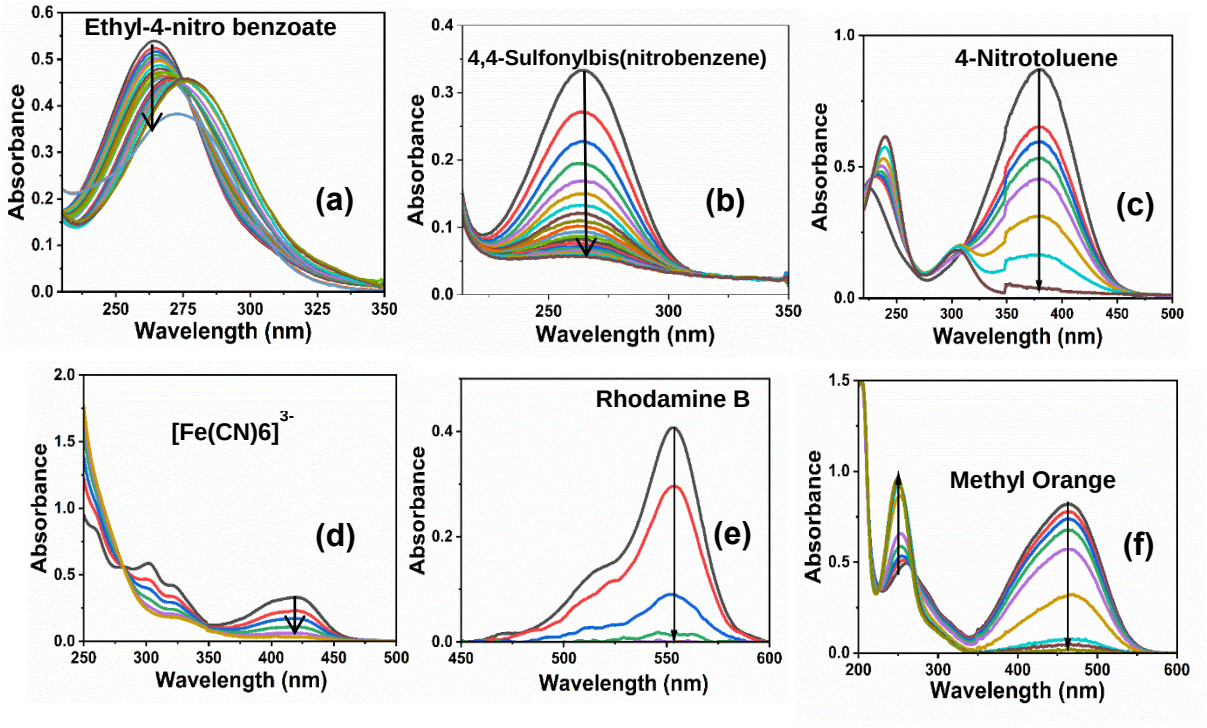

Figure 6.7. UV–vis absorption spectra for catalytic reduction of (a) Ethyl-4-nitro benzoate (b) 4,4-Sulfonylbis nitrobenzene (c) 4 -Nitrotoluene (d) potassium ferricyanide (e) Rhodamine B and (e) Methyl Orange using TA-CuNCs as a nano catalyst.

4-Nitrotoluene and Potassium ferricyanide are converted to 4-Aminotoluene and Potassium ferrocyanide respectively, which have their own industrial applications. Additionally, we have also investigated the potential of the nano catalysts for dye degradation using Rhodamine B and Methyl orange. Absorbance measurements at 553 nm for Rhodamine B and 435 nm for Methyl orange showed consistent decreases over time when treated with nano catalyst, indicating dye degradation. From these studies, it can be concluded that CuNCs, synthesized through environmentally friendly green synthetic strategies and endowed with catalytic properties, show promising potential for diverse applications in the near future.

6.4 Conclusion

In summary, we have investigated the influence of surface ligands on copper nanoclusters (CuNCs) in catalyzing the $NaBH_4$-mediated reduction of 4-nitrophenol to 4-aminophenol. Two types of CuNCs, one capped with tannic acid (TA-CuNCs) and the other with cysteine (Cys-CuNCs) have been synthesized and utilized as nano-catalysts. We have compared the catalytic performance of these ligand-capped CuNCs with that of ligand-free CuNCs in aqueous medium. To understand the catalytic mechanisms at a molecular level, we have utilized the absorption signals of reactants and the fluorescence signals of the CuNCs catalysts. Kinetic data obtained from absorption studies have revealed that the rate constant for the reaction, catalyzed by these nano-catalysts, follows the order: $k_{TA-CuNCs} > k_{CuNCs} > k_{Cys-CuNCs}$. Notably, Cys-CuNCs and ligand-free CuNCs have exhibited an induction time before the reaction commenced, whereas no induction time has been observed with TA-CuNCs. This observation has suggested that surface modification of CuNCs by ligands plays a crucial role in the catalytic reaction. Furthermore, the removal of dissolved oxygen from the reaction medium is found to increase the rate constants for all catalysts and effectively eliminate the induction time. This finding has essentially indicated the influence of dissolved oxygen in facilitating the reverse oxidation of 4-nitrophenol (an intermediate) to 4-nitrophenol. In order to find out the potential of the nano-systems in catalyzing the above reaction, the reduction potentials of these CuNCs are determined through cyclic voltammetry studies. Moreover, the observation of a decrease in the catalytic activity with increasing 4-nitrophenol concentration has pointed out that a Langmuir-Hinshelwood mechanism is responsible for the reaction. Interestingly, from the fluorescence studies (by utilizing the fluorescence property of the nano-catalysts), it has been observed that when the nano-catalysts are added to the mixture of 4-nitrophenol and $NaBH_4$, the fluorescence intensities of the catalysts get reduced drastically at the beginning of the reaction but subsequently get

recovered over time, indicating the progress of the reaction. Quite interestingly, the rate constants estimated from the fluorescence recovery data are found to follow a similar trend to those obtained from absorption data. Furthermore, it has been demonstrated that CuNCs-based nano-catalysts are not only limited to the conversion of 4-nitrophenol to 4-aminophenol but are pretty useful in catalyzing various types of substrates. The outcome of the present work sheds light on the role of surface ligands in nano-catalysis and presents new opportunities in designing new nano-catalysts for practical applications.

6.5. Appendix

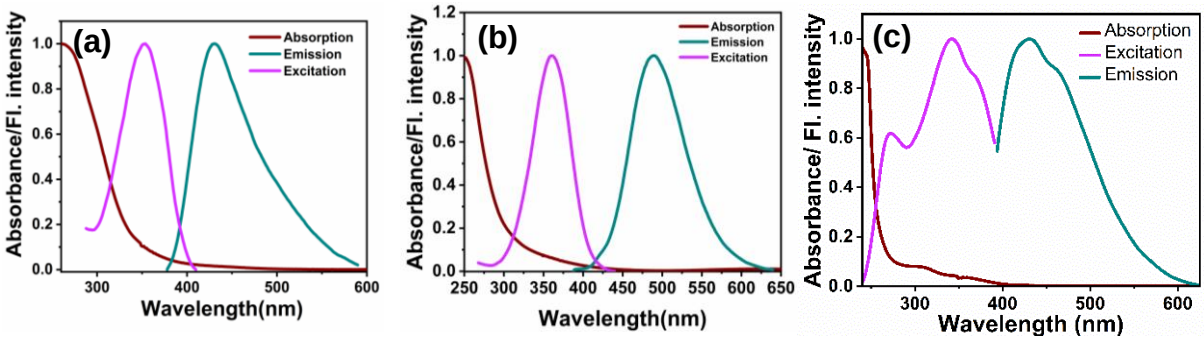

Figure APX.6.1 Normalized absorption, emission and excitation spectra of aqueous solution (a) TA-CuNCs (b) Cys-CuNCs and (c) DMF-CuNCs.

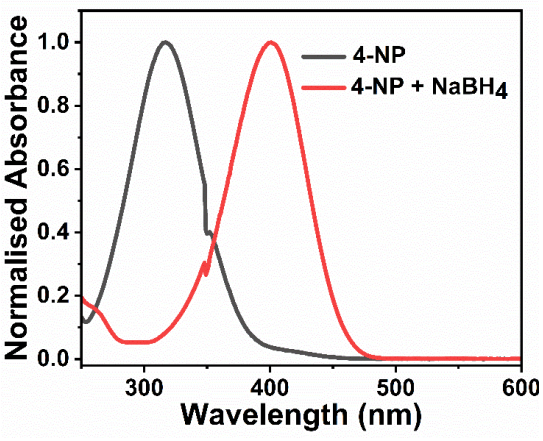

Figure APX6.2. Absorption spectra of 4-NP in the absence and presence of $NaBH_4$.

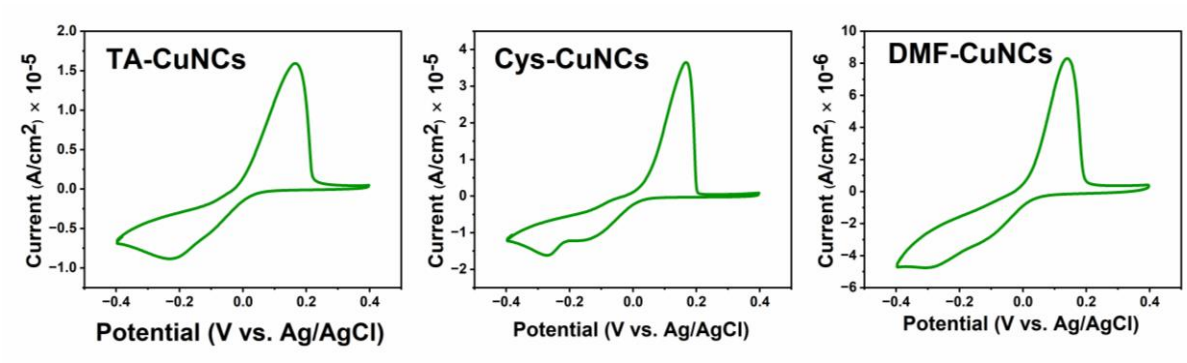

Figure APX6.3. Cyclic voltametric curves of TA-CuNCs, Cys-CuNCs and DMF-CuNCs.

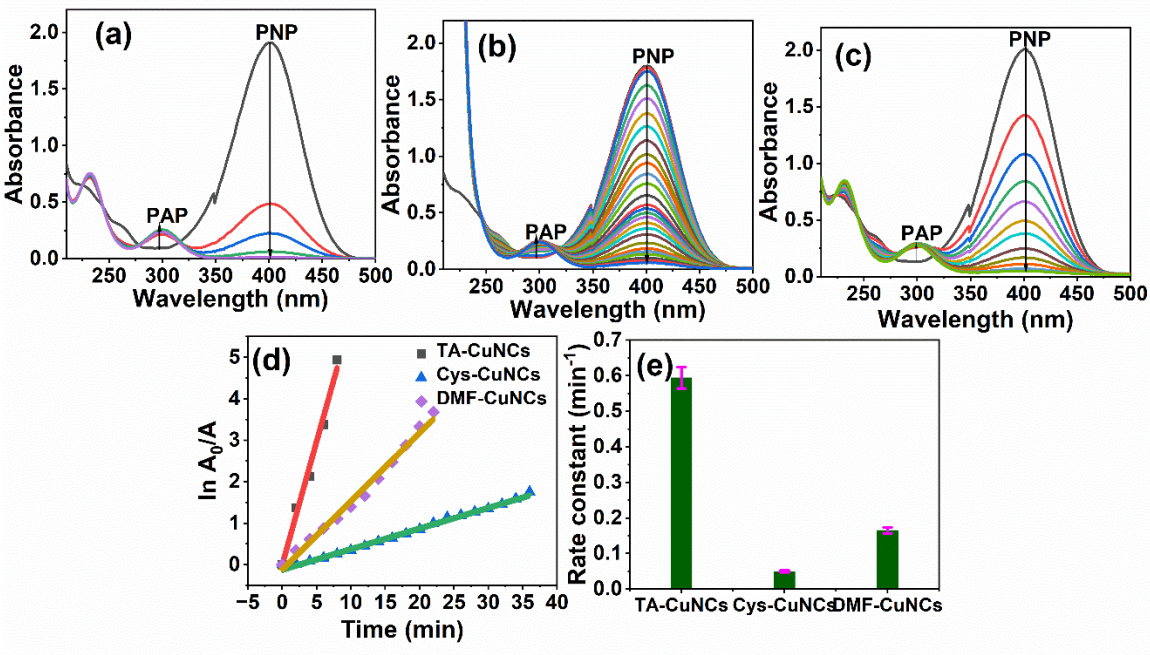

Figure APX.6.4. Absorption spectra of 4-nitrophenol reduced by $NaBH_4$ in the presence of (a) TA-CuNCs (b) Cys-CuNCs and (c) ligand-free CuNCs with 2 min time interval; (d) ln(Ao/At) vs time plot for determination of rate constants; (e) Bar diagram of catalytic reaction rate constant vs various CuNCs. (experiments are done in the absence of dissolved oxygen)

Product characterization

The products underwent comprehensive characterization utilizing HRMS, ^{1}H NMR, and ^{13}C techniques. Following the total reduction, the product was extracted with ethyl acetate. The

resulting product was then dried using Na_2SO_4, and the solvent was evaporated, yielding a solid product that was used for characterization purposes.

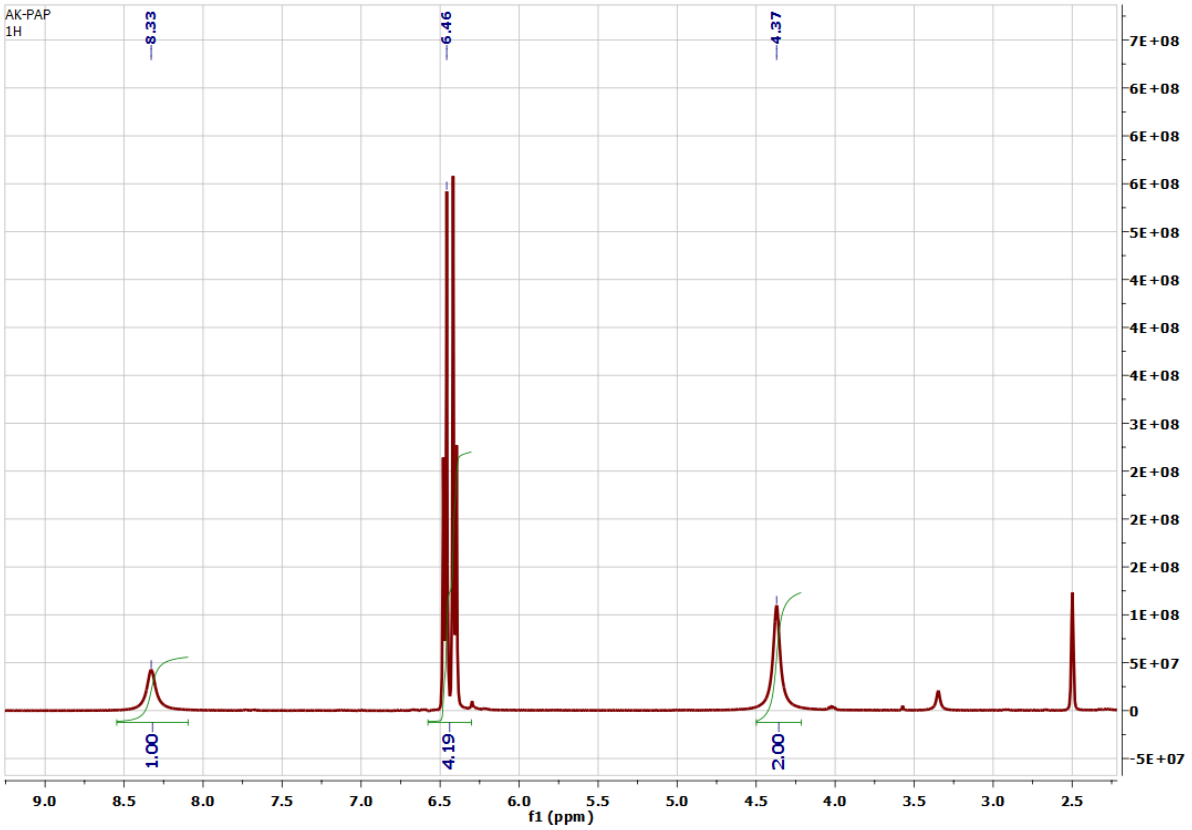

Figure APX6.5. NMR spectra of 4-AP in DMSO-d^6 that were produced by the catalytic reduction of 4-AP.

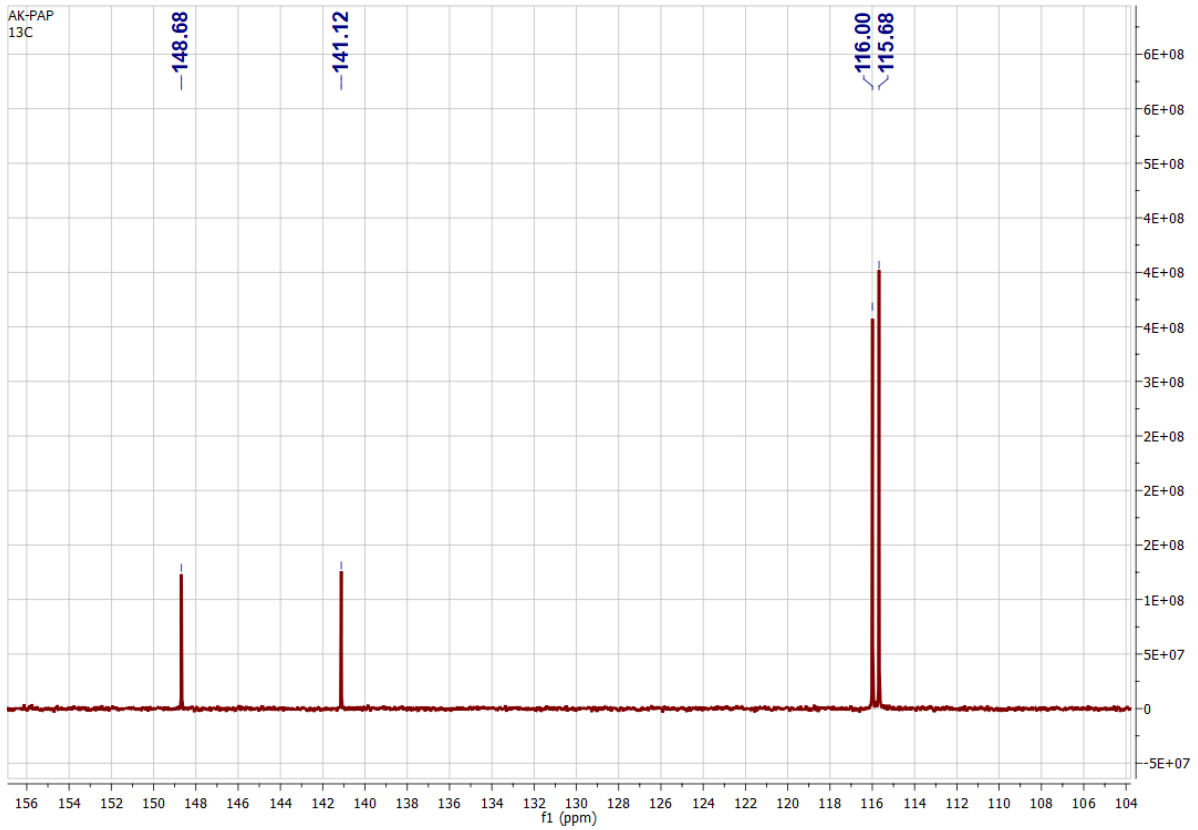

Figure APX6.6. ^{13}C spectrum of p-aminophenol 4-AP resulting from the catalytic reduction in the presence of CuNCs.

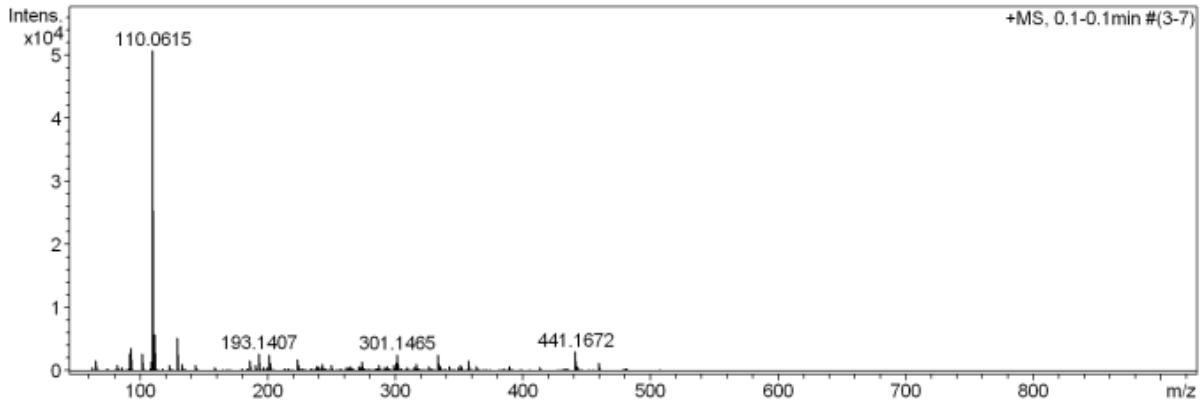

Figure APX6.7. ESI- MASS spectra of 4-AP 4-AP resulting from the catalytic reduction in the presence of CuNCs.

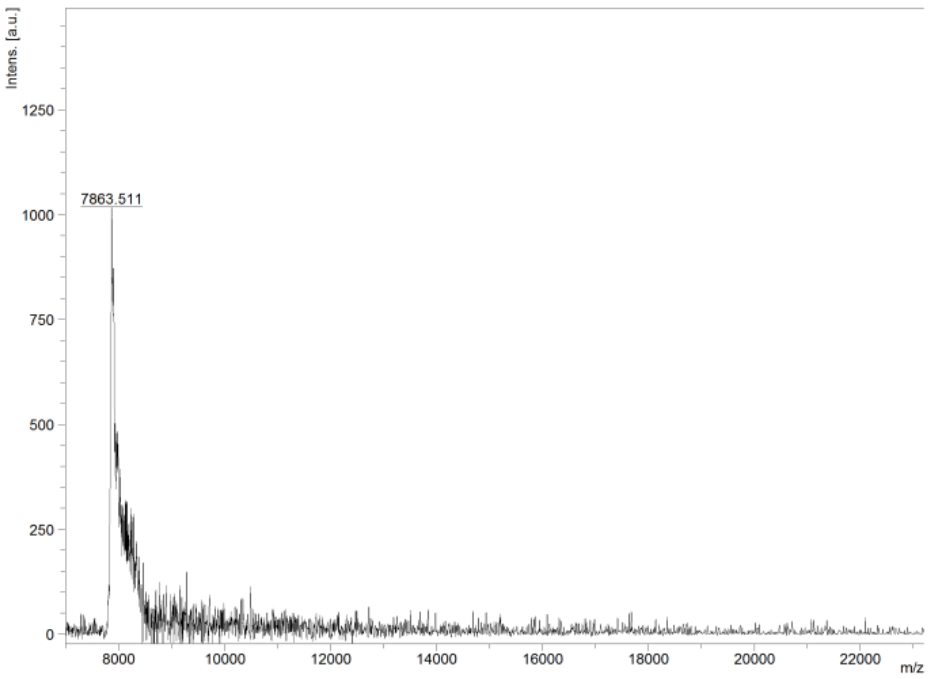

Figure APX6.8. MALDI-TOF MASS spectra of TA-CuNCs.

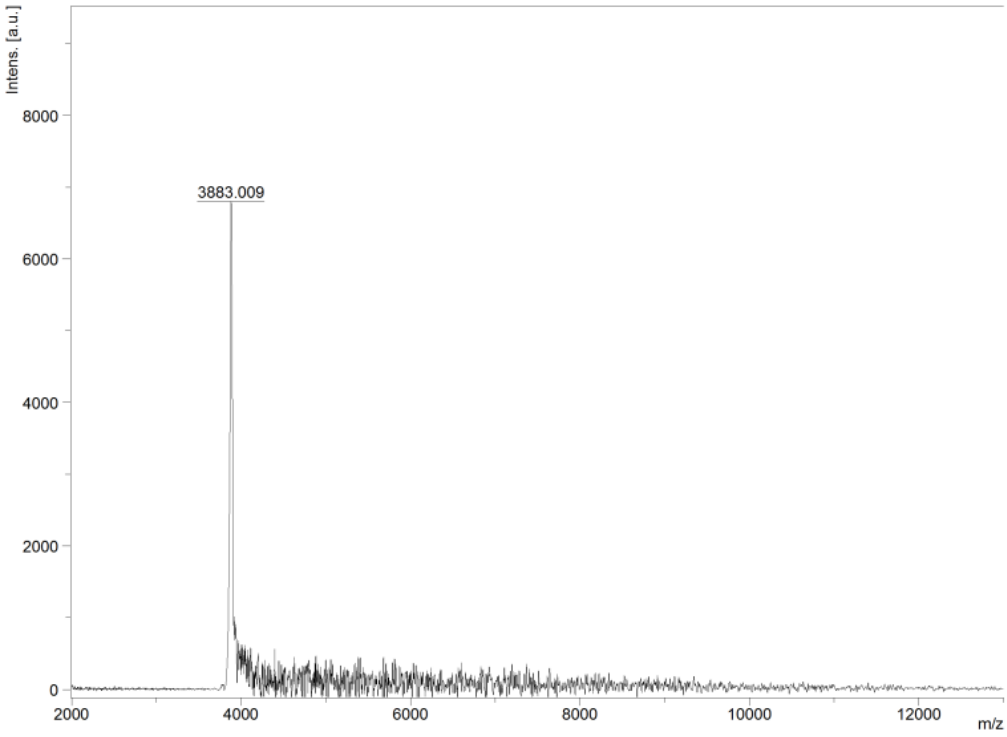

Figure APX6.9. MALDI-TOF MASS spectra of Cys-CuNCs.

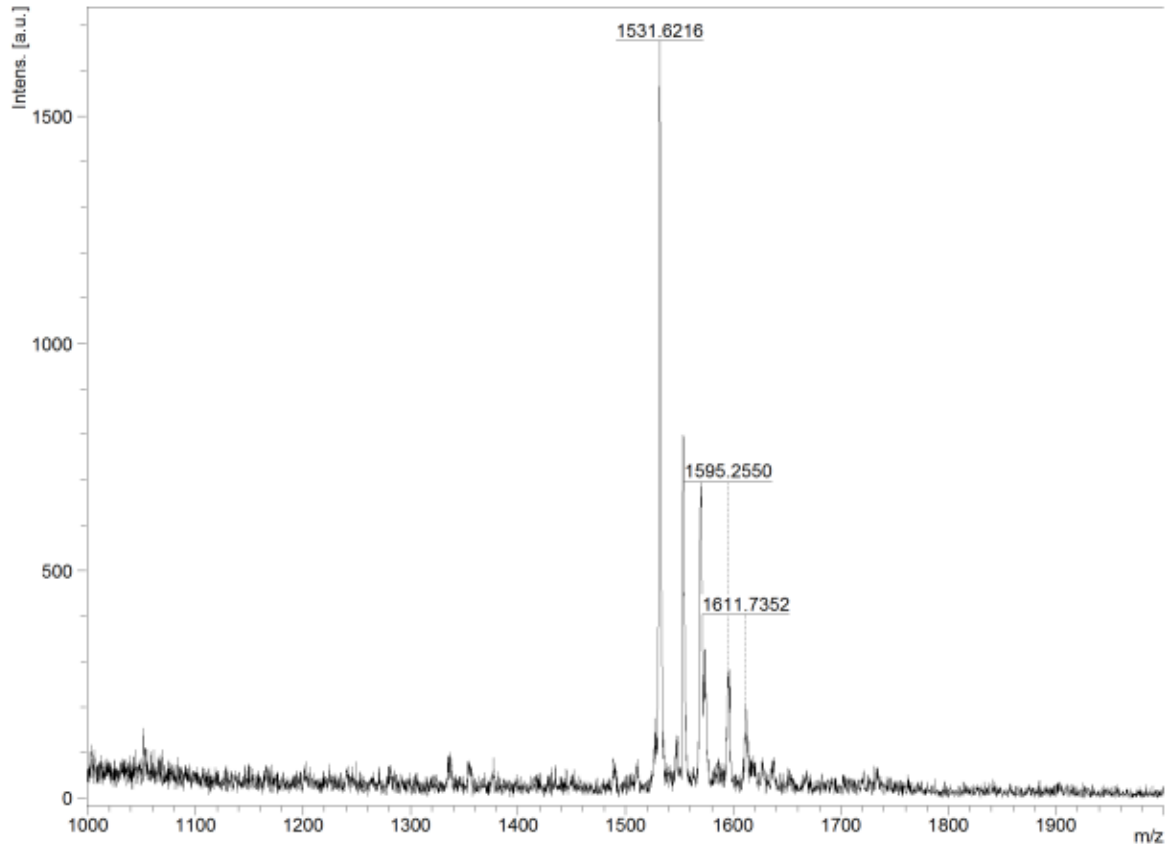

Figure APX6.10. MALDI-TOF MASS spectra of DMF-CuNCs.

Table APX6.1. Fluorescence decay parameters of CuNCs in absence and presence of reagents. (The excitation wavelength is 375 nm)

Sample	τ_1	β_1	τ_2	β_2	τ_3	β_3	$<\tau>$
TA-CuNCs	0.02	90.21	0.85	6.52	2.82	3.26	0.16
TA-CuNCs+PNP	0.01	93.18	0.83	4.54	2.82	2.27	0.11
TA-CuNCs+PNP+ $NaBH_4$	0.05	91.50	1.25	6.60	3.63	1.88	0.19
Cys-CuNCs	0.69	13.63	2.33	9.09	10.01	77.27	8.04
Cys-CuNCs+PNP	0.01	91.03	1.1	2.06	9.16	6.89	0.66
Cys-CuNCs + PNP +$NaBH_4$	0.27	24.00	1.44	32.00	8.81	44.00	4.40
DMF-CuNCs	0.06	80.88	1.15	14.70	5.26	4.41	0.45
DMF-CuNCs + PNP	0.02	90.26	1.04	7.07	4.95	2.65	0.22
DMF-CuNCs + PNP +$NaBH_4$	0.02	91.01	1.20	4.49	5.90	4.49	0.33

[A] concentration of CuNCs are in μM, α is expressed in % scale and τ values (±5 %) are in ns unit

Table APX6.2. The associated diffusion parameters of CuNCs in the absence and presence of reagents were obtained from the FCS study.[a]

CuNCs (30 nM)	τ_D(μs)	R_H(nm)
TA-CuNCs	40.1	0.66
TA-CuNCs + 4-NP	29.6	0.51
TA-CuNCs + 4-NP+$NaBH_4$	39.8	0.64
Cys-CuNCs	39.3	0.69
Cys-CuNCs + 4-NP	28.5	0.58
Cys-CuNCs + 4-NP +$NaBH_4$	34.6	0.61
DMF-CuNCs	37.7	0.61
DMF-CuNCs + 4-NP	30.4	0.44
DMF-CuNCs + 4-NP + $NaBH_4$	35.9	0.57

a ± 5%

References

1. Zheng, K.; Yuan, X.; Goswami, N.; Zhang, Q.; Xie, J. *RSC Adv.* **2014**, *4*, 60581-60596.
2. Tay, C. Y.; Setyawati, M. I.; Xie, J.; Parak, W. J.; Leong, D. T. *Adv. Funct. Mater.* **2014**, *24*, 5936-5955.
3. Jin, R.; Zeng, C.; Zhou, M.; Chen, Y. *Chem. Rev.* **2016**, *116*, 10346-10413.
4. Watanabe, K.; Menzel, D.; Nilius, N.; Freund, H.-J., *Chem. Rev.* **2006**, *106*, 4301-4320.
5. Li, S. Y.; Wang, M. I. N. *Nano LIFE* **2012**, *02*, 1230002.
6. Mahmoudi, M.; Lynch, I.; Ejtehadi, M. R.; Monopoli, M. P.; Bombelli, F. B.; Laurent, S. *Chem. Rev.* **2011**, *111*, 5610-5637.
7. Zhang, L.; Wang, E. *Nano Today* **2014**, *9*, 132-157.
8. Jin, R.; Zeng, C.; Zhou, M.; Chen, Y. *Chem Rev* **2016**, *116*, 10346-413.
9. Lu, Y.; Chen, W. *Chemical Society Reviews* **2012**, *41*, 3594-3623.
10. Shang, L.; Dong, S.; Nienhaus, G. U. *Nano Today* **2011**, *6*, 401-418.
11. Zhao, T.; Zhou, T.; Yao, Q.; Hao, C.; Chen, X. *Journal of Environmental Science and Health, Part C* **2015**, *33*, 168-187.
12. Du, Y.; Sheng, H.; Astruc, D.; Zhu, M. *Chem. Rev.* **2020**, *120*, 526-622.
13. Zhao, Y.; Zhou, H.; Zhang, S.; Xu, J. *Methods Appl. Fluoresc.* **2020**, *8*, 012001.
14. Haldar, K. K.; Kundu, S.; Patra, A. *ACS Appl. Mater. Interfaces* **2014**, *6*, 21946-21953.
15. Strachan, J.; Barnett, C.; Masters, A. F.; Maschmeyer, T. *ACS Catal.* **2020**, *10*, 5516-5521.
16. Pozun, Z. D.; Rodenbusch, S. E.; Keller, E.; Tran, K.; Tang, W.; Stevenson, K. J.; Henkelman, G. *J Phys Chem C Nanomater Interfaces* **2013**, *117*, 7598-7604.
17. Wunder, S.; Lu, Y.; Albrecht, M.; Ballauff, M. *ACS Catal.* **2011**, *1*, 908-916.
18. Sharma, B.; Tanwar, S.; Sen, T. *ACS Sustain. Chem. Eng.* **2019**, *7*, 3309-3318.
19. Roy, S.; Rao, A.; Devatha, G.; Pillai, P. P. *ACS Catal.* **2017**, *7*, 7141-7145.
20. Fang, J.; Zhang, B.; Yao, Q.; Yang, Y.; Xie, J.; Yan, N. *Coord. Chem. Rev.* **2016**, *322*, 1-29.
21. de Heer, W. A. *Rev. of Mod. Phys.* **1993**, *65*, 611-676.
22. Zhai, H.-J.; Pan, L.-L.; Dai, B.; Kiran, B.; Li, J.; Wang, L.-S., *J. Phys. Chem. C* **2008**, *112*, 11920-11928.
23. Neal, R. D.; Hughes, R. A.; Sapkota, P.; Ptasinska, S.; Neretina, S. *ACS Catal.* **2020**, *10*, 10040-10050.
24. Lee, H.; Yoon, D.-E.; Koh, S.; Kang, M. S.; Lim, J.; Lee, D. C. *Chem. Sci.* **2020**, *11*, 2318-2329.
25. Yang, T.-H.; Shi, Y.; Janssen, A.; Xia, Y. *Angew. Chem. Int. Ed.* **2020**, *59*, 15378-15401.
26. Ansar, S. M.; Kitchens, C. L. *ACS Catal.* **2016**, *6*, 5553-5560.
27. Gao, M.; Yang, Y.; Guo, J. *Catal. Letters* **2019**, *149*, 2110-2118.

28. Lopez-Sanchez, J. A., et al. *Nat. Chem.* **2011**, *3*, 551-556.
29. Liu, Y.; Jia, C.-J.; Yamasaki, J.; Terasaki, O.; Schüth, F. *Angew. Chem. Int. Ed.* **2010**, *49*, 5771-5775.
30. Campisi, S.; Schiavoni, M.; Chan-Thaw, C. E.; Villa, A. *Catalysts* **2016**, *6*, 185.
31. Wang, Z.; Fu, H.; Han, D.; Gu, F. *J. Mater. Chem. A* **2014**, *2*, 20374-20381.
32. Park, J. Y.; Aliaga, C.; Renzas, J. R.; Lee, H.; Somorjai, G. A. *J. Catal.* **2009**, *129*, 1-6.
33. Niu, Z.; Li, Y. *Chem. Mater.* **2014**, *26*, 72-83.
34. Bastús, N. G.; Merkoçi, F.; Piella, J.; Puntes, V. *Chem. Mater.* **2014**, *26*, 2836-2846.
35. Álvarez Cerimedo, M. S.; Baronio, L. G.; Hoppe, C. E.; Ayude, M. A. *ChemistrySelect* **2019**, *4*, 608-616.
36. Schrader, I.; Warneke, J.; Backenköhler, J.; Kunz, S. *J. Am. Chem. Soc.* **2015**, *137*, 905-912.
37. Ibrahim, M.; Garcia, M. A. S.; Vono, L. L. R.; Guerrero, M.; Lecante, P.; Rossi, L. M.; Philippot, K. *Dalton Trans.* **2016**, *45*, 17782-17791.
38. Wang, Y., et al. *J. Am. Chem. Soc.* **2016**, *138*, 3278-3281.
39. Yoskamtorn, T.; Yamazoe, S.; Takahata, R.; Nishigaki, J.-i.; Thivasasith, A.; Limtrakul, J.; Tsukuda, T. *ACS Catal.* **2014**, *4*, 3696-3700.
40. Li, G.; Qian, H.; Jin, R. *Nanoscale* **2012**, *4*, 6714-6717.
41. Pradhan, N.; Pal, A.; Pal, T. *Physicochem. Eng. Asp.* **2002**, *196*, 247-257.
42. Esumi, K.; Miyamoto, K.; Yoshimura, T. *J. Colloid Interface Sci.* **2002**, *254*, 402-405.
43. Bukowska, B.; Michałowicz, J.; Krokosz, A.; Sicińska, P. *Blood Cells Mol. Dis.* **2007**, *39*, 238-44.
44. Feng, J.; Su, L.; Ma, Y.; Ren, C.; Guo, Q.; Chen, X. *Chem. Eng. J* **2013**, *221*, 16-24.
45. Ahmaruzzaman, M.; Laxmi Gayatri, S. *Chem. Eng. J* **2010**, *158*, 173-180.
46. Vaidya, M. J.; Kulkarni, S. M.; Chaudhari, R. V. *Org. Process. Res. Dev.* **2003**, *7*, 202-208.
47. Abbar, A. H.; Sulaymon, A. H.; Jalhoom, M. G. *Electrochim. Acta* **2007**, *53*, 1671-1679.
48. Du, Y.; Chen, H.; Chen, R.; Xu, N. *Appl. Catal. A: Gen.* **2004**, *277*, 259-264.
49. Gu, S.; Wunder, S.; Lu, Y.; Ballauff, M.; Fenger, R.; Rademann, K.; Jaquet, B.; Zaccone, A. *J. Phys. Chem. C* **2014**, *118*, 18618-18625.
50. Zhang, J.-T.; Wei, G.; Keller, T. F.; Gallagher, H.; Stötzel, C.; Müller, F. A.; Gottschaldt, M.; Schubert, U. S.; Jandt, K. D. *Macromol. Mater. Eng.* **2010**, *295*, 1049-1057.
51. Sarkar, S.; Sinha, A. K.; Pradhan, M.; Basu, M.; Negishi, Y.; Pal, T. *J. Phys. Chem. C* **2011**, *115*, 1659-1673.
52. Neal, R. D.; Inoue, Y.; Hughes, R. A.; Neretina, S. *J. Phys. Chem. C* **2019**, *123*, 12894-12901.
53. Nasaruddin, R. R.; Chen, T.; Li, J.; Goswami, N.; Zhang, J.; Yan, N.; Xie, J. *Chem. Cat. Chem.* **2018**, *10*, 395-402.
54. Du, J.; Zhao, Y.; Chen, J.; Zhang, P.; Gao, L.; Wang, M.; Cao, C.; Wen, W.; Zhu, C. *RSC Adv.* **2017**, *7*, 33929-33936.

55. Wei, W.; Lu, Y.; Chen, W.; Chen, S. *J. Am. Chem. Soc.* **2011**, *133*, 2060-2063.
56. Cao, H.; Chen, Z.; Zheng, H.; Huang, Y. *Biosens. Bioelectron.* **2014**, *62*, 189-195.
57. Sahu, D. K.; Sahu, K. *J. Photochem. Photobiol., A* **2017**, *347*, 17-25.
58. Lin, Z.; Slee, T.; Mingos, D. M. P. *Chem. Phys.* **1990**, *142*, 321-334.
59. Rajamanikandan, R.; Shanmugaraj, K.; Ilanchelian, M. *J. Clust. Sci.* **2017**, *28*, 1009-1023.
60. Gangula, A.; Podila, R.; M, R.; Karanam, L.; Janardhana, C.; Rao, A. M. *Langmuir* **2011**, *27*, 15268-74.
61. Ai, L.; Yue, H.; Jiang, J. *J. Mater. Chem.* **2012**, *22*, 23447-23453.
62. Murugadoss, A.; Chattopadhyay, A. *Nanotechnol.***2008**, *19*, 015603.
63. Das, J.; Aziz, M. A.; Yang, H. *J. Am. Chem. Soc.* **2006**, *128*, 16022-16023.
64. Yamamoto, H.; Yano, H.; Kouchi, H.; Obora, Y.; Arakawa, R.; Kawasaki, H. *Nanoscale* **2012**, *4*, 4148-4154.
65. Wunder, S.; Polzer, F.; Lu, Y.; Mei, Y.; Ballauff, M. *J. Phys. Chem. C* **2010**, *114*, 8814-8820.
66. Mei, Y.; Lu, Y.; Polzer, F.; Ballauff, M.; Drechsler, M. *Chem. Mater.* **2007**, *19*, 1062-1069.
67. Kalekar, A. M.; Sharma, K. K. K.; Lehoux, A.; Audonnet, F.; Remita, H.; Saha, A.; Sharma, G. K. *Langmuir* **2013**, *29*, 11431-11439.
68. Lu, Y.; Mei, Y.; Walker, R.; Ballauff, M.; Drechsler, M. *Polymer* **2006**, *47*, 4985-4995.
69. Zeng, J.; Zhang, Q.; Chen, J.; Xia, Y. *Nano Lett.* **2010**, *10*, 30-35.
70. Kuroda, K.; Ishida, T.; Haruta, M. *Chemical* **2009**, *298*, 7-11.
71. Signori, A. M.; Santos, K. d. O.; Eising, R.; Albuquerque, B. L.; Giacomelli, F. C.; Domingos, J. B. *Langmuir* **2010**, *26*, 17772-17779.
72. Lu, P.; Campbell, C. T.; Xia, Y. *Nano Lett.* **2013**, *13*, 4957-4962.
73. Mahmoud, M. A.; El-Sayed, M. A. *Nano Lett.* **2011**, *11*, 946-53.
74. Weng, G.; Mahmoud, M. A.; El-Sayed, M. A. *J. Phys. Chem. C* **2012**, *116*, 24171-24176.
75. Liu, X.; Li, C.; Xu, J.; Lv, J.; Zhu, M.; Guo, Y.; Cui, S.; Liu, H.; Wang, S.; Li, Y. *J. Phys. Chem. C* **2008**, *112*, 10778-10783.
76. Kawasaki, H.; Yamamoto, H.; Fujimori, H.; Arakawa, R.; Iwasaki, Y.; Inada, M. *Langmuir* **2010**, *26*, 5926-5933.
77. Kästner, C.; Thünemann, A. F. *Langmuir* **2016**, *32*, 7383-7391.
78. Lawrence, S. A., *Amines:* Cambridge University Press, 2004.
79. Rappoport, Z., The Chemistry of Anilines, Part 1; . *Wiley* **2007**.

CHAPTER 7

Probing the Investigation of Energy Transfer from Non-Plasmonic Fluorescence Bimetallic nanoparticle to Plasmonic Gold Nanoparticles

Understanding the fundamentals behind the photophysical response of a fluorescing species in the vicinity of plasmonic nanoparticles is of great interest due to the importance of this event in various applications. The present work has been carried out to throw light on how plasmonic nanoparticles electronically interact with non-plasmonic nanoparticles. Specifically, in this work, the excitation energy transfer (EET) from fluorescence bimetallic silver capped gold (F-AgAu) to gold nanoparticles (AuNPs) and how this process can be modulated by cetyltrimethylammonium bromide (CTAB) have been investigated at both ensemble average and single particle levels. Steady-state and time-resolved fluorescence studies have revealed that the fluorescence intensity and lifetime of F-AgAu in the presence of AuNPs are significantly quenched. Cyclic voltammetry (CV) and polarity-dependent studies have ruled out the possibility of an electron transfer mechanism. The increased non-radiative decay rate has substantiated that the photoluminescence quenching is due to excitation energy transfer from F-AgAu to AuNPs. Interestingly, investigations have revealed that the energy transfer efficiency is reduced from 87% to 28% in the presence of CTAB due to the formation of a CTAB bilayer over AuNPs. Analysis of the data by conventional EET, nano surface energy transfer (NSET), and stretched exponential models have firmly established that the EET process follows a 1/d4 distance dependence (NSET) rather than conventional 1/d6 distance dependence as predicted with the Fo¨rster resonance energy transfer model. Additionally, single particle level measurements through fluorescence lifetime imaging microscopy (FLIM) studies have clearly demonstrated that the surfactant (CTAB) can play an important role in controlling the EET process from non-plasmonic to plasmonic nanoparticles. The outcome of the present EET between two different classes of nanoparticles is expected to be useful in developing nanoscale systems for various optoelectronic applications.

7.1. Introduction

Non-radiative excitation energy transfer (EET) in nanoscale donor-acceptor systems is an important part of research due to its extensive applications in sensors, bioimaging, photovoltaic devices, light emitting diodes, and other optoelectronics.[1-5] Understanding the mechanism of energy transfer between donors and acceptor play a vital role in developing

and optimizing the system for various applications. It is known that majority of excited state energy transfers are mediated through either Förster resonance energy transfer (FRET) or Dexter resonance energy transfer.[6-7] FRET is a non-radiative energy transfer which happens from a photoexcited donor to an acceptor via dipole−dipole interactions. FRET is a distance-dependant (<10nm) phenomenon which is an important tool to measure the dynamic changes between molecular donor−acceptor pairs in various complex macromolecular systems.[8-10] However, the FRET model is not suitable for many donor-acceptor couples where their dynamic interaction takes place over longer distances. Hence, it's also very important to investigate and understand the longer-range energy-transfer processes. In recent years, nanoparticle (mediated) Surface Energy Transfer (NSET), theorized by Persson and Lang,[11] has gained considerable attention due to its applicability for determining larger distance (beyond FRET limit) donor-acceptor systems.[12-15] It has been demonstrated that NSET is also a non-radiative dipole−dipole energy transfer, but this process happens due to the interaction of the electromagnetic field of a donor dipole with the free conduction electrons of the metal nanoparticle (acceptor), which in contrast to Fröster type energy transfer (FRET) where both donor and acceptor are considered as point dipoles.[11] Several experimental and theoretical studies have established that the separation distance between donor and acceptor is $1/d^4$ dependent on energy transfer efficiency.[11-13]

It is to be noted here that nanoparticles (NPs) with characteristic localized surface plasmon resonance (LSPR) have drawn considerable attention from researchers due to their potential applications in surface-enhanced Raman scattering, photovoltaics, photodetectors, LEDs and biology.[16-22] It is well known that LSPR of metal NPs can either enhance or quench the fluorescence intensity of nearby fluorophores. The effect of metal nanoparticles on the fluorescence property of nearby fluorophores is dependent on various parameters such as distance between fluorophore and nanomaterial, spectral overlap, size and shape of the

metal nanoparticle and orientation of dipole with respect to metal nanostructure.[23-27] The enhancement of fluorescence quantum yield of nearby fluorophores usually happens due to either an enhanced electromagnetic field of LSPR at the metal nanoparticle surface or an increase in the radiative decay rate of the excited fluorophore near the metal nanoparticles.[28-34] Moreover, it has been observed that in many nanocomposite systems, the fluorescence intensity of nearby fluorophores is quenched by metal nanoparticles.[12, 35-43] Several studies have been performed to understand the fundamentals behind this long-range electromagnetic coupling and subsequent fluorescence quenching mechanism at the metal NP surface. It is pertinent to mention here that Silbey and coworkers[38] have demonstrated the quenching of excited donors in the presence of metal surface, and later on, it is extended by Persson and Lang[11] by using a Fermi golden rule. Wu and coworkers[23] have investigated the energy transfer from CdSe/ZnS quantum dots to the various sizes of gold nanoparticles. They have demonstrated that AuNPs of 3 nm size having negligible LSPR follow NSET mechanism, whereas AuNPs of 15 and 80 nm sizes having strong LSPR overlapped with donor emission following FRET mechanism. In another recent work, Wert and coworkers[44] have demonstrated that the energy transfer from terbium(III)-complex (Tb) donors to AuNP (acceptors) of 5, 30, 50, and 80 nm diameter follow NSET model instead of FRET model and also shown that the energy transfer efficiencies were independent of the size of AuNPs. Earlier, Strouse and coworkers[14, 45-46] have shown that the fluorescence quenching of different dyes in the presence of AuNPs follows $1/d^4$ distance-dependent quenching behaviour, which associates with the NSET theory. Patra and co-workers[15, 39-42] have demonstrated the surface energy transfer processes in various AuNPs–based assemblies and reported their applications as spectroscopic rulers, protein conformational studies etc. In another work, Peteanu and coworkers[27] have shown the effect of particle size on NSET from DNA/dye complexes to AuNPs and AuNCs. It can be realized from the discussion of the above reports that

researchers have tried to tune the NSET by adjusting the distance, overlap, size and shape of nanoparticles. Moreover, the above discussion also depicts that most of the studies that are carried out on the nanocomposite systems have employed quantum dots, carbon-based fluorophore and organic dye molecules as donors, and AuNPs and AgNPs as acceptors. However, studies on the interaction between bimetallic non-plasmonic nanomaterials and plasmonic nanoparticles are rather limited. In fact, no studies by focussing on the EET process between F-AgAu to AuNPs have been carried out. It may be noted here that fluorescence bimetallic nanoparticles can be considered as attractive research targets due to their potential applications in sensing, catalysis, antibacterial applications etc.[47-53] Therefore, it will be a worthwhile objective to understand the fundamentals behind the photoluminescence (PL) behaviour of non-plasmonic bimetallic nanomaterials in the vicinity of plasmonic nanoparticles. It will also be interesting to investigate if surface modification on the NPs may provide possible options for surface-mediated modulation of EET process between non-plasmonic to plasmonic nanomaterials.

Keeping the above facts in mind, in the current study, we have investigated the interaction of bimetallic fluorescence silver-capped gold nanoparticle (F-AgAu) with AuNPs and the associated excited state energy transfer (EET) mechanism. Steady-state absorption and emission, time-resolved fluorescence, cyclic voltammetry (CV), fluorescence lifetime imaging (FLIM) microscopic studies, etc., have been employed to gain a molecular-level understanding of the interaction event. F-AgAu has been chosen due to its optical stability and high fluorescence property.[54] Data obtained from the above studies have revealed that the fluorescence quenching of F-AgAu in the vicinity of AuNPs is caused due to the excited state energy transfer from F-AgAu to AuNPs, and the non-radiative excited state energy transfer process can be best described by NSET model rather than by usual FRET model.

Interestingly, the studies have demonstrated that the EET efficiency from F-AgAu to AuNPs can effectively be modulated by modifying AuNPs with CTAB surfactant.

The chemical structures of the compounds that are used in the present study are shown in Scheme 7.1.

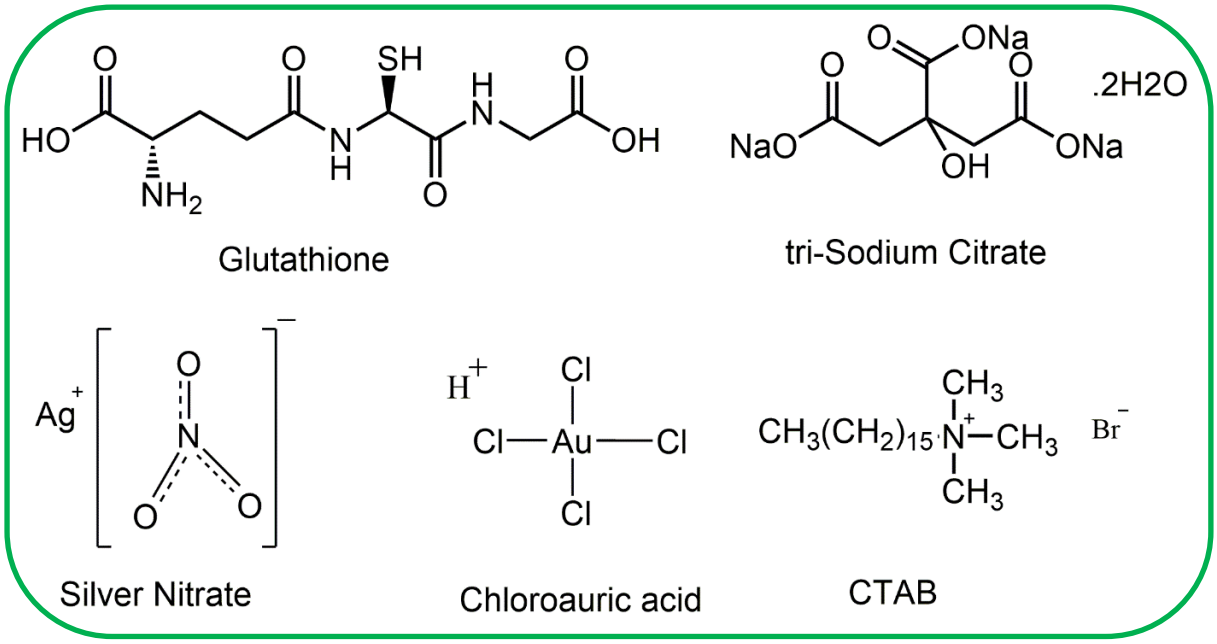

Scheme 7.1. Molecular structures of the chemicals used in this study.

7.2. Result and discussion

7.2.1. Characterization of F-AgAu and Au NPs

The synthesized F-AgAu and AuNPs are characterized by employing spectroscopic and microscopic techniques. Initially, the systems are characterized by steady-state absorption and emission measurements which are provided in the Figure 7.1. It can be seen from Figure 7.1a that F-AgAu shows a broad absorption band without any plasmonic peak. The absence of any characteristic plasmonic bands of silver and gold nanoparticles can be rationalized by considering the plasmon damping phenomenon which might have caused in the present system due the coating of silver nanoclusters on the surface of gold.[56-59] Moreover, it can also

be seen from the Figure 7.1a that F-AgAu possesses high fluorescence property with emission maximum at 570 nm upon excitation at 375 nm. It is reported that the F-AgAu is composed of large gold nanoparticle core covered by silver nanoclusters shell.[54] The fluorescence behaviour of the F-AgAu can be

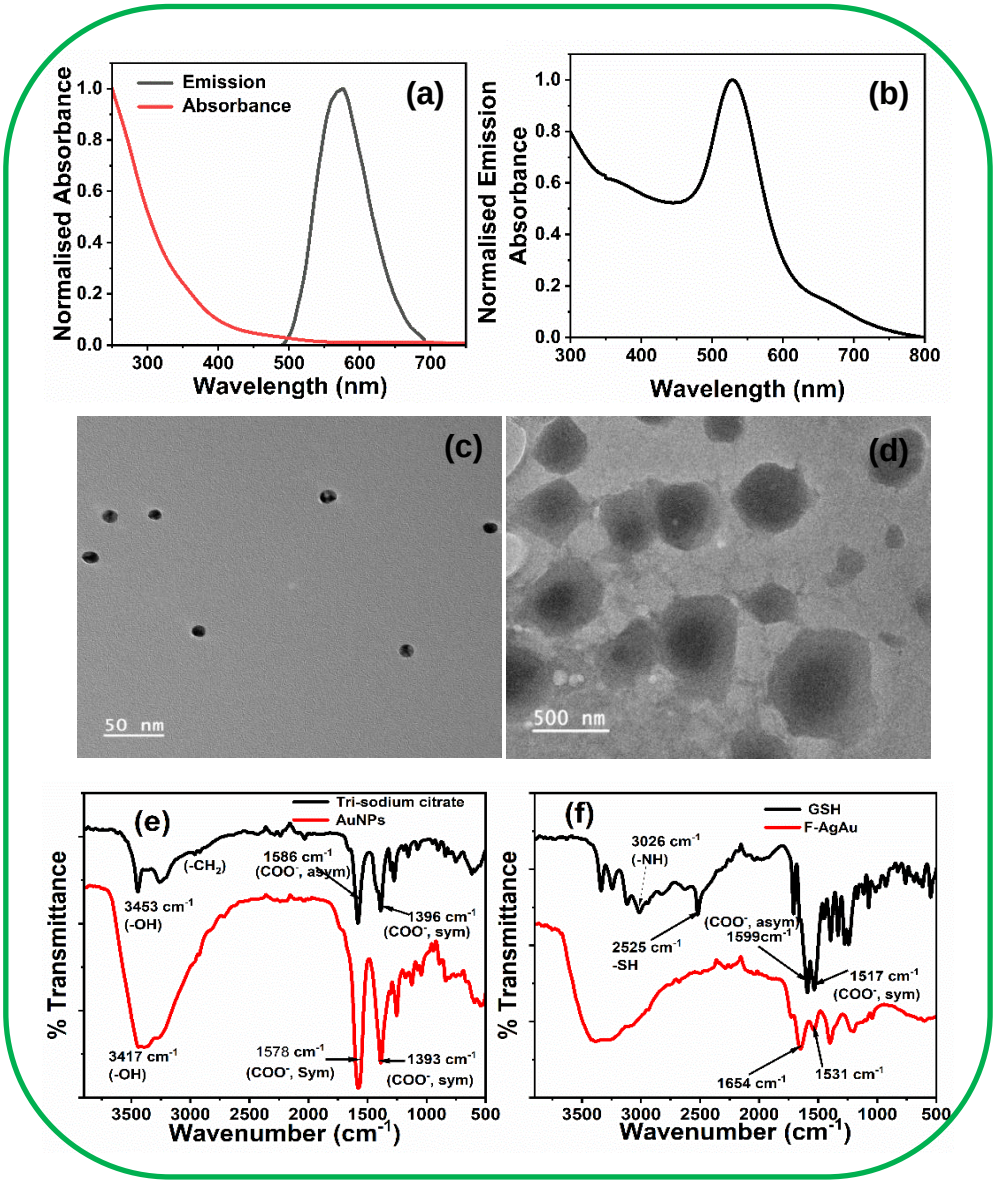

Figure 7.1. (a) Normalized absorption and emission spectra of F-AgAu (b) Normalized absorption spectra of AuNPs. TEM images (c, d) and FTIR (e,f) of AuNPs and F-AgAu, respectively.

substantiated due to the fluorescence property of silver nanoclusters, which are synergistically stabilized by the gold core.[54, 60] The optical characterization of AuNPs has been done by showing the characteristic plasmon peak at 528 nm (Figure 7.1b). The size and morphology of the particles have been determined from TEM images (Figure 7.1c,d). From the TEM images, it can be seen that both particles are spherical in shape. The estimated size of F-AgAu is ~480 nm, and that of AuNPs is ~20 nm. Elemental analysis of those systems is performed from the EDAX spectrum, which is provided in the appendix section. Surface charges of those systems are determined by ζ-potential measurements, which are shown in Figure APX7.1. The surface charges obtained from the ζ-potential measurements are 27.5 mV and -37 mV for F-AgAu and AuNPs, respectively. Moreover, elemental analysis of F-AgAu and AuNPs have been shown in Figure APX7.2 and Figure APX7.3respectively. FTIR measurements have been performed to investigate the incorporation of the ligands over the nanomaterials surface. Figure 7.1e reveals a broad band at 3000−3500 cm^{-1} in both tri-sodium citrate and AuNPs, which corresponds −OH stretching vibration. The sharp peaks around 1396 cm^{-1} and 1586 cm^{-1} are the characteristic peaks for the symmetric and asymmetric stretching of COO− in tri-sodium citrate which are shifted to 1393 cm^{-1} and 1578 cm^{-1} in tri-sodium citrate capped AuNPs indicating the incorporation of citrate group on the surface of AuNPs.

Figure 7.1f shows a peak at 2525 cm^{-1} which corresponds to –S–H stretching vibration of GSH. However, this peak is disappeared in the spectrum of the GSH-capped F-AgAu, which suggests the coordination of GSH with F-AgAu via the thiol group. The N–H stretching frequency (3025 cm^{-1}) in the free GSH ligand disappeared in the synthesized F-AgAu. The peak corresponding to asymmetric (1599 cm^{-1}) and symmetric stretching (1517 cm^{-1}) modes of the carboxylate group of free GSH show a significant shift in F-AgAu. These FTIR data

confirm the surface functionalization of AuNPs and F-AgAu by tri-sodium citrate and GSH, respectively.

7.2.2. Interaction of F-AgAu and AuNPs with CTAB

Prior investigating the excited state energy transfer, the effect of CTAB on the optical properties of F-AgAu and AuNPs has been investigated. From the absorption spectra (Figure 7.2a), it can be observed that in the presence of CTAB, the spectrum of F-AgAu remains almost unchanged, whereas the same for AuNPs has been changed significantly. In the presence of CTAB, the optical density of the localized surface plasmon band (LSPR) of AuNPs, centred at ~528 nm, is observed to decrease with the appearance of a new broad band at NIR region (Figure 7.2a). This change is observed to occur till the concentration of CTAB is increased to 0.6 mM. It is important to mention here that the surface plasmon oscillations of nanoparticles are strongly dependent on the shape of the particles.[61] Generally, rod-shaped AuNPs show two bands associated with the transverse and longitudinal plasmon

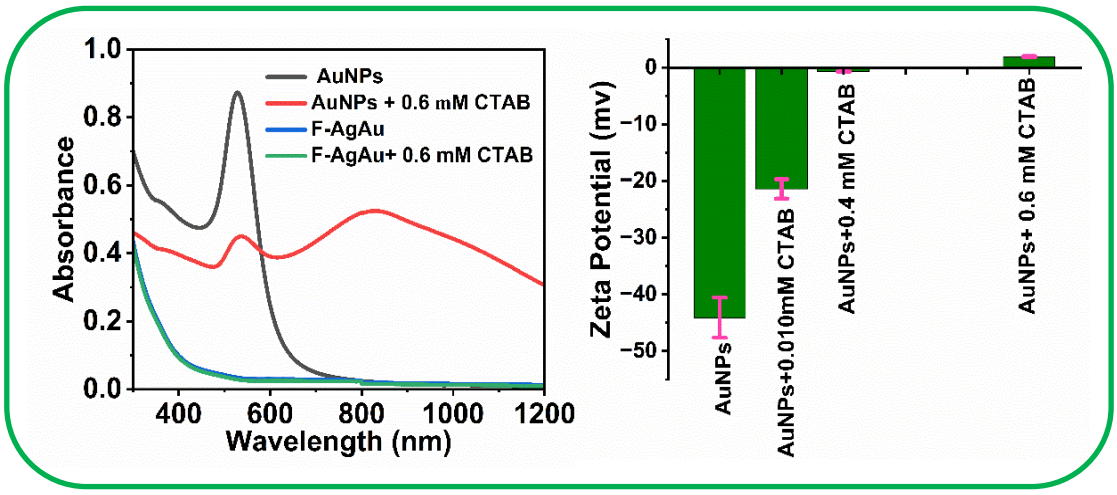

Figure 7.2 (a) Absorption spectrum of AuNPs and F-AgAu (b) Zeta potential measurements of AuNPs in the absence and presence of CTAB (0.6 mM).

resonances.[62-64] Moreover, it has also been demonstrated that agglomeration of AuNPs shows a new band encompassing a red shift and broadening along with the intrinsic band of the spherical AuNPs.[65-67] So, we have looked at this aspect carefully, and from the TEM image (Figure APX7.4) of AuNPs in the presence of CTAB, it has been opined that the changes of the LSPR band (Figure 7.2a) of Au NPs in the presence of CTAB is due to the formation of surfactant-induced aggregates of Au NPs.[65-66] It is to be noted here that in the presence of neutral TX 100 surfactants and negatively charged SDS, no spectral changes of AuNPs have been observed (Figure APX7.5), which implies that the electrostatic interaction between the positively charged CTAB and the negatively charged AuNPs is the driving force for the aggregation formation of AuNPs. Further, to substantiate the surfactant-induced aggregation of AuNPs, the surface zeta potential of AuNPs has been measured in the absence and presence of CTAB. The data for this is provided in the bar plot (Figure 7.2b). It can be seen from the Figure 7.2b that the estimated zeta potential of AuNPs (-37 mV) is significantly changed in the opposite direction upon the addition of positively charged CTAB, indicating the adsorption of CTAB molecules over the surface of AuNPs. In this context, it is also important to understand the nature of the adsorption of the surfactant molecules over the AuNPs surface. Several previous works on this issue have demonstrated that surfactant molecules are self-assembled over the NPs surface either through a micellar or bilayer structure formation.[68-69] It has been shown that when the hydrophobic part of surfactant molecules is attached to the AuNPs surface, and the hydrophilic part is faced towards the aqueous medium, a micellar-like structure is formed. However, the present observation indicates that due to electrostatic interaction, the hydrophilic head group of CTAB is attached to the tri-sodium citrate-capped gold nanoparticles, and therefore, the formation of Micelle can be ruled out. In this context, it is pertinent to mention that Sayed and co-workers[69] have demonstrated the bilayer formation of CTAB on the surface of AuNPs where the surfactant

head group is bound to the gold surface and tail part of CTAB is hydrophobically connected with another CTAB molecules forming a bilayer. In another work, Nogami and co-workers[70] have also shown the CTAB bilayer-induced aggregation and subsequent formation of silver nano-chains on the glass slide. Therefore, on the basis of the literature data and the outcome of the present investigation, it can be reasonably informed that the most favourable association of CTAB molecules over AuNPs proceeds through a bilayer formation. This bilayer acts as a cross-linker between several AuNPs resulting in aggregates of AuNPs.

7.2.3. Steady-State and time-resolved PL Quenching of F-AgAu in the Presence of AuNPs

To investigate the effect of AuNPs, having LSPR band, on the optical properties of F-AgAu, initially steady-state fluorescence titration experiments have been carried out by monitoring the fluorescence of F-AgAu with the increasing concentration of AuNPs (Figure 7.3a). As can be seen from Figure. 7.3a, the fluorescence intensity of F-AgAu gradually decreases with the gradual addition of AuNPs. Figure APX7.6 depicts the absorption spectra of F-AgAu in the absence and presence of AuNPs. All fluorescence data are corrected by equation 2 prior to further analysis, as the systems are not exempted from the inner filter effect.

$$F_{corr} = F_{obs}\, antilog(\frac{OD_{ex}+OD_{em}}{2}) \qquad (7.2)$$

Where F_{corr} is the corrected fluorescence intensity, F_{obs} is the observed fluorescence intensity, OD_{ex} and OD_{em} are the optical density at excitation and emission wavelength respectively. It can be noted that there are several phenomena, such as collision between the excited fluorophore and quencher molecule (dynamic quenching), formation of ground-state complex with the quencher (static quenching), excited-state energy transfer, electron transfer, etc., which are responsible for the fluorescence quenching of fluorophore.[6-7, 71-73] The analysis of fluorescence quenching data through SV plots

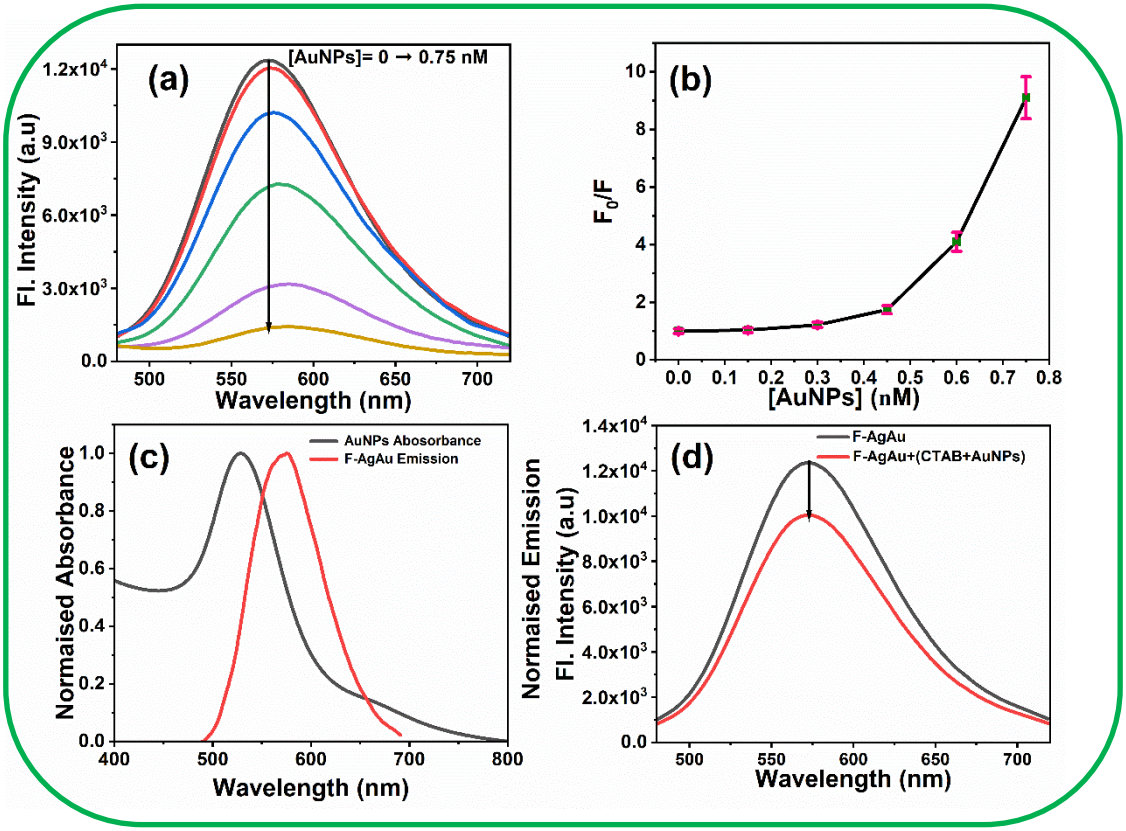

Figure 7.3. (a) Fluorescence spectra of F-AgAu in the presence of increasing concentration of AuNPs. [After the addition of 0.75 nM AuNPs, E= 1-(I/I_0) = 87% where, I and I_0 are PL intensities of donor in the presence and absence of acceptor] (b) Stern-Volmer plot for the quenching of F-AgAu (c) Spectral overlap between LSPR of different AuNPs and PL spectrum of F-AgAu (d) Fluorescence spectra of F-AgAu in the presence of CTAB modified AuNPs.

(Figure. 7.3b) has shown an upward curvature suggesting the presence of both static and dynamic quenching phenomenon in the overall quenching of F-AgAu in the presence of AuNPs. While the adsorption of AuNPs over the F-AgAu due to the interactions between the surface ligands and NPs in the ground state initiates static quenching process, collision between the two interacting species in the excited state of the fluorescing moiety (F-AgAu) causes the dynamic quenching event. The fluorescence quenching efficiency estimated from the FL titration study is ~87%. Interestingly, it has been observed that the FL quenching

efficiency of F-AgAu is reduced when AuNPs is modified with CTAB (Figure. 7.3d). This observation can be attributed to the fact that due to the formation of CTAB bilayer over the AuNPs surface (discussed above), the separation distance between F-AgAu and the surface of AuNPs increases.

Additionally, time resolves fluorescence studies have also been performed to have clear understanding on the quenching mechanism. The fluorescence decay profile of F-AgAu in the absence and presence of AuNPs are provided in the Figure. 7.4a and the relevant decay parameters are calculated in the Table 7.1. From the Table 7.1, it can be seen that the average lifetime of F-AgAu is decreased from 19.48 ns to 2.54 ns in the presence of 0.75 nM AuNPs, confirming the involvement of the dynamic quenching process during the F-AgAu-AuNPs interaction event. It is also to be noted here that metal NPs affect the radiative and non-radiative decay rates of nearby fluorophores, which are responsible for the shortening of the fluorescence lifetime of the fluorescence species.[30, 74-77] So, it is important to estimate

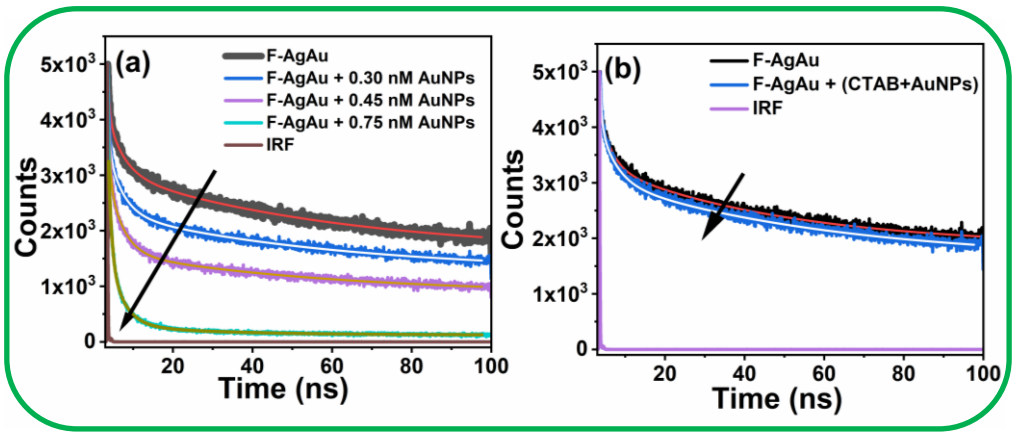

Figure. 7.4 Time-resolve fluorescence decay curve of F-AgAu in the absence and presence of (a) AuNPs and (b) CTAB modified AuNPs. (λ_{ex} = 375 nm).

the radiative and non-radiative decay rates of F-AgAu in the absence and presence of Au NPs, which have been calculated by using the following equations:

$$k_r = \frac{\phi_D}{\tau} \quad (7.3)$$

$$k_{nr} = \frac{1-\phi_D}{\tau} \quad (7.4)$$

where k_r and k_{nr} are the radiative and non-radiative decay rates, respectively. τ is the average lifetime of the donor and ϕ_D is the PL quantum yield. All of the estimated parameters are tabulated in the Table 7.2. It can be seen from the Table 7.2 that the radiative decay rate of F-AgAu remains unchanged, whereas the non-radiative decay rate increases in the presence of AuNPs. The possible reasons for the increment of the non-radiative decay rate, which are responsible for the lifetime shortening of F-AgAu, are excited state energy transfer, photoinduced electron transfer, aggregation of F-AgAu in the presence of AuNPs etc.[6] To figure out the exact mechanism for the FL quenching of F-AgAu in the presence of AuNPs, several control experiments have been performed. The absorption spectrum (Figure APX7.6) of F-AgAu in the presence of AuNPs reveals that there is neither appearance of a new band nor the shifting of band position, which rules out the aggregation-induced FL quenching of

Table 7.1. Fluorescence decay parameters of F-AgAu in the absence and presence of AuNPs and CTAB-modified AuNPs (The excitation wavelength is 375 nm)[a]

Systems	τ_1	α_1	τ_2	α_2	τ_3	α_3	<τ>
F-AgAu	0.35	45	4.00	23	57.47	32	19.48
F-AgAu+0.30 nM AuNPs	0.30	57	3.68	23	57.06	20	12.46
F-AgAu+0.45 nM AuNPs	0.32	62	3.54	25	55.48	13	8.42
F-AgAu+0.75 nM AuNPs	0.68	65	3.52	31	26.19	4	2.54
F-AgAu+0.75 nM(CTAB+ AuNPs)	0.29	50	2.03	20	45.30	30	13.97

[a]α are expressed in % scale and τ values (±5 %) are in ns unit

F-AgAu. Another possibility is the electron transfer from F-AgAu to AuNPs. In this connection, it is important to have an idea about the HOMO and LUMO energy levels of both F-AgAu and AuNPs to understand the electron transfer process.[74-76] So, cyclic volumetric study has been done to estimate the HOMO and LUMO energy levels.[80-82] The current-voltage curve for those systems obtained from the cyclic voltammetry measurements is provided in the Figure APX7.7 and the estimated energy levels are schematically shown in the Scheme APX7.1. It can be seen from the Scheme APX7.1, that the LUMO energy of AuNPs is higher than that of F-AgAu, which can oppose the electron transfer from F-AgAu to AuNPs. Moreover, it is known that a charge transfer complex is formed during the process of photoinduced electron transfer, which involves the transfer of an electron from photoexcited donor to a ground state acceptor.[6] The stability and the formation of the charge transfer complex are dependent on the solvent polarity of the medium.[83-86] To establish whether the electron transfer is happening or not, we have further studied the steady state and time-resolved FL quenching of F-AgAu by changing the solvent polarity from ~78 (H_2O) to ~41 (CH_3CN: H2O:: 7:3 V/V) which are provided in the Figure APX7.8a. Steady-state FL study reveals that in CH_3CN: H_2O (7:3) medium the fluorescence quenching efficiency of F-AgAu by AuNPs is 94% which is 7% higher than that of water medium. Again by visualization, one can see that the slope of the F_0/F vs [Q] plot (Figure APX7.9) corresponding to the fluorescence quenching experiment done in CH_3CN:H_2O (7:3) medium is observed to be steeper than that in water medium. Moreover, fluorescence lifetime corresponding to F-AgAu in the presence of AuNPs in CH_3CN:H_2O (7:3) medium is also found to follow a similar trend (Figure APX7.8b, Table APX7.1, E_{H2O} ~56.7% vs $E_{CH3CN:H2O}$ ~81.3%,). The above results clearly reveal that the FL quenching of F-AgAu in the presence of AuNPs is lower in a polar water medium than that in a relatively less polar medium (CH_3CN:H_2O). As charge transfer complexes are more stable in polar medium as compared

to the nonpolar medium, the above results do not provide evidence in favour of the formation of charge transfer complex.[83-85]

Interestingly, the presence of significant spectral overlap (Figure. 7.3c) between the emission spectrum of F-AgAu and the LSPR band of Au NPs indicates the possible involvement of excited state energy transfer (EET) from F-AgAu to Au NPs. The efficiency (Q_{Eff}) of the non-radiative EET process is estimated from the PL lifetimes of F-AgAu in the absence and presence of Au NPs using the following equation

$$\phi_{Eff} = 1 - \frac{\tau_{D-A}}{\tau_D} \qquad (7.5)$$

where τ_D and τ_{D-A} are the excited state lifetimes of F-AgAu in the absence and presence of AuNPs, respectively. The EET efficiency of F-AgAu in the presence of AuNPs is estimated to be ~ 87 %. Interestingly, it can be observed from Figure. 7.4b that the FL decay traces of F-AgAu in the presence of CTAB-modified AuNPs have minimal changes and the EET efficiency for this system is calculated to be ~ 28 %. These observations suggest that the EET from F-AgAu to AuNPs can be tuned by using CTAB surfactant. This result is helpful for the design and development of suitable inorganic-nanomaterial based donor-acceptor pairs for various energy-related applications.

7.2.4. Mechanism of Energy Transfer from F-AgAu to AuNPs

We note here that AuNPs are known to be efficient quenchers for the nearby fluorophores [24, 87], and the quenching mechanism is attributed to either FRET or NSET mechanism. [23, 36, 88-91] Therefore, it is important to find out which model, FRET or NSET is appropriate for the present excited state energy transfer from F-AgAu to AuNPs in this work. The FRET model is based on the non-radiative dipole−dipole interaction between two molecular dyes having a separation distance of up to 10 nm. Förster distance (R_0) is the most characteristic parameter

of FRET model, which typically varies between 2-8 nm for a given donor-acceptor system. The R_0 can be calculated by using the following equation

$$R_0 = [(8.8 \times 10^{-25})(\kappa^2 \eta^{-4} \phi_D J(\lambda)]^{1/6} \qquad (7.6)$$

Table 7.2. Estimated quantum yields, average lifetimes, radiative rates, non-radiative rates, energy-transfer rates, and efficiency of energy transfer between F-AgAu and AuNPs in the absence and presence of CTAB.

System	ϕ_D	<τ> (ns)	$k_r(10^7$ $S^{-1})$	k_{nr} $(10^7$ $S^{-1})$	$k_{ET}(10^8$ $S^{-1})$	ϕ_{ET}
F-AgAu	0.040	19.48	0.2	4.90		
F-AgAu+AuNPs	0.008	2.54	0.3	38.90	3.4	87%
F-AgAu+(AuNPs+CTAB)	0.030	13.97	0.2	6.90	0.3	28%

where κ^2 (= 2/3) is the orientation factor of the transition dipoles of the donor and the acceptor, η is the refractive index of the medium, ϕ_D is the quantum yield of the donor, and J(λ) is the spectral overlap integral between the donor emission and the acceptor absorption spectrum which has been calculated by equation 7.7

$$J(\lambda) = \int F_D(\lambda)\varepsilon_A(\lambda)\lambda^4 d\lambda \qquad (7.7)$$

where $F_D(\lambda)$ is the area-normalized emission spectrum of the donor, and $\varepsilon_A(\lambda)$ denotes the molar absorption coefficient of the acceptor. In the present study, the R_0 value is estimated to be 27.8 nm for the F-AgAu-AuNPs pair. Therefore, the value of R_0 falls beyond the range of conventional FRET theory.[6] Therefore, FRET mechanism cannot be applicable for our system. It is to be noted here that exchange energy transfer (Dexter's mechanism) may also be responsible for the fluorescence lifetime quenching of F-AgAu in the presence of AuNPs.[7]

So, the fluorescence decay parameters of F-AgAu in the presence of AuNPs are also analyzed through a stretched exponential decay function (Kohlrausch function) to explore the energy transfer process from F-AgAu to AuNPs which has been discussed in the Electronic Supplementary Information (Figure APX7.10).[92-93] The value of the stretching parameter β is very helpful to describe the energy transfer process between donor and acceptor, whether it goes through dipole-dipole or exchange mechanism.[92] The value of the stretching parameter (β) estimated through the Kohlrausch function is found to be 0.272, which is less than 0.5, signifying that the energy transfer between donor and acceptor happens via dipole-dipole mechanism rather than following an exchange mechanism such as Dexter's mechanism.

In view of this, we have resorted to the NSET theory[11], which considers the collective interaction of all dipoles in a thin film near the surface of the metal, creating a 1/d dependent coupling instead of the usual $1/d^3$ dependent coupling of the dipole approximation. Notably, the fluorescence quenching of various fluorophore in the vicinity of metal NPs surface has been successfully explained by many researchers on the basis of NSET theory.[14, 35, 45-46, 94] For the NSET model, the donor-acceptor separation distance (d_0) at which the efficiency of energy transfer becomes 50 % is estimated by using equation 7.8.

$$d_0 = \left(\frac{0.225\phi_D C^3}{\omega_D^2 \omega_F k_F}\right)^{1/4} \qquad (7.8)$$

where ϕ_D is the quantum yield of the donor, c is the velocity of light, ω_D is the angular frequency of the donor electronic transition, ω_F is the Fermi frequency, and k_F is the Fermi wave vector of the metal. For our system ϕ_D= 0.04, c = 3×10^{10} cm s^{-1}, ω_D= 5.2×10^{11} s^{-1}, ω_F= 1.2×10^{8} cm^{-1}, k_F = 8.4×10^{15} rad/s.[23] The estimated d_0 for the F-AgAu-AuNPs pair is 7.3 nm. The distance (d) between F-AgAu and AuNPs is estimated by using the following equation[41]

$$d = d_0^{NSET}\left(\frac{\tau_{DA}}{\tau_D - \tau_{DA}}\right)^{1/4} \qquad (7.9)$$

The separation distance between F-AgAu and the surface of AuNPs is 4.54 nm and 9.21 nm in the absence and presence of 0.6 mM CTAB, respectively. It is reported that the end-to-end distance of CTAB is ~2.0 nm.[95-96] Hence in the present study, the increase in the separation distance between F-AgAu and AuNPs by 4.57 nm in the presence of CTAB strongly validates the NSET model. According to the NSET mechanism, the rate of EET can be expressed by using equation 7.10 and the estimated EET rate are provided in Table 7.2.

$$k_{NSET} = \frac{1}{\tau_D}\left(\frac{d_0}{d}\right)^4 \qquad (7.10)$$

From the table, it can be seen that the rate of EET from F-AgAu to AuNPs is faster than that of the CTAB-modified AuNPs systems, which suggests that the rate of EET can be controlled by simply modifying the AuNPs with CTAB by means of increasing distance between F-AgAu and AuNPs.

To gain more insight into the changes of fluorescence lifetime of F-AgAu in the absence and presence of AuNPs and CTAB-modified AuNPs at single particle level, fluorescence lifetime imaging microscopy (FLIM) study has also been performed. Figure 7.5a,d,g, Figure 7.5b,e,h, and Figure 7.5c,f,i represents the FLIM images, fluorescence decay profiles and fluorescence lifetime distribution of the corresponding FLIM images. As is evident from the images, Figure 7.5f,I, demonstrate a relatively broader lifetime distribution profile than that of are observed in Figure 7.5c; suggesting the heterogeneous distribution of acceptors on the surface of the F-AgAu.[6, 97] The average lifetime of F-AgAu in the absence and presence of AuNPs and CTAB modified AuNPs, obtained from FLIM is estimated to be 4.6 ns, 2.92 ns and 3.8 ns respectively. The efficiency of the excited state energy transfer from F-AgAu to AuNPs and CTAB-modified AuNPs are calculated to be 37% and 17%,

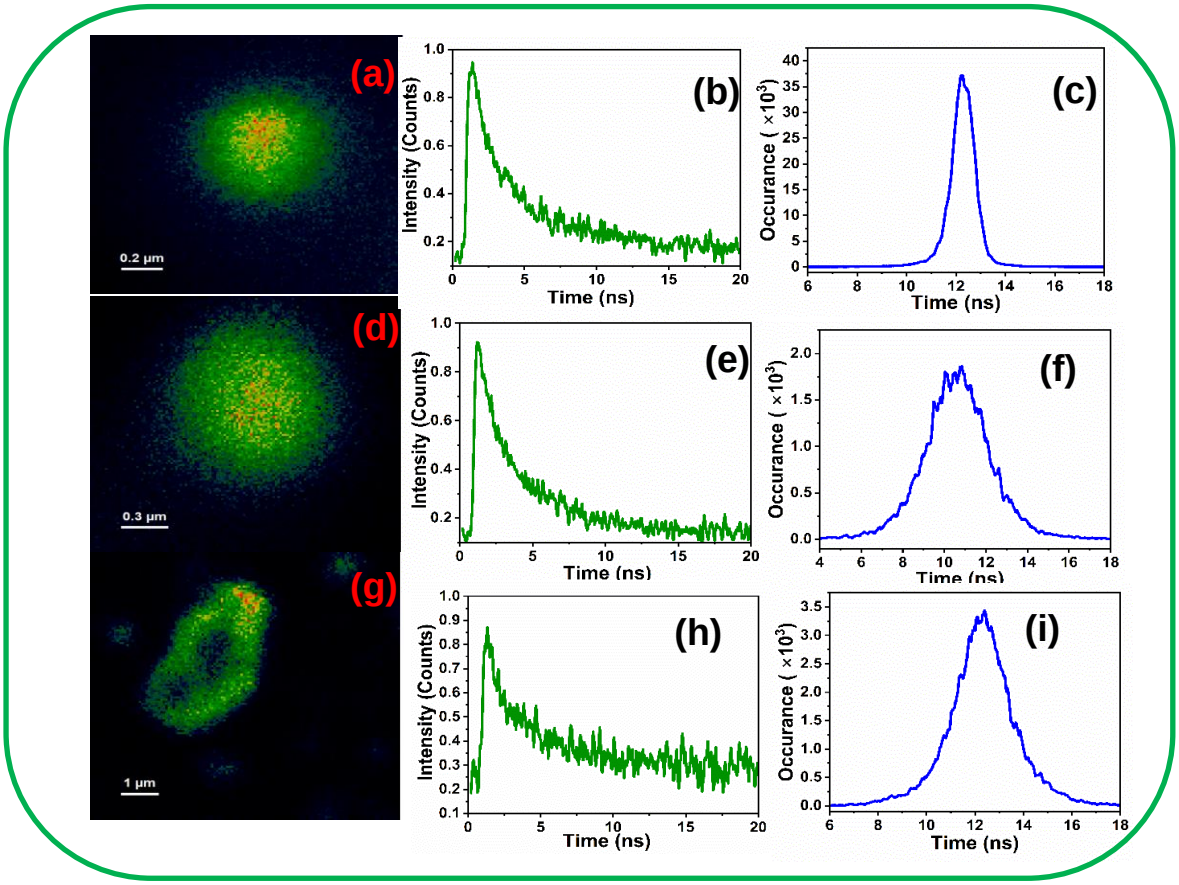

Figure 7.5. Fluorescence lifetime images (a,d,g), fluorescence decay curves (b,e,h) and overall lifetime profile (c,f,i) of F-AgAu, F-AgAu in the presence of AuNPs and F-AgAu in the presence of CTAB-modified AuNPs respectively**.**

respectively. This result is also in agreement with the previous ensemble average measurements.

7.3. Conclusion

In the current study, the excited state energy transfers (EET) from bimetallic non-plasmonic nanomaterials to plasmonic nanoparticles and the role of surface modification of AuNPs by CTAB in controlling the EET process have been investigated. For this purpose, fluorescence bimetallic silver capped gold (F-AgAu), and gold nanoparticle (AuNPs) have

been synthesized and characterized by spectroscopic and microscopic techniques. Several techniques have been employed to understand the photoluminescence behaviour of F-AgAu in the presence of AuNPs. Quite a few interesting results have emerged from this study which are helpful in addressing the associated mechanism of EET. Data obtained from steady-state as well as time-resolved fluorescence studies have revealed that the fluorescence intensity and lifetime of F-AgAu in the presence of AuNPs are significantly quenched, whereas in the presence of CTAB-modified AuNPs, minimal PL quenching of the F-AgAu has been observed. Moreover, cyclic voltammetric (CV) studies and polarity-dependent studies have ruled out the possibility of electron transfer process for the observed fluorescence quenching behaviour of F-AgAu in the presence of AuNPs. Furthermore, the observation of increased non radiative decay rate for F-AgAu in the presence of AuNPs has substantiated that the PL quenching of F-AgAu is caused due to excitation energy transfer from F-AgAu to AuNPs. The efficiency of energy transfer in presence of AuNPs is estimated to be as high as 87 %. Interestingly, the EET is found to be drastically reduced (28 %) when CTAB-modified AuNPs are used. This observation has been rationalized by considering the formation of CTAB bilayer over AuNPs, which increases the distance between F-AgAu and AuNPs and thereby reduces the EET efficiency. More interestingly, analysis of the relevant photophysical data have depicted that the estimated Förster distance (27.8 nm) for the current EET event falls beyond the range that can be predicted from the conventional FRET theory. Based on these findings, it has been concluded that the excited state energy transfer process from F-AgAu to AuNPs follows NSET rather than the conventional FRET model. Moreover, findings revealed by fluorescence lifetime imaging microscopy (FLIM) have clearly demonstrated that the energy transfer efficiency from bimetallic NPs to AuNPs can be tuned by modifying the surface of AuNPs with CTAB. Therefore, outcome of the current EET between the F-AgAu and AuNPs suggest that the present system can be helpful for designing

new nano scale composite systems for the applications in various optical and electronic applications.

7.4. Appendix

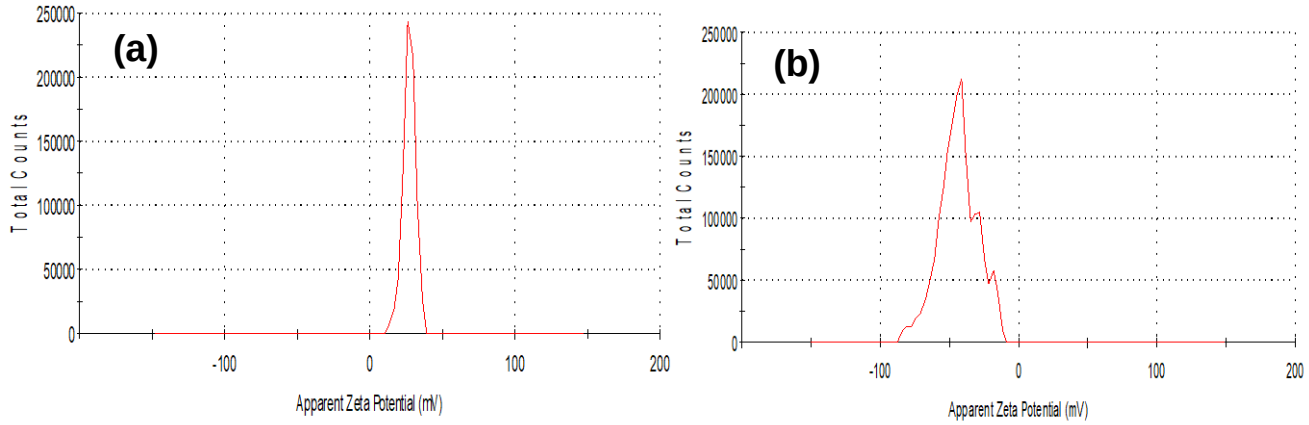

Figure APX7.1. Zeta potential graph of (a) F-AgAu and (b) AuNPs

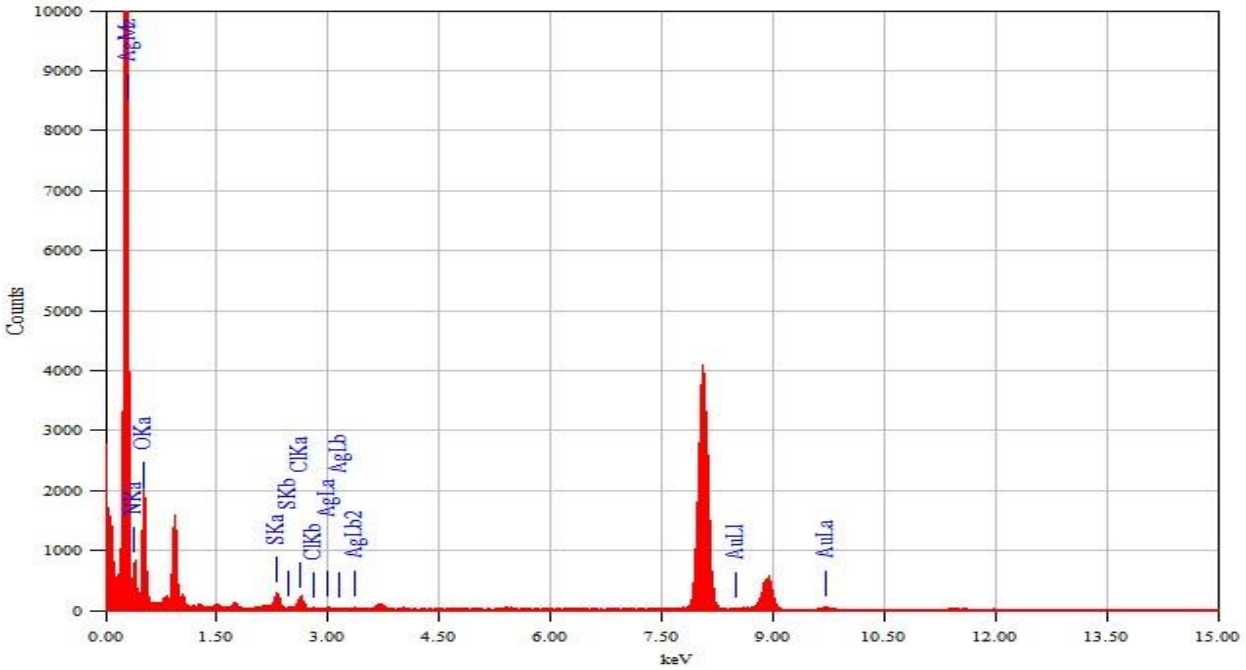

Figure APX7.2. EDAX spectra of F-AgAu.

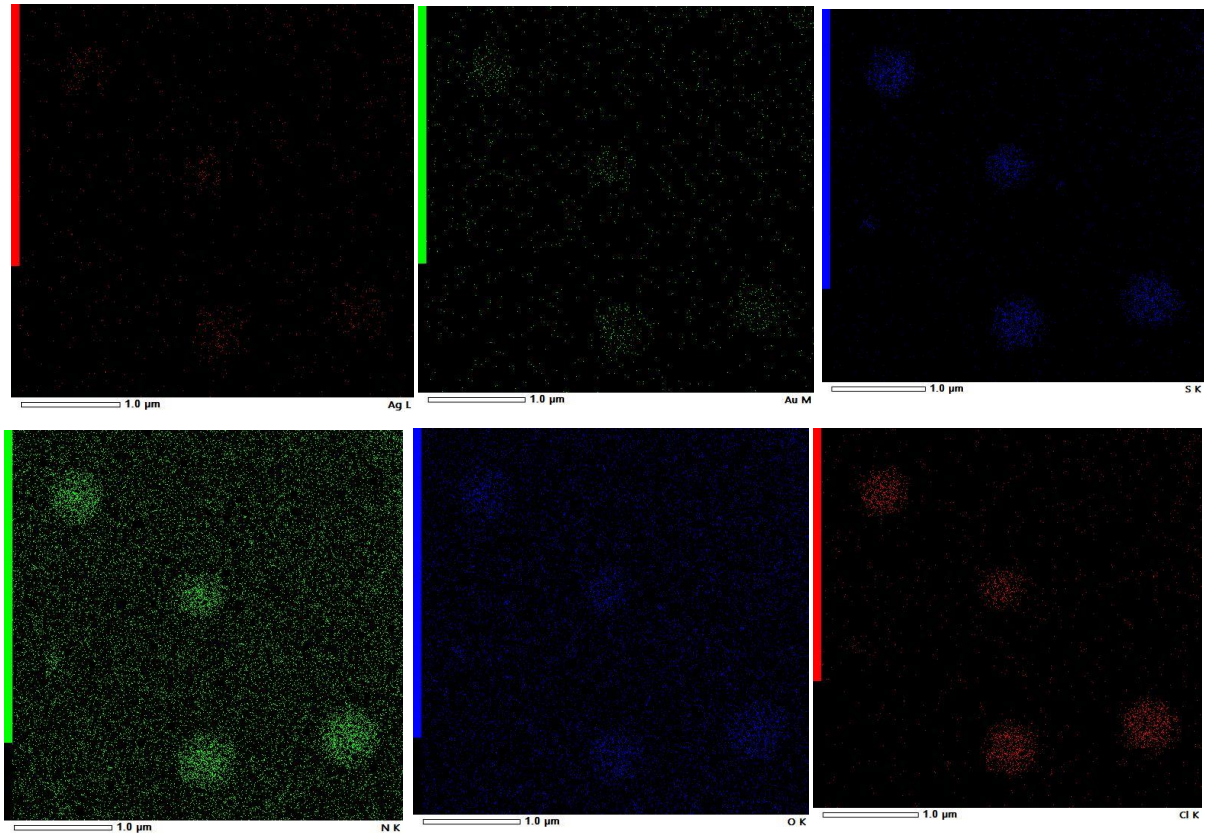

Figure APX7.3. Elemental mapping of F-AgAu.

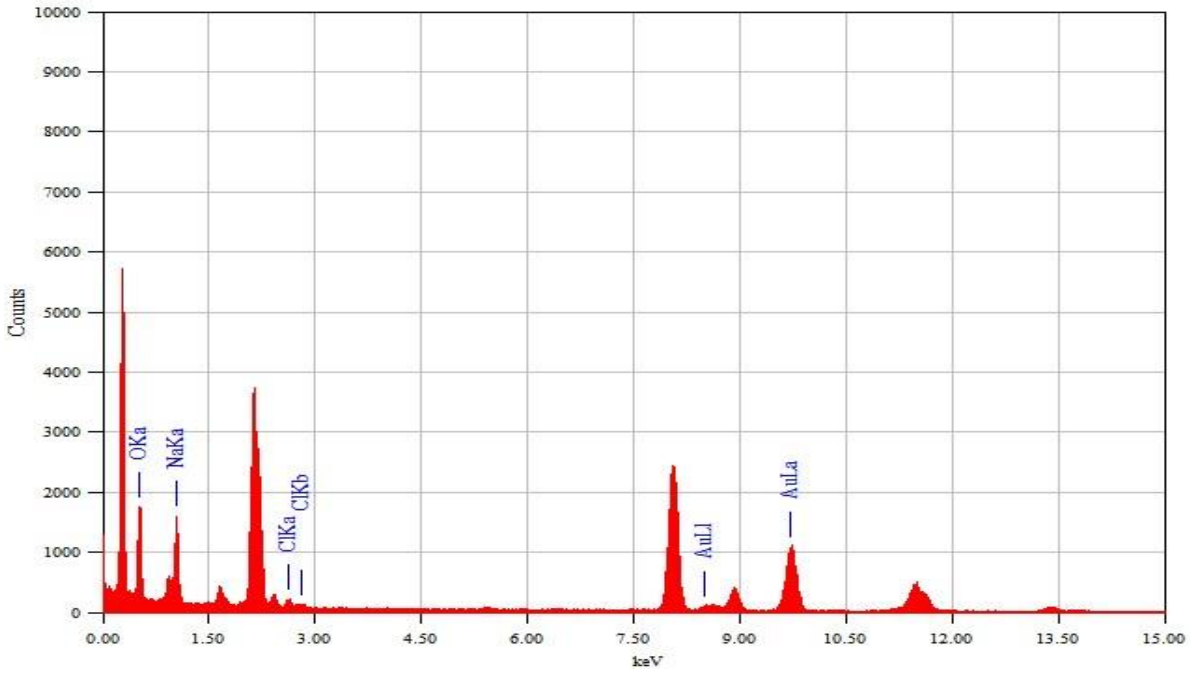

Figure APX7.4. EDAX spectra of F-AuNPs.

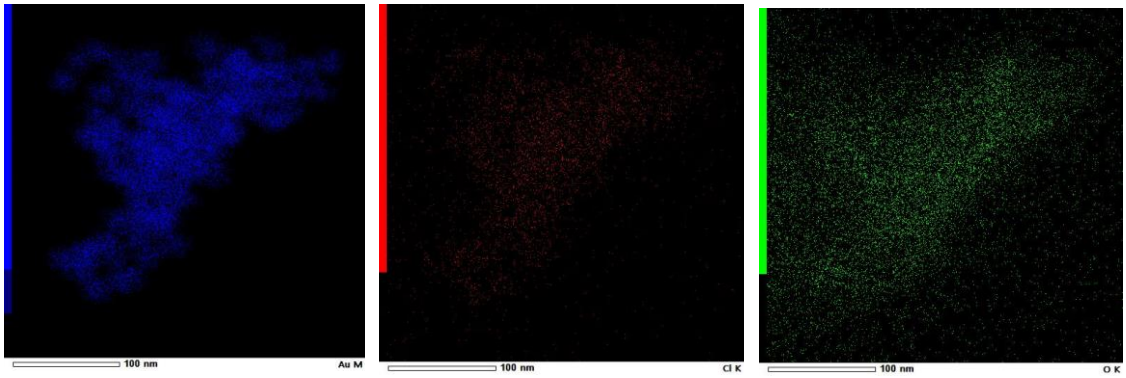

Figure APX7.5. Elemental mapping of AuNPs**.**

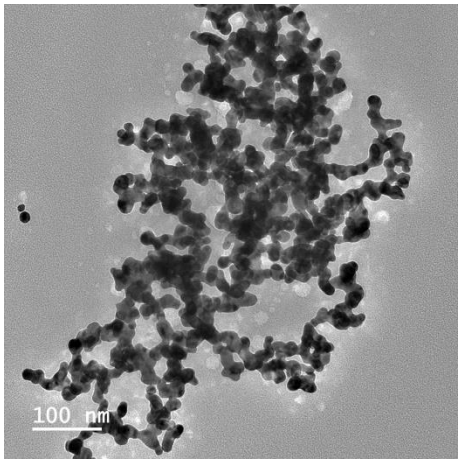

Figure APX7.6. TEM image of AuNPs in the presence of CTAB.

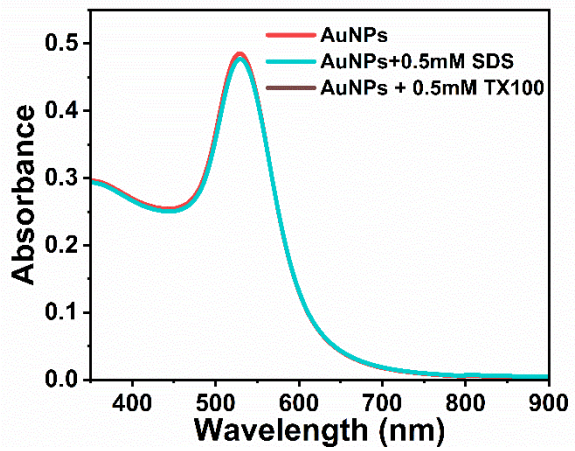

Figure APX7.7. Absorption spectrum of F-AgAu in absence and presence of SDS and TX100.

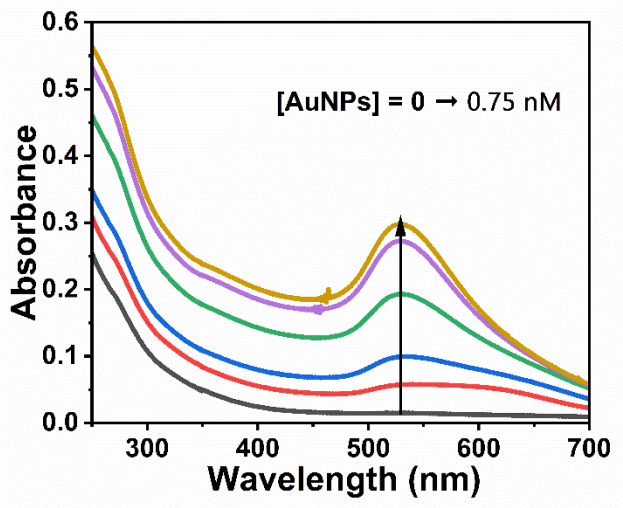

Figure APX7.8. Absorption spectra of F-AgAu in absence and presence of increasing concentration of AuNPs.

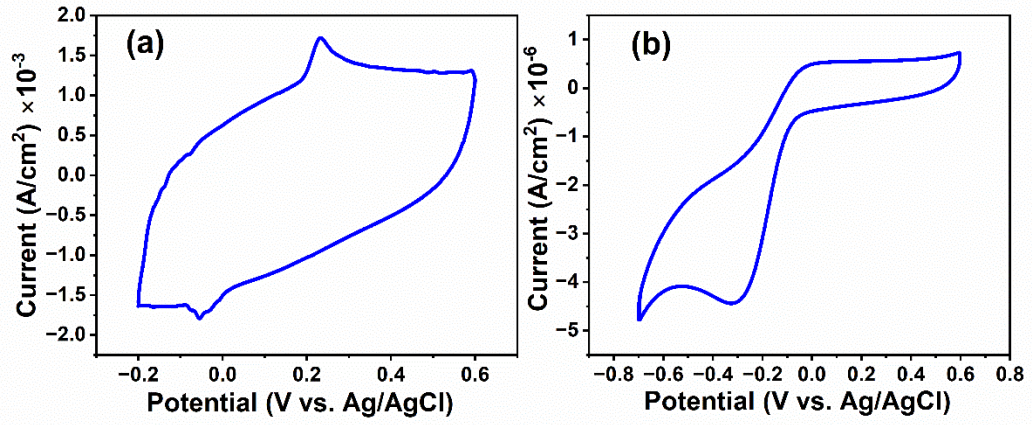

Figure S9. Cyclic voltammetric curves of (a) Ag@Au and (b) AuNPs.

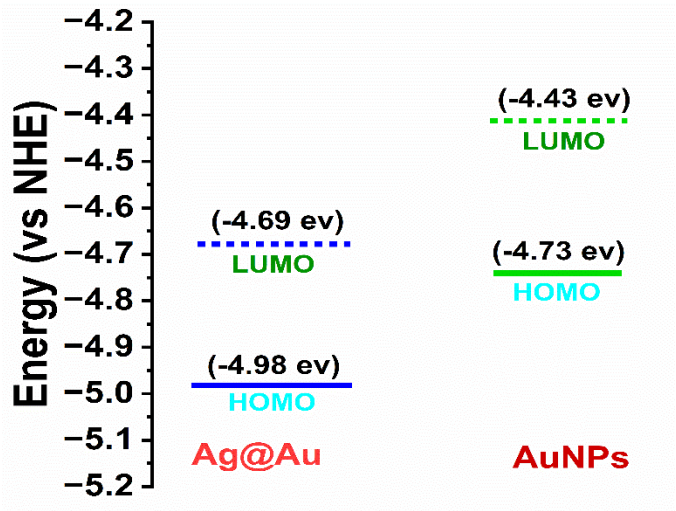

Scheme APX7.1. The energy level diagram representing the HOMO and LUMO levels of Ag@Au and AuNPs.

Effect of solvent polarity on PL quenching studies

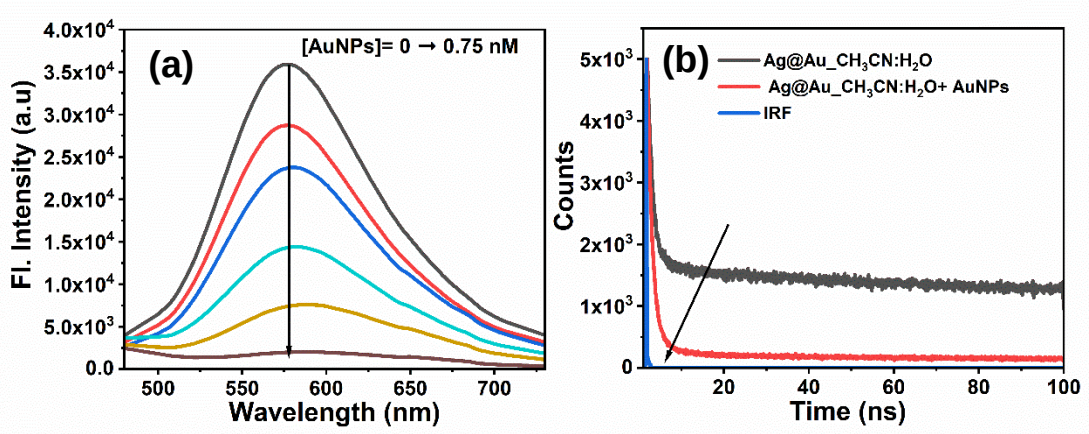

Figure APX7.10. (a) Fluorescence spectra of Ag@Au in the presence of increasing concentration of AuNPs in (a) 0.7:0.3 v/v $CH_3CN:H_2O$. (b) Time-resolved fluorescence decay curve of Ag@Au in the absence and presence of 0.45 nM AuNPs in 0.7:0.3 v/v $CH_3CN:H_2O$.

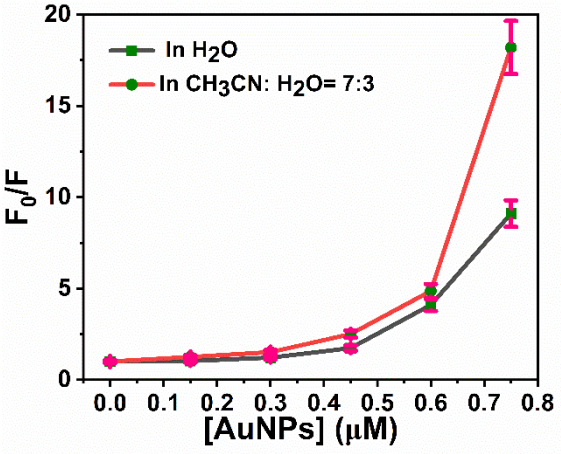

Figure APX7.11. Stern-Volmer plot showing the relative changes in the photoluminescence intensity of Ag@Au as a function of AuNPs concentration in both H_2O (green curve) and 0.7:0.3 v/v CH3CN:H2O (pink curve).

Table APX7.1. PL decay analysis of Ag@Au in the presence of 0.45nM AuNPs in different solvents.

Systems	τ_1	B_1	τ_2	B_2	τ_3	B_3	$\langle\tau\rangle$	Efficiency
Ag@Au_H_2O	0.35	45	4.00	23	57.47	32	19.48	
Ag@Au_ H_2O + 0.45 nM AuNPs	0.32	62	3.54	25	55.48	13	8.42	56.7
Ag@Au_CH_3CNH_2O	1.05	84%	4.16	5%	85.35	10%	9.85	
Ag@Au_CH_3CNH_2O + 0.45 nM AuNPs	1.02	89.69 %	3.39	8.9%	45	1.4%	1.84	81.3%

Stretched exponential fitting of F-AgAu-AuNPs hybrid system

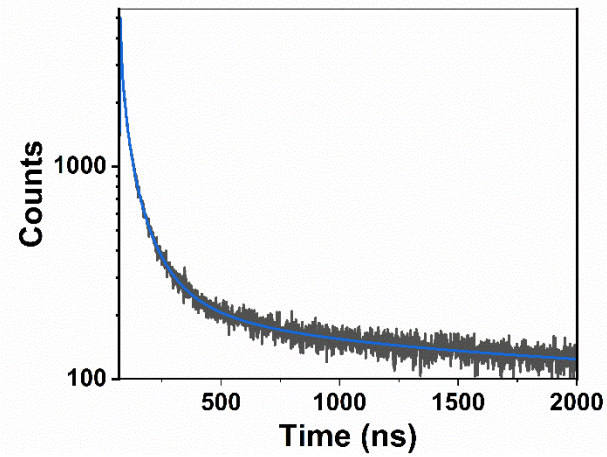

Figure APX7.12. Stretched exponential fitting of F-AgAu-AuNPs hybrid system.

In the case of resonance energy transfer between donor and acceptor molecules, by dipole-dipole or exchange mechanisms (Dexter), the donor fluorescence intensity decay I(t) is described by the modified stretched exponential function (Kohlrausch function) [98-101]

$$I(t) = \exp\left(-\frac{t}{\tau}\right)\exp[-a(\frac{t}{\tau})^{\beta}] \qquad \text{(APX7.1)}$$

It is also demonstrated that an experimental fluorescence decay curve that can be adequately approximated by the stretched exponential function (1) can also be equally well described within the precision limits of the measurements by using following equation[102]

$$I(t) = A_1\, exp^{-a_1\, t/\tau} + A_2 \exp(^{-a_2}\ (t/\tau)^{\beta}) \qquad \text{(APX7.2)}$$

, with the same values of the parameter β in both functions and appropriate choice of the fitting parameters A1, A2, a1, and a2. The importance of Kohlrausch (or stretched exponential) relaxation function to explain relaxation of complex systems are well known. Specifically, in case of condensed matter fluorescence it has been well documented by Bodunov and co-workers[102] that the resonance energy transfer will go via dipole-dipole mechanism when $\beta \leq 0.5$. The authors have analyzed this issue through theoretical investigations of the room temperature stretched exponential fluorescence decay of colloidal quantum dots. The use of the eq. APX7.1 for fitting the experimental non-exponential fluorescence decay of colloidal quantum dot systems at room temperature have led to the separation into the exponential component of the decay (arising out of radiative and non-radiative transitions within the donor), and the non-exponential component (due to additional channels of energy relaxation such as RET). They have shown that a stretched exponential functional form of the fluorescence decay with exponent β < 0.5 can be explained by long-range dipole-dipole resonance energy transfer from donor to acceptor, whereas $\beta >$ 0.5 may arise due to contact mechanism of fluorescence such as exchange energy transfer. We would also like to note here that several other researchers have also used the Kohlrausch function to describe that energy transfer mechanism is mediated via dipole-dipole interaction mechanism.[103] In our study for F-AgAu-AuNPs composite system, the value of the stretching parameter (β) estimated through Kohlrausch function is found to be 0.272 which is less than 0.5 signifying that the energy transfer between donor and acceptor happens via dipole-dipole mechanism rather than following an exchange mechanism such as Dexter mechanism.

References

1. Selvin, P. R. *Nat. Struct. Biol.*, 2000, **7**, 730-734.
2. Nolan, E. M.; Lippard, S. J. *Chem. Rev.*, 2008, **108**, 3443-3480.
3. Brown, M. D.; Suteewong,T.; Kumar, R. S. S.; D'Innocenzo,V.; Petrozza, A.; Lee, M. M.; Wiesner, U.; Snaith, H. J. *Nano Lett.*, 2011, **11**, 438-445.
4. Wang, Y.; Xie, X.; Goodson, T. *Nano Lett.*, 2005, **5**, 2379-2384.

5. Lu, S.; Lingley, Z.; Asano, T.; Harris, D.; Barwicz, T.; Guha, S.; Madhukar, A. *Nano Lett.*, 2009, **9**, 4548-4552.
6. Lakowicz, J. R. pringer:USA,, 2006, pp 55−472.
7. Valeur, B. Wiley-VCH: Weinheim, 2002.
8. Cotlet, M.; Vosch, T.; Habuchi, S.; Weil, T.; Müllen, K.; Hofkens, J.; De Schryver, F. *J. Am. Chem. Soc.*, 2005, **127**, 9760-9768.
9. Arslan, S.; Khafizov, R.; Thomas, C. D.; Chemla, Y. R.; Ha, T. *Science*, 2015, **348**, 344-347.
10. Michalet, X.; Weiss, S.; Jäger, M. *Chem. Rev.*, 2006, **106**, 1785-1813.
11. Persson, B. N. J.; Lang, N. D. *Phys. Rev. B*, 1982, **26**, 5409-5415.
12. Dulkeith, E.; Morteani, A. C.; Niedereichholz, T.; Klar, T. A.; Feldmann, J.; Levi, S. A.; van Veggel, F. C. J. M.; Reinhoudt, D. N.; Möller, M.; Gittins, D. I. *Phys. Rev. Lett.*, 2002, **89**, 203002.
13. Dulkeith, E.; Ringler, M.; Klar, T. A.; Feldmann, J.; Muñoz Javier, A.; Parak, W. J. *Nano Lett.*, 2005, **5**, 585-589.
14. Jennings, T. L.; Singh, M. P.; Strouse, G. F. *J. Am. Chem. Soc.*, 2006, **128**, 5462-5467.
15. Sen, T.; Patra, A. *J. Phys. Chem. C*, 2012, **116**, 17307-17317.
16. Ferry, V. E.; Munday, J. N.; Atwater, H. A. *Adv. Mater.*, 2010, **22**, 4794-4808.
17. Nakayama, K.; Tanabe, K.; Atwater, H. A. *Appl. Phys. Lett.*, 2008, **93**, 121904.
18. Ferry, V. E.; Sweatlock, L. A.; Pacifici, D.; Atwater, H. A. *Nano Lett.*, 2008, **8**, 4391-4397.
19. Ji, W.; Jing, P.; Zhao, J. *J. Mater. Chem. C*, 2013, **1**, 470-476.
20. Hu, L.; Wu, H.; Zhang, B.; Du, L.; Xu, T.; Chen, Y.; Zhang, Y. *Small*, 2014, **10**, 3099-3109.
21. Sobhani, A.; Knight, M. W.; Wang, Y.; Zheng, B.; King, N. S.; Brown, L. V.; Fang, Z.; Nordlander, P.; Halas, N. J. *Nat. Commun.*, 2013, **4**, 1643.
22. Pramanik, A.; Gao, Y.; Patibandla, S.; Mitra, D.; McCandless, M. G.; Fassero, L. A.; Gates, K.; Tandon, R.; Ray, P. C. *J. Phys. Chem. Lett.*, 2021, **12**, 2166-2171.
23. M. Li, S. K. Cushing, Q. Wang, X. Shi, L. A. Hornak, Z. Hong and N. Wu, *J. Phys. Chem. Lett.*, 2011, **2**, 2125-2129.
24. Navarro, J. R. G.; Plugge, M.; Loumaigne, M.; Sanchez-Gonzalez, A.; Mennucci, B.; Débarre, A.; Brouwer, A. M.; Werts, M. H. V. *Photochem. Photobiol. Sci.*, 2010, **9**, 1042-1054.
25. Prajapati, R.; Chatterjee, S.; Bhattacharya, A.; Mukherjee, T. K. *J. Phys. Chem. C*, 2015, **119**, 13325-13334.
26. Prajapati, R.; Bhattacharya, A.; Mukherjee, T. K. *Phys. Chem. Chem. Phys.*, 2016, **18**, 28911-28918.
27. Chowdhury, S.; Wu, Z.; Jaquins-Gerstl, A.; Liu, S.; Dembska, A.; Armitage, B. A.; Jin, R.; Peteanu, L. A. *J. Phys. Chem. C*, 2011, **115**, 20105-20112.
28. Nie, S.; Emory, S. R. *Science*, 1997, **275**, 1102-1106.
29. Naiki, H.; Masuhara, A.; Masuo, S.; Onodera, T.; Kasai, H.; Oikawa, H. *J. Phys. Chem. C*, 2013, **117**, 2455-2459.

30. Munechika, K.; Chen, Y.; Tillack, A. F.; Kulkarni, A. P.; Plante, I. J.-L.; Munro, A. M.; Ginger, D. S. *Nano Lett.*, 2010, **10**, 2598-2603.
31. Chen, Y.; Munechika, K.; Ginger, D. S. *Nano Lett.*, 2007, **7**, 690-696.
32. Ren. Z.; Li, X.; Guo, J.; Wang, R.; Wu, Y.; Zhang, M. Li, C.; Han, Q.; Dong, J.; Zheng, H. *Optics Communications*, 2015, **357**, 156-160.
33. Xie, F.; Pang, J. S.; Centeno, A.; Ryan, M. P.; Riley, D. J.; Alford, N. M. *Nano Research*, 2013, **6**, 496-510.
34. Fort, E.; Grésillon, S. *Journal of Physics D: Applied Physics*, 2008, **41**, 013001.
35. Pons, T.; Medintz, I. L.; Sapsford, K. E.; Higashiya, S.; Grimes, A. F.; English, D. S.; Mattoussi, H. *Nano Lett.*, 2007, **7**, 3157-3164.
36. Zhang, X.; Marocico, C. A.; Lunz, M.; Gerard, V. A.; Gun'ko, Y. K.; Lesnyak, V.; Gaponik, N.; Susha, A. S.; Rogach, A. L.; Bradley, A. L. *ACS Nano*, 2012, **6**, 9283-9290.
37. Dulkeith, E.; Ringler, M.; Klar, T. A.; Feldmann, J.; Muñoz Javier, A.; Parak, W. J. *Nano Lett.*, 2005, **5**, 585-589.
38. Chance, R. R.; Prock, A.; Silbey, R. *J. Chem. Phys.*, 1975, **62**, 2245-2253.
39. Sen, T.; Patra, A. *The Journal of Physical Chemistry C*, 2008, **112**, 3216-3222.
40. Haldar, K. K.; Sen, T.; Patra, A. *J. Phys. Chem. C*, 2008, **112**, 11650-11656.
41. Sen, T.; Haldar, K. K.; Patra, A. *J. Phys. Chem. C*, 2008, **112**, 17945-17951.
42. Sen, T.; Mandal, S.; Haldar, S.; Chattopadhyay, K.; Patra, A. *J. Phys. Chem. C*, 2011, **115**, 24037-24044.
43. Vimal, T.; Pujar, G. H.; Agrahari, K.; Inamdar, S. R.; Manohar, R. *Phys. Rev. E*, 2021, **103**, 022708.
44. Chen, C.; Midelet, C.; Bhuckory, S.; Hildebrandt, N.; Werts, M. H. V. *J. Phys. Chem. C*, 2018, **122**, 17566-17574.
45. Singh, M. P.; Strouse, G. F. *J. Am. Chem. Soc.*, 2010, **132**, 9383-9391.
46. Yun, C. S.; Javier, A.; Jennings, T.; Fisher, M.; Hira, S.; Peterson, S.; Hopkins, B.; Reich, N. O.; Strouse, G. F. *J. Am. Chem. Soc.*, 2005, **127**, 3115-3119.
47. Pang, J.; Xie, R.; Chua, S.; Zou, Y.; Tang, M.; Zhang, F.; Chai, F. *Spectrochim. Acta A Mol. Biomol. Spectrosc.*, 2021, **261**, 120035.
48. Luo, S.; Yang, S.; Wang, X.; Sun, C. *Chemosphere*, 2010, **79**, 672-678.
49. Christensen, S. T.; Feng, H.; Libera, J. L.; Guo, N.; Miller, J. T.; Stair, P. C.; Elam, J. W. *Nano Lett.*, 2010, **10**, 3047-3051.
50. Huang, H.; Li, H.; Feng, J.-J.; Wang, A.-J. Wang, *Sens. Actuators B: Chem.*, 2016, **223**, 550-556.
51. Gopinath, K.; Kumaraguru, S.; Bhakyaraj, K.; Mohan, S.; Venkatesh, K. S.; Esakkirajan, M.; Kaleeswarran, P.; Alharbi, N. S.; Kadaikunnan, S.; Govindarajan, M.; Benelli, G.; Arumugam A. *Microb. Pathog.*, 2016, **101**, 1-11.
52. Shojaeifard, Z.; Heidari, N.; Hemmateenejad, B. *Spectrochim. Acta A Mol. Biomol. Spectrosc.*, 2019, **209**, 202-208.
53. Jena, P.; Bhattacharya, M.; Bhattacharjee, G.; Satpati, B.; Mukherjee, P.; Senapati, D.; Srinivasan, R. *Nanoscale*, 2020, **12**, 3731-3749.
54. Ganguly, M.; Pal, A.; Negishi, Y.; Pal, T. *Langmuir*, 2013, **29**, 2033-2043.

55. Patela, U. Ankita.; Jani, G. K.; Ranchc. K.; Patila. K.; Dharamsi. A. *Int. j. pharm. biol. sci.*, **8**, 5.
56. Henglein, A. *Chem. Phys. Lett.*, 1989, **154**, 473-476.
57. Xu, P.; Lu, X.; Zhao, J.; Li, Y.; Chen, S.; Xue, J.; Ou, W.; Han, S.; Ding, Y.; Ni, W. *Nano*, 2016, **11**, 1650099.
58. Kumar, M.; Dey, J.; Verma, M. S.; Chandra, M. *Nanoscale*, 2020, **12**, 11612-11618.
59. Yuvasri, G. S.; Goswami, N.; Xie, J. in *Principles and Applications of Aggregation-Induced Emission*, eds. Y. Tang and B. Z. Tang, Springer International Publishing, Cham, 2019, DOI: 10.1007/978-3-319-99037-8_10, pp. 265-289.
60. Jana, J.; Aditya, T.; Pal, T. *Dalton Trans.*, 2018, **47**, 3580-3587.
61. Link, S.; El-Sayed, M. A. *Int. Rev. Phys. Chem.*, 2000, **19**, 409-453.
62. Altunbek, M.; Kuku, G.; Culha, M. *Molecules*, 2016, **21**. 1617 (1-18).
63. Meen, T.-H.; Tsai, J.-K.; Chao, S.-M.; Lin, Y.-C.; Wu, T.-C.; Chang, T.-Y.; Ji, L.-W.; Water, W.; Chen, W.-R.; Tang, I. T.; Huang, C.-J. *Nanoscale Res. Lett.*, 2013, **8**, 450.
64. Jana, N. R.; Gearheart, L.; Murphy, C. J. *J. Phys. Chem. B*, 2001, **105**, 4065-4067.
65. Zhao, C.; Hong, C.-y.; Lin, Z.-z.; Chen, X.-m.; Huang, Z.-Y. Huang. *Microchim. Acta*, 2019, **186**, 322.
66. Song, J.; Huang, P.-C.; Wan, Y.-Q.; Wu, F.-Y. Wu. *Sens. Actuators B: Chem.*, 2016, **222**, 790-796.
67. Toma, H.; Zamarion, V.; Toma, S.; Araki, K. *Review J. Braz. Chem. Soc*, 2010, **21**, 1158-1176.
68. Jaschke, M.; Butt, H. J.; Gaub, H. E.; Manne, S. *Langmuir*, 1997, **13**, 1381-1384.
69. Nikoobakht, B.; El-Sayed, M. A. *Langmuir*, 2001, **17**, 6368-6374.
70. Yang, Y.; Shi, J.; Tanaka, T.; Nogami, M. *Langmuir*, 2007, **23**, 12042-12047.
71. Akhuli, A.; Chakraborty, D.; Agrawal, A. K.; Sarkar, M. *Langmuir*, 2021, **37**, 1823-1837.
72. Akhuli, A.; Preeyanka, N.; Chakraborty, D.; Sarkar, M. *ACS Appl. Nano Mater.*, 2022, **5**, 5826-5837.
73. Chatterjee, T.; Mandal, M.; Gude, V.; Bag, P. P.; Mandal, P. K. *Phys. Chem. Chem. Phys.*, 2015, **17**, 20515-20521.
74. Thomas, K. G.; Kamat, P. V. *J. Am. Chem. Soc.*, 2000, **122**, 2655-2656.
75. Chen, Y.; Munechika, K.; Ginger, D. S. *Nano Lett.*, 2007, **7**, 690-696.
76. Xie, F.; Baker, M. S.; Goldys, E. M. *J. Phys. Chem. B*, 2006, **110**, 23085-23091.
77. Kuhnke, K.; Becker, R.; Epple, M.; Kern, K. *Phys. Rev. Lett.*, 1997, **79**, 3246-3249.
78. Lutich, A. A.; Jiang, G.; Susha, A. S.; Rogach, A. L.; Stefani, F. D.; Feldmann, J. *Nano Lett.*, 2009, **9**, 2636-2640.
79. Stevens, D. M.; Qin, Y.; Hillmyer, M. A.; Frisbie, C. D. *J. Phys. Chem. C*, 2009, **113**, 11408-11415.
80. S. K. Haram, A. Kshirsagar, Y. D. Gujarathi, P. P. Ingole, O. A. Nene, G. B. Markad and S. P. Nanavati, *J. Phys. Chem. C*, 2011, **115**, 6243-6249.
81. Shafiee, A.; Salleh, M. M.; Yahaya, M. B. *Sains Malays.*, 2011, **40**, 173-176.
82. Inamdar, S. N.; Ingole, P. P.; Haram, S. K. *ChemPhysChem*, 2008, **9**, 2574-2579.
83. Fukuzumi, S.; Ohkubo, K.; Suenobu, T.; Kato, K.; Fujitsuka, M.; Ito, O. *J. Am. Chem. Soc.*, 2001, **123**, 8459-8467.

84. Heitele, H.; Finckh, P.; Weeren, S.; Poellinger, F.; Michel-Beyerle, M. E. *J. Phys. Chem.*, 1989, **93**, 5173-5179.
85. Pramod, P.; Sudeep, P. K.; Thomas, K. G.; Kamat, P. V. *J. Phys. Chem. B*, 2006, **110**, 20737-20741.
86. Devatha, G.; Roy, P.; Rao, A.; Roy, S.; Pillai, P. P. *J. Phys. Chem. Lett.*, 2020, **11**, 4099-4106.
87. Loumaigne, M.; Praho, R.; Nutarelli, D.; Werts, M. H. V.; Débarre, A. *Phys. Chem. Chem. Phys.*, 2010, **12**, 11004-11014.
88. Kapur, A.; Aldeek, F.; Ji, X.; Safi, M.; Wang, W.; Del Cid, A.; Steinbock, O.; Mattoussi, H. *Bioconjug. Chem.*, 2017, **28**, 678-687.
89. Guo, W.; Wei, Y.; Dai, Z.; Chen, G.; Chu, Y.; Zhao, Y. *Materials (Basel)*, 2018, **11**.
90. Ji, X.; Wang, W.; Mattoussi, H. *Nano Today*, 2016, **11**, 98-121.
91. Jennings, T. L.; Schlatterer, J. C.; Singh, M. P.; Greenbaum, N. L.; Strouse, G. F. Greenbaum and G. F. Strouse, *Nano Lett.*, 2006, **6**, 1318-1324.
92. Bodunov, E. N.; Antonov, Y. A.; Simões Gamboa, A. L. *J. Chem. Phys.*, 2017, **146**, 114102.
93. Kohlrausch, R. *Ann. Phys.*, 1854, **167**, 179-214.
94. Breshike, C. J.; Riskowski, R. A.; Strouse, G. F. *J. Phys. Chem. C*, 2013, **117**, 23942-23949.
95. Hubbard Jr, F. P.; Abbott, N. L. *Soft Matter*, 2008, **4**, 2225-2231.
96. Speranza, F.; Pilkington, G. A.; Dane, T. G.; Cresswell, P. T.; Li, P.; Jacobs, R. M. J.; Arnold, T.; Bouchenoire, L.; Thomas, R. K.; Briscoe, W. H. *Soft Matter*, 2013, **9**, 7028-7041.
97. Agrawal, A. K.; Sahu, P. K.; Seth, S.; Sarkar, M. *J. Phys. Chem. C*, 2019, **123**, 3836-3847.
98. Inokuti, M.; Hirayama, F, *J. Chem. Phys.* **1965**, *43*, 1978-1989.
99. Berberan-Santos, M. N.; Bodunov, E. N.; Valeur, B, *Chem. Phys.* **2005**, *315*, 171-182.
100. Kohlrausch, R, *Annalen der Physik* **1854**, *167*, 179-214.
101. Dexter, D. L, *J. Chem. Phys.* **1953**, *21*, 836-850.
102. Bodunov, E. N.; Antonov, Y. A.; Simões Gamboa, A. L, *J. Chem.l Phys.* **2017**, *146*, 114102.
103. Bodunov, E. N.; Simões Gamboa, A. L, *Semiconductors* **2018**, *52*, 587-589.

Summary and Future Prospects

In the current thesis, our primary objective is to delve into the fundamental aspects underlying the interaction between luminescent coinage metal nanoclusters and analytes of significant importance in both biological and environmental contexts. Furthermore, we have endeavoured to comprehend the crucial influence of the surface chemistry of coinage metal nanoclusters (MNCs) on the binding events with target analytes, as well as its impact on catalysis. These investigations have been conducted utilizing a diverse range of spectroscopic and microscopic techniques, implemented at both ensemble-average and single-particle levels. The significant findings of the current thesis work are outlined below:

(i) It has been observed that the interaction between ultra-small sized MNCs, particularly CuNCs and biomolecules (BSA) does not mediated through "protein-corona" formation which is typically observed with larger nanoparticles when exposed to biological fluids.

(ii) CuNCs can act as effective enzyme inhibitors with regard to the activity modulation of α-Chymotrypsin.

(iii) Notably, our investigations have revealed that the surface ligands of MNCs play a substantial role in shaping the interaction events with target analytes. This influence encompasses the binding mode, thermodynamics of binding, regulation of enzyme activity, and catalysis of a reaction.

(iv) A material-based nanoscale fluorescence sensory system (chitosan capped CuNCs) has been developed for the selective and sensitive detection of highly reactive oxidative species (hROS) and antioxidants within a single chemical entity.

(v) A nanohybrid assembly, consisting of F-AgAu and AuNPs, has been successfully developed. Research findings indicate that efficient excitation energy transfer occurs from F-AgAu to AuNPs, and this process can be regulated by modifying the surface of AuNPs with CTAB.

The current research offers several important physical insights, particularly in understanding the interaction between MNCs and crucial analytes. These insights are expected to be valuable from an application standpoint. It is to be noted here that, in this thesis work, in vivo studies utilizing these systems have not been conducted. This avenue remains open for exploration in the near future, potentially offering real-time applications of the developed systems. Moreover, theoretical studies employing quantum mechanical calculations are anticipated to provide further insights into this aspect.